Université Paris Cité

École Doctorale n°474
Frontière de l'Innovation en Recherche et Education (FIRE)

Institut Curie, Laboratoire Physique des Cellules et Cancer (UMR168)
Équipe Macromolécules et Microsystèmes en Biologie et en Médecine (MMBM)

Tumor-on-Chip Modeling of Pancreatic Ductal Adenocarcinoma (PDAC) Microenvironment Modulation by Photothermal Therapy (PTT) and Epithelial-Mesenchymal Transition (EMT) Dynamics

Thèse de Doctorat en Technologies d'Application Médicale, Diagnostiques, Thérapies et Santé Publique

Présentée par

Anastasiia DUBROVA

Dirigée par **Stéphanie DESCROIX** et **Claire WILHELM**

Soutenue publiquement le **20 novembre 2025**
Devant le jury composé de :

Jaap DEN TOONDER Professeur, Eindhoven University of Technology	Rapporteur
Julie GUILLERMET-GUIBERT DR, CRCT Inserm Toulouse	Rapportrice
Xavier GIDROL DR, Centre CEA de Grenoble	Examinateur
Miryana HEMADI Professeur, Université Paris Cité	Examinatrice
Claire WILHELM DR, CNRS, Institut Curie	Directrice de thèse
Stéphanie DESCROIX DR, CNRS, Institut Curie	Directrice de thèse



INSTITUT
PIERRE-GILLES
DE GENNES
Pour la microfluidique

aviesan
alliance nationale
pour les sciences de la vie et de la santé
ITMO Cancer

Abstract

Pancreatic ductal adenocarcinoma (PDAC) remains one of the most lethal malignancies, characterized by an aggressive biology and a highly treatment-resistant tumor microenvironment. Conventional preclinical models often fail to capture the complexity of PDAC and provide only limited control over individual parameters and their response to treatments, thereby restricting the translation to innovative therapies. Addressing this challenge requires the development of physiologically relevant platforms capable of faithfully recapitulating tumor-stromal interactions and enabling systematic therapeutic evaluation.

This work leverages advanced PDAC-on-chip models as a versatile framework for both biological investigation and preclinical testing. Building on comprehensive analysis of PDAC biology, promising nanoparticle-mediated photothermal therapy (NP-PTT), and existing tumor-on-chip strategies, the research first establishes proof of concept by integrating NP-PTT into a simplified PDAC-on-chip system. This enables controlled assessment of dual-action approaches targeting both cancer cells and their microenvironment. The model is then progressively refined through stepwise complexification, incorporating key stromal elements such as hyaluronic acid and primary stellate cells/cancer-associated fibroblasts. This evolution allows systematic study of epithelial-mesenchymal transition dynamics as a functional readout of stromal cues' importance in relevant *in vitro* model development for prospective therapeutic testing.

Collectively, this work offers a blueprint for the next generation of PDAC-on-chip platforms that move beyond proof-of-concept. By dissecting individual microenvironmental drivers while enabling integration of complexity, these models can serve as translationally relevant tools for mechanistic insight and therapeutic optimization. Ultimately, the convergence of engineered tumor-on-chip systems with innovative treatments such as NP-PTT holds promise to accelerate the development of more effective and personalized strategies against pancreatic cancer.

Keywords: Pancreatic ductal adenocarcinoma – Tumor microenvironment – Tumor-on-chip – Nanoparticle-mediated photothermal therapy – Tumor-stroma interactions – Epithelial-mesenchymal transition

Modélisation sur puce de la tumeur et du microenvironnement de l'adénocarcinome canalaire pancréatique (PDAC) : influence de la thérapie photothermique (PTT) et des dynamiques de transition épithélio-mésenchymateuse (EMT)

Résumé (version française)

L'adénocarcinome canalaire pancréatique (PDAC) demeure l'une des pathologies malignes les plus léthales, caractérisée par une biologie agressive et un microenvironnement fortement résistant aux traitements. La plupart des modèles précliniques conventionnels ne reproduisent pas intégralement la complexité du PDAC et restent limités dans leur capacité à contrôler finement les paramètres individuels et ainsi de mieux comprendre les réponses thérapeutiques. Relever ce défi nécessite le développement de plateformes physiologiquement pertinentes capables notamment de reproduire les interactions tumeur-stroma et de permettre une évaluation thérapeutique systématique.

Ce travail exploite des modèles avancés de PDAC-on-chip à la fois pour l'investigation biologique et les tests précliniques. S'appuyant sur une analyse approfondie de la biologie du PDAC, sur le potentiel prometteur de la photothermie induite par des nanoparticules (NP-PTT) et sur les stratégies existantes de tumor-on-chip, mon projet de thèse a d'abord permis d'établir une preuve de concept intégrant la NP-PTT dans un système PDAC-on-chip simplifié. Cela a permis de mieux comprendre l'effet de la NP-PTT et de sa double action ciblant à la fois les cellules cancéreuses mais aussi leur microenvironnement. Ce modèle de PDAC a ensuite été amélioré en complexifiant progressivement le modèle et plus particulièrement en intégrant des éléments stromaux clés tels que l'acide hyaluronique et des cellules stellaires primaires/fibroblastes associés au cancer. Cette nouvelle génération de PDAC on chip a ainsi permis l'étude systématique des dynamiques de transition épithélio-mesenchymateuse comme indicateur de l'importance des signaux stromaux dans le développement de modèles *in vitro* de PDAC.

Ce travail ouvre ainsi la voie à une nouvelle génération de modèles précliniques visant à mieux comprendre les mécanismes sous-jacents, à accélérer le développement de nouvelles thérapies et à favoriser les avancées translationnelles dans le traitement du PDAC.

Mots-clés : Adénocarcinome canalaire pancréatique – Microenvironnement tumoral – Tumor-on-chip – NP-PTT – Interactions tumeur-stroma – Transition épithélio-mésenchymateuse

TABLE OF CONTENTS

Abstract 2

Résumé (version française) 3

GLOSSARY 9

GENERAL INTRODUCTION 11

CHAPTER 1 Introduction 13

1. Clinical and Biological Background of PDAC 14

1.1 Epidemiology and Prognosis 14

1.2 Pathological and Molecular Foundations of PDAC Initiation 15
1.2.1 PDAC cell of origin & initiation hypothesis 15
1.2.2 PDAC mutational burden 17

1.3 Desmoplastic Stroma and Cellular Reprogramming in PDAC 20
1.3.1 Cellular Components of PDAC TME 20
1.3.2 Extracellular Matrix and its Remodeling in PDAC 29
1.3.3 Epithelial-Mesenchymal Transition (EMT) and Cellular Plasticity 34

1.4 Therapeutic Implications 37

2. Nanoparticle-mediated Photothermal Therapy (NP-PTT): toward alternative treatment paradigms 38

2.1 Hyperthermia as Cancer Treatment 38

2.2 Nanotechnology and Hyperthermia: Photothermia Focus 40

2.3 NP-PTT in PDAC 42

3. State-of-the-art of PDAC preclinical models 51

3.1 Tumor-on-chip models to bridge the gap between preclinical development and clinical applications 51

3.2 PDAC-on-chip: current landscape 53

4. Summary and Thesis Rationale 60

4.1 Research gap 60

4.2 Thesis Scope and Objectives 62

CHAPTER 2 Magnetite Nanoparticle Photothermal Therapy in a Pancreatic Tumor-on-Chip: A Dual-Action Approach Targeting Cancer and its Microenvironment 65

Context & Motivations 66

ABSTRACT 69

TABLE OF CONTENTS 69

I. INTRODUCTION 70

II. RESULTS 73
1. Magnetite Nanoparticles for NIR Photothermia 73

2. PDAC Tumor-on-Chip 3D Model 75
3. Administration of Magnetite Nanoparticles in Tumor-on-Chip 77
4. Implementation of MagNP-PTT in PDAC tumor-on-chip and its Impact on Collagen Matrix 79
5. PTT-Induced Cell Death in PDAC tumor-on-chip: Effects of Rest Time and EMT Impact 83

III. DISCUSSION *88*

IV. CONCLUSION *90*

V. EXPERIMENTAL PROCEDURES *91*

VI. SUPPLEMENTARY INFORMATION *97*

Challenges, limitations & future directions **103**

CHAPTER 3 Bioengineering a Complex PDAC-on-Chip Microenvironment to Replicate *In Vivo*-like EMT **109**

Context and Motivations **110**

ABSTRACT *112*

TABLE OF CONTENTS *112*

I. INTRODUCTION *113*

II. RESULTS *115*
1. Comparative analysis of PDAC cell lines for relevant model selection 115
2. Mid, but not low, molecular weight HA enhances CD44 expression in cancer spheroids on chip when incorporated at single-cell stage 120
3. Incorporation of mid molecular weight HA in PDAC-on-chip is associated with a moderate EMT shift 123
4. Stromal conditioned media, but not direct single-CAF co-culture, drives EMT in PDAC-on-chip 126

III. DISCUSSION *129*

IV. EXPERIMENTAL PROCEDURES *133*

V. SUPPLEMENTARY INFORMATION *138*

Challenges, limitations & future directions **143**

GENERAL CONCLUSION **154**

REFERENCES **157**

ANNEX A **187**

ANNEX B **219**

LIST OF FIGURES

Figure 1.1: Latest available PDAC cancer statistics in the scope of other cancers worldwide. **15**

Figure 1.2: Initiation and progression of pancreatic cancer. **18**

Figure 1.3: Schematic representation of the complex PDAC microenvironment with various cell types and critical characteristics that impact therapy failure. **21**

Figure 1.4: PSCs transition from quiescent to activated state. **22**

Figure 1.5: Crosstalk between pancreatic cancer cells and components of the tumor microenvironment. **23**

Figure 1.6: Summary of the acknowledged tumor-promoting and tumor-restraining CAF populations in PDAC. **27**

Figure 1.7: ECM alterations in PDAC. **29**

Figure 1.8: Hyaluronic acid and its primary signaling cascades. **33**

Figure 1.9: EMT in PDAC progression and TME remodeling. **36**

Figure 1.10: Mechanism of NP-PTT in cancer. **41**

Figure 1.11: PDAC-on-chip systems. **55**

Figure 2.1. Magnetite nanoparticle physico-chemical investigation. **75**

Figure 2.2: Development of the 3D PDAC tumor-on-chip model. **76**

Figure 2.3: Administration of magnetite nanoparticles and imaging within tumor-on-chip. **79**

Figure 2.4: Nanoparticle-mediated photothermia heating setup and matrix impact characterization. **83**

Figure 2.5: Temperature-dependent cells death evaluation after MagNP-PTT. **85**

Figure 2.6: Characterization of MagNP-PTT effects of tumor spheroids gene expression. **87**

Figure 2.S1 : Fe_3O_4@PO-PEG-NH_3^+ hydrodynamic diameter and zeta potential. Magnetization curves. **97**

Figure 2.S2 : Vis-NIR absorbance spectra of Fe_3O_4 NPs. **97**

Figure 2.S3 : 3D PDAC model in collagen type I on chip with characteristic protrusions. **97**

Figure 2.S4 : Alamar Blue cell metabolic activity analysis of healthy human mesenchymal stem cells (hMSCs) vs pancreatic cancer cells (PANC-1) as a function of MagnNPs. **98**

Figure 2.S5 : Laser surface power distribution at P_{laser}=2 W at 6,1 cm vs 4 cm distance with Gaussian nonlinear fit through least squares regression. **98**

Figure 2.S6 : Comparison of two-photon second harmonic generation (SHG) microscopy imaging with collagen hybridizing peptide imaged with confocal microscopy for collagen fiber visualization. **98**

Figure 2.S7 : Nanoparticle-mediated photothermia matrix impact characterization. **99**

Figure 2.S8 : Nanoparticle-mediated photothermia impact on collagen fiber structure. **100**

Figure 2.S9 : 3D PDAC model in collagen type I on chip, control no NPs, 2W/cm^2 PTT. **100**

Figure 2.SS1: Collagen hybridizing peptide staining imaging of various collagen matrices generated under identical conditions imaged with confocal microscopy. **105**

Figure 2.SS2: Collagen hybridizing peptide staining imaging of collagen matrices response to NP-PTT around 46°C imaged with confocal microscopy. **106**

Figure 3.1: Comparative analysis of spheroid features from five PDAC cell lines. **117**

Figure 3.2: EMT marker expression and on-chip viability assessment of epithelial cell line-spheroids. **119**

Figure 3.3: Impact of hyaluronic acid (HA) on CD44 expression in PDAC-on-chip as a function of molecular weight, time and incorporation method. **122**

Figure 3.4: Impact of hyaluronic acid (HA) on EMT marker expression in PDAC-on-chip as a function of molecular weight, time and incorporation method. **125**

Figure 3.5: Impact of CAF-derived stromal factors on EMT marker expression in PDAC-on-chip as a function of time and exposure method. **128**

Figure 3.S1: Comparative analysis of spheroid formation from five PDAC cell lines in agarose micromolded 6-well plates, 5x10^5 cell/well. **138**

Figure 3.S2: Comparative analysis of spheroid formation from five PDAC cell lines in agarose micromolded 6-well plates, 1x10^6 cell/well. **139**

Figure 3.S3: Alcian blue staining to quantify HA presence change in a collagen matrix over 7 days. **140**

Figure 3.S4: Evolution of spheroids' area in PDAC-on-chip. **141**

Figure 3.SS1: Impact of CAF-derived stromal factors on EMT marker expression in PDAC-on-chip as a function of time and exposure method. **144**

Figure 3.SS2: Examples of E-cadherin and Vimentin markers imaging that may induce inconsistencies in automatized image processing algorithms. **145**

Figure 3.SS3: Impact of hyaluronan on spheroid CD44 & E-cadherin marker correlation and CD44 overexpression in PDAC-on-chip as a function of time and exposure method. **147**

Figure 3.SS4: Hybrid spheroid (HPAF:HPaSteC 1:5) monitoring for EMT markers over time. **150**

Figure 3.SS5: Viability of PDAC spheroids co-cultured with single CAFs in collagen on chip 24h following NP-PTT exposure. **152**

LIST OF TABLES

Table 1.1: Summary of the NP-PTT studies in the context of PDAC treatment development. _____ **45**

Table 1.2: Summary of the PDAC-on-chip models available in literature up to date._____ **57**

Table 2.S1 : List of primer sequences used in RT-qPCR. _____ **101**

GLOSSARY

α-SMA	α-smooth muscle actin
ADM	Acinar-to-ductal metaplasia
apCAF	Antigen-presenting cancer-associated fibroblast
CAF	Cancer-associated fibroblast
DMEM	Dulbecco's modified Eagle's medium
ECM	Extracellular matrix
EMT	Epithelial-mesenchymal transition
EndMT	Endothelial-to-mesenchymal transition
FBS	Fetal bovine serum
GLOBOCAN	Global Cancer Observatory
iCAF	Inflammatory cancer-associated fibroblast
IONPs	Iron oxide nanoparticles
IPMN	Intraductal papillary mucinous neoplasm
MCN	Mucinous cystic neoplasm
MDSC	Myeloid-derived suppressor cell
MHT	Magnetic hyperthermia
MMP	Matrix metalloproteinase
MSC	Mesenchymal stem cell
myCAF	Myofibroblastic cancer-associated fibroblast
NIR	Near-infrared
NP	Nanoparticle
NP-PTT	Nanoparticle-mediated photothermia
P/S	Penicillin/streptomycin
PanIN	Pancreatic intraepithelial neoplasia

PanNET	Pancreatic neuroendocrine tumor
PBS	Phosphate buffer saline
PDAC	Pancreatic ductal adenocarcinoma
PDMS	Polydimethylsiloxane
PDO	Patient-derived organoid
PDX	Patient-derived xenograft
PSC	Pancreatic stellate cell
PTT	Photothermal therapy
TAM	Tumor-associated macrophage
TIMP	Tissue inhibitor of metalloproteinase
TME	Tumor microenvironment
ToC	Tumor-on-chip

GENERAL INTRODUCTION

While the word "cancer" may soon eclipse heart disease in the tally of lives it claims, pancreatic cancer, and pancreatic ductal adenocarcinoma (PDAC) in particular, remain one of the most aggressive and treatment-refractory cancers, with a five-year survival rate still in the single digits despite decades of research. This is more than a cold statistic — it is a profound shift in the landscape of global health that calls for understanding. Yet the burden of this rise is not uniform, as it is shaped by the unique biological and microenvironmental features of PDAC that underlie its poor prognosis. Characterized by an extraordinarily complex tumor microenvironment that creates barriers to drug delivery and therapeutic efficacy, the poor prognosis of this malignancy remains a major challenge. Overcoming it demands a much deeper mechanistic understanding of PDAC biology coupled with innovative strategies for therapy development that faithfully capture the tumor's microenvironment complexity.

Against this backdrop, the development of physiologically relevant PDAC-on-chip platforms has emerged as a critical step toward improving our understanding of the pathology as well as the preclinical evaluation of novel therapies. By enabling controlled reconstruction of tumor-stroma interactions in a 3D microenvironment, such tumor-on-chip devices hold the potential to bridge the gap between simplified *in vitro* models and the complexity of human disease. This approach allows systematic investigation of both tumor biology and therapeutic responses in a controlled yet adaptable setting. Among promising modalities for PDAC treatment, nanoparticle-mediated photothermia (NP-PTT) has emerged, combining targeted cytotoxicity with potential microenvironmental modulation. However, preclinical evaluation of NP-PTT — and other emerging therapies — remains constrained to animal models and oversimplified *in vitro* systems that inadequately recapitulate human PDAC microenvironment and hinder precise assessment of mechanistic implications, thus slowing translational progress.

This thesis addresses these challenges through an integrated research trajectory that combines an in-depth review of PDAC biology with NP-PTT principles and the development of advanced PDAC-on-chip platforms as well as their applications. Together, the three chapters of this thesis form a coherent progression — from conceptual groundwork to experimental innovation and model refinement — aimed at deepening mechanistic insight while advancing translational applications of novel therapies in PDAC.

Chapter 1 lays the foundation by providing a comprehensive bibliographical review of the field. It contextualizes the unique challenges of PDAC biology, surveys the state of nanoparticle-mediated photothermal therapy in the context of PDAC, and examines the current landscape of PDAC-on-chip models. This chapter establishes the rationale for integrating NP-PTT with microfluidic modeling of PDAC and identifies the critical knowledge gaps that this thesis seeks to address.

Chapter 2 presents an original experimental work in the form of a published article. Here, we introduce and validate an NP-PTT-enabled PDAC-on-chip model, applying a dual-action approach that simultaneously targets cancer cells and the surrounding extracellular matrix. This study demonstrates the feasibility of combining NP-PTT with microfluidic PDAC modeling and provides the first proof-of-concept for a platform capable of investigating the interplay between localized photothermal treatment and microenvironmental remodeling.

Chapter 3 extends this work by advancing the complexity of PDAC-on-chip platform. Presented as an article draft, this chapter explores the stepwise complexification of the model to increase its physiological relevance for therapeutic testing. In particular, it investigates the integration of hyaluronic acid, a major extracellular matrix component of PDAC, in parallel with the incorporation of stromal cells-derived cues to model tumor-stroma crosstalk. This chapter focuses on the platform's ability to replicate *in vivo*-characteristic epithelial-mesenchymal transition under varying stromal conditions, thereby providing a systematic framework for evaluating stromal cues importance in the context of PDAC model development and therapy testing.

Collectively, this manuscript develops and applies a multidisciplinary approach that bridges fundamental PDAC biology, therapeutic innovation, and microphysiological modeling. The work presented here offers both conceptual and experimental contributions, establishing a foundation for future advances in the design of next-generation tumor-on-chip models that more faithfully reflect the complexity of PDAC and their application for preclinical evaluation of NP-PTT with the potential to expand to other therapeutic modalities.

CHAPTER 1

Introduction

1. Clinical and Biological Background of PDAC

1.1 Epidemiology and Prognosis

With cancer emerging as the principal cause of death worldwide, pancreatic cancer stands out for its exceptionally poor prognosis, defined by nearly equal incidence and mortality rates. According to the Global Cancer Observatory,[1] while pancreatic cancer ranks 12th in global incidence — far behind more prevalent cancers such as lung, breast, and colorectal, which occur four to five times more frequently (Figure 1.1A) — its mortality rate is disproportionately high. Of the 510,992 cases diagnosed in 2022, 467,409 individuals died by the end of the year. This translates to over 90% mortality, a staggering contrast to the 30%, 50%, and 70% survival rates observed in lung, colorectal, and breast cancers, respectively (Figure 1.1B). Furthermore, the number of pancreatic cancer cases is projected to increase by more than 78% over the next 20 years — the highest growth rate among the major cancer types (Figure 1.1C).

Overall, pancreatic cancer can be subdivided into two types: pancreatic ductal adenocarcinoma (PDAC) and pancreatic neuroendocrine tumor (PanNET). While PanNET arises in the endocrine tissue of the pancreas and accounts for only under 5% of pancreatic cancer cases, PDAC involves abnormality in the exocrine glands of the pancreas and presents the most prevalent pancreatic neoplasm, standing for around 90% of the condition incidence, including its variants.[2,3] Therefore, this work is specifically focused on the study of the latter pancreatic malignancy.

PDAC survival is highly dependent on the cancer stage, in particular, its spreading. As such, in the case of localized PDAC that has not spread outside the pancreas the 5-year relative survival rate is assessed to be around 44%, while for regionally or distantly metastasized cancer this number plummets at 16% and 3% respectively. This brings the surveillance epidemiology, and end results (SEER) stages combined relative survival rate at 8-13% according to different sources.[4–6] Yet a bigger pitfall is in the challenge of early PDAC diagnosis due to asymptomatic disease development. Lack of specificity and sensitivity in the current screening tools results in a poorly trackable malignancy that often progresses silently and rapidly, leading to widespread metastasis. Consequently, despite recent advancements in identifying potential risk factors and in developing early diagnostic methods, most patients are diagnosed when the disease has already progressed, significantly limiting curative treatment options and overall survival.

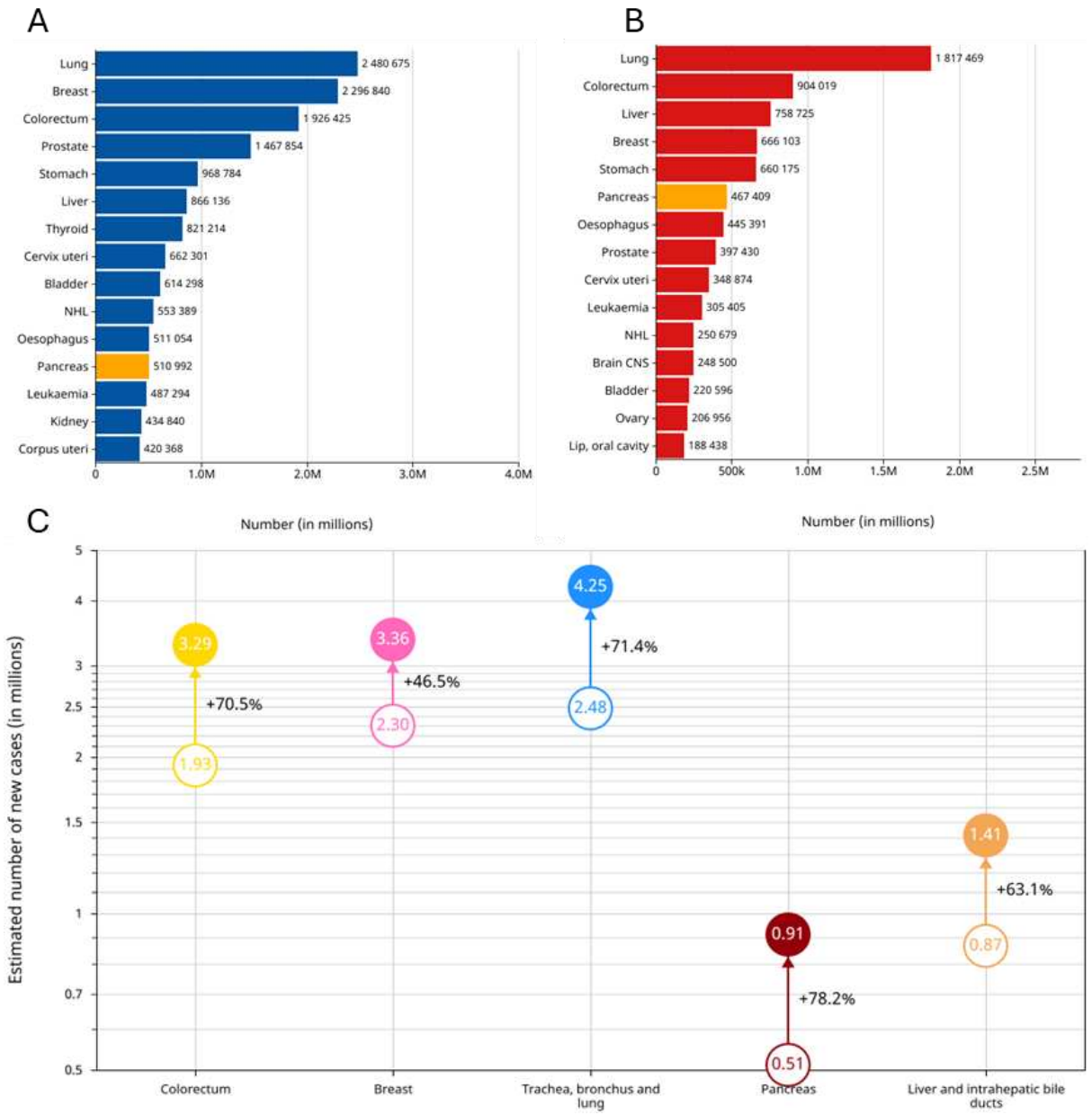


Figure 1.1: Latest available PDAC cancer statistics in the scope of other cancers worldwide. **A**. PDAC vs other cancers incidence rate in 2022. **B**. PDAC vs other cancers mortality rate in 2022. **C**. PDAC vs other top 4 cancers incidence growth trend projection over the next 20 years. *Figures were generated via GLOBOCAN interactive platform*.

1.2 Pathological and Molecular Foundations of PDAC Initiation

1.2.1 PDAC cell of origin & initiation hypothesis

The exocrine gland of pancreas involved in PDAC initiation accounts for over 80% by volume and primarily consists of pancreatic acinar cells, centroacinar cells and duct cells, where the former are responsible for the production of digestive enzymes (e.g., proteases, amylase, lipase, nucleases etc.) and the latter two — for bicarbonate ions to neutralize stomach-derived acidity and create an optimal pH for enzyme activity.[7] In a healthy pancreas, acinar cells are polarized epithelial cells that are terminally differentiated, and

they transport digestive enzymes into the pancreatic ductal network lined with ductal cells that will further facilitate bicarbonate-rich fluid transport into the duodenum, thereby increasing the alkalinity in the small intestine.[8,9]

Similar to other organs in the human body, homeostatic balance within pancreas is crucial for function maintenance through regular cell renewal and, under stress conditions, a characteristic process of acinar-to-ductal metaplasia (ADM). During ADM, fully differentiated acinar cells can dedifferentiate (through embryonic progenitor-like cells) into ductal-like cells, losing their characteristic morphology and function while acquiring ductal-like traits — a process initially aimed at tissue regeneration after injury or inflammation.[8]

However, such cell plasticity is what is often hijacked by tumorigenic processes, eventually leading to pancreatic intraepithelial neoplasias (PanINs) development — microscopic precursor lesions typically resulting in invasive PDAC. Most recent nomenclature identifies three types of morphological grading of lesions, PanIN 1, PanIN 2 and PanIN 3, preceding the fully-developed invasive adenocarcinoma.[9] Such classification is mainly based on nuclear heterogeneity and changes in cellular architecture, with PanIN 1 — the earliest abnormality — characterized by mucin production atypical to healthy ducts and the presence of initial papillary formations, while still preserving nuclear homogeneity and basal positioning. At the PanIN 2 stage, partial loss of nuclear polarity is observed, accompanied by their crowding, cell enlargement, and more pronounced papillary formations. Finally, as PanIN 3 progresses, more severe nuclear and architectural abnormalities are accumulated, such as the complete loss of nuclear polarity, organization and cell cohesion, increase in cell crowding and expansion that distorts the ductal lumen, forming complex architectural patterns (e.g., papillary, cribriform, budding). The changes, however, are still limited to the ductal epithelium at this stage with no stromal invasion. As neoplastic cells in PanIN 3 breach the basement membrane through enzymatic degradation, they invade the surrounding pancreatic tissue, allowing cancer cells to interact and recruit stromal components to build tumor microenvironment (TME).

Other mucin-producing macroscopic cystic precursors to PDAC exist including mucinous cystic neoplasms (MCNs) and intraductal papillary mucinous neoplasms (IPMNs). Unlike PanINs, both IPMNs and MCNs are macroscopically visible and often identified with imaging. IPMNs arise within the pancreatic ductal system, typically in the head of the pancreas, and may involve the ductal network, while MCNs are found exclusively in the pancreatic body or tail and almost entirely in women, characterized by a distinctive ovarian-type stroma. Both lesion types carry a risk of progression to invasive carcinoma, although

typically lower than that of PanINs.[10]

1.2.2 PDAC mutational burden

Based on gene expression profiling, multiple classification systems of PDAC developed over the years[11-13] with newer classifications emerging based on different approaches.[14] There is significant overlap between the various classification systems, where classical and basal-like tumor-specific subtypes represent the most common, simplified classification based on tumor's transcriptional program and differentiation state (Figure 1.2A). While both classical and basal cells can coexist within the same tumor (hybrid), basal tumors were linked with extracellular matrix (ECM)-rich, fibrotic stroma that promotes invasion associated to poor prognosis, and classical tumors correlate with higher chemosensitivity and better prognosis.[14,15]

Due to frequent exposure of pancreas to inflammatory insults (e.g., pancreatitis), oxidative stress and cytokine release increase along with DNA damage, creating a permissive environment for KRAS-driven reprogramming primarily through MAPK/ERK and PI3K signaling pathways. With a somatic KRAS mutation taking place, the regulation is lost, leaving the gene permanently active and its downstream signaling effects — context dependent.[16] Upon combination with inflammatory stimuli (e.g., IL-6, TNF-α, TGF-α, EGF), a mutagenic and pro-survival environment is created, promoting further DNA damage, activating survival pathways and impairing immune surveillance. Furthermore, it is followed by the natural selection of mutant clones to gain growth advantage, resist apoptosis and recruit supportive stroma to become the first seed for PanIN. In addition, transforming growth factor-β (TGFβ)-activated pathway is capable of inducing ADM, thereby favoring KRAS-driven carcinogenesis.[17] When combined with ADM, the metaplastic process becomes irreversible and progressive, leading to the formation of the first low-grade PanINs (Figure 1.2B).[8] KRAS-activating mutation is present in up to 95% of PDAC cases.[18]

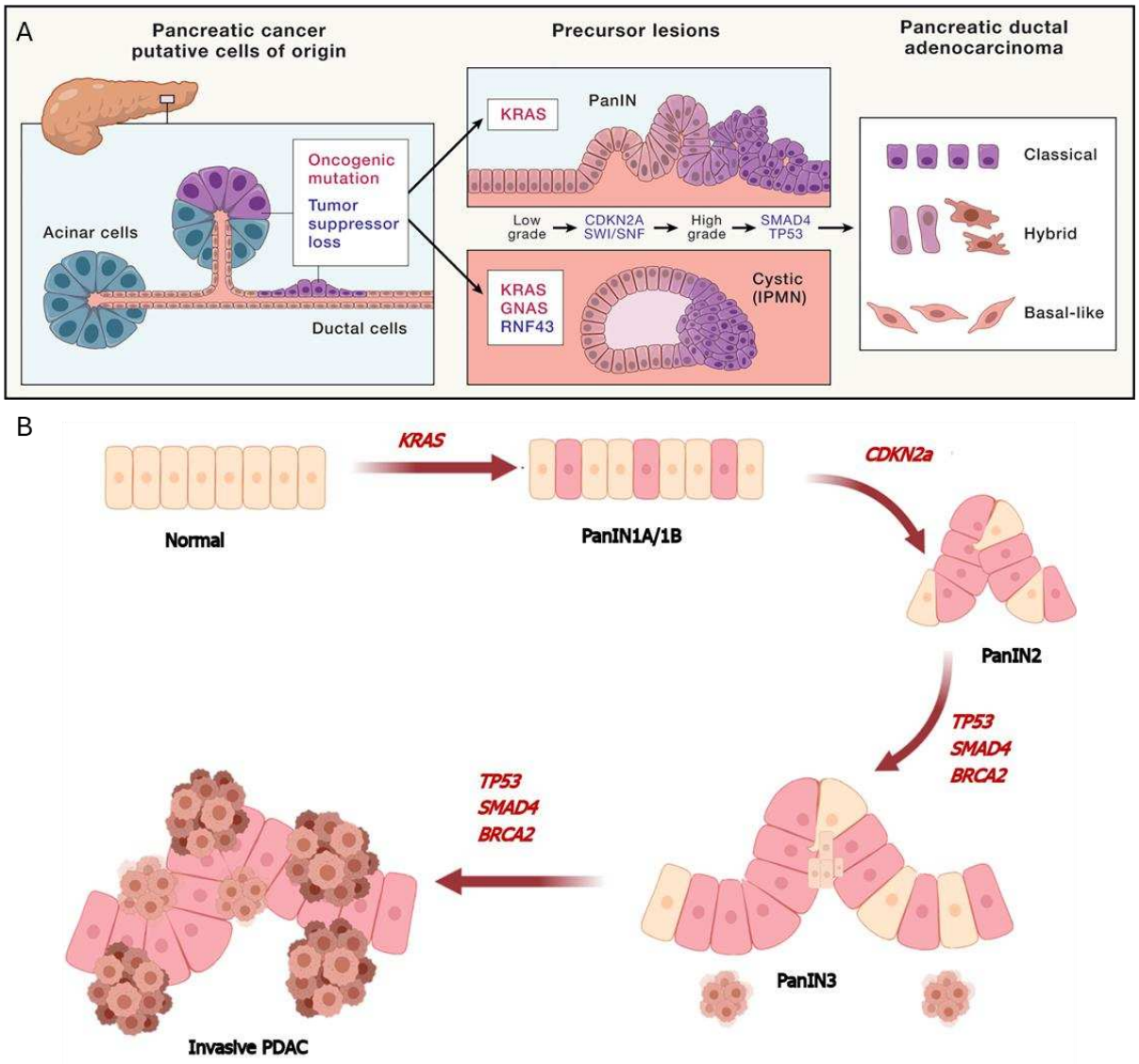


Figure 1.2: Initiation and progression of pancreatic cancer. A. Cancer development from putative cells of origin (acinar and ductal cells) through precursor lesions to PDAC subtypes. Oncogenic mutations and tumor suppressor loss drive transformation. These precursor lesions ultimately give rise to PDAC, classified into classical, hybrid, and basal-like molecular subtypes. *(Adapted from Halbrook et al., Cell. 2023.)* **B**. Stepwise progression from normal pancreatic ductal epithelium to invasive PDAC through several PanIN stages. An initial KRAS mutation drives the transition from normal cells to PanIN 1A/1B. Loss of CDKN2A promotes progression to PanIN2, followed by alterations in TP53, SMAD4, BRCA2 leading to high-grade PanIN3. *(Adapted from Sim et al., World Journal of Gastroenterology. 2022.)*

As PanINs progress toward invasive malignancy, further genetic alterations accumulate. Second most commonly altered gene in PDAC is CDKN2A (p16) that is typically lost or mutated during intermediate-grade PanIN development (PanIN 2) and is found in approximately 90% of PDAC cases.[10,18–20] CDKN2A encodes a crucial cell-cycle regulator, p16/INK4A, that is responsible for pausing cell cycle progression from G1 to S phase, thereby controlling cell division under inappropriate conditions. When inactivated or mutated, it leads to uncontrolled proliferation and tumor progression. With KRAS-mutated

cells already present at this stage, CDKN2A loss enables them to bypass senescence, further promoting tumorigenesis (Figure 1.2B).

Progressing towards high-grade dysplasia, inactivating somatic mutations in TP53 and SMAD4 tumor suppressor genes occur (Figure1.2B). TP53 encodes a transcription factor commonly known as the "guardian of the genome", and is the most frequently mutated gene in human cancers.[21] In PDAC, the gene is mutated in up to 85% of cases[22], with the mutant p53 protein typically acquiring gain-of-function properties that promote unchecked cell division, impair DNA damage response pathways (including G1/S and G2/M checkpoints' loss), suppress pro-apoptotic genes, and foster epithelial-mesenchymal transition (EMT). In addition, CDKN2A products further support TP53 function by stabilizing p53, making their concurrent inactivation a significant driver of accelerated tumor progression.[23]

As atypia propagates through PanIN 3, SMAD4 inactivation typically occurs just before the emergence of fully invasive PDAC. While SMAD4 encodes a central mediator of the TGFβ signaling pathway and acts as its key co-transcription factor, this gene's loss-of-function mutation is present in over 50% of pancreatic cancer cases. However, a substantial subset of SMAD4 wild-type PDACs harbor mutations in other TGFβ pathway components (e.g., TGFβR1, TGFβR2, ACVR1B or SMAD3), ultimately disrupting TGFβ signaling through alternative routes. With SMAD4 lost, TGFβ is decoupled from its tumor-suppressive roles and is able to enter SMAD-independent pro-tumorigenic pathways.[22]

Altogether, these four mutations represent the classical, well-established genetic hallmarks of PDAC development and are commonly found in the cells that breach the epithelial basement membrane, driving the transition from PanIN 3 to invasive carcinoma. Although the canonical mutations are prevalent across both classical and basal PDAC subtypes, certain patterns suggest a higher frequency of TP53 and SMAD4 mutations in basal-like tumors, contributing to the more aggressive disease course. However, these mutations are not exclusive to any single subtype, and other factors contribute to the molecular heterogeneity observed in PDAC.[24] While the mutational landscape of PDAC extends beyond these core alterations, including BRCA2 or less frequent mutations in genes, such as ARID1A or MLL3, these lie beyond the scope of this chapter. In addition, it is evidenced that these gene mutations provoke synergistic and co-dependent effects, yielding a sophisticated tumorigenic network that is yet to be fully understood.[22] Once these mutations are acquired and the barrier is crossed, the transformed cells gain the ability to interact with and remodel the surrounding stromal microenvironment.

1.3 Desmoplastic Stroma and Cellular Reprogramming in PDAC

PDAC stands out from other solid tumors due to its extreme desmoplasia and stromal predominance, which can constitute up to 90% of the total tumor volume.[25,26] This characteristic is attributed to the dense accumulation of ECM proteins and a diverse array of stromal cells that continuously engage in dynamic and reciprocal interactions, rendering the PDAC's TME highly dynamic and multifunctional. The excessive and aberrant fibrotic response to tumor growth — referred to as desmoplastic reaction or **desmoplasia** — drives further ECM deposition and extensive stromal remodeling. Indeed, the PDAC microenvironment is abundant in both a variety of cells including pancreatic stellate cells (PSC), various subtypes of cancer-associated fibroblasts (CAFs) and immune cells (tumor-associated macrophages (TAM), myeloid-derived suppressor cells (MDSC), regulatory T&B cells) along with nerve cells as well as a wide range of ECM components such as collagen, fibronectin, laminin, hyaluronic acid, among others.[27,28] Altogether, this complex desmoplastic stroma functions not only as a structural scaffold but also as a key regulator of tumor progression, immune evasion, and therapeutic resistance (Figure 1.3).

1.3.1 Cellular Components of PDAC TME

While desmoplasia had long been recognized as a hallmark of pancreatic cancer, its active roles in tumorigenesis, angiogenesis, therapy resistance, and metastasis facilitation became more evident following the isolation and experimental application of pancreatic stellate cells (PSCs) in 1998.[29-31] Currently, PSCs are believed to be the primary generators of rich PDAC stroma with increased evidence of PSCs playing vital roles in both healthy and malignant pancreas functioning.[32]

PSCs are resident cells of the healthy pancreas, located close to the basolateral aspects of pancreatic acinar cells or surrounding the pancreatic ducts and blood vessels. These cells comprise approximately 4-7% of pancreas parenchyma and are primarily recognized for storing vitamin A-rich cytoplasmic lipid droplets in their quiescent state.[33,34] In the healthy pancreas, quiescent PSCs are thought to regulate ECM turnover via balanced production of matrix metalloproteinases (MMPs) and tissue inhibitors of metalloproteinases (TIMPs), contribute to structural homeostasis of the tissue, and possibly participate in localized innate immune functions and exocrine support.[35] However, the full extent of their physiological roles under basal conditions remains incompletely understood.

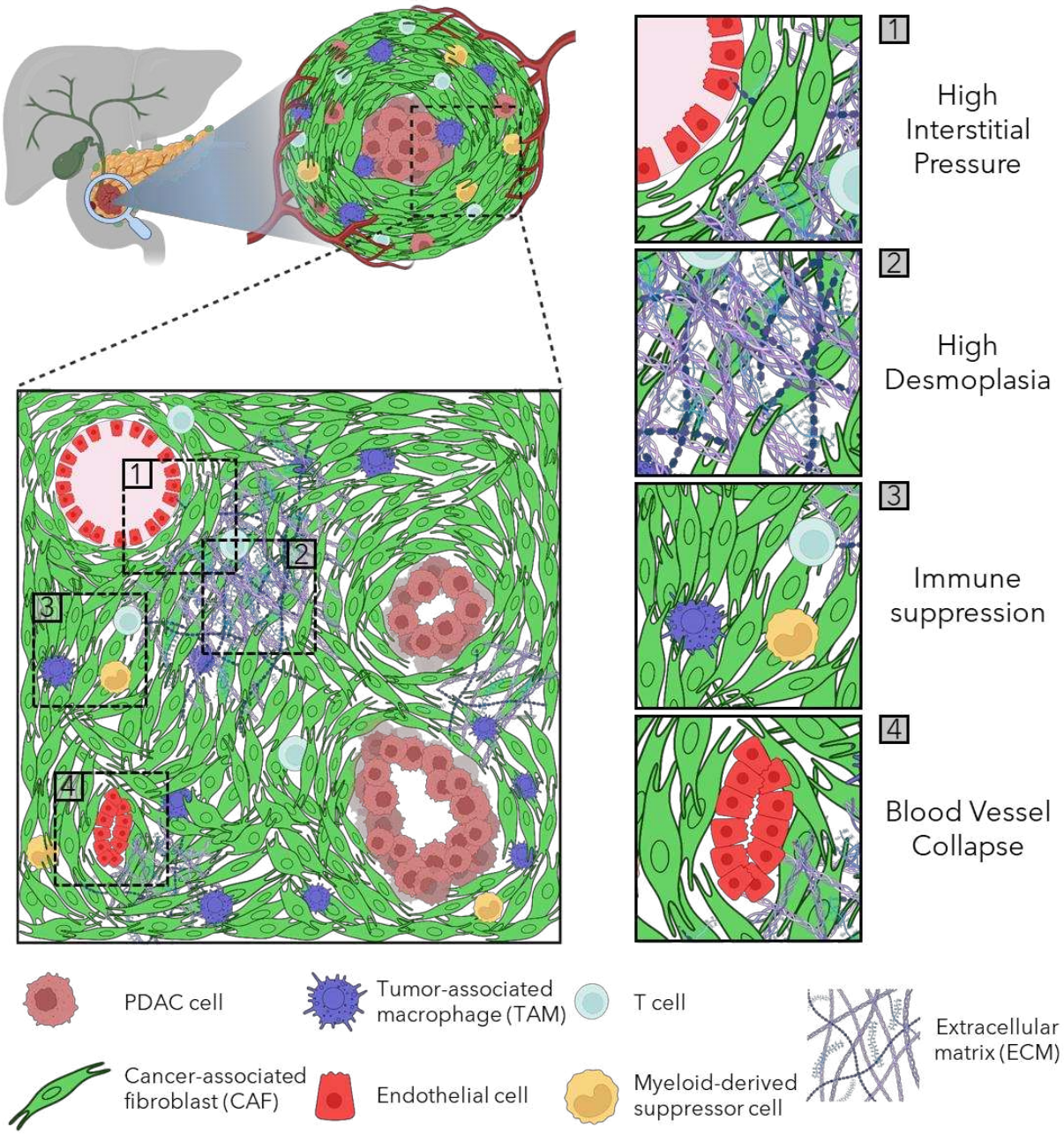


Figure 1.3: Schematic representation of the complex PDAC microenvironment with various cell types and critical characteristics that impact therapy failure. *(Adapted from Heinrich et al., Advanced Drud Delivery Reviews. 2021.)*

Now, the tables turn completely when PSCs become activated as early as during primary stages of PanINs. In response to external stress, such as pancreatic injury or inflammation, dormant PSCs are activated and transdifferentiated into myofibroblast-like cells, characterized by the loss of vitamin A-containing lipid droplets and the expression of α-smooth muscle actin (α-SMA, ACTA2), a hallmark of their activated state (Figure 1.4). Activated PSCs migrate from their original niches and accumulate densely around tumor glands, while also becoming widely distributed throughout the tumor stroma.[36]

Once activated, PSCs become one of the key drivers of ECM remodeling, particularly

through the production of fibrillar collagens type I and III, which increase matrix stiffness, as well as other ECM components like fibronectin, laminin, hyaluronan, and ECM-remodeling enzymes such as MMPs and TIMPs (Figure 1.4). Moreover, activated PSCs proliferate significantly more than their quiescent counterparts and can comprise up to 50% of the desmoplastic stroma, thereby amplifying ECM deposition and the secretion of cytokines and chemokines. This excessive ECM accumulation leads to fibrosis and disrupts normal pancreatic tissue architecture and function.[35,37]

Extracellular signals involved in fibrogenesis during PDAC include a wide range of activating stimuli: cytokines and growth factors (e.g., TGF-β, CTGF, IL-6, IL-10, TNF-α, PDGF), hypoxia-related factors such as HIF-1, oxidative stress, non-coding RNAs, ion fluxes, and several oncogenic signaling pathways including Sonic Hedgehog (SHH), PI3K/AKT, Notch, WNT/β-catenin, MAPK, Rho/ROCK, NF-κB, and JAK/STAT among others. Several reviews have comprehensively detailed these signaling mechanisms involved in PSC activation.[38-40]

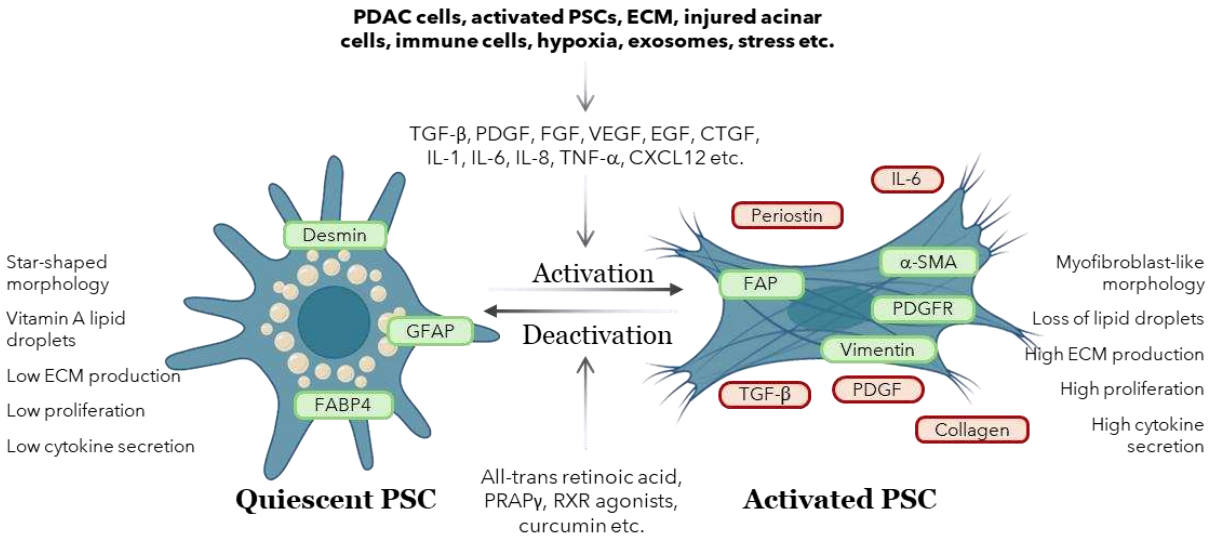


Figure 1.4: PSCs transition from quiescent to activated state. Quiescent PSCs store vitamin A in lipid droplets and express markers like desmin, GFAP, FABP4 among others, while activated PSCs lose lipid droplets, upregulate α-SMA, vimentin, FAP among others and secrete profibrotic and pro-tumorigenic factors.

The resulting fibrotic matrix generates high solid stresses that compress intratumoral blood vessels, reducing perfusion and oxygenation, thereby fostering hypoxia and impairing vascular function and effective angiogenesis.[41,42] Increased matrix stiffness and inflammatory signaling subsequently support autocrine signaling of PSCs, sustaining their prolonged activation and thus, chronic remodeling of the TME.[38] Moreover, as the tumor progresses, PSCs engage in dynamic interactions with cancer cells via the same means of secreted pro-inflammatory mediators and ECM remodeling, which in turn aid cancel cell growth, survival, invasion, and therapy resistance — ultimately creating a self-reinforcing,

pro-tumorigenic feedback loop, from now on referred to as PDAC's *"vicious circle"* (Figure 1.5) (*since this will be a recurring theme of this chapter*).

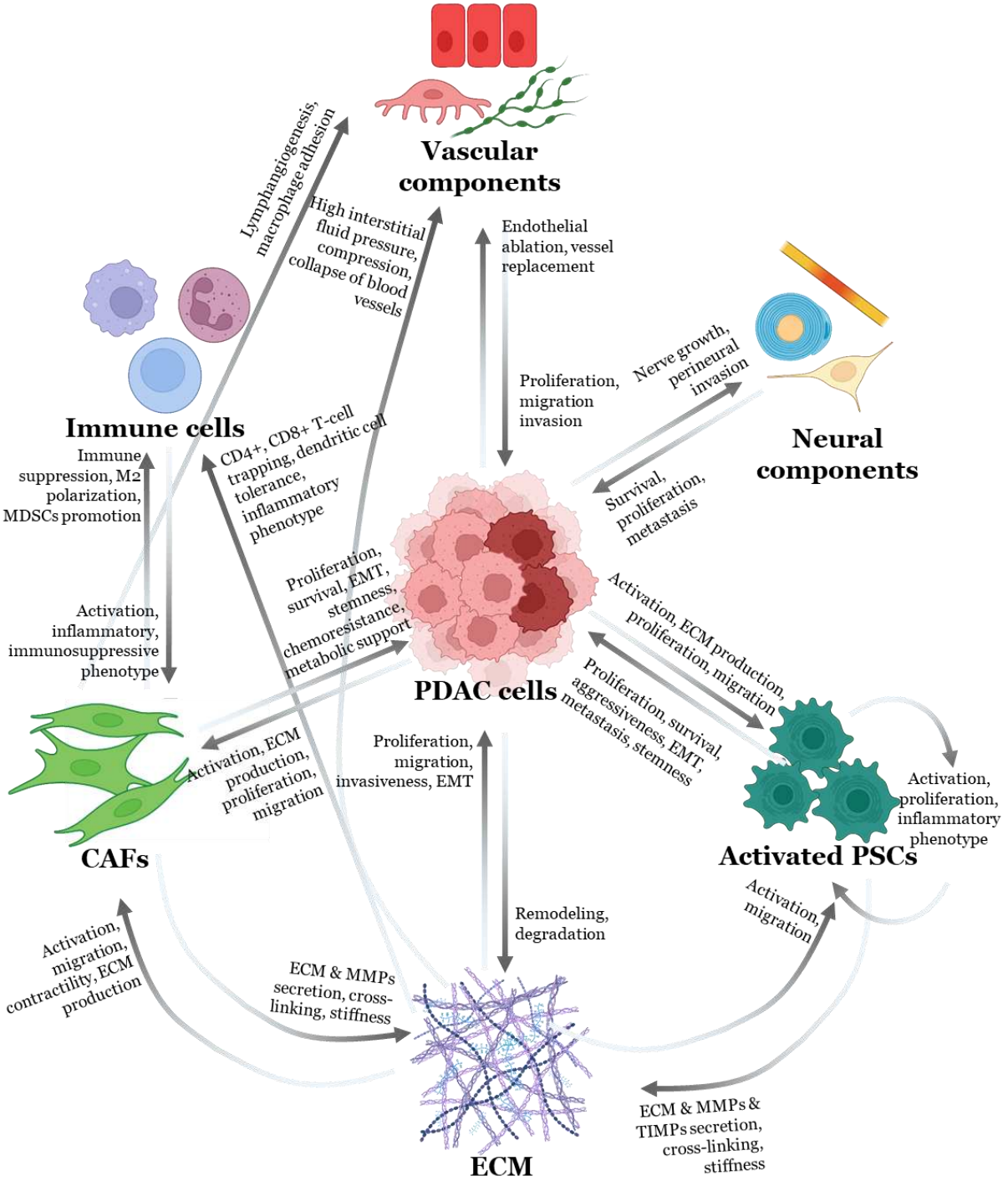


Figure 1.5: Crosstalk between pancreatic cancer cells and components of the tumor microenvironment. PDAC cells engage in bidirectional interactions with stromal, immune, endothelial and nerve cells and ECM components. CAFs are activated by PDAC cells and, in turn, promote ECM remodeling, fibrosis, and tumor proliferation. Immune cells contribute to an inflammatory microenvironment, while endothelial cells and pericytes regulate vascular remodeling and angiogenesis. ECM becomes stiff and desmoplastic, further enhancing tumor progression. These reciprocal interactions create a self-sustaining cycle ("vicious circle") that drives PDAC growth, invasion, and therapy resistance.

Activated PSCs preferentially give rise to the myofibroblastic CAF (myCAF) subpopulation of CAFs within PDAC's TME[43,44] but can also be precursors of inflammatory CAFs (iCAFs).[45] While PSCs-derived CAFs are central,[46] emerging lineage-tracing studies have shown that PSCs contribute to only a small fraction (10-15%) of the total CAF population in PDAC,[43,47,48] highlighting the presence of other significant sources. This finding challenges the conventional view and suggests that PSC-derived CAFs represent a specialized subset rather than the dominant population.

Tissue-resident fibroblasts are a heterogeneous population of cells normally present in the pancreas. Under tumor cell-derived signaling pathways, they typically give rise to myCAF population.[43,49] Tumor-infiltrating mesenchymal stem cells (MSCs), recruited from the bone marrow or other reservoirs, can migrate to the TME and differentiate into CAFs under the impact of cancer-associated cues.[43] MSCs possess high multilineage potential and self-renewal capacity. Adipose-derived MSCs have been shown to differentiate into distinct CAF subpopulations *in vitro*,[50] depending on culture conditions: direct contact co-culture with PDAC cells induces differentiation into both myCAFs and iCAFs, while indirect co-culture yields only iCAFs. A groundbreaking lineage tracing study revealed that the splanchic mesenchyme — the fetal cell layer surrounding the endoderm from which pancreatic epithelium originates – gives rise to the majority of resident fibroblasts in normal pancreas.[51] During tumorigenesis, splanchic-derived cells dramatically expand to form CAF subtypes that comprise a substantial fraction of pancreatic cancer tissue mass. Single-cell RNA profiling identified shared gene expression signatures among fetal splanchic mesenchyme, adult fibroblasts, and CAFs, suggesting a persistent transcriptional program underlies this lineage differentiation.[51]

In addition, cellular transitions like endothelial-mesenchymal transition (EndMT) and mesothelial cell transition can contribute to CAF populations in PDAC TME. Endothelial cells can undergo EndMT to become CAFs.[52-54] TNF-α, which is abundant in PDAC, strongly induces EndMT in human endothelial cells through downregulation of the endothelial receptor TIE1.[54] EndMT-derived CAFs can secrete HSP90α to promote M2 macrophage polarization and tumor growth.[52,53] Antigen-presenting CAFs (apCAFs) exclusively derive from mesothelial cells via downregulation of mesothelial features (e.g., mesothelin expression) and upregulation of fibroblastic characteristics — transition induced by IL-1 and TGF-β signaling.[55] Additional but less common CAF precursors include pericytes, smooth muscle cells, adipocytes.[43]

Diverse cellular origins of CAFs in PDAC have several important implications not only

on CAF functional heterogeneity (e.g., myCAFs, iCAFs, apCAFs etc.) but also their spatial organization, temporal dynamics as well as therapeutic targeting strategies.[46–49] Understanding this origin-to-subtype relationship is crucial for developing both relevant models as well as targeted therapeutic approaches.

MyCAFs represent the classical activated fibroblast phenotype and are characterized by high expression of contractile and ECM proteins.[47,56] MyCAFs produce dense collagen-rich matrix responsible for the desmoplastic reaction, ECM remodeling, and generate contractile forces and tissue stiffness through α-SMA and fibroblast activation protein (FAP) expression.[43,57] Extensive myCAF molecular signature is provided elsewhere.[43,56–58] Located in direct contact with tumor cells, they are primarily activated by TGF-β signaling from tumor cells and/or other stromal cells ("vicious circle"). MyCAF ultimately form a protective barrier, secreting metabolites to fuel tumor cell proliferation.[57,59]

iCAFs are located distant from tumor cells within desmoplastic stroma and exhibit a pro-inflammatory secretory profile (IL-6, IL-8, CXCL12, leukemia inhibitory factor (LIF) etc.[47,56,58,60–62]) that recruits and activates immunosuppressive cells like MDSCs and regulatory T cells.[47,60] Activated by IL-1 signaling through the NF-κB pathway, iCAFs are characterized by low α-SMA expression and display increased glycolysis compared to myCAFs, particularly under hypoxic conditions, supporting fast energy demand and cell proliferation & activation.[57,63] IL-6 secreted by iCAFs is a crucial mediator of chemoresistance and poor prognosis since its elevated levels have been associated with increased cancer cell survival, systemic metabolic dysfunction and tumor cachexia.[60,64]

apCAFs are characterized by the unique expression of major histocompatibility complex (MHC) class II machinery (but not only)[55,56,58] present in mesothelial cells that apCAFs exclusively derive from.[55] ApCAFs can directly present antigens to CD4+ T cells and induce regulatory T cells formation in an antigen-specific manner thus, inducing immunosuppression. In addition, apCAF demonstrated remarkable plasticity in 2D, switching from to myofibroblasts and losing MHC II expression, which suggests that specific 3D microenvironmental cues are required to maintain the apCAF phenotype.[58]

Today, it is well established that heterogeneity of CAFs in PDAC extends far beyond the traditional myCAF, iCAF, apCAF classification and moreover, is confirmed to be patient-specific.[65–68] Recent advances in single-cell RNA sequencing and spatial transcriptomics have revealed a complex landscape of specialized CAF subtypes. Those are being categorized diversly in literature based on their molecular signature, for instance, according to prognostic marker presentation (FAP+/CXCL12+,[69,70] LRRC15+,[71] Meflin+,[72] FKBP7+[73]),

or functional support (tumor-like CAFs, heat shock protein-high tCAFs, vascular CAFs, interferon-response CAFs, reticular-like CAFs, dividing CAFs)[56] — the list being neither exhaustive nor unified as CAF heterogeneity remains a subject of active research up to date with emerging subtypes and refined classifications to become a central pillar for targeted theragnostic development.

Furthermore, CAF populations exhibit outstanding cell plasticity and interconversion between subtypes under response to environmental cues such as metabolic stress, spatial dynamics or TGFβ-mediated differentiation.[74] Not only apCAF are able to transform in myCAF, but iCAF ⇔ myCAF interconversion is also common thanks to TGFβ-mediated signaling pathway, IL-1α/IL-6 axis or Rho effector protein kinase N2 (PKN2) modulation.[43-45,58] Genetic/epigenetic alterations as well as spatial and mechanical cues, like cancer cell proximity and ECM stiffness, have also been shown to modulate CAF identity [43,75] ("vicious circle"). Comprehensive understanding of CAF subpopulations and their plasticity is crucial for treatment stratification and precision strategies. This is yet reinforced by the remarkable dual nature of CAFs that function as both tumor promoters and tumor suppressors depending on their subtype, activation state, and microenvironment context.

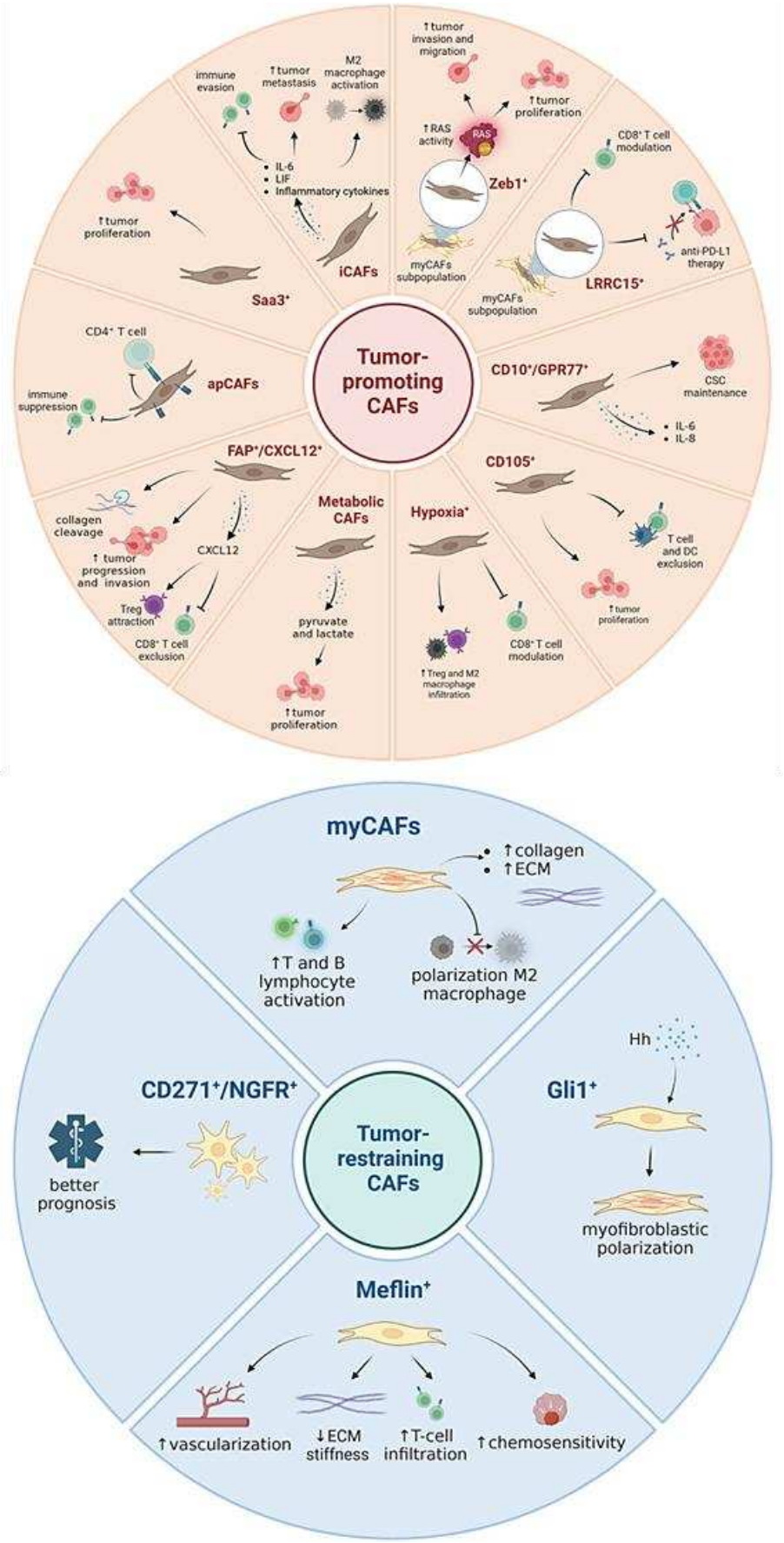


Figure 1.6: Summary of the acknowledged tumor-promoting and tumor-restraining CAF populations in PDAC. *(Adapted from Brichkina et al., Cancers. 2023.)*

Complex CAF duality has fundamentally changed our understanding of PDAC biology and therapeutic approaches (Figure 1.6). Spatio-temporal context, signaling gradients, CAF plasticity and metabolic reprograming — all contribute to the dual nature of CAFs. The most abundant myCAFs, being typically localized around tumor cells, create physical barriers that limit drug penetration, immune cell infiltration and therapeutic efficacy. As they are also responsible for ECM remodeling and metabolite exchange with cancer cells, myCAFs thereby support cancer cell metabolism and invasion.[47,76,77] Paradoxically, several studies demonstrate tumor-restraining properties of myCAFs, as shown through αSMA+ CAF depletion that leads to more aggressive, poorly differentiated tumors.[68,77–79] In addition, high αSMA expression and tumor stromal density was correlated with better overall survival in some patient cohorts[68] (*wait, it's the same stroma as the super fibrotic, desmoplastic one that functions as a structural scaffold and a key regulator of tumor progression, immune evasion, and therapeutic resistance in PDAC? yeees.....but it also helps restrain it from progressing; nobody said it was going to be easy*). Hence, it is believed that collagen I secreted by myCAFs serves as a tumor-restrictive component. Similarly, inhibition of paracrine SHH signaling, known to activate CAF and induce desmoplastic reaction, was shown to accelerate progression of PDAC and worsen tumor differentiation in several studies.[80,81] These are few out of many more studies that have shown that non-specific (or not specific enough) CAF depletion leads to pro-tumorigenic outcomes.[68,80]

On the other hand, iCAF are considered to be mainly tumor-promoting due to immunosuppressive factors they release, like CXCL12[76] (repels cytotoxic T cells), IL-6[76] (promotes cancer cell proliferation, EMT), LIF[82] (mediates paracrine signaling to promote chemotherapy resistance), and cells they recruit, like MDSCs and TAMs. Similarly, apCAFs are thought to impose pro-tumor effect due to Treg differentiation and subsequent immune suppression.[55] However, a recent study challenges that by showing that apCAFs can activate effector CD4+ T cells in mice, contributing to the anti-tumor immune response.[83] In addition, several specialized CAF subpopulations have been identified to induce tumor-suppressing action such as Meflin+ CAFs that are associated with higher chemosensitivity, tumor vessel area, reduced matrix stiffness or Gli1+ CAFs that contribute to myofibroblastic polarization through SHH.[78]

The complex landscape of CAF subtypes in PDAC represents both a challenge and an opportunity for developing more effective treatments for this devastating disease. The balance between tumor-promoting and tumor-restraining CAF subpopulations will become a critical determinant for therapeutic intervention. The field, therefore, is moving towards

precision targeting of specific CAF subpopulations. Rather than depleting all CAFs, more nuanced strategies are needed such as CAF reprogramming toward tumor-restraining phenotypes, selective targeting of specific CAF subtypes, metabolic interventions and patient stratification as well as combination therapies.

1.3.2 Extracellular Matrix and its Remodeling in PDAC

Stemming from the signature feature of PDAC — desmoplasia — is its dense, highly organized ECM that is another major player in the formation of fibrotic and stiff TME. Consisting of a variety of structural proteins, proteoglycans, adaptor proteins and matrix remodeling enzymes, ECM composition is able to adjust as a function of surrounding TME. Dynamic 3D protein network of both the interstitial connective tissue matrix and basement membrane of the ECM undergo dramatic remodeling and increase in content, actively participating in tumor initiation, progression, metastasis, and therapeutic resistance (Figure 1.7).[65,84,85]

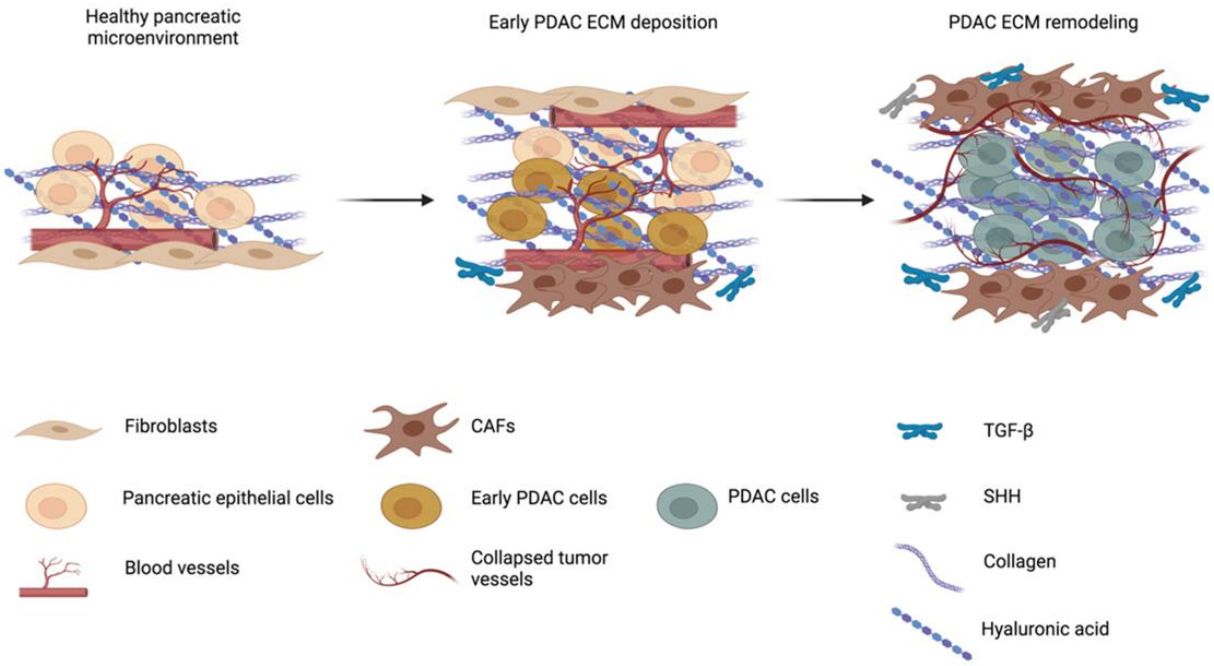


Figure 1.7: ECM alterations in PDAC. In healthy conditions pancreatic epithelial cells are embedded within ECM supported by fibroblasts and blood vessels. During tumorigenesis, CAFs increase ECM deposition via signals like TGF-β and SHH, creating a dense, rigid matrix around early PDAC cells. Combined with abnormal, leaky vessels, this TME promotes PDAC growth and invasiveness through pro-tumorigenic pathway activation. *(Adapted from Ferrara et al., Cancers. 2021.)*

Collagen type I in PDAC

Collagen family dominates in PDAC ECM, accounting for more than 90% of total ECM proteins and being the primary structural component of the matrix.[85] Subsequently, fibrillar collagens (main contributors of ECM stiffness and fiber alignment) — collagen I and

III — represent ~90% of total collagens in PDAC ECM and increase at least 2.6-fold during development from normal pancreas to PDAC, according to proteomic analyses.[86] Other collagens include collagen IV (basement membrane component) and collagen V, VI, VII, XII, XIV, XV that have specialized functions in tumor progression.[84]

Among more than 10 collagen types that have been detected in PDAC tissues, type I collagen (COL1A1, COL1A2) is by far the most abundant. Its main sources are activated PSCs and myCAFs that respond to tumor-derived signals by drastically upregulating collagen synthesis.[86] The deposition of type I collagen in PDAC follows distinct spatial patterns, with the highest concentrations observed in the peritumoral regions and areas of active desmoplastic reaction. This heterogeneous distribution creates microenvironmental niches with varying mechanical properties, influencing local cell behavior and drug penetration.[87,88]

Beyond spatial heterogeneity, evidence highlights that PDAC stroma can also be classified functionally, based on the relative abundance of collagen and activated fibroblasts. Histopathological analyses of resected PDACs demonstrated that collagen accounts for roughly 38% of tumor tissue, while α-SMA and/or FAP-positive fibroblasts comprise about 33%, although these proportions vary considerably between patients.[65] From these observations, the Activated Stroma Index (ASI) — the ratio of α-SMA+ fibroblastic area to collagen deposition — was proposed as an independent prognostic marker, where a high ASI correlates with significantly worse survival.[89] Although that connotation have also been challenged in recent studies.[90]

Building on this concept, PDAC stroma can be broadly categorized into three subtypes: fibrogenic stroma (collagen-rich but relatively poor in CAFs), fibrolytic stroma (CAF-rich but collagen-poor), and inert stroma (low in both). Among these, fibrolytic stroma is most strongly associated with poor survival, underscoring the pathogenic contribution of highly activated CAF populations in the absence of sufficient collagen counterbalance.[91,92] At the transcriptomic level however, two major stromal signatures have been identified: "activated stroma", which associates with adverse outcomes, and "normal stroma", which is characterized by a collagen-rich but fibroblast-poor composition and is linked to improved prognosis, mostly overlapping with the three-subtype classification.[93] It is worth mentioning that the designation of "activated stroma" refers to a tissue-level transcriptomic and histological subtype, and should not be confused with the term "activated PSCs/CAFs", which describe the cellular phenotype.

Type I collagen is a primary determinant of tissue stiffness in PDAC, increasing the

elastic modulus of pancreatic cancer tissues from 1-4kPa in healthy pancreas to 10-40kPa in tumor regions *in vivo*[94–96], while *ex vivo* Vincent et al. showed some tumor areas exceed 100kPa.[97] This remarkable increase in stiffness stems from collagen cross-linking that upregulates in hypoxic conditions common in PDAC,[98,99] fiber alignment that leads to anisotropic mechanical properties, and matrix density that increases with decreased porosity.[100,101]

In turn, type I collagen profoundly influences pancreatic cancer cell phenotype and behavior via mechanisms of mechanotransduction, integrin signaling, EMT and metabolic adaptation. Cancer cells sense and respond to matrix stiffness through integrin-mediated signaling pathways as it activates FAK and mechanosensitive transcriptional coactivators YAP/TAZ, leading to enhanced proliferation, anti-apoptotic signaling and invasive capacity[102] (*yes-yes, the same matrix that restrained tumor expansion not so long ago*). Integrin-FAK-ROCK-YAP/TAZ signaling cascade governs the core reciprocal relationship, ultimately increasing the expression of the fibroblast activation hallmark α-SMA ("vicious circle"). A critical aspect of cell-ECM reciprocity involves mechanically-activated TGF-β signaling[103] and we remember from the preceding discussion how actively it participates in pro-tumorigenic functions. Moreover, cancer cells can utilize collagen-derived amino acids as an alternative energy source adapting its metabolic needs.[104] Beyond integrin-mediated signaling, other mechanosensitive pathways contribute to the reciprocal cell-ECM relationship.[105]

Hence, dense collagen networks create physical barriers that impede drug penetration due to small pore size and tortuous diffusion paths that contribute to therapeutic resistance. Current approaches to address this problematic focus on cross-linking inhibition, enzymatic collagen network degradation, collagen-integrin signaling disruption and metabolic support blockade, with some of them showing promising results,[106–108] while others failing.[98,109,110] At this stage, it is crucial to remember that any stromal component depletion is not fully predictable yet in PDAC, so we must be cautious when developing novel stroma-targeting strategies.

Hyaluronan in PDAC

Hyaluronan or hyaluronic acid (HA) is another abundant and highly functionally significant component of PDAC ECM. It is a major glycosaminoglycan composed of repeating disaccharide units of D-glucuronic acid and N-acetyl-D-glucosamine whose structure is preserved across species (Figure 1.8).[111,112] In PDAC, HA content is significantly increased (up to 12-fold[113,114]) compared to normal pancreas and this accumulation begins

early in pancreatic carcinogenesis, with increased HA deposition observed already in PanIN lesions.[86] As a result, 80% of primary PDAC tissues show strong HA expression.[114,115] While the exact mechanisms of HA accumulation in PDAC remain unclear, its abundance within the stroma is highly associated with much poorer overall survival as compared to patients with low-level stromal HA.[115,116]

Hyaluronan is synthesized by three hyaluronan synthases, HAS1, HAS2, and HAS3, located at the plasma membrane and degraded by hyaluronidases, mainly HYAL1 and HYAL2.[114] HYAL1 cleaves the products of HYAL2 into small fragments (~0.8 kDa) that were primarily digested from high molecular weight (HMW) chains into ~20 kDa HA fragments.[115] Under healthy conditions, the amounts of HA are controlled by a balance of synthesis and degradation. In PDAC, HA turnover is also tightly regulated but dysbalanced: HAS2 is often overexpressed, driving excessive synthesis, while HYALs expression patterns vary. Notably, clinical correlations are complex — some studies associate high HYAL1 levels with aggressive disease through increased low molecular weight (LMW)-HA signaling,[117] whereas others report poor prognosis with low HYAL1 expression, potentially due to unchecked HMW-HA accumulation and severe stromal barrier effects.[118] In addition, although the overarching effect of HA accumulation seems to be negative, HA was shown to induce diverse effects based on its molecular weight.[114,119] LMW HA (generated by HAS3, HYAL1-2 or ROS fragmentation) has been associated with tumor-promoting effects, whereas HMW HA may exhibit tumor-suppressive properties, although literature remains inconclusive on this dichotomy.[120–122] While exogenous HA addition increased migration of PDAC cells, with LMW forms being particularly active[120], an alternative study suggested it was primarily HMW that promoted cancer cell migration.[123] There is a similar lack of clarity on the exact classification of high, mid, or low molecular weight HA, with these ranges often varying or not specified.[114,120] Here, the definition given by Monslow et al is followed of HMW HA ranging from 1000 to 6000 kDa, medium molecular weight (MMW) from 250 to1000 kDa, and LMW from 10 to 250 kDa.[111]

HA can be synthesized by both tumor and stromal cells and is found in tumor and stromal components; however, it predominantly accumulates in the desmoplastic compartment of PDAC.[115,124] HA binds to large amounts of water (up to 15 water molecules per disaccharide)[125], contributing to increased interstitial fluid pressure (IFP).[126] Elevated IFP (can exceed 10-fold that of normal pancreas) leads to vascular compression, impaired perfusion, and the formation of a diffusion barrier that restricts delivery of chemotherapeutic agents and immune cell infiltration.[125–128] HA was shown to serve as a nutrient source for

PDAC cells *(yes, for those who produced them, cruel, I know but* "vicious circle") and a stimulant for cell migration.[127] In addition, high levels of stromal HA were associated with low immune scores due to T-cell infiltration restriction.[116]

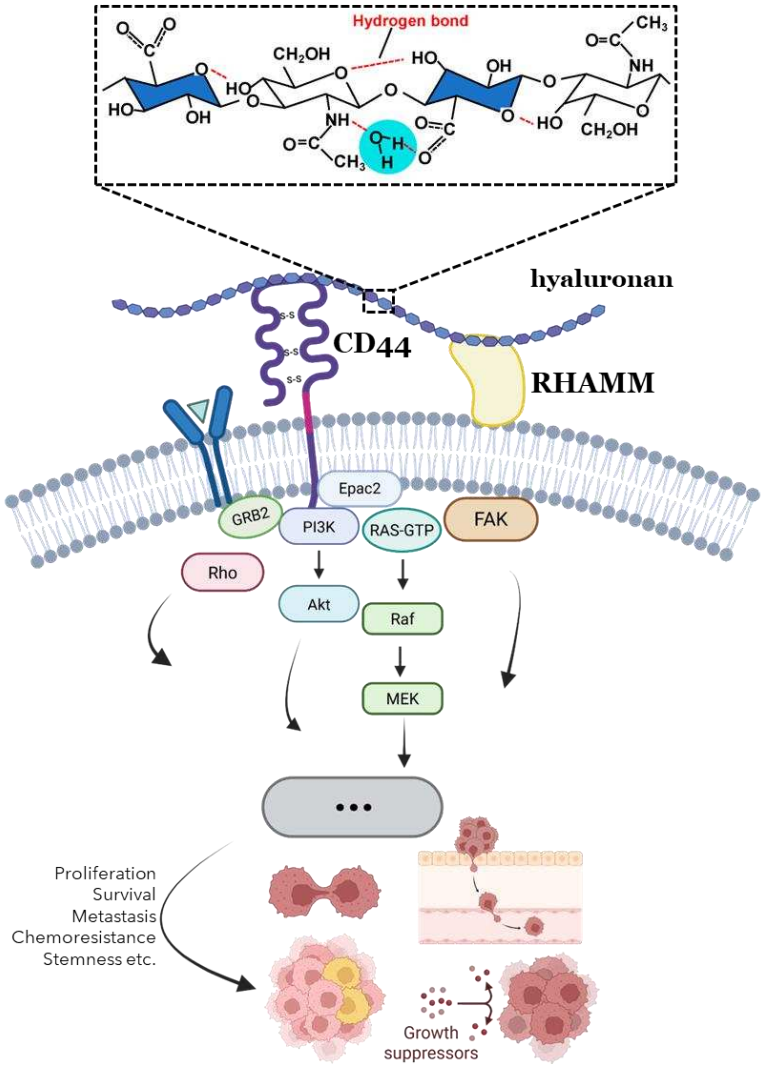


Figure 1.8: Hyaluronic acid and its primary signaling cascades. HA is a linear glycosaminoglycan composed of repeating disaccharide units of glucuronic acid and N-acetylglucosamine, which is highly hydrophilic and can retain large amounts of water. Binding of HA to CD44 and RHAMM activates multiple intracellular cascades, leading to enhanced cell proliferation, survival, metastasis and stemness.

Soon after synthesis, HA is ejected by the cells into the extracellular space, where it binds to and interacts with specific cell surface receptors like CD44 and RHAMM (receptor for HA-mediated motility) (Figure 1.8).[129] It has been demonstrated that CD44 is increasingly expressed on the PDAC cell membrane. CD44-HA binding activates downstream cascades such as PI3K/AKT, RAS/MAPK, and Wnt/β-catenin, thereby promoting proliferation, motility, and survival.[130] [131] CD44 exists in multiple isoforms, CD44 standard (CD44s) and specific CD44 variant (CD44v), with CD44v frequently upregulated in PDAC and linked to chemoresistance, EMT induction and cancer cell stemness.[132] Although the exact

implications of variable CD44 isoforms remain unclear.[130] In primary tissues, over 70% of samples have shown positive CD44 expression with almost 3.4-fold overexpression as compared to control tissues, associated with poorer survival.[133,134] PDAC-cell lines, however, exhibit heterogeneous, phenotype-dependent expression patterns, with epithelial-like cell lines showing reduced expression and mesenchymal-like lines maintaining or increasing expression.[131] In addition, size-dependent clustering of CD44 occurs, with HMW-HA inducing receptor clustering and LWM-HA — disrupting it.[119]

RHAMM interacts with HA primarily in the contexts of tissue injury and tumor evasion, enhancing cytoskeletal reorganization and cell motility. In PDAC, RHAMM overexpression correlates with aggressive tumor behavior and poor prognosis.[135] Some PDAC cell lines show context-dependent negative correlation between RHAMM expression and HA production as well as inverse expression patterns with CD44.[129,136]

Given its dual physical and biochemical roles, HA has been explored as a therapeutic target. The pegylated recombinant hyaluronidase PEGPH20 transiently degrades HMW-HA, lowers IFP, and re-expands collapsed vasculature, enhancing drug delivery in preclinical models. However, despite promising early-phase results, phase III trials failed to improve overall survival.[137] On the other hand, it was also demonstrated that the inhibition of HA synthesis by 4-methylumbelliferone (4-MU) significantly decreases cell migration.[138] Recent efforts have demonstrated intricate relationship between CD44 and iron-bound HA in PDAC cells.[139–142] Higher CD44 expression was associated with higher iron content within cells, making them vulnerable to ferroptosis-guided therapies. In contrast, higher content of internalized iron was correlated to EMT in PDAC cells. While these studies provide significant insights into CD44's role in metal metabolism and ferroptosis, specific mechanisms by which HA itself (as distinct from CD44) contribute to PDAC pathogenesis remain less well characterized. The focus in these studies has primarily been on CD44 as a receptor and mediator, with HA serving as a metal-binding carrier molecule.

Given the significant patient-to-patient variation in HA expression and distribution patterns, HA levels' and effects' changes during disease progression, size-sensitivity, future success will require more sophisticated understanding of HA biochemistry to address the multifaceted roles of this crucial ECM component.

1.3.3 Epithelial-Mesenchymal Transition (EMT) and Cellular Plasticity

The dynamic crosstalk between activated stromal cells and remodeled ECM not only shapes the biomechanical landscape of PDAC but also exerts deep impact on tumor cell

plasticity. Intercellular signaling-derived cytokines, ECM stiffness, aberrant collagen presence and organization, HA accumulation, CAFs — all synergize to trigger transcriptional programs that suppress epithelial cell characteristics and promote mesenchymal features, thereby initiating EMT (Figure 1.9A).

Unlike the classical binary view of EMT, contemporary research reveals a complex spectrum of cellular states that profoundly influence PDAC biology, metastasis, and treatment response.[143] PDAC employs two fundamentally different (though not mutually exclusive) EMT mechanisms: classical EMT (C-EMT) and partial EMT (P-EMT) (Figure 1.9B).[144] C-EMT is characterized by transcriptional repression of epithelial genes and upregulation of mesenchymal transcription factors like SNAIL, ZEB1, and TWIST with tumors exhibiting poor differentiation, single-cell dissemination, complete loss of E-cadherin expression and association with quasi-mesenchymal/basal PDAC subtypes.[145,146] In turn, P-EMT is associated with well-differentiated tumors/classical PDAC subtypes and involves protein relocalization rather than transcriptional changes, where E-cadherin is redistributed from cell junctions to cytoplasm without gene repression and cells retain epithelial gene expression while gaining mesenchymal characteristics and migrating collectively.[144]

Key molecular markers of EMT states include E-cadherin (CDH10, Claudinh-4,7, EpCAM as indicators of epithelial identity and vimentin, N-cadherin, fibronectin as mesenchymal indicators, although these are not exhaustive. Interestingly, research also established CD44 as a regulator of cell plasticity and EMT in PDAC via its iron transporting functions.[140,142] EMT mechanisms are orchestrated by a plethora of signaling pathways in PDAC like PI3K, SMAD4, WNT and Notch signaling with TGF-β representing the most potent EMT inducer.[147–151]

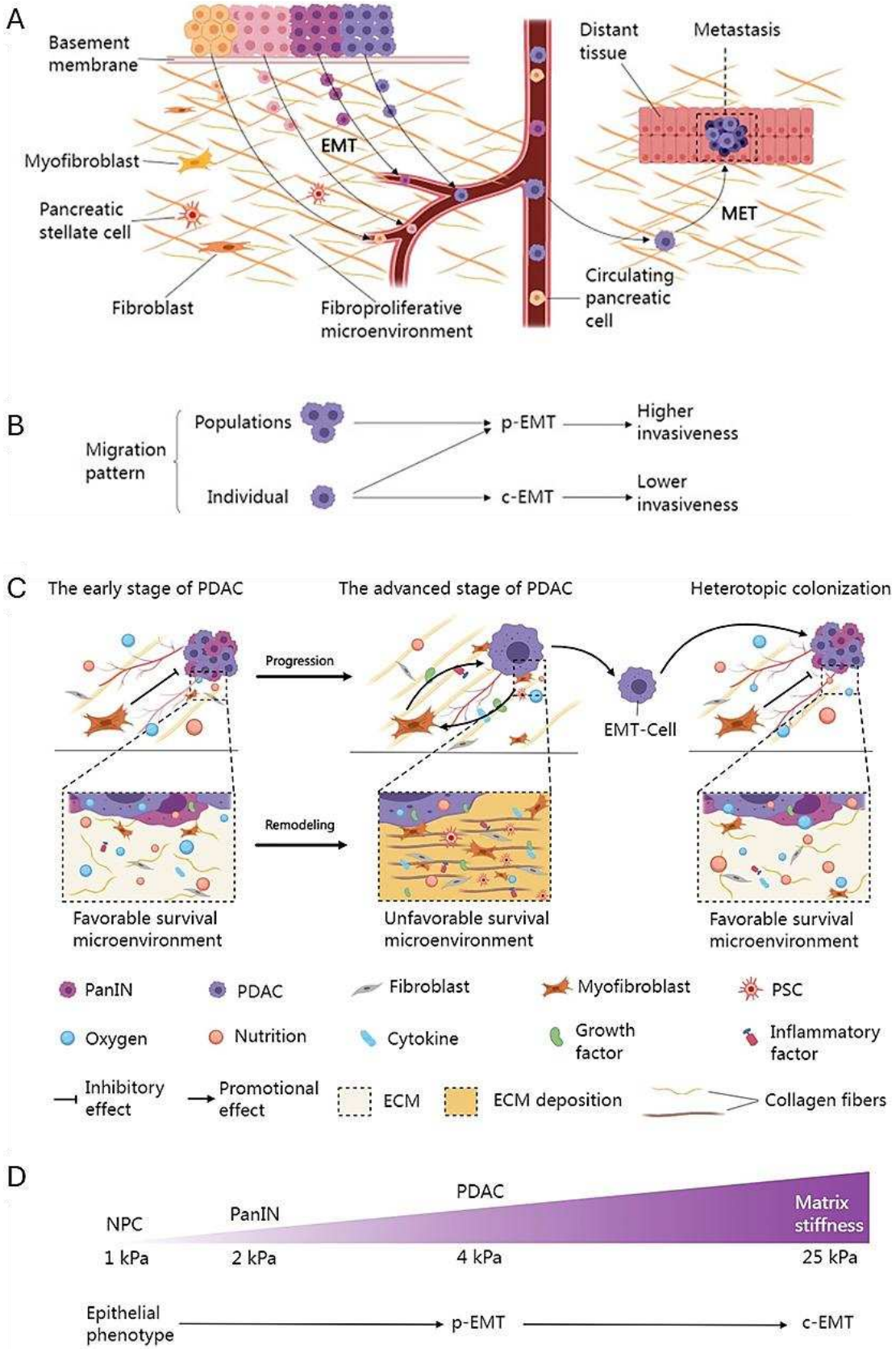


Figure 1.9: EMT in PDAC progression and TME remodeling. A. Circulatory features of PDAC enable EMT at any stage, facilitating invasion and dissemination. After extravasation and colonization at distant sites, cells undergo MET to complete metastasis. **B**. PDAC cell migration occurs via two EMT programs: p-EMT, involving individual cells or cell clusters with high invasive potential, and c-ETM, occurring in single cells with lower invasive capacity. **C**. In early PDAC, mesenchymal cells

restrain tumor growth, while oxygen and nutrient supply are sufficient for progressions. At advanced stages, the TME is remodeled with organized collagen fibers, activated stromal cells, and ECM deposition. Crosstalk between stromal and cancer cells through cytokines, inflammatory mediators, and growth factors promotes tumor progression. The remodeled environment reduces blood and nutrient availability, pushing PDAC toward EMT and invasion for survival. **D**. EMT contributes to changes in ECM stiffness during PDAC development. (*Adapted from Yang et al., Cell Death & Disease. 2023.*)

Complex and dynamic desmoplastic stroma is an extremely active contributor to EMT in PDAC, where CAFs act as the primary orchestrators of EMT in cancer cells either through direct EMT induction or via pro-EMT cytokine secretion (e.g., TGF-β, IL-8, IL-6 etc.), exhibiting distinct regulatory properties depending on subpopulation.[146] CAFs driving EMT in tumor cells, create a reciprocal relationship ("vicious circle") that occurs at quite early stages of neoplastic formation, even before real tumor formation.[143,146] In addition, matrix secreted proteins like collagens, HA, fibronectin provide signaling cues, activating downstream EMT signaling and modulating cell behavior as well as directly promoting EMT via mechanotransduction (Figure 1.9C-D).[152] PDAC cells undergoing EMT actively secrete factors that transform quiescent stromal cells into activated, tumor-promoting phenotypes and those stromal cells, once activated, reciprocally amplify EMT in tumor cells by the means of cytokine, growth factor cascades ("vicious circle").

EMT in PDAC enhances not only cellular motility and invasion but also contributes to chemoresistance, immune evasion, and the acquisition of cancer stem cell-like traits.[153] Notably, EMT is reversible, and cells undergoing mesenchymal-epithelial transition (MET) can reepithelialize at metastatic sites to form new tumors (Figure 1.9A).[154] This plasticity allows tumor cells to dynamically switch phenotypes depending on microenvironmental context. The predominance of P-EMT states, distinct mechanistic programs, and extensive crosstalk within TME highlights the need to deeper explore these mechanisms to address the fundamental drivers of metastasis and treatment resistance.

1.4 Therapeutic Implications

Despite a wealth of preclinical studies targeting various molecular pathways and tumor-stroma interactions, translation into clinical benefit has been disappointing. Surgical resection remains the only curative option with fewer than 20% of tumors eligible for surgery.[155] Even among those able to undergo resection, recurrence rates are high due to micrometastatic disease and residual tumor cells. Current gold standard for first-line therapies relies on established chemotherapy regimens of FOLFORINOX and gemcitabine + nab-paclitaxel (Abraxane®).[156] Other targeted therapies are available for specific patient subgroups, for example presenting particular mutations or microsatellite instabilities,

however, these applications accommodate less than 10% of PDAC cases.[157] Radiotherapy is occasionally used in a neoadjuvant or palliative setting, though its clinical benefit remains under debate.[158,159] Immunotherapies are deemed ineffective as PDAC is highly resistant to immune checkpoint inhibitors and is largely unresponsive to first-line immunotherapy approaches due to immunosuppressive TME.[160,161]

The latest therapeutic developments in late-stage clinical trials are focusing intensively on the complex TME components that drive PDAC resistance. CAF-targeting strategies include subtype reprogramming towards tumor-suppressive or quiescent states as well as metabolic interference.[162–164] ECM proteins remain challenging targets despite their central role in drug resistance. With unsuccessful non-specific matrix degradation, current strategies focus on targeting tumor-derived ECM proteins rather than global matrix depletion as tumor cell-derived ECM components correlate more strongly with poor survival than stromal-derived proteins.[86,165,166] EMT targeting represents another promising but complex therapeutic frontier. While EMT pathway inhibition may restore chemosensitivity, the field has learnt that complete EMT ablation may not be beneficial either, as mesenchymal features can provide both tumor-promoting and tumor-restraining functions depending on the context ("vicious circle").[167–169] Current developments collectively represent a shift toward precision medicine as well as combination treatment approaches that offer meaningful clinical responses in specific disease subtypes.

2. Nanoparticle-mediated Photothermal Therapy (NP-PTT): toward alternative treatment paradigms

While the trajectory of cancer treatment discovery is increasingly oriented toward precision medicine — leveraging molecular diagnostics to target specific genetic or phenotypic alterations — such approaches often benefit only narrowly defined patient subsets. In PDAC, where actionable mutations are limited and heterogeneity is high, this limits the widespread applicability of targeted therapies. Non-specific, biophysically driven approaches, such as hyperthermia and nanoparticle-mediated photothermia (NP-PTT), aim to complement the need for precise molecular targeting by exploiting the tumor's physical and stromal features. These therapies may offer broader applicability and meaningful therapeutic impact particularly when synergized with other treatment modalities.

2.1 Hyperthermia as Cancer Treatment

The definition of hyperthermia or thermal therapy can be given as a localized, regional or global elevation in body temperature between 39-42°C (mild), 42-45°C

(moderate) and >45°C (high or ablative), and has been vastly studied over time for cancer treatment, either on its own or in conjunction with other therapies. It uses controlled heat to damage and kill cancer cells or enhance the effectiveness of other treatments while sparing healthy cells.[170–173]

Hyperthermia exerts its anticancer effects through multiple interconnected mechanisms. At the cellular level, elevated temperatures directly damage cancer cells, disrupting cell membranes and interfering with DNA synthesis and repair pathways.[174,175] Cancer cells are particularly vulnerable to heat stress due to their altered TME, characterized by hypoxia, acidic pH, and poor vascularization. Hyperthermia also alters tumor blood flow and oxygenation. At mild temperatures (39-42°C), it increases perfusion and oxygen delivery to tumors, potentially improving the effectiveness of radiation therapy and chemotherapy by reducing hypoxia-induced treatment resistance.[176] Thermal therapy activates several components of the immune system, stimulating natural killer cells, dendritic cells, and T lymphocytes as well as promoting the release of heat shock proteins to act as danger signals.[177–179] The consequences of hyperthermia may accumulate over time and include direct thermal cytotoxicity, thermal sensitization, blood flow and oxygenation perturbation, impaired DNA repair. Hyperthermia can also affect the ECM, altering collagen fiber architecture through collagen denaturation or impacting the matrix indirectly by acting on ECM enzymes (MMP and TIMP) through enhanced MMP or decreased TIMP activities, responsible for matrix degradation and its inhibition respectively.[180–182]

External (e.g., hot air, water, infrared radiation) (extrinsic hyperthermia) or internal heat sources (e.g., magnetic nanoparticles) (intrinsic hyperthermia) can be used to increase temperature within the body, where local, regional and whole-body thermal therapies can be distinguished.[183,184] Currently, a few hyperthermia systems are already routinely used to treat cancer patients, demonstrating proven efficacy across numerous tumor types.[185–188] Hyperthermic intraperitoneal chemotherapy (HIPEC) represents the most widely adopted and successful clinical application of hyperthermia that treats peritoneal carcinomatosis by enhancing cisplatin cytotoxicity through improved drug uptake and DNA adduct generation.[189] Research also demonstrated potential for modulated electro-hyperthermia[190] and external hyperthermia[191] in the context of PDAC drug resistance through chemotherapy support, but mainly in early preclinical studies with clinical investigation taking its beginnings.[192,193]

2.2 Nanotechnology and Hyperthermia: Photothermia Focus

The field of thermal therapies continues to evolve with improved heating technologies, better understanding of thermal dose-response relationships, and novel combination strategies. In this context, precise temperature control and monitoring become crucial.

The development of nanomaterial-based approaches changed the game by allowing for distant, localized heating with minimized side effects. While extrinsic heating induces nonspecific and unlocalized tissue heating, nanoparticle-mediated hyperthermia allows for targeted heating in the cancer tissue environment with limited adverse effects on healthy tissue (Figure 1.10). Conceptually, NPs serve as an intratumoral heat source by absorbing and dissipating the energy from an external source, thus reversing the direction of heat loss (inside-out hyperthermia) and minimally damaging the collateral tissue.[194]

For distant localized heating, magnetic and light-absorbing nanoparticles (NPs) are currently the most advanced materials. Magnetic hyperthermia (MHT) is the most well-known type of localized heat treatment that transforms energy delivered by an external magnetic field to magnetic NPs, iron oxide NPs being the most common nanoheaters.[195,196] However, MHT is limited by the high NP concentration required to achieve significant heating as well as clinical implementation concerns.[197]

In this regard, nanoparticle-mediated photothermia (NP-PTT) uses near-infrared (NIR) laser light as an energy source which, combined with NIR-absorbing nanomaterials, allows for lower power densities and deeper tissue penetration than visible light, potentially reducing the concentration of NPs thanks to their strong absorption cross-sections.[198,199] Despite initial concerns that the required laser illumination might harm healthy bystander tissues and that optical penetration is limited, PTT has received considerable attention in recent years. The development of nanomaterials (e.g. plasmonic gold-based nanorods, nanostars, or nanoshells; graphene nanocomposites or semiconductor nanomaterials) with strong optical absorbance in the NIR-I (700-950 nm) and II (1000-1700 nm) windows,[200] allowing light responsiveness at lower laser powers and in-depth penetration of biological tissues, mitigates both issues.[201,202] In PTT, initially plasmonic nanoparticles (e.g., gold-based nanoparticles) were injected into tumors and treated with laser light to induce the coordinated oscillations in NPs' conduction band electrons, which in turn, caused the applied NIR light absorption or scattering.[201,203] As a result, absorbed light is transformed into heat, provoking permanent damage of the adjacent pathological tissue.

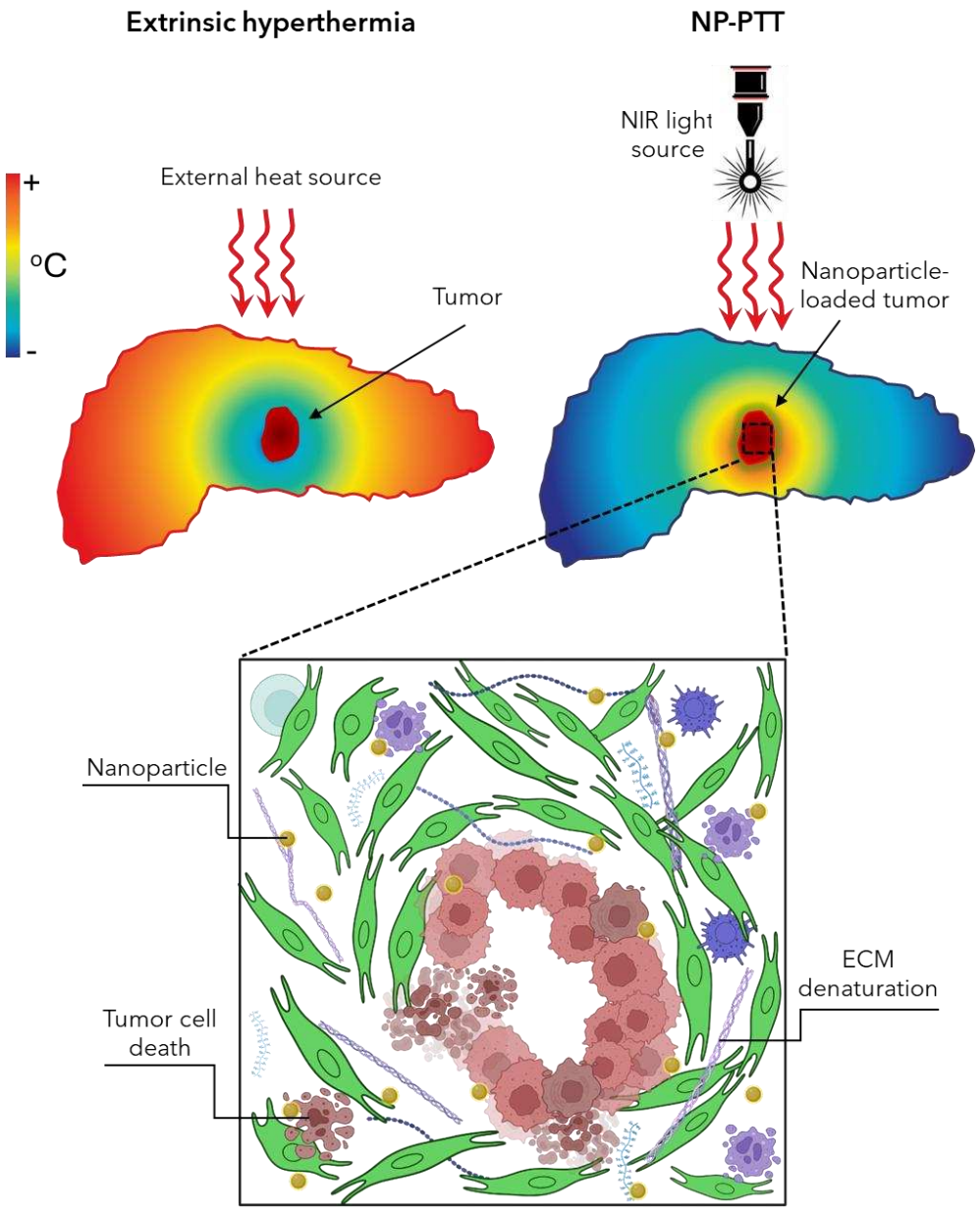


Figure 1.10: Mechanism of NP-PTT in cancer. NPs accumulate in the TME and, upon NIR light exposure, convert light energy into localized heat, as compared to non-localized extrinsic hyperthermia heating. The resulting effects may include tumor cell death (apoptosis, necrosis, ablation etc.), ECM denaturation, stromal remodeling among others allowing to induce immediate cytotoxicity, immunological and therapeutic enhancement effects.

My PhD supervisor Claire Wilhelm with her team were one of the first ones to compare both magnetic hyperthermia and photothermia, illustrating that at the doses expected to reach tumors intravenously, only PTT can provide heating at therapeutic level.[204,205] In addition, iron oxide NPs, particularly non-oxidized magnetite Fe_3O_4, while typically being used for magnetic hyperthermia, have recently been verified by the team of C. Wilhelm as effective photothermal agents due to their significant absorbance in the NIR.[205-207] Furthermore, iron oxide NPs can be degraded by cells as a result of a combination

of effective biodegradation and management of free iron ions by iron homeostasis processes such as detoxification and storage of surplus iron ions in the form of ferritin.[208] Iron oxide NPs may, hence, be favored over state-of-the-art photothermal agents since gold and carbon-based materials possess potential risks of low biodegradability and toxicity.[209,210]

The transition from conventional bulk heating methods to targeted nanoparticle-based thermal delivery has enabled clinical success in challenging applications, including PDAC, where traditional approaches have shown limited effectiveness. NanoTherm® therapy, an approved nanoparticle-mediated hyperthermia treatment, uses iron-oxide NPs injected directly into tumors, activated by alternating magnetic fields, has received approval in Europe for recurrent glioblastoma and by US FDA for prostate cancer but not for PDAC. "NoCanTher ThermoTherapy (NTT) Agent" represents the most clinically advanced application of magnetic nanoparticle hyperthermia for PDAC.[211] It uses sterile magnetic fluid containing iron oxide NPs that is administered intratumorally alongside standard-of-care chemotherapy that has shown enhanced drug penetration and significant tumor volume reduction. These results have led to the approval and initiation of a clinical investigational study in 2020 at the Vall d'Hebron University Hospital (Barcelona, Spain) of the NTT Agent combined with conventional chemotherapy in patients with locally advanced PDAC. However, these approaches require specialized alternating magnetic field infrastructure and careful patient selection due to contraindications (e.g., metallic implants) as well as NP-dependent heat distribution and MRI-related artefacts. For the pancreas, a deep-seated organ, heterogenous heating can be a challenge. In this regard, NP-PTT could address several of these constraints since photothermal agents can be excited by NIR light, which penetrates tissue to a clinically significant depth (up to 3 cm)[212] and could be delivered via minimally invasive endoscopic laparoscopic optical fibers directly into the tumor site.[213] Moreover, photothermal nanoagents can achieve rapid, high-peak heating within a short period of time, potentially inducing direct tumor ablation and/or local immune activation.[214,215]

2.3 NP-PTT in PDAC

NP-PTT has emerged as a promising therapeutic approach for PDAC, with the field developing diverse nanoparticle platforms including gold NPs, iron oxide NPs, carbon-based material, quantum dots, copper-based systems, and novel materials, such as melanin-like NPs, that can be excited by NIR I or the emerging NIR II lasers, and have been tested both *in vitro* and *in vivo*. An exhaustive literature review summarizing the most

prominent studies on NP-PTT applications in PDAC is presented in Table 1.1.

Although up to date the NP-PTT studies for PDAC remain at preclinical stage, they show great potential in terms of both cancer cells and tumor microenvironment effects. Bianchi et al. recently explored the canonical gold NPs to quantitatively evaluate their effect on cell death in both pancreatic and breast cancer cell lines, including an extensive thermal analysis (internalization, max absolute and relative temperatures, effective thermal enhancement, heating kinetics etc.)[216] Numerous other studies demonstrated not only significant impact on cancer cell proliferation, death and tumor growth but also metastasis reduction, ECM disruption as well as sustained immunomodulation by combining PTT with other treatment agents. For instance, in the study by Robert et. al the researchers demonstrated not only inhibition of tumor growth in 3D cancer spheroids but also a repolarization of macrophages from M2 to M1, with sustained antitumor effects long after treatment using hybrid Au-polymer NPs loaded with a PI3Kγ inhibitor.[217] In another *in vitro* study Yang and colleagues have combined NP-PTT with both chemo- and gene therapies using biodegradable charged polyester vectors (BCPVs) nanocarrier and graphene quantum dots (GQDs) co-loaded with doxorubicin (DOX) and small interfering ribonucleic acid (siRNA).[218] Via simultaneous delivery of chemo- and gene therapeutic agents, KRAS gene mutation was suppressed in cancer cells, inhibiting cell proliferation, migration and invasion.

The majority of studies included *in vivo* investigation by means of orthotopic or subcutaneous mouse xenografts with 3 studies using patient-derived xenografts (PDX) or organoids (PDO). Wang et al. engineered amorphous iron-oxide NPs co-loaded with indocyanine green (ICG) photosensitizer and the toll-like receptor (TLR-7) agonist (IMQ) for image-guided PTT.[219] Using MRI to guide laser delivery in orthotopic Panc02-H7 mouse tumors, this IMQ@IONs/ICG platform achieved complete ablation of primary tumors and dramatic reduction of mesenteric metastases. The treatment also triggered *in situ* immunogenic cell death and systemic CD8+ T cell response, substantially prolonging mice survival. Other studies have shown similar outcomes: subcutaneous or orthotopic PDAC xenografts treated with NP-PTT (alone or combined with other therapies) exhibit marked tumor growth inhibition, cell death induction via various mechanisms and sometimes full tumor eradication. Patient-derived sample-based studies support these results, demonstrating reduced myCAFs count, ECM disruption, vasodilation when PTT was combined with chemotherapy in PDX models[220,221] and immune response promotion when

combined with immunotherapy in PDO models.[222]

It can be appreciated in the "nanoagent" column of Table 1.1 that a very diverse variety of sophisticated NPs has been explored for NP-PTT in PDAC. In fact, not a single study used the same formulation, developing unique, targeted, hybrid multifunctional systems. This indicates that the field currently is focused on evolving active targeting nanosystems, especially in the framework of synergized therapies, where the NPs are used not only to dissipate heat into the tumor surroundings but also deliver therapeutics more effectively. Indeed, the vast majority of studies employed NP-PTT combined with other treatment modalities, which follows the novel paradigm of hyperthermia treatments to be applied in a synergistic approach rather than as a solo treatment.

Despite promising preclinical results, NP-PTT in PDAC still faces major barriers such as heterogeneous NP distribution and therefore heating, as well as precise temperature control, especially in *in vivo* models. While most of the studies were conducted on *in vivo* mouse models, they incorporated NP-PTT characterization in 2D corresponding cell cultures, examining photothermal conversion, NP uptake and heating. It can be observed that a substantial part of the studies did not include direct temperature measurements to carefully associate the induced effect with heating. Optimal PTT protocols emphasize temperature control over simple laser settings. Therefore, real-time temperature monitoring and feedback control, ensuring therapeutic efficacy while preventing thermal damage to healthy tissues remains a priority.

As such, NP-PTT strategies may represent a complementary direction to precision oncology that addresses critical barriers in PDAC such as desmoplasia, drug delivery inefficiency, and treatment resistance in a multifaceted manner. However, the absence of robust preclinical models that fully recapitulate PDAC's stromal and immune milieu contributes to high attrition rates in therapy development. Thus, more complex PDAC-representative models that enable precise temperature control and monitoring are still needed to better predict clinical outcomes.

Table 1.1: Summary of the NP-PTT studies in the context of PDAC treatment development. "Model" column represents *in vitro* studies highlighted in blue and *in vivo* studies (or combined) – in yellow.

Ref	Year	Model	Nanoagent	Laser settings	T°C	Stand-alone PTT or combined	Outcomes
[223]	2013	PANC-1	Iron-oxide core/gold-shell nanoparticles (goldmag®)	808 nm, 3.2, 4.7, 6.3, 7.9 W/cm^2, 5 min	up to 80°C	PTT	Reduction in cell proliferation
[224]	2013	1.4E7, PANC-1	Au NPs	808 nm, up to 2 W/cm^2, 10 min	33°C	PTT	Increased mitochondrial permeability transition, loss of mitochondrial function, ROS production, cell apoptosis
[225]	2014	PANC-1	Multiwall carbon nanotubes (MWCNTS) functionalized with PEG	808 nm, 2 W/cm^2, 3 min	40–43°C	PTT	Mitochondrial membrane depolarization, free radicals' flux and oxidative state in cells
[226]	2017	MiaPaCa-2	Aggregated gold nanoparticles (GNPS) impregnated into a gemcitabine–polymer conjugate matrix	640 nm, 1.4 W/cm^2, 1 min	45-52°C	PTT + chemotherapy	Cytotoxicity increase as compared to GEM NPs without PTT
[227]	2017	MiaPaCa-2, PANC-1	Plasmonic hollow gold nanoshells (GNS) coated with pegylated thermosensitive lipids to ratiometrically co-deliver two drugs, bortezomib and gemcitabine (GNS-L/GB)	808 nm, 4 W/cm^2, 3 min	unknown	PTT + chemotherapy	Synergistic cytotoxicity, improved internalization by cancer cells
[218]	2018	MiaPaCa-2, PANC-1	Nanocarrier of biodegradable charged polyester vectors (BCPVs) and graphene quantum dots (GQDs) co-loaded DOX and SIRNA (GQD/DOX/BCPV/SIRNA nanocomplexes)	650 nm, 0.2 W/cm^2, 15 min	unknown	PTT + chemotherapy + gene therapy	Simultaneous DOX & SIRNA delivery, suppression of Kras gene expression, inhibition of cell as proliferation, migration, and invasion
[228]	2019	PANC-1	Polydopamine-coated and paclitaxel (PTX)-loaded PLGA microspheres (MS), gold NPs-adhered and PTX-loaded PLGA-Ms	808 nm, 2 W/cm^2, 3 min	unknown	PTT + chemotherapy	Increased ROS generation, increase in early apoptosis, downregulation of antioxidant enzyme
[229]	2021	PANC-1	MnO_2 overlaid gold nanoparticle (AuNPs)-based nanoenvelope (pttne:MnO_2@AuNPs) functionalized with cholecystokinin (CCK) peptide	808 nm, 0.25 W, 4 min	unknown	PTT	SERS-guided PTT, targeted cellular uptake, cell viability decrease via apoptosis

			sequence				
[230]	2024	PANC-1	Silver nanoparticles functionalized with IGG molecules	808 nm, 2 W/cm^2, 2 min	unknown	PTT + immunotherapy	Dysfunction in Golgi apparatus, activation of caspase-3-mediated apoptosis
[216]	2024	Pan02	Gold nanorods (GNRS)	808 nm, 4.5 W/cm^2, 5 min	44-54°C	PTT	Cell viability decrease due to late apoptosis or secondary necrosis
[231]	2025	PANC-1	Core liposome (L2) decorated by gold nanoparticle with outer bilayer (L1) (L2@aunp@L1) + FOLFIRINOX	808 nm, 1-2 W, 5 min	45°C	PTT + chemotherapy	Controlled drug release, synergistic therapy reduced cell survival time as compared to stand-alone treatments
[217]	2025	RAW264.7, KPC cells	IPI-549-encapsulated AuNRs@PLA-b-PEG nps	808 nm, 1 W/cm^2, 5 min	42°C	PTT + immunotherapy	Controlled drug release, better uptake and heating of cancer cells while sparing macrophages, M2-to-M1 macrophage repolarization, tumor spheroid growth inhibition, promoted macrophage antitumor effects
[232]	2014	BxPC-3, subcutaneous BxPC-3 tumor-bearing nude mice	Graphene oxides modified with iron oxide nanoparticles (GO-IONP) coated with PEG	808 nm, 2 W/cm^2, 5 min	up to 64°C	PTT	Dual-modality mapping of regional lymphatic system by MRI, ablation of metastatic lymph nodes, reduced systematic toxicity of PTT to surrounding tissues
[233]	2017	Orthotopic SW1990 tumor-bearing BALB/c nude mice	Anti-UPAR antibody, polyethylene glycol, and ICG modified gold nanoshells (UIGNS)	808 nm, 1-2 W/cm², 5-10 min	50-60°C	PTT	Higher median survival rate of interventional PTT compared to clinical intervention iodine-125 interstitial brachytherapy (IBT-125-I), complete tumor ablation, tumor volume decrease, improved long-term survival in mice
[234]	2017	PANC1-CTSE, orthotopic PANC1-CTSE tumor-bearing nude mice	Gold nanocluster-based platform (PTT-carrier gold nanocluster, active targeting ligand U11 peptide, Cathepsin E (CTSE)-sensitive PDT therapy prodrug, CTSE-sensitive imaging agent (cyanine dye Cy5.5))	750 nm, 2 W/cm^2, 5 min	unknown	PTT + PDT	Increased cell apoptosis, ROS generation, tumor volume decrease, increased survival rate, increased efficacy of CTSE-sensitive nanocluster aus-U11
[235]	2017	MIA PaCa-2, subcutaneous MiaPaCa-2 tumor-bearing BALB/c nude mice	Transferrin (Tf)-conjugated gold nanoshell-coated rod-like mesoporous silica (GNRS) + GEM	808 nm, 0.5 W/cm^2, 1 min × 3 times, 1 min interval	unknown	PTT + chemotherapy	Improved gemcitabine penetration and accumulation in tumor tissues, increased blood flow, vascular permeability and oxygenation, tumor volume decrease
[236]	2017	Capan-2, subcutaneous Capan-2 tumor-	Cyclopamine (neo-adjuvant) + biomimetic gold nanorods (GNRS) coated with erythrocyte membrane	808 nm, 2 W/cm^2, 5 min	48-57°C	PTT	ECM disruption, improved tumor perfusion, tumor volume decrease

		bearing nude mice	(MGNRS)				
[237]	2019	SW1990, orthotopic SW1990 tumor-bearing BALB/c nude mice	Honeycomb-like gold nanoparticles (HGNs)	808 nm, 2 W/cm^2, 5 min	55°C	PTT + brachytherapy	HGNs-mediated IPT–BT increased use efficiency in tumor site, enhanced BT by attenuating X-ray, reduced side effects to the healthy tissue; double-stranded DNA damage, improved oxygen supply
[238]	2019	BxPC-3, PANC-1, ASPC-1, SW1990, orthotopic BxPC-3 tumor-bearing BALB/c nude mice	Single-walled carbon nanotubes (SWNTS) conjugated with COOH/PEG/CY7/CY7-IGF-1Ra	785 nm, 1 W/cm^2, 5 min	43-48°C	PTT	Optical imaging-guided PTT, increased survival in mice, cell damage through coagulative necrosis, pyknosis, apoptosis, and loss of adhesion
[239]	2020	Subcutaneous and orthotopic Pan 02 and NIH 3T3 tumor-bearing C57BL/6 mice	Small albumin-paclitaxel complexes (HSA-PTX) encapsulated in CAP- (a FAP-α responsive cleavable amphiphilic peptide) modified thermosensitive liposomes (CAP-TSL) (HSA-PTX@CAP-ITSL)	808 nm, 0.5-0.8 W/cm^2, 3 min	45-50°C	PTT + chemotherapy	Small sized HSA-PTX release in deep tumor regions promoted by expanded tumor interstitial space; increased mice survival
[240]	2020	Subcutaneous Capan-1 tumor-bearing BALB/c nude mice	Reduced graphene oxide@gold nanostar (RGO@AuNS) coated with lipid bilayer, dimethyldioctadecylammonium bromide/1,2-dioleoyl-sn-glycero-3-phosphoethanolamine (DODAB/DOPE) functionalized with FADODAB/DOPE-FA Nanocarrier	808 nm, 1.2 W/cm^2, 10 min	55°C	PTT + gene therapy	Inhibited tumor proliferation; suppressed liver metastasis
[220]	2020	BxPC-3, PANC-1; immunodeficient nude BALB/C mice PDX	Abraxane@mose2 (FDA-approved Abraxane and hydrophobic mose2 nanosheet)	808 nm, 1 W/cm^2, 5-10 min	54°C	PTT + chemotherapy	Reduction of α-SMA+ CAFs; augmentation of stromal disrupting
[241]	2020	Orthotopic MIA PaCa-2 tumor-bearing nude mice	Visualizable, photothermally controlled, drug release nanosystem (VPNS): naluf4:Nd@naluf4 NPs as the luminescent core, octabutoxyphthalocyanine palladium(II) (PDPC) as photothermal agent, phosphorylated gemcitabine (PGEM)	730 nm, 200 mW/cm^2, 10 min	unknown	PTT + chemotherapy	Triggered release of PGEM, cellular apoptosis, tumor volume decrease
[242]	2020	BxPC-3, subcutaneous BxPC-3 tumor-bearing BALB/c nude mice	Camptothecin (CPT) loaded PAAB@ICG nanoparticles	808 nm, 1 W/cm^2, 5 min	unknown	PTT + chemotherapy	Higher cytotoxicity with combined therapy, tumor volume decrease, drug penetration increase

[243]	2021	CFPAC-1; subcutaneous CFPAC-1 tumor-bearing mice	Semiconducting polymer nano-radiopharmaceutical with intrinsic photothermal capability and labeling with therapeutic radioisotope 177Lu (177Lu-SPN-GIP)	808 nm, 1 W/cm^2, 5 min	45°C	PTT + radiotherapy	Enhanced therapeutic capability of 177Lu-SPN-GIP compared with RT or PTT alone, suppressed growth of tumor stem cells, inhibited EMT marker expression
[244]	2021	Pan 02-luc tumor-bearing BALB/c nude mice	Thymopentin (TP5)-ICG nanofibrils	808 nm, 0.6 W/cm^2, 10 min	46.5°C	PTT + immunotherapy	Inhibited tumor growth, increased proliferation and differentiation of CD3+CD4+, CD3+CD8+ T cells, DCs maturation
[245]	2021	Pan 02 tumor-bearing C57BL/6 mice	Two types of polydopamine (DP)-coated NPs (N/PGEM/dp-5 and N/PGEM/dp-16) co-loaded with GEM and NLG919, a potent indoleamine-2, 3-dioxygenase (IDO) inhibitor	808 nm, 1.18 W/cm^2, 5 min	unknown	PTT + chemotherapy + immunotherapy	Tumor growth decrease of both primary tumor and the unirradiated distal tumor
[246]	2021	Pan 02, orthotopic and subcutaneous Pan 02 tumor-bearing C57BL/6 mice	Immune checkpoint blockade (BMS-202) loaded small-sized albumin NPs (HSA-BMS) encapsulated in size-adjustable thermo- and fibrotic matrix-sensitive liposomes (HSA-BMS@CAP-ILTSL)	808 nm, 0.5 W/cm^2, 10 min	44°C	PTT + immunotherapy	Reduced tumor hypoxia, relieved interstitial pressure, increased recruitment of endogenous immune cells; recovered activity of T lymphocytes, accompanied by secreting relevant cytokines (TNF- α and IFN- γ); tumor growth decrease, metastatic nodules decrease
[247]	2021	Panc02-H7, bone marrow DCs, subcutaneous and orthotopic Panc02-H7 tumor-bearing C57BL/6 mice	Fe_2P nanorods modified with DSPE-PEG2000-Mal (Fe_2P-PEG-Mal nanorods) + αpd-L1 (adjuvant)	980 nm, 0.5 W/cm^2, 10 min	up to 62°C	PTT + immunotherapy	Immunogenic tumor cell death due to ferrous iron-mediated Fenton reaction, increased infiltration of cytotoxic T lymphocytes, reduced metastasis
[248]	2022	Subcutaneous BxPC-3 tumor-bearing mice	Collagenase-functionalized biomimetic Dox loaded Au nanocages (AuNCs/Dox) AuNCs/Dox, M@AuNCs/Dox and Col-M@AuNCs/Dox	808 nm, 1 W/cm^2, 10 min	42-50°C	PTT + chemotherapy	Deeper penetration thanks to collagenase functionalization, collagen degradation, cell viability decrease with combination therapy vs. without NIR treatment
[219]	2022	Orthotopic Panc 02-H7 tumor-bearing C57BL/6 mice	Imiquimod (IMQ) loaded amorphous iron oxide NPs (IONS) coated with DSPE-PEG and ICG (IMQ@ions/ICG)	805 nm, 1 W, 10 min	ΔT up to 35°C	PTT + immunotherapy	Strong antitumor immunity triggered by *in situ* immunogenic cell death (ICD) combined with released IMQ, increased CD8+ T-cells in spleen and tumors; eradicated primary tumors, reduced mesentery metastases, increased survival time, minimal damage to normal tissue
[249]	2022	PANC-1, hTERT-HPNE, subcutaneous	Mn-doped Prussian blue (MNPB) NPs	808 nm, 1 W/cm^2,	44°C	PTT + chemodyna	Increased intracellular ROS and cell death; reduced cancer cell migration; decreased

		tumor-bearing BALB/c nude mice		15 min		mic therapy	matrix MMP-2 and MMP-9; tumor elimination via ferroptosis-mediated MAPK pathway
[250]	2022	PANC-1, PSCs, subcutaneous PANC-1+PSCs tumor-bearing mice	Lipid (C-G) NPs co-encapsulated with the acidic-pH responsive photothermal corconaine dye CTH and GEM	808 nm, 1 W/cm^2, 10 min	48°C	PTT + chemotherapy	Deactivation of PSCs through TGF-β/SMAD pathway, decrease in the expression of α-SMA and Collagen I, disruption of the ECM, increase in chemotherapeutic efficacy
[251]	2023	Subcutaneous SW1990 tumor-bearing BALB/c nude mice	Polypyrrole nanoparticles (PPY NPs) loaded with DOX, entrapped with a thermoresponsive ligand, lauric acid (LA) with bromelain (BL) grafted onto the surface	808 nm, 0.5-1 W/cm^2, 5 min	>60°C	PTT + chemotherapy	Hydrolyzation of collagen in ECM, enhanced DOX permeability, tumor growth inhibition
[221]	2023	Orthotopic SW1990 tumor-bearing BALB/c nude mice; PDX models	PDAC cell membrane-coated gold nanocages (AuNCs), to co-deliver GEM and nitrogen oxide (NO) donor (L-Arg)	808 nm, 1 W/cm^2, 5 min	54°C	PTT + chemotherapy	NO-promoted deeper GEM penetration, vasodilation-enhanced GEM chemotherapeutic efficacy; reduced tumor volume, increased mice survival; reduced metastasis
[252]	2023	Subcutaneous stroma-rich PL45 cells + hPSCs + Matrigel tumor-bearing BALB/c nude mice	CD71-specific targeting aptamers and paclitaxel (PTX)-modified polydopamine (PDA) nanospheres with the conjugation of peptidomimetic AV3 (termed Apt-PDA@PTX/AV3 bioconjugates)	808 nm, 2.5 W/cm^2, 5 min	52°C	PTT + chemotherapy	Desmoplastic stroma decrease through hPSCs deactivation, enhanced tumor perfusion, PTX-induced DNA damage and cell death
[253]	2024	Subcutaneous Panc 02 tumor-bearing C57BL/6 mice	Mesoporous silica ($mSiO_2$) coated black titanium dioxide ($bTiO_2$) NPs, in which resiquimod (R848) was loaded and DOTA-Gd was conjugated ($bTiO_2$@$mSiO_2$@Gd/R848)	808 nm, 1.5 W/cm^2, 5 min	55°C	PTT + immunotherapy	Promoted DC maturation; tumor volume decrease; increases the number of CD8+ and CD4+ T cells
[254]	2024	Pan 02, subcutaneous Pan 02 tumor-bearing BALB/c nude mice	Carbonic anhydrase (CA)-targeting cisplatin prodrug-decorated nanoparticle (IRNPs-SBA/PTIV)	1064 nm, 0.5 W/cm^2, 10 min	42-43°C	PTT + chemotherapy	Tumor growth decrease, negligible side toxicity, reduction of hypoxic and acidic TME
[255]	2024	BxPC-3, subcutaneous BxPC-3 tumor-bearing BALB/c nude mice	Transferrin-coated, tumor homing peptide decorated bimetallic magnetic NPs copper-doped iron oxide nanosystems embedded with IR820 photothermal agent and iron ions (PCTIFL)	808 nm, 1 W/cm^2, 10 min	unknown	PTT + PDT	IR820-mediated ROS generation, synergistic metal ion-triggered ferroptosis, dual MRI/NIR imaging, tumor volume decrease
[256]	2024	BxPC-3 tumor-bearing BALB/c nude mice	Triphenyl phosphonium-functionalized high-branch virus-like gold nanoparticles (Dox@TPAu)	808 nm, 1 W/cm^2, 5 min	unknown	PTT + chemotherapy	Mitochondrial function disruption, tumor volume decrease, reduced adverse effects to surrounding tissue, decrease in α-SMA+,

							FAP+ CAFs, decreased tumor vascular density
[222]	2025	Pan02-luc, SW-1990-LUC, subcutaneous SW1990 tumor-bearing BALB/c nude mice, patient-derived organoids	ICG photosensitizer + STING agonist (c-di-GMP) (adjuvant)	808 nm, 8 min	42–48°C	PTT + immunotherapy	Induction of pyroptosis via the caspase-1/GSDMD pathway, tumor volume decrease, mice survival increase, increased mature dcs, tumor infiltrating T-cells

3. State-of-the-art of PDAC preclinical models

PDAC preclinical modeling is crucial for meaningful treatment evaluation in the context of complex PDAC TME. Conventional *in vitro* models for therapeutic treatments development, such as 2D monolayer cultures, are unable to replicate the tumor microenvironment, which involves cell-to-cell and cell-to-matrix interactions. Although 2D cell culture procedures are straightforward, they are oversimplified representations of tumors that do not mimic closely the structural organization or pathophysiologic features of tumors.[257] On the other hand, animal models are *in vivo* research platforms that provide with an *in vivo* context for studying neoplastic development, behavior, and therapy. However, they have their own set of issues due to their time, resource, and skill requirements, and their usage is increasingly being questioned by many public bodies for ethical reasons. Furthermore, animal models often fail to accurately replicate human physiology, particularly the immune component.[258]

Three-dimensional (3D) culture models have shown to have great potential to bridge the gap between 2D cell cultures and animal models, providing a more physiologically relevant, *in vivo*-like environment, making them valuable tools in cancer research and medication development.[259] Tumor spheroids and tumoroids are attractive models, especially with emerging patient sample-based models,[260] because they mimic, at least partially, *in vivo* 3D cellular architecture. However, their main issue persists in being a static environment.

3.1 Tumor-on-chip models to bridge the gap between preclinical development and clinical applications

In regard to these limitations, microfluidic tools are becoming increasingly popular as a basis for 3D cell cultures in the investigation of tumor-stroma interactions, intravasation/extravasation mechanisms, angiogenesis and more, since they allow to maintain and examine 3D tissue samples in a controlled dynamic environment while recapitulating the physiological dynamic features.[261] The following section includes parts adapted from the review we wrote with Charlotte Bouquerel and the team that extensively summarizes not only the current trends in tumor-on-chip (ToC) models development quantitatively, based on extensive literature review, but their potential and applications for discovering and testing novel therapeutic agents, originally published in Lab on a Chip in August 2023.[262]

Microfluidic technologies, and organ-on-chip approaches in particular, have enormous potential for the development of a new generation of 3D *in vitro* tumor models. ToC models contain several features which make them highly attractive for both basic and translational research: (a) the capacity to control the cellular, mechanical and physicochemical conditions on-chip, (b) the compatibility with a wide range of analytical methods, including transcriptomic analysis and live imaging, (c) the possibility to produce human and/or immunocompetent models, and (d) the relatively short experimental time of several days, as compared to other 3D cancer models such as PDX or organoids, thereby supporting timely clinical decision-making.

The beauty of the ToC approach is the possibility to dissect the role of each parameter of the reconstituted TME. Various studies have explored the integration of different cell types and their spatial organization, ECM properties, on-chip generation of biochemical gradients, control of gaseous environment or even different mechanical forces at play. In modelling cellular composition, cancer cell lines continue to be the predominant tool in ToC studies (69%). However, up to date, around one third of ToC have already integrated primary cells to better mimic the tissue of origin (most of them being HUVEC). In addition, while still remaining a minority (<10%), more complex cellular models like PDOs, PDX or fresh tumor samples were used to approach the *in vivo* cell composition as closely as possible. As for the ECM modelling, current ToCs primarily use collagen-based matrix, followed by the common use of Matrigel as well as a wide range of other hydrogels such as fibrin, gelatin, and agarose, or more sophisticated hybrid hydrogels and *in vivo* extracted matrix (decellularized ECM). In addition, researchers have been able to implement physico-chemical components into ToC modeling such as compressive or shear stresses, interstitial fluid pressure and oxygen gradients among others, which are recognized as active players in tumorigenic signaling cascades, further elevating the complexity of ToC systems.

The variety of information that can be extracted from ToC studies is vast. Considering ToC studies of the past 15 years, the most common readouts used in ToC are drug-induced cell death (52% of ToC publications), followed by proteomic (23%), transcriptomic (14%) and secretome (8%) analysis. Additionally, more readouts such as imaging of hydrogel fibers, diffusion of a compound through the matrix, vessel permeability, cell migration, cell-to-cell interactions can also be obtained from ToC studies. This classification does not cover the whole spectrum but focuses on the most represented analytical readouts used in ToC that allow precise and efficient testing of the response to anti-cancer treatments, including chemotherapy, immunotherapy, radiotherapy as well as newly developing targeted

therapies and combination treatment approaches.

As a result, ToC ability to precisely and individually manipulate TME parameters enables researchers to dissect the influence of these TME parameters on tumor development, growth, invasion, and response to drugs in a physiologically realistic setting. While still presenting several challenges in standardization and the need for robust clinical validation, by combining a short establishment time and high control of several TME features, ToC models are expected to better predict patient's treatment response. At this stage, of course, ToC cannot replace all existing *in vitro* and *in vivo* models, and the future landscape will likely involve a combination of animals, organoids, and organ-on-chip platforms. Nevertheless, considering the high failure rate of clinical trials and the increasing emphasis on the 3Rs (replacement, reduction, refinement) principles by regulatory agencies worldwide, the success of ToC for clinical applications will be determined by its ability to detect and validate new therapeutic targets and to assist clinicians in defining the optimal therapeutic choices and sequences for patients.

3.2 PDAC-on-chip: current landscape

ToC technology is particularly valuable in the context of PDAC preclinical model development as it allows to finely tune its complex microenvironment and dissect the impact of its individual components on cancer progression and treatment response. As shown in Table 1.2, over two-thirds of the total of 24 identified studies on PDAC-on-chip models up to date were published in the past five years, highlighting the growing importance of such model development. Latest systems are rather advanced and include co-culture of PDAC cancer cells with stromal (fibroblasts or PSCs), endothelial, immune cells in 3D matrices and variable chip geometries. By enabling 3D culture in a closed, perfusable system, PDAC-on-chip models have already allowed investigation of tumor-stroma crosstalk, response, immune infiltration and invasion in a controlled setting.

Based on the information given in Table 1.2, we can observe that different studies focused on various components of ToC: either complexification of cellular composition or chip geometry or readout multiplexing. While several studies used tumor-derived murine cells[263-265] or human PDAC cell lines,[266-268] most of the systems included primary cells at least partially[269-278] or fully,[279-284] with patient-derived cells overtaking in the recent years, advancing the *in vivo* relevance of the models. In this way, Haque et al. may represent one of the most advanced cellular components in PDAC-on-chip as they incorporated patient biopsy-derived organoids (PDOs) together with PSCs and macrophages, showing that

targeting stromal cells (PSCs) by all-trans retinoic acid or macrophages by Clodrosome® improved therapeutic effect of gemcitabine on cancer cells.[278] Such patient-specific chips may allow drug screening prior to clinical applications, potentially identifying effective therapies for individual patients. Goluba et al. also emphasize that their chip is a "robust platform for functional precision medicine applications," supporting drug sensitivity assays and real-time biomarker monitoring.[284]

Marlene Geyer, who defended her thesis on the topic of "Development of Novel Microfluidic-based Pancreatic-Cancer-on-a-Chip Models" in 2023, also contributed greatly to PDAC-on-chip model development. Geyer and colleagues published two consecutive articles, where they first used PDAC PDOs co-cultured with PSCs,[282] then further co-cultured with HUVECs and PMBCs,[283] demonstrating the progressive model sophistication. This enabled drug sensitivity studies in the context of normoxic vs hypoxic and co-culture conditions as well as stromal barrier and its biochemical microenvironment function in immune cell infiltration. However, the chip geometries used by Haque (Figure 1.11A) and Geyer (Figure 1.11C) were rather simple: PDMS chip with two vertical channels separated by a porous membrane and the commercialized OrganoPlate® (Mimetas) 2 or 3-lane chips, respectively, supporting only unidirectional diffusion, thus potentially limiting mass transport and inducing steep concentration gradients.

In this way, Mohan et al. advanced the chip geometry, creating a transverse and normal diffusional environments for multidirectional signaling (TANDEM) openable chip with four vertically stacked acrylic layers, each serving a different purpose (Figure 1.11D).[274] Not only does it allow to study essential stroma-related phenomena, but it also enables multiplexing, allowing for *in situ* hydrogel analysis using both imaging techniques and direct physical access and sample extraction. While researchers mainly opted for compartmentalized chips with or without membrane separation, several studies developed lumen chips for PDAC modelling. Although more straightforward in fabrication and utilization, "perfect" in their simplicity they allow to mimic and investigate complex phenomena. Nguyen et al. described a chip in which a biomimetic ductal channel containing pancreatic cancer cells is juxtaposed to a blood vessel consisting of an endothelialized perfused lumen (Figure 1.11B).[263] They observed that pancreatic tumor cells invaded and occupied the lumen of the biomimetic blood vessel, resulting in apoptotic endothelial cells in proximity to cancer cells. On the contrary, endothelial cells in the biomimetic blood vessels in absence of tumor cells invasion did not exhibit apoptotic activity.

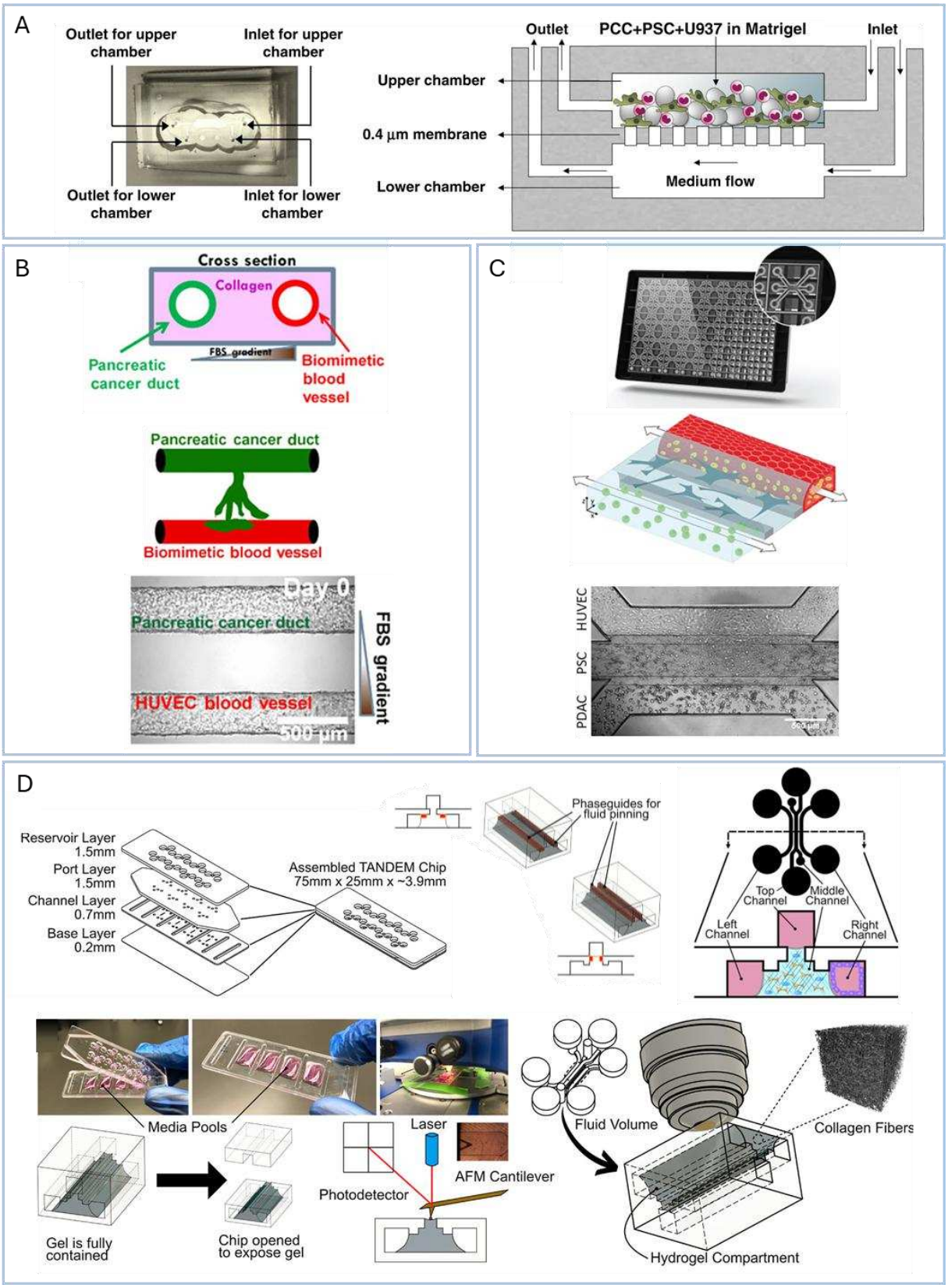


Figure 1.11: PDAC-on-chip systems. A. Haque et al. porous polyester membrane PDMS chip to co-culture PDAC organoids with PSCs and macrophages in 3D Matrigel matrix in the top chamber perfused with media through lower chamber.[278] **B**. Nguyen et al. lumen ToC composed of two cylindrical channels embedded in 3D collagen I matrix. One channel is coated with endothelial cells mimicking a perfusable blood vessel, and the other channel coated with PDAC cells to mimic a pancreatic cancer duct.[263] **C**. Geyer et al. system with commercial OrganoPlate 3-lane (MIMETAS)

including 40 chips with 3 chambers each, where endothelial cells (2D) and PDAC organoids (3D in Matrigel) are seeded in the lateral chambers and PSCs (3D in collagen I) are seeded in the central chamber.[283] **D**. Mohan et al. transverse and normal diffusional environments for multidirectional signaling (TANDEM) openable chip featuring central chamber with PSCs (3D in collagen I) with PDAC cells (2D) in the adjacent chamber.[274]

ECM composition seemed to be the most stable parameter in PDAC-on-chip systems as most of the models relied on Collagen type I utilization in various concentrations (2-10 mg/mL)[263–274,285,286] with less common Matrigel[276,278,279,281–283] use and occasional alternative gels, like basement membrane extract,[275] alginate-[280] or even egg white-based hydrogels.[277]

Over the course of these studies researchers have been able to extract numerous functional readouts using the developed PDAC-on-chip platforms. Apart from the aforementioned insights on tumor-stroma crosstalk and 3D microenvironment arrangement, drug screening and therapy testing was a popular output with less common immune-tumor interplay studies and metastasis modeling. Lastly, advanced PDAC diagnostic platforms with chip-based technology are evolving in parallel to improve not only treatment outcomes but also early disease detection.[287–290]

PDAC-on-chip platforms have markedly advanced the ability to recapitulate key features of pancreatic TME, including stromal density, biochemical gradients, and perfused vasculature. Models incorporating PDOs, PSCs, and immune components now permit investigation of tumor-stroma interactions, drug penetration, and mechanical stress in physiologically relevant contexts. Nevertheless, important limitations persist. Most systems still fail to fully reproduce the spatial heterogeneity and multi-scale complexity of *in vivo* PDAC, including the dynamic remodeling of the extracellular matrix, the immune-suppressive niche, and the mechanical coupling between tumor, vasculature, and surrounding pancreas. Integration of standardized readouts, real-time imaging, large-scale screening, and clinically validated endpoints remains limited, hindering cross-study comparability. At this stage PDAC-on-chip cannot fully replace existing *in vivo* and *in vitro* models and the future landscape will likely involve a combination of PDAC-on-chip with animals and organoids.[19,260,291] To realize their translational potential, future PDAC-on-chip models must strive for higher complexity without sacrificing scalability, incorporate diverse patient-derived components to capture inter-patient variability, and adopt harmonized validation frameworks.[292] Achieving this will position PDAC-on-chip technology not only as an experimental tool, but as a robust preclinical bridge capable of guiding therapeutic development and personalizing treatment strategies in this highly resistant malignancy.

Table 1.2: Summary of the PDAC-on-chip models available in literature up to date.

Ref	Year	Chip architecture & materials	Cellular composition	ECM composition	TME features	Functional readouts
[269]	2013	Compartmentalized PDMS chip consisting of three inlet channels that converge to form a single central culture channel	Human primary PSCs expanded + PANC-1, neonatal human dermal fibroblasts (NHDF) single 3D	Collagen I 2–4 mg/mL + sodium hyaluronate 2 mg/mL	N/A	Paclitaxel dose-response testing
[266]	2014	Compartmentalized chip in PDMS attached to a PS slide; 3 channels separated by pillars: cell, hydrogel, vascular channels	PANC-1, 2D	Collagen I 2 mg/ml	Gas channel-enabled oxygen gradient	Comparison of growth rate in normoxia flask, normoxia device and hypoxia device; increased migration in the device with cells maintained under 1% oxygen
[267]	2017	Commercialized (ChipShop) 8-chamber compartmentalized chip: into cyclic olefin polymer (COP) chamber (HepaChip®) with dielectrophoresis (DEP)-assisted cell assembly	PANC-1, BxPC-3, MIA PaCa-2, 2D	Collagen I coating 1 mg/ml	Continuous perfusion	Cisplatin dose-response testing
[270]	2018	Compartmentalized chip 7-chamber (3 cell loading chambers + 4 media channels) PDMS chip	PANC-1, PSCs, single 3D	Collagen I 2 mg/mL	N/A	Co-culture-mediated PSC activation and cancer cell migration; gemcitabine, paclitaxel and oxaliplatin drug sensitivity testing
[271]	2019	Transwell membrane (polycarbonate) chip	Primary human microvascular endothelial cells, primary human PSCs + patient-derived luciferase expressing PDAC cell lines 366, 449, and 608, 2D	coating: 0.1% gelatin on the top and 2 mg/mL collagen on the bottom surface of the membrane	Hemodynamic flow, hear stress	Transcriptomic changes correlation with the *in vivo* xenograft and patient transcriptome; gemcitabine dose-response correlation with patient's clinical response;
[285]	2019	Commercialized (OrganoPlate®, Mimetas) 3-lane compartmentalized chip	S2-028, single 3D	Collagen I 7.2 mg/mL	Interstitial flow	Interstitial flow-mediated gemcitabine resistance
[263]	2019	Two-lumen-in-collagen bilayer PDMS chip	primary mouse pancreatic cancer cells PD7591, HUVECs, 2D	Collagen I 2.5 mg/mL	Chemotactic agent gradient	PDAC cells-driven endothelial ablation correlation to *in vivo* PDAC models
[264]	2020	Compartmentalized 3-chamber chip with 4th capillary channel on top, separated by a porous PC membrane	mouse tumor-isolated KPC2, eKIC, mKIC, single 3D	Collagen I 6 mg/mL	Interstitial flow	Intratumoral heterogeneity-mediated gemcitabine resistance
[279]	2020	Multiwell PDMS, polyester, PEGDM array	Patient-derived organoids,	Matrigel	Interstitial	Co-culture-mediated pro-fibrotic

		with a central vascularized lumen (InVADE platform) surrounded by parenchymal compartment	HUVECs, human dermal fibroblasts		flow	changes, gemcitabine drug sensitivity
[265]	2020	Lumen PDMS chip	Mouse tumor-isolated KPC2, eKIC, mKIC, 2D	Collagen I 6 mg/mL	N/A	Local invasion of cancer cells with intratumoral heterogeneity
[272]	2021	Compartmentalized chip 7-chamber (3 cell loading chambers + 4 media channels) PDMS chip	PANC-1, BxPC-3, Capan-1, THP-1, human PSCs, single in 3D	Collagen I 2 mg/mL	N/A	Co-culture-mediated PSC & THP-1 cell activation and cancer cell migration; gemcitabine, 5-fluorouracil, oxaliplatin, and paclitaxel drug sensitivity and effect testing
[273]	2021	Commercialized compartmentalized three-channel chip (DAX-1, AIMBiotech Pte. Ltd.)	PANC-1, single 3D; PSCs, HUVECs, 2D; patient-derived T cells	Collagen I 3 mg/mL	Lateral pressure gradient	Endothelial barrier-mediated T cell infiltration; activation-mediated T cell infiltration
[278]	2022	Porous polyester membrane PDMS chip	Biopsy-isolated primary cancer cell organoids or MIA PaCa-2 co-cultured with human PSCs & U937, 3D	Matrigel 50%	Continuous perfusion	Anti-stroma agents (all-trans retinoic acid (ATRA), Clodrosome®) to improve ex vivo gemcitabine response; bidirectional effect between PSCs and primary cancer cells
[280]	2023	Tree-branched PDMS chip composed of two liquid inlets, a concentration gradient generator, cylindrical chambers, and ten liquid outflow tracts	Patient-derived primary cancer cell spheroids, 3D	Carboxymethyl cellulose + alginate microgels for spheroid formation	Drug concentratio n gradient	High-throughput gemsitabine and S-1 drug evaluation; patient-dependent drug sensitivity correlation with clinical study
[286]	2023	Compartmentalized PDMS chip with a three-channel bottom layer and a single channel top layer separated by an electrospun membrane (designed by Rhinoceros®,Robert McNeel & Associates)	Human pancreatic ductal epithelial cells (HPDE) 2D co-culture with PSCs single 3D; Human foreskin fibroblasts (HFF1) single 3D	Collagen I 10 mg/mL	N/A	PDAC cancer cells supernatant-mediated fibroblast activation, bortezomib drug sensitivity testing
[281]	2023	Microwell array PDMS chip with flow layer and side injection port protected by a valve	Patient biopsy-derived organoids	Matrigel	N/A	Microfluidic vs standard matrigel-based organoid culture comparison; RAF and MEK kinases-targeting therapy testing; selective GSK-3β inhibitor in combination with gemcitabine testing; NK Cells and TriKE immunotherapy testing
[282]	2023	Commercialized (OrganoPlate®, Mimetas) 2-lane compartmentalized chip	Patient-derived organoids, PSCs single 3D	Matrigel	Interstitial flow	Drug sensitivity studies, as a function of mono- vs co-culture and hypoxia vs normoxia
[283]	2023	Commercialized (OrganoPlate®, Mimetas) 3-lane compartmentalized chip	Patient-derived organoids, PSCs single 3D, HUVECs,	Matrigel, Collagen I	Interstitial flow	Cell spatial organisation changes and immune cell (PMBC) infiltration under

			PMBCs in suspension	4 mg/mL		Co-culture conditions; stromal (PSCs) barrier function, biochemical microenvironment and immune cell infiltration sensitivity to stromal targeting compounds testing
[284]	2024	PET membrane chip in COC/OSTE with single superimposed channels	Patient-derived organoids dissociated into single primary human pancreatic tumor cells, HUVECs, 2D	N/A	Continuous perfusion	Biomarker secretion comparison to 2D tissue culture plates
[268]	2024	Compartmentalized 3-chamber chip with poly-d-lysine (PDL) or polydopamine (PDA) surface functionalization	BxPC-3, Capan-2, PANC-1, single 3D	Collagen I 2.5 & 4 mg/mL	N/A	PDA coating optimization for optimal collagen attachment and PDAC spheroid growth
[274]	2024	Transverse and normal diffusional environments for multidirectional signaling (TANDEM) openable chip with four acrylic layers: blank bottom layer for clear microscopy imaging; channel layer with three channels bonded face-down to the blank layer; port layer with multiple inlet/outlet ports + a single channel aligned above the middle channel of the channel layer; top layer with reservoirs aligned to port locations	PANC-1, 2D, human PSCs, single 3D	Collagen I 2, 4 & 6 mg/mL	N/A	COMSOL-based computational transport model; single vs dual-plane diffusion rate comparison
[275]	2024	Compartmentalized 5-channel PDMS chip	PANC-1 co-culture with human PSCs, single 3D	Cultrex® Basement Membrane Extract 6–9 mg/mL1	Interstitial flow	Hydraulic conductivity of the interstitial space characterization; collagen I and HIF-1a production; losartan and gemcitabine drug sensitivity testing
[276]	2025	Commercialized (Dynamic42 GmbH) polybutylene terephthalate (PBT) chips with two chambers each consisting of 3 vertically stacked channels separated by porous membranes and equipped with individual inlets and outlets	PANC-1 + patient-derived PSCs spheroids, HUVECs, Peripheral blood mononuclear cells (PBMC)	Collagen I 0.1 mg/mL or Matrigel	Continuous perfusion	Dynamic administration of the histone deacetylases (HDAC) inhibitor suberoylanilide hydroxamic acid (SAHA); monocyte polarization and tumor spheroid infiltration
[277]	2025	Compartmentalized four-channel chip	PANC-1, primary normal human dermal fibroblasts, single 3D	Egg white/gelatin hydrogel, Collagen I 6 mg/mL	N/A	EW/gelatin hydrogel characterization via cancer spheroid growth, co-culture-mediated exogenous angiogenic cytokine and growth factor secretion

4. Summary and Thesis Rationale

4.1 Research gap

Despite considerable progress in the molecular and cellular characterization of PDAC and incremental broadening of therapeutic options, clinical outcomes for most patients remain bleak. Conventional modalities — including surgery, gemcitabine- or FOLFORINOX-based chemotherapy, and, in select cases, radiotherapy — offer only limited benefit, particularly in advanced diseases, where median survival rates are still measured in months. Owing to the tumor's aggressive biology, high metastatic potential, and, critically, its extraordinary treatment-refractory TME, we remain rather powerless in the face of this malignancy.

A defining feature of PDAC is the extensive desmoplastic stroma, composed predominantly of fibrous collagen, hyaluronan, activated PSCs/CAFs, and immune infiltrates. This complex and bidirectional tumor-stroma crosstalk drives ECM deposition, alters matrix stiffness, elevates interstitial fluid pressure, and induces vascular collapse, even further multiplexing the directionality of pro-tumor signaling cascades, thereby impeding drug perfusion. Beyond acting as a physical barrier, the stroma serves as a dynamic signaling hub that promotes EMT, immune evasion, metabolic rewiring and chemoresistance *(and how many "vicious circles" did you count throughout this chapter?)*. While this may sound discouraging from a patient's (and throughout this chapter) perspectives, from a biological and evolutionary standpoint, the remarkable adaptability and self-sufficiency of the PDAC system are striking. Overcoming its intertwined resistance mechanisms remains one of the most significant unmet challenges in PDAC therapy.

Within this context, NP-PTT has emerged as a promising experimental modality capable of delivering spatiotemporally controlled hyperthermia to induce direct tumor cytotoxicity and modulate stromal architecture. Yet, despite the encouraging findings with sophisticated targeting nanoagents, most NP-PTT research in PDAC remains confined to subcutaneous or orthotopic xenograft models in immunodeficient mice. These systems, while offering complexity, incompletely reproduce the biochemical, vascular, and immunological features of the human PDAC environment, and can sometimes be even misleading in some aspects, like the extreme levels of elevated interstitial fluid pressure, NP distribution, and dynamic stroma remodeling. In addition, local thermal gradients are poorly characterized in animal models, owing to their inherent complexity that also hampers careful monitoring of NP-PTT impact on individual tumor components. This disconnect

between preclinical models and clinical reality hinders translation and the rational design of combination regimens that NP-PTT is aimed at.

Microfluidic PDAC-on-chip platforms provide an attractive opportunity to address some of these limitations. These devices enable co-culture of tumor, stromal, endothelial, and immune components in perfused, 3D configuration, recapitulating key aspects of ECM deposition, interstitial transport, and stroma-mediated resistance while still providing the ability to dissect the effects of individual TME components independently. However, while cutting-edge PDAC-on-chip models include multiple cellular components, with half of studies incorporating PSCs, their spatial organization and architecture can be improved. Researchers have mainly co-cultured PSCs separately from cancer cells, either in adjacent channels[269,274,277,282,283] or even separated by another chamber,[270,272] membrane[273,286] in 2D,[271,273] or 3D,[269,270,272,274-277,282,283,286] while *in vivo*, PSCs are in close proximity to the tumor cells, creating a surrounding niche, suggesting the best modelling would include 3D tumor cells surrounded by 3D PSCs culture to recapitulate the tumor-stroma architecture of PDAC. Several studies have integrated simultaneous co-culture of PDAC cells with PSCs such as Kpeglo et al. who cultured single PDAC cells with single PSCs in 3D matrix, or Deipenbrock et al. who produced cancer cell/PSC hybrid spheroids.[275,276] However, with these models we face either single cancer cell mixture with PSCs or similarly, spheroids with intermixed single cells that exclude the "tumor aggregate component surrounded by single PSCs". In this way, Haque et al. and Lai et al. approached the closest tumor-surrounding TME by co-culturing PDOs directly with single PSCs or fibroblasts, respectively, in the ECM on chip.[278,279]

In addition, very few studies have explored matrix complexification with proteins other than Collagen I or Matrigel that not only is highly batch-dependent but also lacks several human peptide motifs and may affect gene expression. Kpeglo et al. utilized basement membrane extract (BME) as an ECM scaffold to stimulate PSC-derived collagen production, thereby imitating stromal cell-mediated ECM deposition characteristic of PDAC.[275] While conceptually valuable for modeling, detectable collagen production may require 5-10 days, and when present, it mostly resembles dispersed, disorganized deposits rather than dense, fibrous collagen network observed *in vivo*. Lastly, to the best of my knowledge, none of the PDAC-on-chip models up to date have attempted to incorporate hyaluronic acid within the matrix, while it may be debated to be the second most crucial component in PDAC ECM due to its immense role in interstitial fluid pressure increase and subsequent drug perfusion decrease. It is worth mentioning that these are not the only avenues for refinement — further progress will also hinge on incorporating features such as

functional vasculature, dynamic immune-stroma interactions, and real-time microenvironmental monitoring, which remain technically complex and less straightforward to implement in current PDAC-on-chip platforms.

Finally, PDAC-on-chip technologies have primarily been applied to evaluate chemotherapeutics and, less commonly, anti-stroma or immunotherapies, with no reported implementation in photothermal oncology. Considered altogether, we can identify a dual knowledge gap:

1. NP-PTT studies lack physiologically relevant preclinical platforms that capture tumor-stroma crosstalk, stromal dynamics and allow to dissect the impact on individual parameters.
2. PDAC-on-chip systems remain underutilized for emerging therapies such as NP-PTT, leaving the mechanistic impact of NP ablation on stromal and cancer cell architecture and function largely unexplored.

Integrating NP-PTT into advanced PDAC-on-chip models offers a compelling strategy to bridge this gap. Such platforms could enable precise control over NP delivery, light exposure, and thermal gradients, while allowing real-time monitoring of their effects on tumor and stromal components. In the long term, this approach could potentially refine treatment parameters, identify synergistic combinations, and improve predictive validity for clinical translation, ultimately accelerating the development of nanothermally driven therapies for oncological applications.

4.2 Thesis Scope and Objectives

In essence, the field of NP-PTT for PDAC can be divided into two interconnected trajectories: the development of physiologically relevant models, and the optimization of NP-PTT treatment strategies. Although both trajectories have advanced independently, this thesis posits that they should be studied in concert. At this early stage of NP-PTT development, it is crucial to dissect the treatment's impact on both tumor cells and their microenvironment step by step, while progressively increasing the complexity and physiological relevance of the *in vitro* platform.

The overarching objective of this thesis is to establish and utilize PDAC-on-chip systems as mechanistic testbeds for NP-PTT, enabling precise control over NP delivery, light application, and thermal gradients, alongside real-time monitoring of cellular and ECM responses. This dual focus aims not only to characterize the direct cytotoxic effects of NP-

PTT on cancer cells but also to investigate its capacity to remodel stromal architecture, influence EMT, and potentially enhance therapeutic susceptibility.

To achieve this, the thesis is structured around two main experimental phases. The first centers on the integration of magnetite NP-PTT into an early PDAC-on-chip system, applying a dual-action approach to target both malignant and stromal compartments. The second phase advances the model's physiological complexity by co-culturing pre-formed tumor spheroids with dispersed PSCs or CAFs under both direct and indirect 3D contact conditions, and by incorporating hyaluronic acid into the ECM to better mimic one of the key barrier components of PDAC stroma. This allows systematic assessment of how stromal co-culture and matrix composition influence EMT dynamics in cancer cells with the goal to recapitulate the essential invasive feature of PDAC and study its modulation via NP-PTT in the future.

Through this combined strategy, the work presented in this thesis seeks to provide both a methodological framework and mechanistic insights to support the translational advancement of NP-PTT in PDAC.

CHAPTER 2

Magnetite Nanoparticle Photothermal Therapy in a Pancreatic Tumor-on-Chip: A Dual-Action Approach Targeting Cancer and its Microenvironment

Context & Motivations

Despite recent advances in nanomedicine and microphysiological systems, the clinical translation of nanoparticle-mediated photothermal therapy (NP-PTT) for PDAC remains hindered by the lack of physiologically relevant preclinical platforms that allow for stepwise therapeutic evaluation under finely controlled conditions. This gap underpins the motivation for the work presented in this chapter: to merge the precision of advanced tumor-on-chip technology with the emerging promise of NP-PTT in a unified platform capable of both mechanistic dissection and therapeutic evaluation.

The added value of this study lies in investigating a dual-action of NP-PTT in a PDAC-on-chip model that enables simultaneous targeting of cancer cells and their surrounding matrix under controlled conditions, while providing real-time monitoring of treatment effects. This represents a significant step toward narrowing the gap between promising NP-PTT preclinical data and eventual clinical translation by enabling systematic evaluation of nanoparticle delivery, photothermal activation, and microenvironmental response in a foundational PDAC-on-chip system. While this platform does not yet approximate the full complexity of *in vivo* disease, it provides a solid basis that can be progressively expanded for stepwise evaluation of NP-PTT.

This chapter builds upon the conceptual groundwork laid earlier in this thesis by addressing two interconnected objectives. First, it seeks to establish a robust NP-PTT protocol within a PDAC-on-chip platform, enabling controlled application of PTT while preserving relevant microenvironmental features. Second, it aims to characterize the dual impact of NP-PTT on both cancer and ECM compartments, thereby providing insights into its potential to disrupt tumor-stroma crosstalk and overcome PDAC's intrinsic resistance mechanisms.

Together, the experimental work presented here demonstrates the feasibility and advantages of integrating NP-PTT into a PDAC-on-chip system. This includes the development of tailored magnetite nanoparticle formulations, optimized photothermal activation parameters, and quantitative analysis of cytotoxic and matrix-remodeling effects. To the best of our knowledge, these efforts constitute the first demonstration of a NP-PTT-enabled PDAC-on-chip model, offering a proof-of-concept for a translational platform that unites therapeutic innovation with high-fidelity modeling of the human tumor microenvironment.

This context has led to the study detailed in the remainder of this chapter, originally

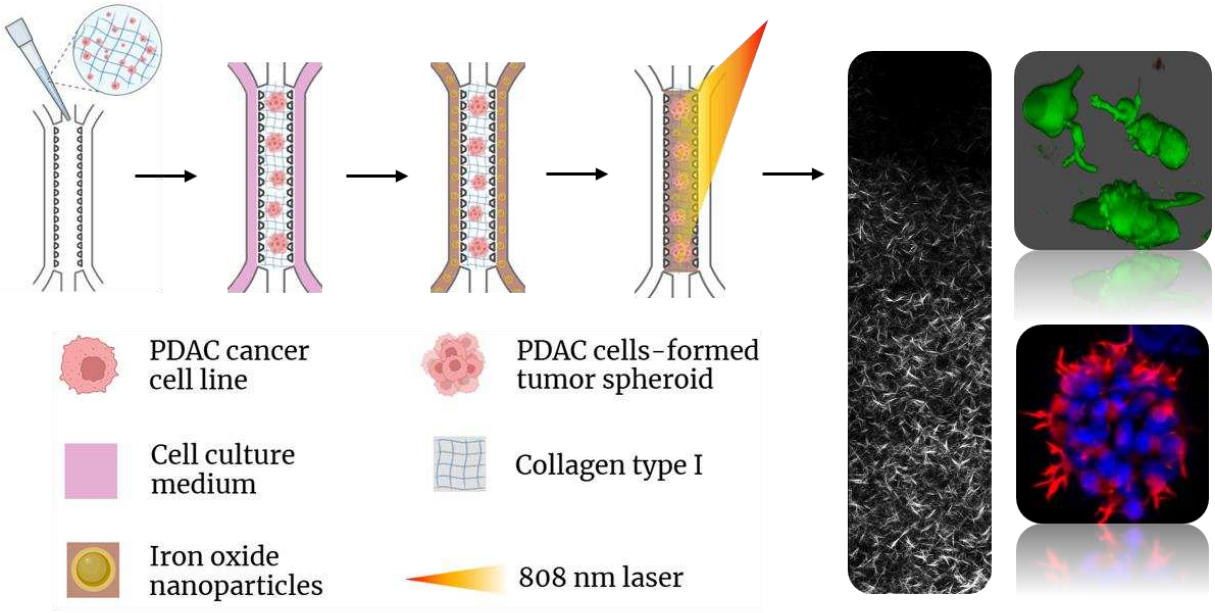
published in ACS Nano in May 2025 *(Anastasiia Dubrova, Charles Cavaniol, Aurore Van de Walle, Paul Mathieu, Zoé Fusilier, Nader Yaacoub, Yoann Lalatonne, Stephanie Descroix, Claire Wilhelm)*.[293] **Chapter 2** has been adapted from that publication. The chapter therefore contains typical sections including ***Abstract***, ***Introduction***, ***Results***, ***Discussion*** and ***Experimental Procedures***, followed by the paper's ***Supplementary information***.

An **additional section** follows the paper, dedicated to discussing the ***challenges, limitations, and future perspectives*** of the study in greater detail.

ABSTRACT

The application of magnetite nanoparticles (MagNPs) for photothermal therapy (MagNP-PTT) has recently expanded in cancer treatment. This study introduces MagNP-PTT in a tumor-on-chip model to target highly aggressive pancreatic ductal adenocarcinoma (PDAC). A tumor-on-chip system was developed using PANC-1 PDAC cells embedded in a collagen type I extracellular matrix and cultured for one week to form tumor spheroids. This platform serves as the foundation for applying PTT in a model system that is aimed to mimic the native tumor microenvironment. MagNPs efficiently penetrate the tumor spheroids, achieving controlled heating via near-infrared (NIR) light. By adjusting nanoparticle concentration and laser power, temperature increments of 2°C between 38–48°C were established. Temperatures above 44°C significantly increased cell death, while lower temperatures allowed partial recovery. Beyond inducing cancer cell death, MagNP-PTT altered the extracellular matrix, and triggered a slight epithelial-mesenchymal transition marked by increased vimentin expression. These findings highlight MagNP-PTT as a dual-action therapy, targeting both tumor cells and their microenvironment, offering a novel approach for overcoming stromal barriers in pancreatic cancer treatment.

TABLE OF CONTENTS



KEYWORDS: Magnetite Nanoparticles, Photothermal Therapy, Tumor-On-Chip, Extracellular Matrix, Pancreatic Ductal Adenocarcinoma, Tumor Microenvironment

I. INTRODUCTION

Pancreatic ductal adenocarcinoma (PDAC) is a highly aggressive tumor comprising over 90% of pancreatic cancer cases, with a 5-year survival rate of less than 8%.[2,294] Its incidence and mortality rates are strongly correlated, contributing to its status as one of the deadliest cancers globally.[295] The biological hallmark of PDAC is its complex microenvironment characterized by a dense tumor stroma occupying up to 90% of the tumor volume due to excessive protein secretion and deposition into the extracellular matrix (ECM). Consequently, a cascade of mechanical and biological events take place, notably hypovascularity, increased interstitial fluid pressure, hypoxia, and immunosuppression, ultimately hindering drug penetration.[67,296,297]

Current PDAC treatments remain limited as resectable PDAC mostly rely on surgery combined with chemotherapy,[10] while advanced PDAC are managed with chemotherapy only yielding limited efficacy (median overall survival: 6-12 months).[2] To face the pitfalls of current treatments, innovative approaches are currently of principal interest. An emerging tool that could address the specific features of PDAC and the limitations of its current treatments is hyperthermia. Hyperthermia involves a local temperature increase within the tumor in a range of 38-48°C with the aim of inducing a tumor-suppressing effect. Given PDAC's significant stromal component, hyperthermia becomes yet more valuable for combination therapy development by simultaneously targeting both cancer cells and tumor stroma. Generic hyperthermia involves external irradiation modalities, such as microwaves, radiofrequency, ultrasound, global heating — all presenting challenges in localization of impact. In contrast, the introduction of nanoparticles to the field allowed for their consideration as intrabody localized heat sources that can be remotely activated to release heat locally into the surroundings. Combining hyperthermia with nanoparticles permitted precise cancer tissue targeting in both *in vitro* and *in vivo* studies with minimized side effects on healthy tissue thanks to tumor-localized impact achieved through distant stimulation.[205,298–302] Besides, since the arrival of nanoparticles use in medicine, hyperthermia is also being regarded as an adjunctive therapy to established chemo-, immune- or radiotherapy, to increase the chemotherapeutic or ionizing radiation effects.[303–307]

Specifically, hyperthermia has the capacity to affect both the cancer cells and their surrounding extracellular matrix within the tumor niche giving further potential to overcome poor drug penetration limitation through synergistic effect.[303–305,307] Nanoparticle-mediated magnetic hyperthermia (MHT) initially emerged as the state-of-the-art technique for achieving localized temperature elevation.[298,300,302,308] However, the effectiveness and clinical

relevance of MHT have been challenged by the need for high nanoparticle concentrations to induce significant heating. Remarkably, PTT demonstrates efficient performance at significantly lower nanoparticle concentrations compared to MHT,[205,309,310] yet introducing another drawback, which is the limited penetration of light into deep-seated tumors. Nevertheless, PTT is now increasingly envisioned for nanoparticle-mediated anticancer thermal therapy in clinical settings. Plasmonic nanoparticles, such as Au/Ag nanorods, nanoshells, nanostars, were subsequently introduced for nanoparticle-mediated photothermal therapy (NP-PTT), leveraging their efficacy as efficient light absorbents due to their localized surface plasmon resonance properties in the near-infrared (NIR) region and subsequent heat dissipation into the surrounding tissue. However, their application is often limited due to the inherent cytotoxicity of these materials, which restricts the safe concentration range. In contrast, recent studies have highlighted novel polydopamine-, humas serum albumin- and black phosphorus-based systems as promising non-toxic alternatives, with high photothermal conversion efficiency, making them strong candidates for PTT while alleviating concerns related to long-term biocompatibility.[311–313] However, the application of these materials may be limited by their poor penetration in deeper tissues due to their optical properties, making them less effective for treating tumors located at greater depths. Interestingly, magnetic NPs with a magnetite core have recently been described as good competitors to the other materials for photothermal conversion due to their valence band transition between Fe^{2+} and Fe^{3+} that confer absorption in the NIR region,[207,314] including the second biological window NIR-II.[315] In addition, magnetic NPs may offer enhanced targeting precision through external magnetic fields. This, in turn, expanded the use of magnetic NPs from MHT agents to promising PTT candidates. In addition, the growing interest in magnetic NPs' use for PTT is also driven by the innate properties of iron biocompatibility and biodegradability within tissues that leverages them over commonly used metals like gold or silver. Beyond reduced toxicity, magnetic NPs offer further possibility of employing the magnetic properties of the material, notably, as contrast agents for MRI or via magnetic guidance to the tissue of interest.

Given the recent emergence of magnetic nanoparticles for PTT as well as the yet nascent stage of PTT in clinical cancer treatment,[316,317] there is now a need to fully understand the effects of these treatments, both on cancer cells and their microenvironment. To achieve this, relevant *in vitro* models must replicate the complexity of tumor tissues as closely as possible while maintaining precise control over experimental conditions. This is particularly important for novel cancer treatment development, as it has been demonstrated that the composition of the tumor microenvironment (TME) is a key

player in the tumor response to drugs.[84,318–320] Current strategies such as 2D models or spheroids/organoids offer fast preliminary screening but do not allow for a tunable 3D ECM, while animal models do not respond to treatment similarly to humans. In turn, tumor-on-chip models offer a promising alternative to recapitulate the 3D human TME *in vitro* while providing a fine control over the system to investigate therapeutic modes of action comprehensively.[262,321–325] Up to date, several PDAC tumor-on-chip models have been developed, [263,270,278,279,282] however, most of them were primarily focused on model development rather than exploring novel therapeutic strategies. While to the best of our knowledge, there have been no reports of MagNP-PTT applications in tumor-on-chip, several studies of nanoparticle-based PTT for anticancer applications have been conducted both *in vitro* and *in vivo* for some tumor types,[326] including PDAC.[235,250] They have demonstrated several successful results including tumor volume reduction, stimulation of antitumor immunity and effective cancer cell targeting. However, there is an evident gap for studies on nanoparticle-based PTT in tumor-on-chip platforms that we are aiming to bridge with this study.

Herein, we propose to incorporate MagNP-PTT into a microfluidic chip for investigating the impact of localized heating on the TME within a PDAC tumor-on-chip model. Specifically, this was achieved using magnetic iron oxide nanoparticles as an internal heat source within tumor-on-chip, exploiting their capacity to be stimulated with a NIR laser. The objective is to examine the response of the key components of simplified PDAC tumor-on-chip model combining pancreatic cancer cells and collagen type I-based ECM to such treatment. As primary indicators of the MagNP-PTT effect, we assessed collagen matrix denaturation and cancer spheroid cell death across a range of hyperthermia temperatures. Initially, we demonstrated a temperature-dependent sharp transition of the collagen matrix from an organized fiber mesh to the absence of defined structure around 46°C, with little-to-no detectable effect at lower temperatures. When evaluating the effect of MagNP-PTT on tumor cells, progressive cancer cell death and tumor spheroid deterioration was observed with increasing temperatures. In addition, we have identified that cancer cell viability is influenced by the duration of the rest period after MagNP-PTT treatment and before the assessment of cell survival. Extended resting periods of 24 hours have shown higher viability in samples heated at temperatures ranging from 40-44°C compared to those assessed after a 2-hour rest period. However, such an effect was not observed at higher temperatures (44-48°C). Investigating the phenotypic changes of the surviving cells we have demonstrated potential upregulation of EMT marker expression. Overall, these results establish the analysis of the MagNP-PTT -triggered impact on a tumor-on-chip and set a solid foundation

for future development of the synergistic therapies of MagNP-PTT with some of the established anticancer therapies where the therapeutic window combination will play a key role.

II. RESULTS

1. Magnetite Nanoparticles for NIR Photothermia

Recently, iron oxide nanoparticles have emerged as efficient photothermal agents, surpassing their prior role as agents for magnetic hyperthermia. However, for effective photothermal conversion, magnetite Fe_3O_4 is preferred over maghemite Fe_2O_3. This preference arises from the mixed Fe^{2+}/Fe^{3+} valence state of Fe_3O_4, which induces NIR optical absorbance via intervalence charge transfer,[314,327,328] a feature absent in g-Fe_2O_3, which only contains Fe^{3+}. It is nonetheless admitted that maintaining iron in its stochiometric +2-oxidation state in ultrasmall chemically synthesized nanoparticles (d < 10 nm) can be challenging because of the oxidation of magnetite nanoparticles to maghemite at low temperatures in water.[327] Therefore, magnetic nanoparticles are generally considered to be at least partially oxidized to maghemite. Remarkably, larger biogenic magnetosomes synthesized by magnetotactic bacteria retain their magnetite composition and are often described as the only magnetic crystals allowing for pure magnetite. Magnetic nanoparticles synthesized through sol–gel microwave-assisted method were recently characterized as magnetite-composed, by Mossbauer or Fourier transform infrared spectra.[329] This is exceptional for small nanoparticles with a high surface-to-volume ratio, which typically favor the formation of maghemite in aqueous media. Notably, the benzyl alcohol route not only produces highly crystalline nanoparticles but also acts as a reducing agent, converting ferric salt (iron (III) acetylacetonate) into Fe^{2+} ions. Besides, this synthesis allows for fine control of coating agents for stabilization.[330] Herein, PO-PEG-NH_2 coating was selected (Figure 2.1A) to increase NPs' stability and optimize NPs' interactions with biological systems thanks to the hydrophilic and antifouling properties of PEG. The synthetized nanoparticles displayed an average diameter of 9 nm as observed with TEM imaging (Figure 2.1B) with hydrodynamic size 31.4 +/- 12.6 nm, polydispersity index (PDI) 0.275 and positive zeta potential of +14.8 +/- 6.9 mV (Figure 2.S1). PTT efficiency at 808 nm is attributed to the absorbance in the NIR region (Figure 2.1C, Figure 2.S2A) due to the high proportion of magnetite within the as-synthesized iron oxide nanocrystals. The Mössbauer spectrum (Figure 2.1D) consists of asymmetrical magnetic sextet with broadened and overlapped lines. The fitting model involves considering a distribution of hyperfine fields correlated to that of isomer shift. The mean isomer values (< d> @ 0.50) which remain

independent on the fitting procedure are consistent with the coexistence of magnetite and maghemite.[331] The mean isomer shift confirms that magnetite is the dominant component, accounting for 79%. The PEG coating on the nanoparticle surface is confirmed by FTIR, showing characteristic bands at 580 cm^{-1} for Fe-O vibrations from the iron oxide nanoparticles and at 1110 cm^{-1} for C-O vibrations from the PEG chains (Figure 2.1E), indicating successful PEGylation. Consequently, they were tested for photothermal conversion in a standard tube setup (Figure 2.1F), using a volume of 100 µL, increasing NP concentrations (2 to 64 mM) and employing laser power densities of 1 W/cm^2 at 808 nm. Corresponding light to heat conversion coefficients were calculated (Figure 2.S2B) and found independent of NP concentration, yielding a consistent value of 27 ± 2 %. The resultant heating (Figure 2.1G) positioned them as efficient NIR photothermal agents, approaching the efficacy of magnetosomes.[205]

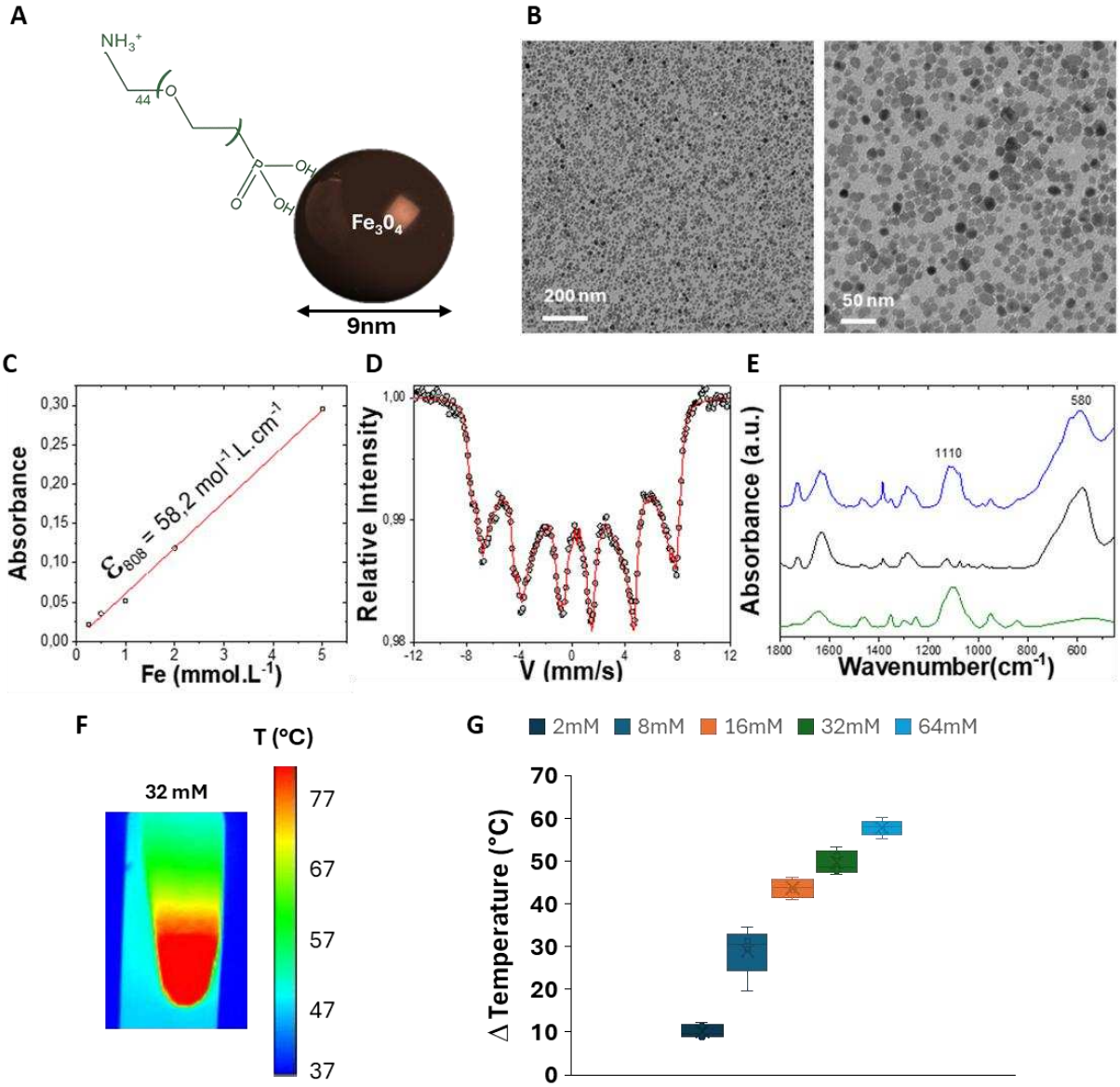


Figure 2.1. **Magnetite nanoparticle physico-chemical investigation. A**. Schematic representation of nanoparticle coating. **B**. TEM imaging of nanoparticles in suspension. **C**. 808 nm absorbance measurement as a function of iron concentration. **D**. Mössbauer spectra for the as-synthesized 9 nm NPs (black circles), with the calculated spectrum representing a mixture of 79% magnetite and 21% maghemite (red line). **E**. FTIR spectra of PO-PEG-NH_2 molecules (green curve), bare 9 nm NP (black curve), and 9 nm NP coated with PO-PEG-NH_2 (blue curve). **F**. Representative image of the thermal camera recording of in-tube NPs [32 mM] heating with an 808 nm laser at 1 W/cm^2. **G**. Temperature profile change of in-tube NPs heating at concentrations 2-64 mM and laser power 1 W/cm^2.

2. PDAC Tumor-on-Chip 3D Model

To recapitulate PDAC tumor-on-chip, a mixture of pancreatic cancer cells (PANC-1) and collagen type I (6 mg/mL) was introduced into the central channel of a chip (AimBiotech™, Figure 2.2A) enabling a capillary-based confinement of the hydrogel with cells in the central chamber (Figure 2.2B). This straightforward PDAC tumor-on-chip model comprising PANC-1-grown tumor spheroids in collagen type I matrix on a chip was chosen to assess the effect of MagNP-PTT treatment on the tumor microenvironment. In brief, PDAC cells were seeded in collagen I on chip and left to mature and self-organize into tumor spheroids within the matrix for a week before the MagNP-PTT exposure. After this 7-day period, cells spontaneously formed small tumor spheroids of around 100 µm in diameter (Figure 2.2C, D0 vs D7). The viability of these spheroids was confirmed with live/dead assay, where the green (live) signal significantly prevails over the red (dead) (Figure 2.2D). In addition, the morphology and volumetric distribution of spheroids within the collagen matrix was visualized via 3D confocal imaging (Figure 2.2E). Spheroids of different sizes were evenly distributed within the chip, with some spheroids developing protrusions (Figure 2.2F, Figure 2.S3), which can be indicative of invasive cancer cell behavior. In addition, we visualized our tumor microenvironment system with PDAC spheroids uniformly surrounded by collagen fibers (Figure 2.2G-I). This reflects the dynamic and reciprocal interplay between the tumor spheroids and their microenvironment, which is also highly characteristic of the *in vivo* tumor niche.[84,85]

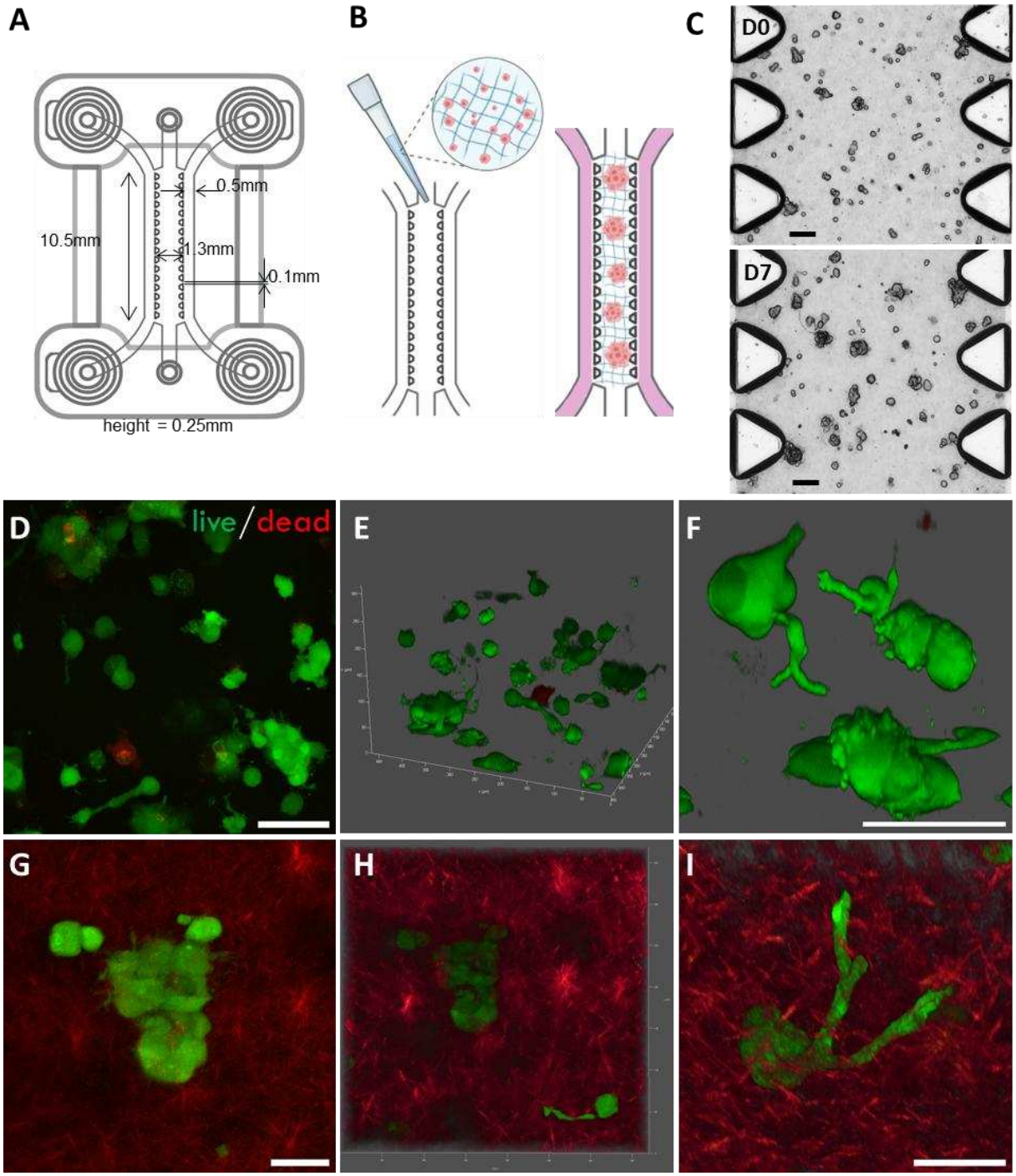


Figure 2.2: **Development of the 3D PDAC tumor-on-chip model. A**. Schematic representation of microfluidic chip idenTx3, AimBiotech™. **B**. Schematic representation of cancer cell seeding in collagen on chip with subsequent spheroid formation. **C**. Bright field microscopy images of PDAC tumor spheroid development from single cells (D0) vs after 7 days of maturation in collagen on the chip (D7). Scale bar = 100 µm. **D-F**. Confocal microscopy images of Live/Dead assay (dead = red; live = green) with (D) z-projection of the 3D stack, at day 8 on-chip, (E-F) 3D confocal stack reconstructions. Scale bar = 100 µm. **G-I**. Second harmonic generation (SHG) microscopy image of a tumor spheroid (green) with the surrounding collagen matrix (red) z-projection of the 3D stack (G), reconstructed 3D images (H-I). Scale bar = 50 µm.

3. Administration of Magnetite Nanoparticles in Tumor-on-Chip

Using the PDAC tumor-on-chip model, where cancer cells have self-organized within the matrix over one week and display reflections of a tumor-like organization, the next step involved the injection of NIR-heat-generating magnetite nanoparticles into the chip. The principle of introducing NPs into the chip (Figure 2.3A) involves their passive diffusion over a 24-hour period from the lateral channels, each being injected with a given NPs concentration, into the PDAC tumor microenvironment modelled in the central chamber of the chip. Figure 2.3B displays intact tumor spheroids in collagen on chip after 24h incubation with NPs at [Fe]=32 mM, while Figure 2.3C illustrates the viability of these spheroids through live/dead confocal imaging 3D reconstruction, confirming the absence of adverse cytotoxic effects induced solely by the NPs. In addition, we conducted an Alamar Blue metabolic assay to assess the cytotoxicity of MagNPs on both pancreatic cancer cells (PANC-1) and healthy human mesenchymal stem cells (hMSCs). Following a 24-hour incubation with MagNPs at concentrations of 2, 4, 8, 16, and 32 mM, no significant reduction in cell metabolic activity was observed. Even at the highest nanoparticle concentration (32 mM), the metabolic activity remained around 80%, indicating minimal cytotoxic effects (Figure 2.S4).

Transmission electron microscopy (TEM) was further used to localize the NPs at the nanoscale within the chip. NPs were consistently found adsorbed on the collagen fibers (Figure 2.3D). They were also detected both at the outer region of cells, near the plasma membrane within the ECM, as well as being endocytosed by the cells (Figure 2.3E). Subsequently, many NPs were identified inside endosomes within the cancer cell cytoplasm (Figure 2.3F). Overall, this imaging demonstrates excellent penetrability of NPs within the collagen-based matrix, successful NP endosomal internalization by tumor spheroid cells and lysosomal storage confirming their ubiquitous presence in our system. Additionally, Perls Prussian Blue staining performed *in situ* within the chips detected the presence of iron in tumor-on-chip injected with NPs as compared to control, with blue coloration observed inside and around the spheroids as well as diffused within the matrix (Figure 2.3G). The intensity of the blue color increased with NP concentration, 8 vs 32 mM, and blue extracellular matrix coloration surrounding the spheroids was most pronounced at 32 mM. To quantitatively assess iron loading in cells within the collagen matrix following external administration of MagNPs, single-cell magnetophoresis was performed to determine the iron mass per cell (see the corresponding section in *Materials & Methods*). As expected, nanoparticle uptake per cell exhibited a broad distribution due to passive diffusion but

increased with the administered dose. The measured iron content per cell (mean ± SD) was 5.4 ± 3.6 pg, 12.9 ± 7.4 pg, and 28.3 ± 17.3 pg for administered doses of 8 mM, 16 mM, and 32 mM, respectively.

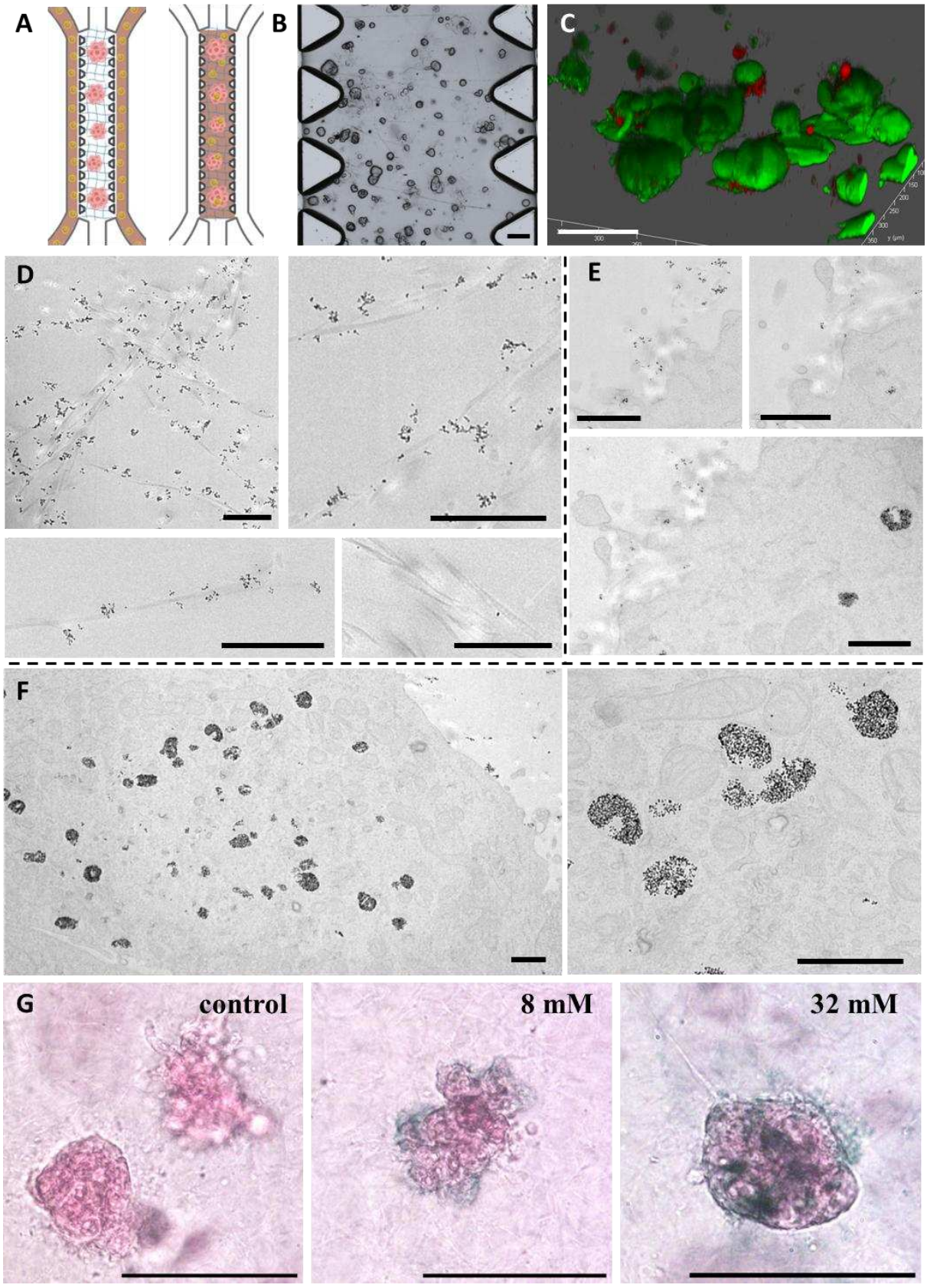


Figure 2.3: **Administration of magnetite nanoparticles and imaging within tumor-on-chip**. **A**. Schematic representation of on-chip NP administration and diffusion. **B**. Bright field microscopy image of tumor spheroids on chip on D8, 24h after NP incubation. **C**. Confocal microscopy images of Live/Dead assay (dead = red; live = green), 3D confocal stack reconstruction of tumor spheroids on chip on D8, 24h after NP incubation. Scale bar = 100 μm. **D-F**. TEM imaging of NPs adsorbed on collagen fibers (D), NPs endocytosis in cells (E), NPs internalized on cell endosomes (F). NPs appear as dark contrast. Scale bar = 1 μm. **G**. Perls Prussian Blue staining of iron deposits (in blue) in PDAC spheroids in collagen on chip. Scale bar = 100 μm.

4. Implementation of MagNP-PTT in PDAC tumor-on-chip and its Impact on Collagen Matrix

The next step was to irradiate the NP-containing chips with an 808 nm NIR laser. A dedicated setup was developed to enable irradiation of microfluidic chips with a laser and measure the induced temperature elevation (Figure 2.4A). The setup consists of a water bath-supplied holder for the chip, which maintains microenvironment within the chip at 37°C, an 808 nm laser unit, and an infrared thermal camera to visualize and record temperature change. The optimal distance between the laser and the chip was identified to be 6.1 cm (Figure 2.S5) to maximize the homogeneity of the surface laser power distribution (i.e., flatter laser power Gaussian distribution) while maintaining a high attainable laser power range. This configuration helped reduce, though not completely eliminate, temperature variation along the length of the chip during laser exposure.

We next characterized our MagNP-PTT setup by investigating both the temperature increase in the presence of NPs as well as its distribution within the system. The initial step was to assess the efficiency of light-to-heat conversion in the system design. NPs were introduced into the central channel of the chip either via direct injection of the nanoparticle solution (in water) or through their diffusion over 24-hour period from the lateral channels into the collagen type I (6 mg/mL) matrix containing pancreatic cancer spheroids. Temperature elevation was measured for increasing iron concentrations of NPs (8, 16, and 32 mM) and laser power densities (1 and 2 W/cm^2). For both conditions (NPs in water and diffused in the collagen with embedded cells), a similar pattern of temperature increase was observed with increasing NP concentration and laser power (Figure 2.4B). However, the overall temperature increase was higher for NPs heating in water compared to NPs within collagen with cells. This suggests reduced NP diffusion within collagen matrix, potentially due to the interactions of NPs with collagen fibers, as observed by transmission electron microscopy imaging (Figure 2.3D). As a result, with the given NP concentration and laser power ranges we can elevate the temperature within the tumor-on-chip by ΔT=1-12°C (starting from 37°C) and thus cover the full range hyperthermia temperatures (38-48°C) in

the tumor-on-chip.

To further evaluate the effect of MagNP-PTT on tumor-on-chip, the next step involved investigating how MagNP-PTT-induced heating affects the collagen type I matrix. For this, collagen matrix at 6 mg/mL on chip was subjected to NP-mediated laser heating and subsequent collagen fiber imaging to examine structural impact. While second harmonic generation (SHG) microscopy is a state-of-the-art method for collagen fibers visualization, collagen hybridizing peptide (CHP) staining is emerging as well due to its ability to exclusively bind to collagen fibers through triple helix hybridization.[332] To explore the comparability of the two techniques, we first imaged untreated collagen matrix on chip (control) with two-photon microscopy to simultaneously observe the SHG and CHP signals (Figure 2.S6). As a result, both images revealed an isotropic mesh of fibrils of around 1 μm in diameter. Remarkably, the SHG signal was fully overlapped by the CHP staining signal, demonstrating excellent comparability on methods' output. However, the CHP fluorescent image showed more signal present than the SHG image, suggesting that CHP staining provides with a higher degree of sensitivity, allowing to visualize collagen degradation at microstructural level.[332–334]

MagNP-PTT treatment was then applied to assess its impact on collagen matrix structure. While several studies have investigated collagen I thermal denaturation under various temperature modulation approaches as well as analytical methods,[335–337] results show variability in collagen denaturation points and responses to increased temperature. Factors influencing this variability include collagen source, extraction method, concentration, solvent, degree and/or method of crosslinking, among the others.[338] For type I collagen, the range of temperatures leading to irreversible thermal changes have been reported to be between 37°C and 55°C, where the loss of fibrillar structure was observed.[339]

In this study, to assess the impact of NP-mediated heating within our collagen matrix on chip, NPs were let to diffuse from the lateral channels of the chip into the collagen matrix for 24 hours before heating, followed by the CHP staining imaging to study collagen structure changes after laser exposure. The control chip (Figure 2.4C) with 32 mM NPs diffused in a chip demonstrated no significant matrix structure changes across the chip (Figure 2.4D). Chips, containing NPs at 16 mM (Figure 2.4E) and 32 mM (Figure 2.S7) concentrations, were exposed to the laser powers at 2.5 W/cm^2 and 1 W/cm^2 respectively for 20 min, heating the matrix within the range of temperatures known to cause collagen type I degradation. The resulting temperature gradient along the chip ranged from 44°C to

49°C for 16 mM (Figure 2.4 G-H) and from 42°C to 48.5°C for NP at 32 mM (Figure 2.S6 E-F).

These gradients induced varying responses within the collagen matrix, allowing not only to explore the impact of a wider range of hyperthermia temperatures within a unique matrix but also representing a better model of temperature distribution of the *in vivo* setting. We observed a rather dichotomous effect, where no significant matrix alterations were detected at temperatures below 46°C with a drastic disappearance of detectable collagen fibers around 46°C, consistent with previous reports for similar collagen source.[339] Bright field images of the chip revealed transparent zones where temperature increased above 46°C, while areas at lower temperatures remained light brown due to the presence of NPs in the collagen (Figure 2.4E). TEM imaging further demonstrated the few remaining partially denaturated collagen fibers with NPs adsorbed on them (Figure 2.S8 A). CHP staining confocal images corroborated these observations, showing a transition from intact collagen matrix with a dense network fibril network (Figure 2.4F [5]), similar to the control (Figure 2.4D), to nearly fully denatured fibrils that were no longer detectable (Figure 2.4F [1-4]). Depending on the temperature gradient across the sample centered around the collagen denaturation point, an aperture within the collagen matrix could form (Figure 2.S6 C) with different fibril organizations around it. Two outcomes upon partial collagen matrix denaturation were observed: i) a gradual matrix transition from a well-defined fibril mesh to the absence of visible fibrils (Figure 2.S6 D [2-4], Figure 2.S8 B) and ii) accumulation of detected collagen damage at the aperture border (increased CHP fluorescence, Figure 2.S6 D [1]), likely, due to collagen fiber accumulation from matrix folding caused by contact point loss after denaturation. Therefore, although there is a clear transition from an intact to an undetectable matrix state due to fibrillar denaturation, a more complex matrix restructuring occurs at a finer level around the denaturation point.

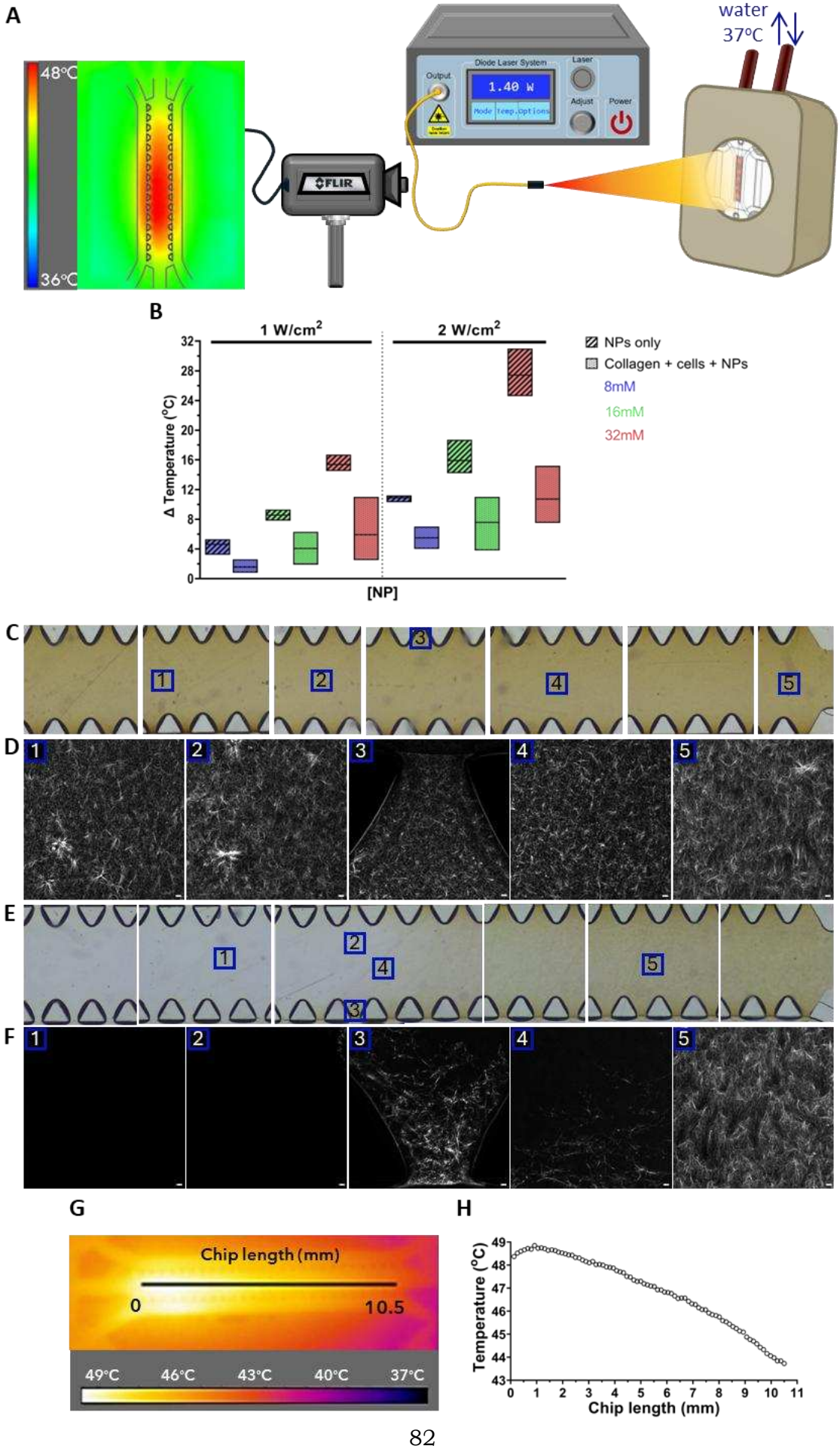

A
48°C
36°C
FLIR
Diode Laser System
Output
1.40 W
Laser
Adjust
Power
water
37°C
B
1 W/cm²
2 W/cm²
Δ Temperature (°C)
[NP]
NPs only
Collagen + cells + NPs
8mM
16mM
32mM
C
D
E
F
G
Chip length (mm)
0
10.5
49°C
46°C
43°C
40°C
37°C
H
Temperature (°C)
Chip length (mm)

Figure 2.4: **Nanoparticle-mediated photothermia heating setup and matrix impact characterization. A**. Scheme of MagNP-PTT setup. **B**. Temperature increase (ΔT) as a function of NP concentration and surface laser power for NPs heating in chip VS NPs diffused in collagen + cells on chip. Data are represented as a boxplot with line at mean. **C**. Bright field images of the control chip with NPs at 32 mM diffused in collagen. **D**. Collagen hybridizing peptide staining imaging of different areas in the control chip with 32 mM NPs with confocal microscopy. **E**. Bright field images of the chip (16 mM NPs) with partially denaturated collagen. **F**. Collagen hybridizing peptide staining imaging of variously denaturated areas in the exposed chip with 16 mM NPs, confocal microscopy. **G**. Corresponding thermal camera heating recording within the chip with representative temperature gradient along the length of the chip. **H**. Temperature variation as a function of the chip length.

5. PTT-Induced Cell Death in PDAC tumor-on-chip: Effects of Rest Time and EMT Impact

Following the MagNP-PTT set up for tumor-on-chip applications and PDAC tumor-on-chip model establishment, we next studied the effect of local heating of on-chip PTT on PDAC tumor spheroid survival. The combination of different NP concentrations (8, 16 & 32 mM) and surface laser powers (1-2 W/cm^2), as illustrated in Figure 2.5A, allowed to heat the samples in the overall range of 38 to 48°C. Figure 2.5A also showed that once the laser is turned on, the temperature in the chip rises during the first few minutes followed by a plateau that remains until the laser is off. The cell death analysis was then divided into 5 temperature study groups stemming from the final temperature reached within the sample, grouped into five 2°C-range bins starting from 38 to 48°C. Figure 2.5A evidenced that all the intra-group temperature variations in time are well confined by the predefined 2°C temperature window for all the groups. Besides, temperature profiles were extracted as a function of position in the width of the chip (Figure 2.5B) across all the samples used in this study. Temperature distribution in the width of the chip, more specifically the central chamber enclosed by the pillars, is homogeneous within each group and consistent between the groups. A respective control with PTT exposure at 2 W/cm^2 without NPs was performed to confirm the absence of heating and negative effect on the tumor spheroids in the absence of NPs in the system (Figure 2.S9).

Laser exposure was performed for 20 min, and heating effects on cancer cell death were first evaluated 2 hours post-treatment (Figure 2.5C). For temperatures up to 40°C, the morphology and dead/live signal proportion in images was similar to the control conditions, with PANC-1 cells maintaining as compact spheroids, indicating minimal adverse effects. In contrast, tumor-on-chip systems heated above 42°C showed a progressive impact on cell viability and spheroid integrity (Figure 2.5C). The dead cell (red) signal gradually increased from the 42-44°C group to the two highest temperature groups (44-46°C and 46-48°C), where spheroid integrity was strongly impaired, with single cancer cells becoming more distinct (Figure 2.5C). To quantitatively analyze cell viability, an algorithm was developed,

where the live and dead signals were segmented using machine learning independently for each condition and sample. These two signals were then quantified by computing their representative areas in 3D to determine their total presence within the sample and calculate their ratio as an indicator of cell viability. This quantitative analysis confirmed the overall trend of increasing cell death with increasing temperature (Figure 2.5E). Little-to-no detrimental effects were observed after heating 1-3°C above 37°C with the dead-to-live ratio median at 0.15 and the interquartile range spanning from 0.05 to 0.3. In contrast, exposure to temperatures above this range significantly impacted cell viability compared to controls. However, even in the highest temperature group, the median dead/live ratio reached was around 0.3 with the interquartile range spanning up to 0.9, indicating equal levels of dead and live cells. Thus, while MagNP-PTT caused substantial cell death due to local heating, a significant proportion of pancreatic cancer cells remained alive even after heating to 48°C for 20 min.

Next step consisted in assessing the effect of rest time on cell survival after MagNP-PTT treatment. Cells were thus allowed to rest for 24 hours before evaluating their survival across the same temperature range. Confocal imaging revealed that tumor-on-chip heated at the lowest temperatures (38-44°C) exhibited high cell viability and spheroid integrity similar to controls (Figure 2.5D). In contrast, both the second highest (44-46°C) and the highest (46-48°C) temperature groups showed significant cell death showed marked elevation of the amount of dead signal, with a noticeable increase in spheroid fragmentation into single cells. The quantitative analysis of cell death confirmed these observations, showing that tumor spheroids heated on-chip up to 44°C displayed no adverse viability effects compared to controls, while significant dead signal was observed in chips heated at 44-46°C, with even greater levels in the 46-48°C range (Figure 2.5F). Such study of two post-treatment times allowed to explore whether MagNP-PTT heating could induce the stratification of heated cells into three groups: dead cells from temperature increase, unaffected live cells, and damaged cells not yet irreversibly changed. This implies that over longer periods, the dead-to-live ratio may be influenced by proliferating live cells or recovering damaged cells. To assess such potential response stratification, we proceeded with the group-by-group comparison temperature range effect for 2h vs 24h post-treatment rest time (Figure 2.5G). While no significant differences were observed for the lowest range (38-40°C) due to low cytotoxic impact of PTT, for the 40-42°C and 42-44°C groups, a marked decrease in the dead-to-live ratio from 2 to 24 hours suggests that cell proliferation and recovery were more prominent than further cell death. In contrast, for the 44-46°C and 46-48°C ranges, dead/live ratios did not differ significantly between 2 and 24 hours, remaining

more elevated as compared to controls for both time points (Figure 2.5G). Thus, while 24 hours post-treatment may promote live cell proliferation and recovery in the 40-44°C range, these effects do not offset irreversible damage at higher temperatures (44-48°C).

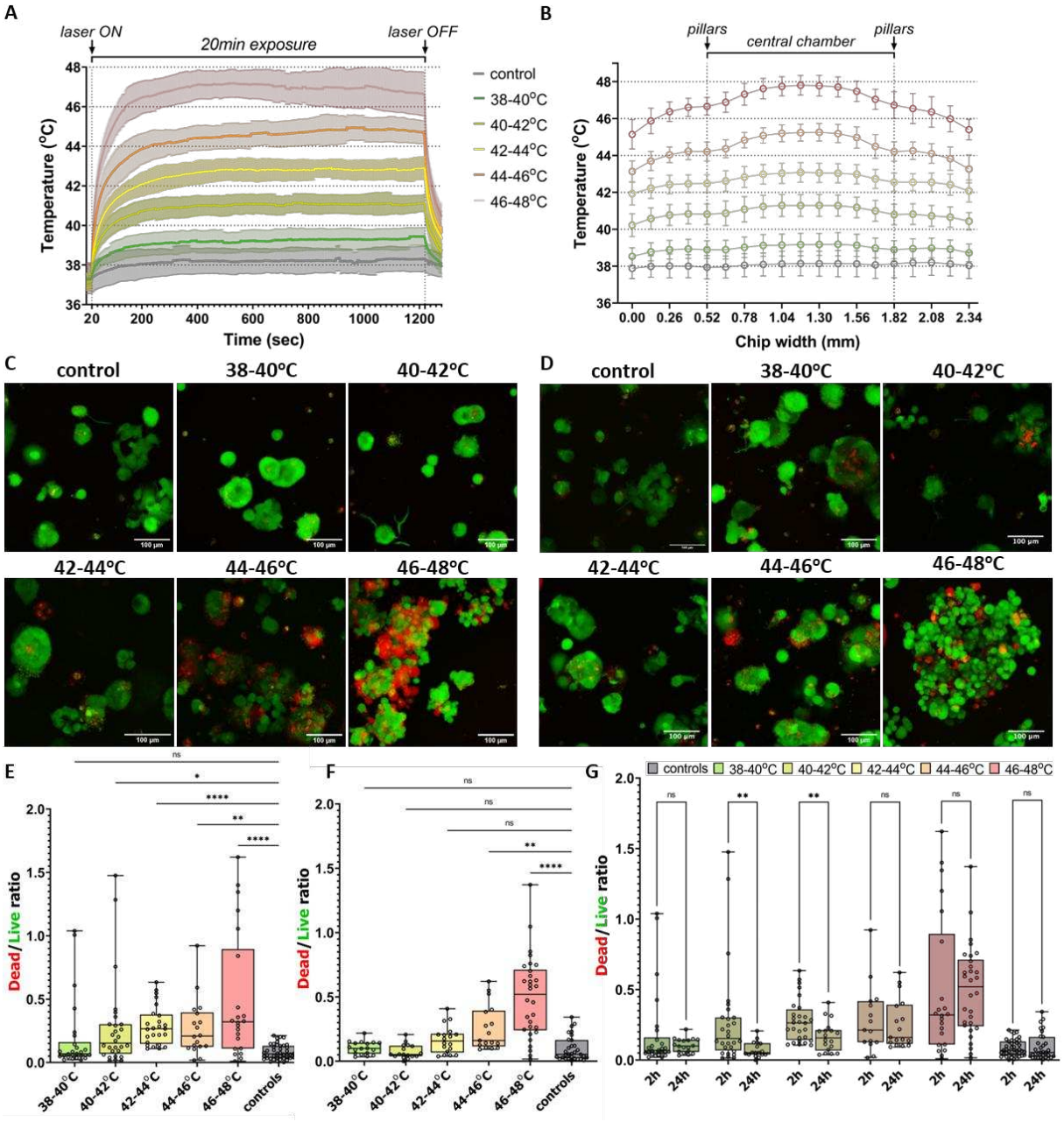


Figure 2.5: Temperature-dependent cells death evaluation after MagNP-PTT. A. Temporal temperature profile within the chip over 20 min of laser exposure for the 5 studied temperature groups. Data are represented as mean ± SD of all the experimental data (n>3). B. Spatial temperature distribution profile along the width of the chip, including central channel with two side channels, for the 5 temperature groups studied. Data are represented as mean ± SD of all the experimental data (n>3). C-D. PDAC cell viability in collagen on chip 2h (C) and 24h (D) after MagNP-PTT exposure. Representative confocal microscopy images (Z projection, SD type) for each of the studied temperature groups, live/dead (Calcein Green/Texas Red) viability assay. Scale bar = 100 µm. E-F. Live/dead assay quantification 2h (E) and 24h (F) after MagNP-PTT exposure, showing cell death estimate as a function of the temperature group. G. PDAC cell recovery evaluation after MagNP-PTT

exposure. Comparison of dead-to-live signal ratio for 2h vs 24h after laser exposure for all the studied temperature groups as an estimate for cell recovery after temperature increase. Data are presented as box & whiskers plot (min to max) including all experimental data points (>3 independent experiments for each condition, ≥2 chips per experiment, ≥3 independent ROIs analyzed per chip). *p< 0,1; **p< 0,01; ***p< 0,001; ****p< 0,0001.

Finally, a more in-depth study on cellular effects was conducted by retrieving the cells after 24 hours post-treatment with MagNP-PTT (40-44°C – temperature, at which significant recovery was observed 24h after exposure) and analyzing their gene expression. Genes involved in apoptosis inhibition (*mcl1*, Myeloid Celleukemia 1 and *birc5*, baculoviral IAP repeat containing) along with mesenchymal (*vimentin*, N-cadherin (*cdh2)*, focal adhesion kinase (*fak)*, fibrillin (*fbn1*), zinc finger transcription factor (*zeb*)) and epithelial markers (E-cadherin (*cdh1*), *a* -catenin (*a-cat*)) were studied (see Table 2.S1 for the corresponding primers' sequences). It is worth noting that detecting effects on cell death under these conditions is challenging, as the RNA being analyzed corresponds to living cells or those in recovery.

As a result, apoptosis-related genes *birc5* and *mcl1* showed no significant changes due to the treatment, suggesting that MagNP-PTT does trigger apoptosis resistance under our exposure conditions. In contrast, a moderate increase in *vimentin* and *fak* genes was observed, along with non-significant increases in *zeb* and *fbn1*. Notably, the cadherin markers (E and N), *cdh1* and *cdh2*, as well as α-catenin, remained unchanged. Thus, the mesenchymal markers (*vimentin, fak, zeb, fbn1*) increased post-treatment, while the epithelial markers (*cdh1, a-cat*) remained unchanged, indicating a slight potential for epithelial-mesenchymal transition triggered by the PTT treatment. In addition, this mild effect was confirmed by immunofluorescence imaging of E cadherin and vimentin on-chip, where PTT slightly increased vimentin expression in the sample post MagNP-PTT exposure (Figure 2.6D) as compared to controls without (Figure 2.6B) and with NPs (Figure 2.6C) that were not exposed to the laser. On the other hand, E-cadherin expression remains unchanged across samples. This may be stemming from the fact that PANC-1 are characterized to belong to a quasi-mesenchymal PDAC cell line subtype, expressing lower levels of epithelial-associated genes.[340,341] All in all, these results indicate that while the surviving cells post-MagNP-PTT exposure may undergo potential EMT profile changes as evidenced by modest changes in some gene expressions, they also open a promising avenue for exploring the intricate interplay between PTT anticancer therapies and cellular plasticity. In particular, understanding these mechanisms could not only inform the optimization of thermal therapies (e.g., duration, dosage, therapeutic window etc.) but also shed light on potential synergistic strategies development with other treatments

(e.g., chemotherapy, immunotherapy etc.) to harness the efficacy of cumulative therapeutic effect.

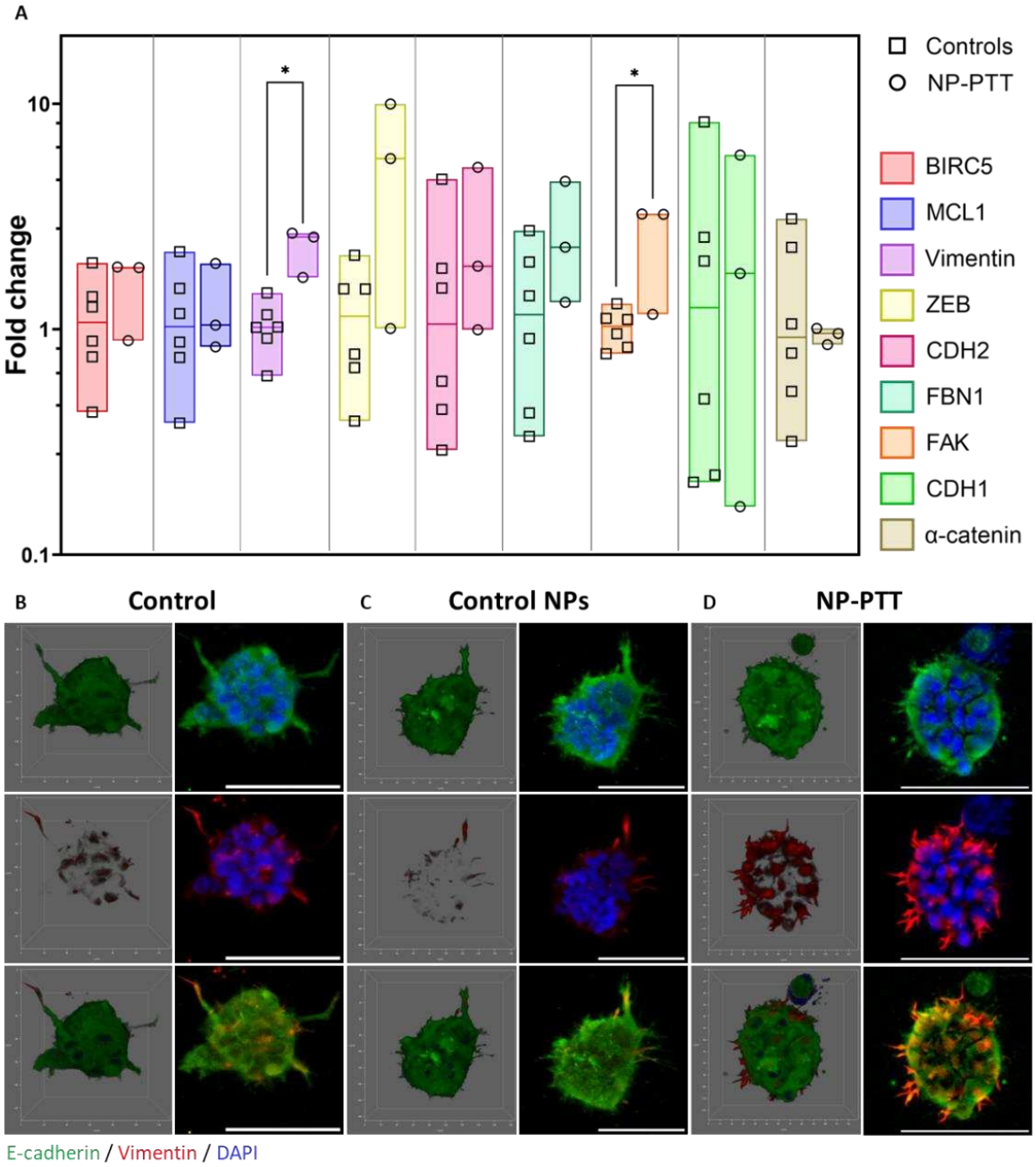


Figure 2.6: Characterization of MagNP-PTT effects of tumor spheroids gene expression. A. Expression of a panel of mesenchymal, epithelial and apoptotic genes measured by RT-qPCR for control samples cultured in collagen on chip and after MagNP-PTT exposure at 40-44°C, 24h rest time. **B-D.** 3D reconstructed confocal images (left panel) and Z-projections of 3D stacks (STD method) (right panel) of single spheroids for control (B), control with NPs (C) and post-MagNP-PTT samples (D) immunostained for E-cadherin (green), Vimentin (red) and DAPI (blue). Scale bar = 100 μm.

III. DISCUSSION

With the emergence of nanotechnology for novel therapy development, the possibilities for innovative PDAC treatments expanded a lot. However, most of those nanomaterial-based strategies are mainly applied for anticancer agents' delivery.[342] In contrast, treatments with nanoparticles being the active players are still viewed under the paradigm of non-traditional, pilot approaches. Among them, magnetic hyperthermia and in particular nanoparticle-mediated photothermia have been moderately explored in the scope of anticancer PDAC treatment.[221,232,235,236,238,343] With the recent development of magnetic nanoparticles for PTT applications, their integration into clinical cancer treatment remains at a very early stage. It is thus essential to gain a comprehensive understanding of the impacts of these therapies on both cancer cells and their surrounding microenvironment.

Our study illustrates the effectiveness of MagNP-PTT in inducing cell death within a PDAC tumor-on-chip model. The magnetite nanoparticles used, initially reported as magnetic hyperthermia agents, demonstrated efficient near-infrared light-to-heat conversion efficiency compatible with the chip design. Their ability to diffuse through the collagen matrix and penetrate cancer spheroids allowed for precise temperature control. By optimizing nanoparticle concentration and laser dose, temperature elevations could be finely adjusted, spanning from 38 to 48°C, encompassing the range of hyperthermal treatments. Thanks to our unique NP-PPT set up compatible with tumor-on-chip, we explored the impact of magnetite NP-mediated PTT both on pancreatic cancer cells and collagen type I-based ECM through heating-induced cell death as well as matrix denaturation respectively. We aimed to provide here the first example of such therapy efficiency with tumor-on-chip models with a promising outlook for *in vivo* applications.

Significant impact on tumor cell viability can be observed shortly after the treatment when heating at as low as 40-42°C and progressing to up to 48°C. This decreased cell survival is associated with spheroid disintegration and appearance of single cell aggregates suggesting the presence of adverse, potentially irreversible events. On the other hand, the amount of time cancer cells were left to rest post-treatment before evaluating their viability considerably affects their survival. Following 24h rest period, the viability of cells heated at 40-44°C was markedly increased as compared to 2h rest, suggesting the events of either residual live cells' proliferation and/or reversibility of cell damage induced over the 24h period. In contrast, exposure to higher temperatures resulted in irreversible cellular damage certainly due to stronger, thus, more persistent adverse effects on cancer cells. It is

worth noting that, although MagNP-PTT has shown a positive effect on pancreatic cancer cell death, partial cell survival persists after treatment even at high temperature. This, in turn, links to the novel paradigm of hyperthermia applications, where they are mostly considered as promising candidates for synergistic anticancer treatment strategies.[173,344]

Several studies of hyperthermia combined with conventional chemotherapy have been proven successful both *in vitro* and *in vivo*, mainly through improved drug delivery.[175,191] Hence, an efficient use of hyperthermia-based combination therapies may positively affect the therapeutic window of established drugs and allow to increase the efficiency of existing anticancer approaches for PDAC. Reported improvement in chemotherapy delivery is, in part, considered to occur thanks to partial ECM denaturation. These include the ECM stiffness, density, interstitial pressure among the others that are initially increased through PDAC desmoplasia-triggered chain of events – all in all leading to decreased drug penetration. Our study highlights the potential of MagNP-PTT not only for inducing targeted cell death but also for addressing the critical challenge of drug delivery in PDAC. On-chip PTT at a temperature above 46°C was found to disrupt the ECM with no detectable fibril structure. This disruption may potentially enhance drug delivery by modifying the tumor microenvironment as well as increase vascular permeability and reduce interstitial fluid pressure, overcoming the mechanical barriers posed by the stroma. Consequently, PTT not only directly targets cancer cells but might also foster a more favorable environment for therapeutic agents to penetrate effectively, reinforcing its role as a synergistic strategy.

Finally, the temperature- and time-dependent effects on cell viability and morphology underscore the importance of optimizing treatment parameters, which could improve outcomes in thermal therapies. While MagNP-PTT shows promise, translating these findings to *in vivo* models and clinical settings remains a challenge, necessitating further exploration of heat generation in a real tumor, and the long-term effects and safety of such treatments.

Overall, this work positions MagNP-PTT as a compelling strategy for treating PDAC, paving the way for more effective therapeutic interventions. The precision of NP-mediated PTT offers solutions for targeted therapy, with the capability to selectively induce cell death in tumor spheroids while minimizing damage to surrounding healthy tissue. Furthermore, the tumor-on-chip model used in this study provides valuable insights into the complex interactions between nanoparticles, the ECM, and cancer cells, enhancing our understanding of tumor dynamics and guiding the development of more effective

therapeutic strategies. Future studies could focus on the intricate interactions within the tumor microenvironment by developing advanced PDAC tumor-on-chip model to include more of the crucial players in PDAC establishment and progression, such as pancreatic stellate cells and other ECM proteins, and the potential integration of MagNP-PTT with current chemotherapeutic treatments to enhance patient outcomes.

IV. CONCLUSION

In conclusion, this study presents the implementation of NP-mediated photothermal therapy for tumor-on-chip applications using a simple PDAC tumor-on-chip model. Evaluation of MagNP-PTT effect on the PDAC tumor microenvironment showed promising results in inducing targeted, temperature-dependent cancer cell death and collagen extracellular matrix degradation. Furthermore, gene expression analysis revealed a modest increase in mesenchymal markers following PTT, while epithelial markers remained unchanged, indicating a mild epithelial-mesenchymal transition. These findings underscore the potential of MagNP-PTT therapy while setting the foundation and underlining the importance of further investigation and optimization of MagNP-PTT treatments for potential *in vivo* applications. Moving forward, further studies into the responses of cancer cells and stromal components to MagNP-PTT in a more complex PDAC tumor-on-chip model, integrating pancreatic stellate cells and ECM proteins, such hyaluronic acid, will be essential for understanding the broader impacts of MagNP-PTT on pancreatic cancer.

V. EXPERIMENTAL PROCEDURES

Cell line and culture

In this work, human pancreatic cancer cell lines PANC-1 were used, purchased from the American Type Culture Collection (ATCC, CRL-1469TM). Cells were continuously cultured in 2D in T75 flasks in a humidified incubator at 37°C with 5% CO_2 in high glucose DMEM medium (Gibco 61965-026, GlutaMAX™) supplemented with 1% of penicillin-streptomycin (P/S) (Gibco 15140-122), and 10% fetal bovine serum (FBS) (Gibco 10270-106), with each passage taking place at 80-90% confluence level and proceeding from passage 3 to 20.

3D culture on chip

Commercially available microfluidic devices (DAX-1, idenTx 3, AIM Biotech, Singapore) suited for 3D cell culture were used in this project (gas-permeable cyclic olefin copolymer (COC)-based material with central chamber width 1.3 mm, side chamber width 0.5 mm, height 0.25 mm, pillar distance 0.1 mm). They were cut to obtain single chips from the initial plate of 3 and sterilized with UV before usage.

To model the PDAC microenvironment on chip, PANC-1 single cells were seeded in collagen type I in the central chamber of the chip. For collagen mixture, collagen type I HC, rat tail (Corning, USA, ref. 354249) was mixed with PBS 10X, NaOH 1 M, MiliQ H_2O according to manufacturer's instructions to yield 6 mg/mL mixture of physiological osmolarity and pH. The cell seeding suspension was prepared by detaching cells from the flask at 80-90% confluence and resuspending in the collagen mixture. The cell-collagen suspension was then introduced in the central chamber of the chip at concentration of 500 000 cells/mL (~5000 cells/chip). All the manipulations with collagen were performed at 4°C to avoid premature collagen polymerization. After seeding, collagen with cells in the chip is polymerized for 15 min at room temperature followed by 30 min in the incubator (37°C, 5% CO_2). Finally, the chips were supplied with cell culture medium via the side channels and incubated at 37°C with 5% CO_2. Tumor spheroid growth from single cells proceeded for 7 days before nanoparticle incubation and PTT exposure.

Nanoparticles synthesis and characterization

Iron oxide (Fe_3O_4) NPs coated with PO-PEG-NH_2, 9 nm core diameter, 30 nm hydrodynamic diameter were produced by a non-aqueous sol-gel procedure as detailed in 51. Pegylation was modified by replacing POPEGCOOH by POPEGNH2 (specific polymers,

catalog #SP-1P-14-001).

The core size of the nanoparticles (NPs) was determined from TEM images taken using a FEI CM10 electron microscope. Samples were prepared by dropping the colloidal solution onto a holey carbon-coated Cu grid. Hydrodynamic size and zeta potential were analyzed with a Nano ZS (red badge) ZEN3600 Zetasizer at neutral pH and 37°C. Infrared spectroscopy using KBr pellets was employed to qualitatively assess the efficiency of PO-PEG-NH2 coupling on iron oxide NPs. The FTIR spectra were recorded with a Bruker FTIR (Tensor 27) and are reported in terms of absorption frequency (cm−1). The 808 nm epsilon was determined from UV−visible spectra of aqueous NPs solution varying the iron concentration from 0.25 to 5 mM and was recorded using a spectrophotometer (V-630 UV−vis Spectrophotometer, Jasco). The crystalline composition of the iron oxide was determined using Mössbauer spectroscopy at 300K with the aid of a 57Co/Rh gamma-ray source in a transmission scheme with a triangular velocity form. The hyperfine structure was modelled by means of a least-squares fitting procedure involving Zeeman sextets composed of Lorentzian lines using MOSFIT (made home software). To describe the broadening of lines, several magnetic subcomponents (hyperfine magnetic field distribution) have been considered. The isomer shift (IS) values were referred to that of α-Fe at 300 K. Magnetic properties were assessed using a Vibrating Sample Magnetometer (VSM, Quantum Design, Versalab), with magnetization curves measured at 300 K over a field range of -30,000 to 30,000 Oe.

The light-to-heat conversion efficiency of the NPs was calculated from heating curves using the equation $\frac{\Delta T m C B}{P_0 - \frac{P_0}{10^A}}$ where DT is the temperature increase (from the initial temperature to the plateau), A is the sample absorbance, m is the sample mass, C is the specific heat capacity (4.18 J.g-1.K-1) and B is the heat dissipation constant (0.008 s-1 under the set-up condition).

For biological experiments, NPs were diluted in RPMI 1640 medium (Gibco 32404-014) supplemented with 1% of penicillin-streptomycin (P/S, Gibco 15140-122), and 10% fetal bovine serum (FBS, Gibco 10270-106) to prepare desired NP concentrations. Final concentrations of 8, 16 and 32 mM were used. The NP solutions were then introduced into the chips via side chambers and left for 24h at 37°C with 5% CO_2 to diffuse into the central chamber. The remaining NP solution was flushed with RPMI medium from the side chambers before laser exposure.

Magnetite nanoparticle photothermal therapy (MagNP-PTT) in-chip setup

To implement nanoparticle-mediated photothermia heating in a microfluidic chip, the setup was developed. For this, the chip was first placed into a 3D-printed holder supplied with circulating warm water to bring the chip up to the initial temperature of 36.5-37.5°C before starting the laser exposure. An 808 nm laser (Laser Components S.A.S France) is positioned in front of the chip at 6.1cm distance. This distance was identified as optimal to obtain a higher degree of homogeneity of laser surface power distribution that follows a Gaussian distribution profile while preserving high laser power range. In this study, the chips were exposed to the laser for 20 min at 1 W/cm^2 (3.12 A) to 2 W/cm^2 (4.89 A). Temperature increase was recorded at 1.0 Hz with an infrared thermal camera (FLIR A6751) and processed with FLIR ResearchIR Max software.

Cell death rate evaluation

Cell survival rate was evaluated through confocal microscopy imaging, live/dead assay. LIVE/DEAD™ Cell Imaging Kit (Invitrogen™, R37601) solution prepared according to manufacturer's instructions and incubated for 30 min at 37°C with 5% CO_2. Confocal microscopy (Leica DMi8) was performed with x25 magnification lens in water-immersion mode. The resulting images were obtained as 3D images (z-stacks, step size 2.0 µm) with two channels: Calcein Green & Texas Red, identifying live and dead signal respectively. To analyse the images quantitatively, an algorithm was developed with an interactive machine learning tool, Ilastik 1.4.0rc6, to transform the images into probability maps of signal vs background. These images were further processed in ImageJ software by applying the threshold (P(signal) > 0.5) to convert the images into binary information and calculate the total area of signal in 3D. This was done for each 3D image, for live and dead signals separately. The ratio of red to green signals was then calculated as an estimate for cell death rate: $ratio = \frac{\sum_{xyz} Pixels,dead}{\sum_{xyz} Pixels,live}$.

Collagen matrix visualization

To assess collagen fibrils upon NP-PTT exposure, collagen was stained with collagen hybridizing peptide, 5-FAM conjugate (F-CHP, 3Helix Inc., FLU200 / FLU60). For this, 5 µM solution of F-CHP was prepared in PBS followed by heating at 80°C for 5 min in a water bath and quenching on ice for 60-90 sec. The quenched solution was then introduced into the chips immediately and incubated overnight at 4°C protected from light. Next day, the chips were washed with 4 rounds of PBS of 30 min each before imaging. Stained collagen fibrils were then imaged for fluorescence with an inverted confocal microscope (Leica DMi8) with

x40 magnification lens in oil-immersion mode.

Alternatively, collagen fibers were visualized with second harmonic generation (SHG) microscopy using the inverted two-photon laser-scanning confocal microscope (Leica SP8) with a femtosecond laser (Chameleon Vision II, Coherent Inc.), Exc/Em 940/490 nm.

Nanoparticles internalization characterization

Self-formed spheroids in collagen on chips were analyzed by Transmission Electron Microscopy (TEM) to observe spheroids' integrity and nanoparticle localization within the cells and the matrix as well as the impact of NP-PTT on spheroids. For this, spheroids were imaged either after extraction from collagen (via collagenase A digestion (1 mg/mL in DMEM+10% FBS+1% P/S, Roche Diagnostics GmbH)) or directly within the preserved collagen matrix. Spheroids (with or without the matrix) were washed with 0.1 M cacodylate buffer (Sigma-Aldrich) and fixed with glutaraldehyde 5% followed by 2x washes with cacodylate buffer. Samples were further dehydrated, embedded in Epon, ultrasectioned for 70 nm slices and placed onto copper grids. Finally, imaging was performed with a Hitachi HT7700 electron microscope operated at 80 kV (Elexience, France) with the help of MIMA2 MET – GABI, INRA, Agroparistech, 78352 Jouy-en-Josas, France.

Intracellular ferric ions were visualized with the Prussian blue (Perls') chemical reaction. Tumor spheroids in collagen on chip were initially fixed with 4% paraformaldehyde (PFA) for 30 minutes at room temperature. Iron staining was performed by treating the cells with potassium hexacyanoferrate (II) trihydrate (Sigma) under acidic conditions for 15 minutes. The nuclei were subsequently stained with Nuclear Fast Red solution for 15 minutes.

Iron loading of cells within the collagen matrix was measured with single-cell magnetophoresis. This technique has been previously described in detail in [74]. Briefly, the PANC-1 cells at concentration of 500 000 cells/mL were seeded in collagen matrix at 6 mg/mL in a 48 well-plate. MagNPs were prepared at concentrations 8, 16 and 32 mM in cell culture media and loaded into the wells for further incubation for 24h at 37°C with 5% CO_2 to let the MagNPs passively diffuse into the collagen matrix and get internalized by the cells. Following the incubation, collagen matrix was digested with collagenase Type II, Cls II (Sigma-Aldrich, C2-BIOC) at 2 mg/mL for 45min and the cells with internalized NPs were recovered to assess their magnetization when subjected to a magnetic field and consequently, the quantity of internalized iron oxide. The iron oxide mass within cells was estimated based on the magnetic moment derived from the calculated cellular magnetic

force. For a cell with diameter d and velocity v, the internalized iron mass was determined using $m_{Fe} = \frac{M(Fe_2)}{M(Fe_2O_3)} \frac{\rho}{M_V} \frac{3\pi\eta dv}{grad(B)}$, where $M(Fe_2)$ and $M(Fe_2O_3)$ represent the magnetic moment density of Fe_2 and Fe_2O_3, respectively, Mv denotes the magnetic moment density of a nanoparticle in a B = 0.145 T field (grad(B) = 17 T m^{-1}), while ρ and η correspond to the nanoparticle density and the viscosity of water, respectively.

Relative Quantification of Gene Expression by Real-Time PCR

Tumor cells were collected from either control (tumor spheroids grown on chip for 9 days), control+NPs (tumor spheroids grown on chip for 9 days with 24h NP incubation from D7 to D8) or post-NP-PTT at 40-44°C (tumor spheroids grown on chip for 9 days with 24h NP incubation from D7 to D8, laser exposure on D8 and 24h rest time). At least 6 independent samples were analyzed for each of the control conditions and at least 10 for post-NP-PTT condition per experiment, for each independent data point. Three independent experiments were performed. The total RNA was isolated using the NucleoSpin RNA mini kit (Machery-Nagel, Thermo Fisher Scientific, #740955.50) according to manufacturer's instructions. Reverse transcription was carried out using the High Capacity cDNA Reverse Transcription kit (Thermo Fisher Scientific, #4368814) with random primers, following the manufacturer's protocol. Both the extracted RNA and resulting cDNA were assessed for concentrations and purities using the Nanodrop device (Ozyme). Real-time quantitative PCR was performed using Power SYBRGreen qPCR Master Mix (Thermo Fisher Scientific, #A25742) on the QuantStudio 3 instrument (Applied Biosystems). The expression of Ribosomal protein P0 (RPLP0) expression was used as a reference gene to normalize the Ct values of the target genes. The normalized Ct values were then compared to those of the controls, and gene expression fold changes were calculated using the comparative Ct method: $2^{-(\Delta Ct_{postTreatment} - \Delta Ct_{controls})}$. Primer sequences are provided in Table 2.S1.

Immunofluorescence staining

The conditions stained include tumor spheroids in collagen on chip of: control (tumor spheroids grown on chip for 9 days), control + NPs (tumor spheroids grown on chip for 9 days with 24h NP incubation from D7 to D8) and post-NP-PTT at 40-44°C (tumor spheroids grown on chip for 9 days with 24h NP incubation from D7 to D8, laser exposure on D8 and 24h rest time). Subsequently, all samples were fixed on D9 with paraformaldehyde (PFA, 4% in PBS) for 45 min at RT and washed thoroughly with PBS. They were then permeabilized with Triton (Triton X−100, 0.1% in PBS) for 20 min at RT and blocked with a blocking solution containing 4% bovine serum albumin (BSA) and 0.1%

Triton X-100 in PBS for 3 hours at ambient temperature. The tumor spheroids on chip were then incubated with mouse anti-E-cadherin (1:200, Invitrogen SHE78-7) and guinea pig anti-Vimentin (1:400, ProGen GP53) primary antibodies in blocking solution overnight at room temperature. The following day, the samples were washed three times with PBS and incubated overnight at room temperature with Alexa Fluor 488-conjugated goat anti-mouse IgG (H+L) (1:400, ThermoFisher A11029) and Alexa Fluor 647-conjugated donkey anti-guinea pig IgG (H+L) (1:100, ThermoFisher A21450) secondary antibodies in blocking solution also containing 300 nM DAPI (D3571, Invitrogen) at 1:500 dilution. Finally, the chips were washed three times with PBS before imaging. Imaging was conducted in z-stack sections using a Leica DMi8 inverted confocal microscope (Leica Microsystems).

Statistical analysis

All data distributions were first tested for variances homogeneity, and normality (D'Agostino-Pearson test, $\alpha=0.05$). Accordingly, the Kruskal-Wallis nonparametric test was performed with multiple comparisons (Dunn's correction, $\alpha=0.05$). For two-factor analysis, Mann-Whitney two-tailed pairwise comparison was performed ($\alpha=0.05$). All statistical significances are represented as $*p < 0.05$, $**p < 0.01$ and $***p < 0.001$. All graphical representations and statistical analysis were performed with GraphPad Prism 9 software. The number of independent experiments was systematically greater than 3.

VI. SUPPLEMENTARY INFORMATION

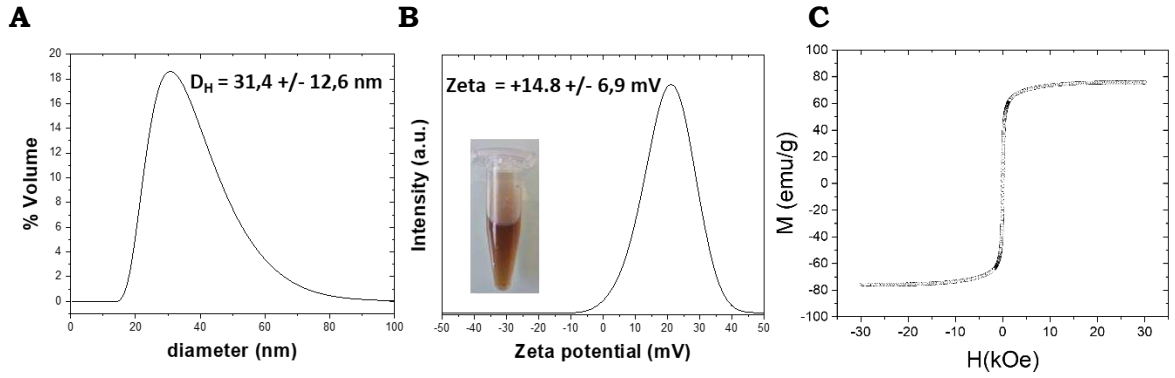


Figure 2.S1 : Fe_3O_4@PO-PEG-NH_3^+ hydrodynamic diameter (**A**) and zeta potential measured at 37°C and iron oxide solution appearance at 10 mM Fe (**B**). (**C**) Magnetization curves at 300 K.

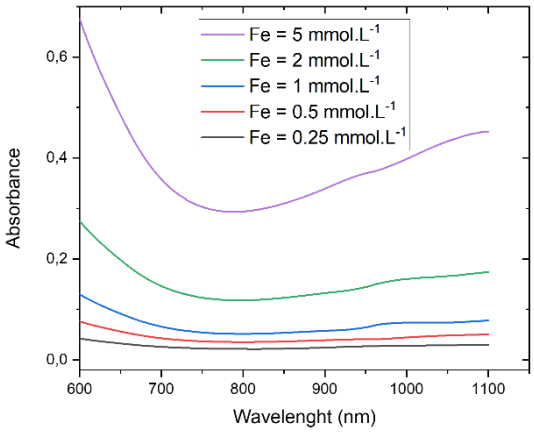


Figure 2.S2 : Vis-NIR absorbance spectra of Fe_3O_4 NPs from 0.25 to 5 mM iron concentration.

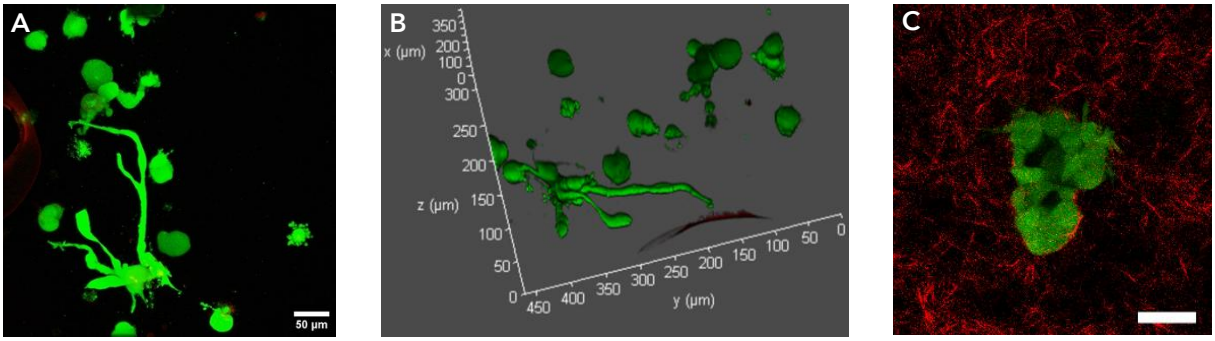


Figure 2.S3 : **3D PDAC model in collagen type I on chip with characteristic protrusions**. Confocal microscopy images of Live/Dead assay ((dead = red; live = green)) of (**A**) z-projection of the 3D stack and (**B**) 3D representation on D8 of cancer cell-formed spheroids developed protrusions. (**C**) Second harmonic generation (SHG) microscopy image of a tumor spheroid (green) with the surrounding collagen type I matrix (red). Scale bar = 50 µm.

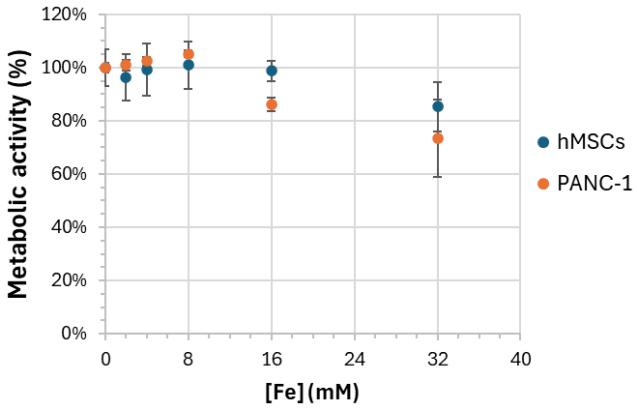


Figure 2.S4 : Alamar Blue cell metabolic activity analysis of healthy human mesenchymal stem cells (hMSCs) vs pancreatic cancer cells (PANC-1) as a function of MagnNPs at concentrations 2-32 mM.

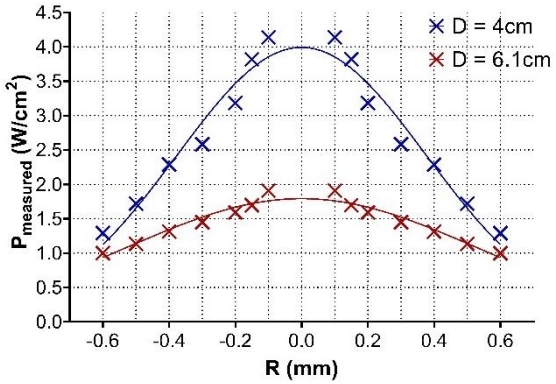


Figure 2.S5 : Laser surface power distribution at P_{laser}=2 W at 6,1 cm vs 4 cm distance with Gaussian nonlinear fit through least squares regression.

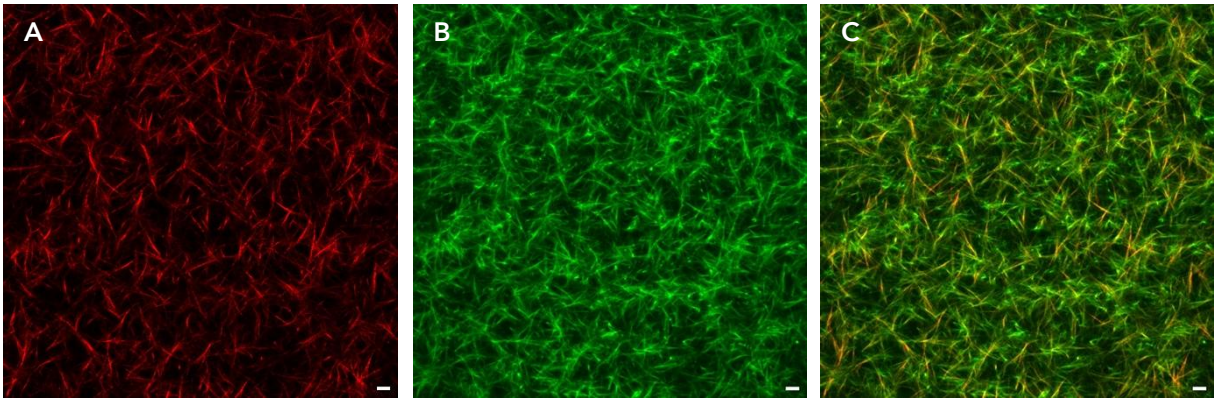


Figure 2.S6 : **Comparison of two-photon second harmonic generation (SHG) microscopy imaging with collagen hybridizing peptide imaged with confocal microscopy for collagen fiber visualization**. Collagen type I on chip at 6 mg/mL is visualized with **A**. SHG signal. **B**. CHP signal. **C**. Overlap. Scale bar = 10 µm.

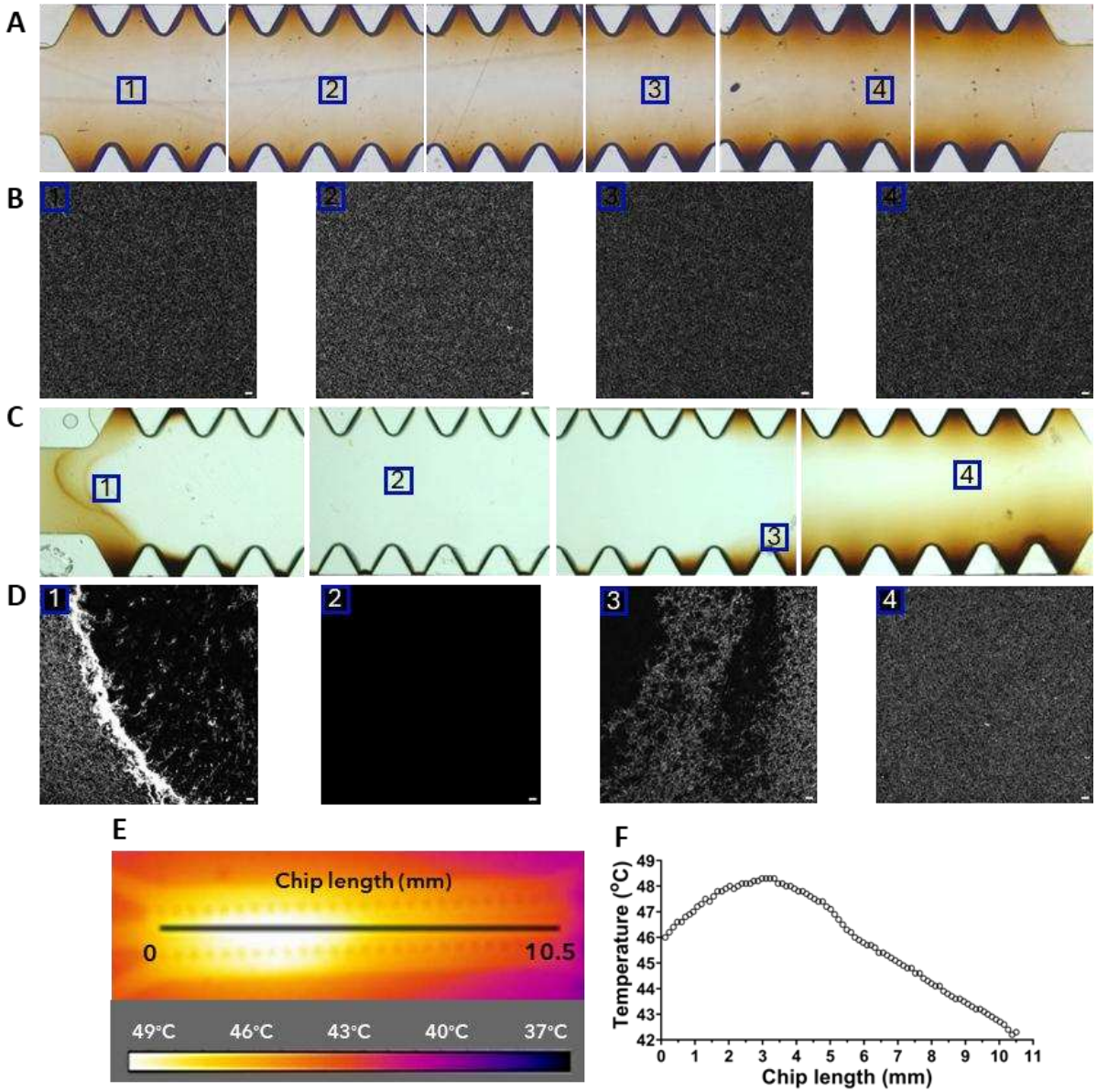


Figure 2.S7 : **Nanoparticle-mediated photothermia matrix impact characterization**. **A**. Bright field images of the control chip with NPs at 32 mM diffused in collagen. **B**. Collagen hybridizing peptide staining imaging of different areas in the control chip with 32 mM NPs with confocal microscopy. Scale bar = 10 µm. **C**. Bright field images of the chip (16 mM NPs) with partially denaturated collagen. **D**. Collagen hybridizing peptide staining imaging of variously denaturated areas in the exposed chip with 16 mM NPs, confocal microscopy. Scale bar = 10 µm. **E**. Corresponding thermal camera heating recording within the chip with representative temperature gradient along the length of the chip. **F**. Temperature variation as a function of the chip length.

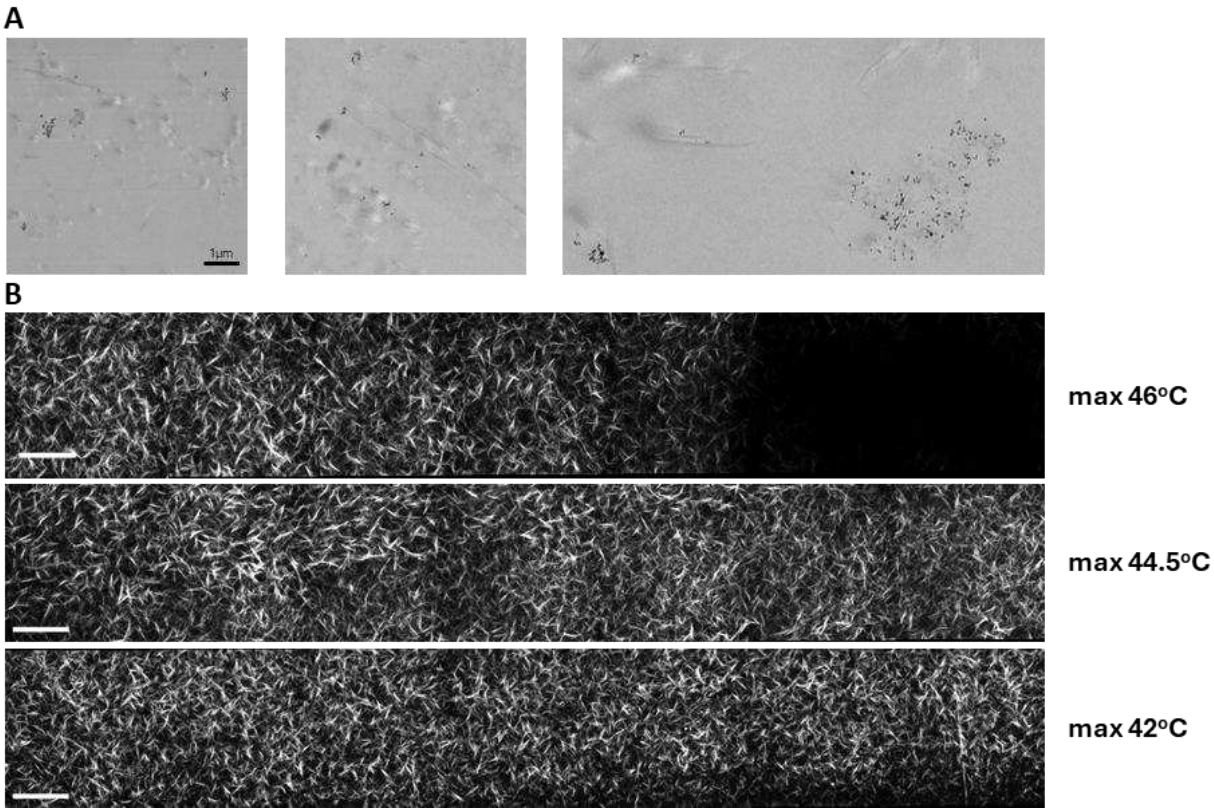


Figure 2.S8 : **Nanoparticle-mediated photothermia impact on collagen fiber structure**. **A**. TEM imaging of few remaining partially denaturated collagen fibers with adsorbed NPs (appear in dark contrast). **B**. SHG microscopy images of collagen denaturation following differential temperature exposure as a result of NP-PTT.

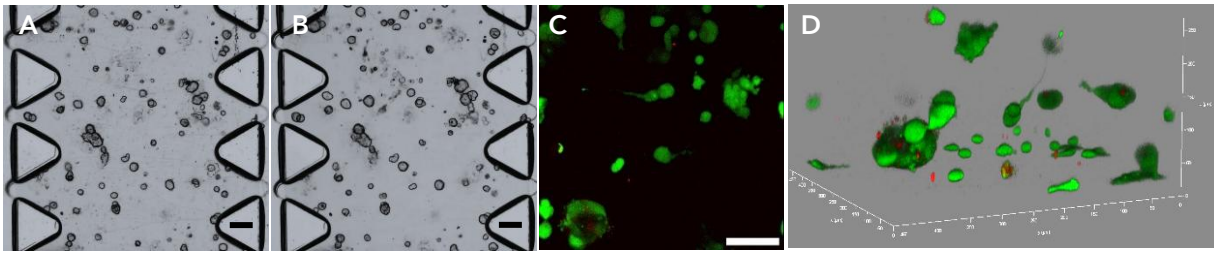


Figure 2.S9 : **3D PDAC model in collagen type I on chip, control no NPs, 2W/cm² PTT**. **A-B**: Bright field microscopy images of control 2 W/cm², on D7 before (**A**) and on D8 after (**B**) laser exposure. Scale bar = 100 µm. **C-D**. Confocal microscopy images of Live/Dead assay ((dead = red; live = green)) of (**C**) z-projection of the 3D stack and (**D**) 3D representation on D8. Scale bar = 100 µm.

Table 2.S3 : List of primer sequences used in RT-qPCR.

Gene name	Forward primer (5' to 3')	Reverse Primer (5' to 3')
BIRC5	AGC CAA ATT CGT TGT CAT AC	GGT CTC CTC TGA CTT CAA CA
MCL1	CAG CGA CGG CGT AAC AAA C	ACA AAC CCA TCC CAG CCT CTT T
Vimentin	TAC AGG AAG CTG CTG GAA GG	ACC AGA GGG AGT GAA TCC AG
ZEB	TTC ACA GTG GAG AGA AGC CA	GCC TGG TGA TGC TGA AAG AG
CDH2	AGC CAA CCT TAA CTG AGG AGT	GGC AAG TTG ATT GGA GGG ATG
FBN1	GCT CCC AAA CCC TGC AAT TT	GGC AGT TGT GTT GCT TGG TTG
FAK	ATC CCA CAC ATC TTG CTG ACT T	GCA TTC CTT TTC TGT CCT TGT C
CDH1	ATT GCT CAC ATT TCC CAA CTC C	CTC TGT CAC CTT CAG CCA TCC T
α-catenin	GCG AAG GAG AGC CAG TTT CT	ATG TTG CCT CGC TTC ACA GA

Challenges, limitations & future directions

In this section, I reflect on experimental approaches that presented some challenges and/or limitations, particularly ***nanoparticle-mediated photothermia*** translational considerations, nuanced ***tumor-stroma interactions*** and ***model complexity*** implications, outlining ***directions for future work*** to further advance this line of research.

Nanoparticle-mediated photothermia (NP-PTT)

While integration of NP-PTT into a PDAC-on-chip model opens new opportunities for photothermal treatment evaluation and acceleration towards clinical applications, some of the challenges along the way have to be considered, such as nanoparticle behavior characterization, precise temperature measurements and *in vivo*-relevant therapeutic settings. As such, while the nominal NP concentration introduced into the system is known, the actual concentration following the diffusion of the NPs into the collagen matrix and internalized by cells remains unmeasured. This uncertainty may lead to discrepancies between the applied dose and the effective intratumoral exposure. In addition, NP aggregation — an intrinsic risk for magnetite formulation — could alter both their biodistribution and photothermal efficiency. While these phenomena are expected to take place in an *in vivo* setting, the associated limitations have to be carefully considered for translational purposes.

In addition, while the concentrations of iron oxide NPs used in this study ensured measurable photothermal responses in the chip setting, they may be higher than those required in clinical translation. Nevertheless, iron oxide is generally considered biocompatible, since cells can process and recycle iron through physiological pathways. Still, refining dosing regimens to align more closely with clinically relevant concentrations will be an important step in bridging *in vitro* findings with therapeutic application.

Tumor-stroma interactions under NP-PTT

Another layer of complexity arises from the impact of NP-PTT on tumor-stroma interactions. Our results confirmed that exposure above ~46°C leads to denaturation of the extracellular matrix and extensive, but not complete, cell death. While this stromal disruption may initially appear advantageous by loosening the dense pancreatic tumor matrix, partial stromal ablation carries potential risks.[68,77–80,137] Similar to reports on other stroma-targeting agents, the survival of a subset of stromal or cancer cells in a remodeled environment could paradoxically favor more aggressive phenotypes and facilitate

dissemination.

This underscores the paradigm that NP-PTT should not be considered as a stand-alone intervention but rather a synergistic strategy. By transiently reducing stromal density, NP-PTT could enhance the penetration and efficacy of subsequent therapies, including chemotherapy, immunotherapy, or targeted agents, which can be even directly included in the NP design and released locally upon demand. However, this benefit depends critically on treatment timing. If administered too early, stromal remodeling may not be sufficient to enhance drug access; if applied too late, residual resistant cells may have already adapted to the altered environment. Establishing the optimal therapeutic window for NP-PTT will therefore be critical for translation. In this regard, PDAC-on-chip models, yet again, offer a uniquely suited environment, as they enable fine control over treatment parameters and continuous monitoring of both tumor and stromal responses, providing a powerful tool to define and optimize such therapeutic windows, especially in combination strategies.

Model complexity

The ultimate layer of complexity stems from the tumor-on-chip model itself. Starting with the extracellular matrix, collagen hybridization peptide staining revealed a more nuanced picture on the matrix organization and its response to NP-PTT. While bulk collagen denaturation consistently occurred at ~46°C, we observed variability in collagen fiber organization across some of the experiments, with networks ranging from highly meshed anisotropic to more or less organized collagen matrices with fibers of variable length and thickness (Figure 2.SS1), despite identical gel preparation, polymerization, and handling protocols.

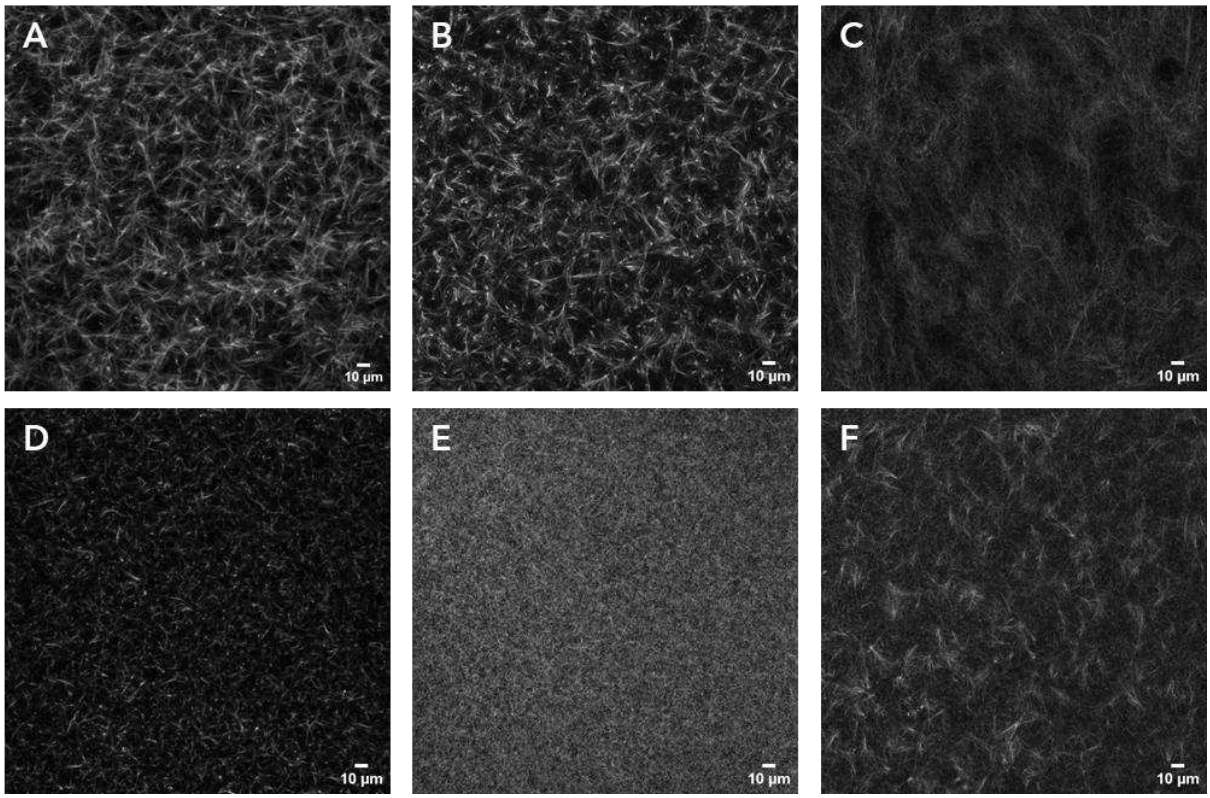


Figure 2.SS1: **Collagen hybridizing peptide staining imaging of various collagen matrices generated under identical conditions imaged with confocal microscopy. A**. Dense anisotropic collagen mesh with clear nucleation points and thick collagen fibers up to 20-30 µm length. **B**. Less dense anisotropic collagen mesh with clear nucleation points and thinner collagen fibers up to 20-30 µm length. **C**. Partially aligned collagen mesh without clear nucleation points and very thin collagen fibers up to 20-30 µm length. **D**. Less dense anisotropic collagen mesh with clear nucleation points and thin collagen fibers up to 10-20 µm length. **E**. Very dense anisotropic collagen mesh with some nucleation points and collagen fibers up to <10 µm length. **F** Dense anisotropic collagen mesh with few nucleation points and thin collagen fibers of highly disperse size. Scale bar = 10 µm.

In addition, collagen remodeling appeared to proceed through transitional stages, with heterogeneous responses upon heating. Some regions displayed smooth denaturation fronts (Figure 2.SS2 A), whereas others developed sharp, sheet-like borders of partially denaturated fibers (Figure 2.SS2 B), sometimes with residual fiber fragments persisting withing the denaturated zones (Figure 2.SS2 C). These differences likely stem from the intrinsic freedom of collagen to self-organize within the system in the absence of crosslinkers or other physico-chemical drivers as well as uneven stress release within the gel, as suggested by the increased fiber alignment of fibers around chip pillars during denaturation (Figure 2.SS2 D).

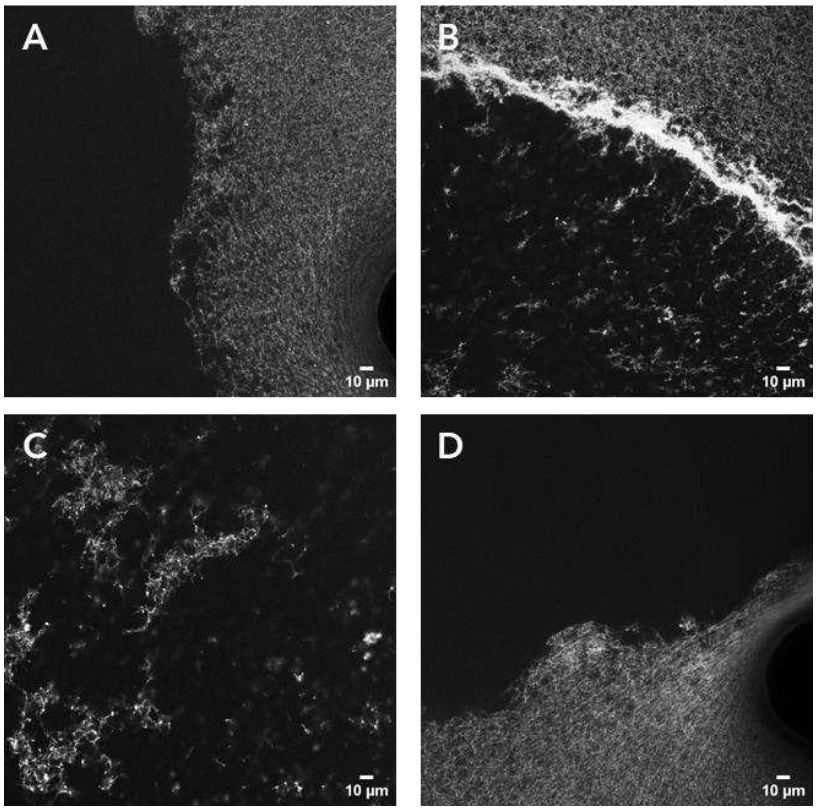


Figure 2.SS2: **Collagen hybridizing peptide staining imaging of collagen matrices response to NP-PTT around 46°C imaged with confocal microscopy. A**. Dense anisotropic collagen mesh with clear nucleation points and thick collagen fibers up to 20-30 µm length. **B**. Less dense anisotropic collagen mesh with clear nucleation points and thinner collagen fibers up to 20-30 µm length. **C**. Partially aligned collagen mesh without clear nucleation points and very thin collagen fibers up to 20-30 µm length. **D**. Less dense anisotropic collagen mesh with clear nucleation points and thin collagen fibers up to 10-20 µm length. Scale bar = 10 µm.

Such variability highlights both the richness of the model and the challenge of interpreting NP-PTT outcomes in the context of matrix remodeling. Beyond more precise monitoring with advanced imaging and physico-chemical readouts, future iterations could integrate strategies to tune ECM architecture and reproducibility, for example, by modulating collagen crosslinking, supplementing with additional matrix proteins relevant to PDAC, and engineering more isotropic chip geometries to reduce stress anisotropy. Addressing these aspects would not only refine the fidelity of the model but also provide deeper mechanistic insights into how ECM remodeling under NP-PTT might translate into *in vivo* tumor response.

Beyond the extracellular matrix, the cellular composition of the tumor microenvironment represents another degree of complexity for NP-PTT translation. In our model, so far, we primarily evaluated the effects of heating on tumor spheroids embedded in collagen, but the presence of stromal cells could profoundly alter both the thermal response and the therapeutic outcome. For instance, if cancer-associated fibroblasts were

incorporated, the timing of their death relative to cancer cells would carry important implications. Early stromal ablation might improve drug accessibility, but it could also risk triggering compensatory pathways if tumor-promoting CAFs are selectively depleted, or conversely, could be detrimental if tumor-suppressive CAF subtypes are removed. A similar argument applies to immune cells, where differential susceptibility of immunosuppressive versus cytotoxic subsets to hyperthymia could shift the therapeutic balance either toward immune evasion or immune activation. Since NP-PTT inevitably exposes both malignant and non-malignant components of the TME to heat stress, delineating these cell-type-specific responses remains critical for predicting outcomes and designing combination strategies.

Future directions

Looking ahead, future iterations of the PDAC-on-chip platform should aim to integrate both the structural and cellular dimensions of the tumor microenvironment to address the limitations identified here. On the structural side, coupling collagen with other ECM proteins, introducing defined crosslinking strategies, and refining chip geometries could help reduce variability in fiber architecture and denaturation dynamics, while advanced real-time imaging and biophysical readouts would enable yet higher precision monitoring of thermal gradients and ECM remodeling. On the cellular side, incorporating stromal fibroblasts, endothelial cells, and eventually, immune subsets will allow systematic dissection of how NP-PTT impacts heterogeneous cell populations, including their temporal sequence of death and functional consequences for tumor progression or suppression. Combined with quantitative nanoparticle tracking and improved local thermometry, such a complexified PDAC-on-chip model would provide a uniquely powerful platform to define the therapeutic window for NP-PTT alone and in synergistic combinations, Ultimately, these refinements would bring the system closer to faithfully capturing the multifaceted *in vivo* PDAC microenvironment, while retaining the experimental control and resolution that make organ-on-chip technologies uniquely suited for guiding the translation of nanomedicine-based therapies.

CHAPTER 3

Bioengineering a Complex PDAC-on-Chip Microenvironment to Replicate *In Vivo*-like EMT

Context and Motivations

By engineering a simplified PDAC-on-chip platform to evaluate the impact of nanoparticle-mediated photothermal therapy on tumor microenvironment, our previous study demonstrated the potential of next generation PDAC *in vitro* models to develop and evaluate new therapeutic approaches in a highly controlled setting. The second and final study of this manuscript presented in **Chapter 3** further explores the PDAC-on-chip model development through its stepwise complexification to increase its relevance for prospective therapeutic testing. In particular, the model's ability to replicate *in-vivo*-characteristic epithelial-mesenchymal transition (EMT) under various key stromal elements is investigated.

The added value of this study lies in the systematic comparison of stromal cues that are known to influence EMT *in vivo* but remain insufficiently included in conventional *in vitro* models. First, hyaluronic acid (HA), a major extracellular matrix component in PDAC, was incorporated into the system using distinct strategies to assess its capacity to modulate CD44 expression and EMT markers. Second, stroma-tumor crosstalk was explored by introducing primary pancreatic stellate cells or primary cancer-associated fibroblasts (CAFs), both directly and via their conditioned media, enabling dissection of contact-driven versus paracrine effects. Finally, by evaluating the temporal stability of EMT induction, we investigated whether stromal-driven EMT responses are transient or sustained over time.

Together, these advances extend the PDAC-on-chip platform beyond tumor spheroid mono-cultures, moving toward a more complex and clinically relevant microenvironment. This stepwise approach not only deepens mechanistic insight into EMT regulation by stromal factors but also provides a foundation for further refining of *in vitro* models that more faithfully reflect PDAC complexity and may serve as testing grounds for future therapeutic interventions.

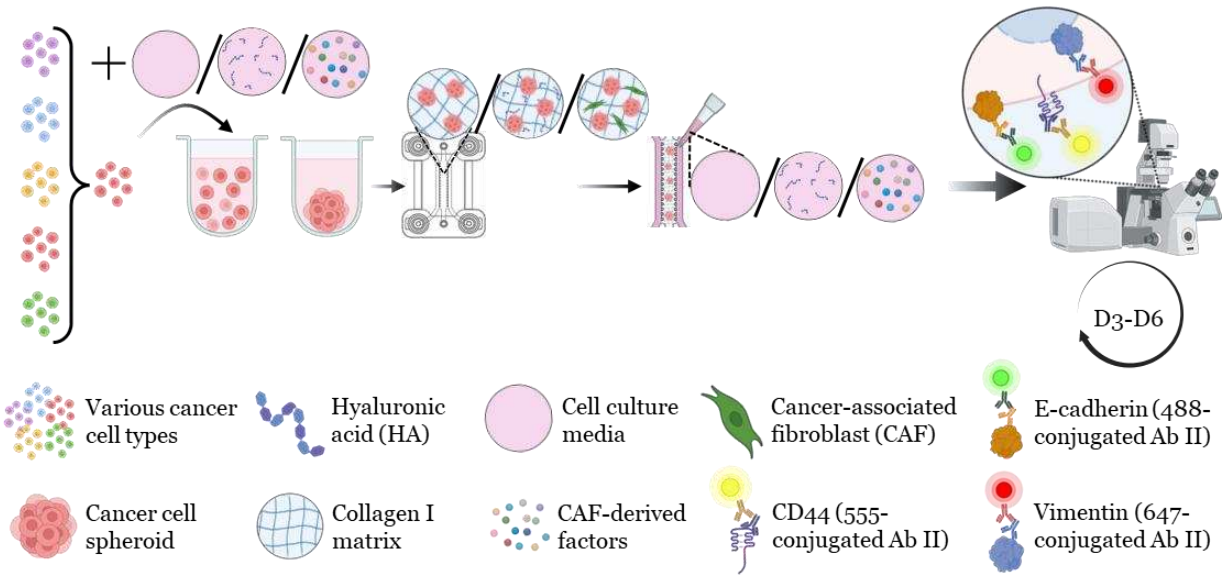
This chapter is organized in the form of a paper draft, containing typical sections including ***Abstract***, ***Introduction***, ***Results***, ***Discussion*** and ***Experimental Procedures***, followed by the paper's ***Supplementary information***. As additional analyses for this study are still ongoing to further strengthen and validate findings, the final discussion and conclusions of this work remain subject to refinement. The study was conducted with the valuable assistance of interns, Lorraine Olagne, Margaret (Nel) Straub and Viet Duc (Henry) Ho, whose contributions supported various experimental and analytical aspects of this work.

An **additional section** follows the paper, dedicated to discussing the ***challenges, limitations, and future perspectives*** of the study in greater detail.

ABSTRACT

Epithelial-mesenchymal transition (EMT) is a critical driver of pancreatic ductal adenocarcinoma (PDAC) progression and therapy resistance, with multiple environmental factors influencing its induction. Tumor-on-chip models provide a powerful platform to recreate the 3D architecture and controlled microenvironment of tumors, enabling mechanistic studies of tumor-stroma interactions that are difficult to achieve in conventional *in vitro* and *in vivo* models. Yet, current PDAC-on-chip systems remain limited in their ability to fully capture physiologically relevant EMT dynamics. Here, we developed a PDAC-on-chip platform to dissect how the extracellular matrix and stromal fibroblasts contribute to EMT. Following a selection of an appropriate cell cancer model, we generated cancer spheroids and embedded them in collagen I matrix under various conditions: (i) with hyaluronic acid (HA), (ii) co-cultured with stromal cells, or (iii) exposed to stromal cell-derived conditioned media. EMT was evaluated through the expression of canonical markers, E-cadherin and Vimentin, at days 3 and 6 of on-chip culture. The study revealed that HA exerts a modulatory role on EMT depending on its molecular weight and mode of integration and stromal cell-derived soluble factors robustly drive EMT induction, thereby highlighting the critical microenvironmental components for physiologically relevant PDAC-on-chip modeling and therapeutic testing.

TABLE OF CONTENTS



I. INTRODUCTION

Pancreatic ductal adenocarcinoma (PDAC) remains one of the most lethal cancer malignancies, primarily due to its early dissemination and profound resistance to conventional therapies.[27,320] One of the defining features of PDAC is its extensive and highly heterogeneous tumor microenvironment (TME), characterized by a largely dense desmoplastic stroma with abundant cancer-associated fibroblasts (CAFs) and a highly altered extracellular matrix (ECM) by increased presence of matrix proteins, particularly collagens and hyaluronic acid (HA), as well as their spatial reorganization.[27,85,102,115,296] Rather than being a passive scaffold, this stromal compartment actively drives tumor progression, epithelial-mesenchymal transition (EMT) and metastasis, fostering therapy resistance and creating an immunosuppressive, pro-tumorigenic microenvironment.

A central hallmark of PDAC progression is EMT, a process whereby epithelial tumor cells acquire mesenchymal features, including enhanced motility, invasive capacity, and resistance to apoptosis.[143,168,345] EMT is known to be strongly influenced by tumor-stroma interactions and ECM composition: CAFs interact with cancer cells both through direct cell-to-cell interactions as well as secretion of growth factors and cytokines (e.g., TGF-β, IL-6) that trigger EMT-related signaling cascades, while fibrillar collagens and HA remodel the physical and biochemical environment to promote invasive phenotypes.[102,346] *In vivo*, the convergence of cellular and matrix-derived cues generates a dynamic niche that sustains partial and reversible EMT states, which are increasingly recognized as key mediators of PDAC aggressiveness.[144] It is therefore crucial to include the EMT cancer cell shift to reliably replicate *in vivo*-like features of PDAC in preclinical model development.

Despite extensive knowledge of EMT at the molecular level, it remains difficult to disentangle the relative contribution of specific TME components to EMT induction in PDAC. Traditional 2D cultures oversimplify the cellular context and fail to recapitulate the gradients and spatial organization of the native tumor. Novel use of patient-derived organoids (PDOs) while provide valuable *in vivo*-derived 3D epithelial models, lack stromal and ECM elements. Lastly, mouse models are advanced tools that reproduce the EMT and its natural complexity, however, they are poorly suited for dissecting the impact of individual microenvironmental components.[347,348] To address this, microfluidic tumor-on-chip technologies have emerged as powerful intermediate *in vitro* systems that combine controlled microenvironmental design with physiologically relevant 3D architecture, enabling mechanistic dissection of EMT induction by defined tumor-stroma interactions.[262]

While several PDAC-on-chip models have included various stromal components,

including pancreatic stellate cells (PSCs), CAFs and immune cells, focusing mainly on their roles in drug sensitivity and stromal barrier formation, few have begun to incorporate EMT as a readout.[269,274,277,283,286] For example, the team of Hyo-Jeong Kuh reported a multichannel microfluidic system to co-culture pancreatic cancer cells and stellate cells, where they studied E-cadherin and Vimentin expression changes via immunostaining, demonstrating a slight shift towards EMT upon co-culture.[270,349] In the study, however, single cells were placed in different channels, separated by a media channel, which significantly decreases the interaction of cancer cells with the stromal cells. In addition, the majority of investigation was conducted with an intrinsically mesenchymal PANC-1 cell line, hence, potentially biasing the outcome. Haque et al. co-cultured PDOs directly with PSCs in 3D and analyzed for EpCAM expression, however, only qualitatively.[278] Geyer et al. have also co-cultured PDOs with PSCs but in separate channels, tracking gene expression changes in mono vs co-culture under hypoxic vs normoxic conditions.[282] While they reported an increase in both Vimentin and E-cadherin expression in hypoxic conditions, which is higher in the case of monoculture as compared to co-culture, these results contrast with the broader understanding of the EMT-related changes and effects of cancer and stromal cell co-culture, suggesting that further investigation is needed to reconcile these differences.

Several of these studies have assessed cell invasiveness by quantifying invasion distance or scores.[263,265,278] While these approaches provide valuable insights into migratory behavior, they do not directly capture the molecular and phenotypic transitions that define EMT. Moreover, despite the promise of ToC platforms to probe EMT, important limitations persist. In most systems, stromal cells are positioned in adjacent compartments rather than surrounding tumor aggregates, and the ECM composition is typically limited to collagen I or Matrigel, omitting other matrix components like hyaluronan, which plays a central role in PDAC.

Hyaluronan or hyaluronic acid (HA) is a large hydrophilic glycosaminoglycan present in PDAC TME in variable molecular weights, where it exerts multifaceted effects on both cancer cells and stromal components.[114,115,120] While under healthy conditions, HA levels are maintained by a dynamic balance between synthesis via HA synthases (HAS1, HAS2, HAS3) and degradation by hyaluronidases (HYAL1 & HYAL2), in PDAC this balance is disrupted.[115,120] Cancer cells and CAFs produce HA in excess, often accompanied by altered hyaluronidase activity, resulting in marked stroma accumulation. This excessive deposition increases water retention and compresses intratumoral vasculature, thereby impairing drug perfusion and fostering a pro-EMT microenvironment through increased stiffness and

hypoxia.[296,350,351] While elevated HA accumulation has consistently been associated with poor prognosis and increased tumor cell motility, its specific role in regulating EMT remains less well defined.[114,115]

Here, we describe a PDAC-on-chip system designed to progressively increase physiological complexity while preserving experimental tractability. The study begins with a comparative evaluation of PDAC cell lines during spheroid formation, providing the basis for subsequent model development. Pre-formed spheroids are then either (i) embedded within collagen matrix supplemented with hyaluronan, introduced either directly during spheroid formation, into the surrounding ECM, or via the culture medium, or (ii) co-cultured with stromal fibroblasts, either as dispersed cells in direct contact with tumor spheroids to mimic epithelial-stromal proximity, or indirectly, through exposure to fibroblast-conditioned medium to capture paracrine interactions. Using EMT-related marker expression changes as a functional readout, we systematically assess how these stromal components — biochemical and cellular — influence PDAC cell state. By establishing a system that recapitulates some of the key drivers of EMT in PDAC, this work highlights essential components required in 3D *in vitro* systems to mimic *in vivo* PDAC biology, thereby guiding the future development of physiologically relevant platforms for therapeutic testing.

II. RESULTS

1. Comparative analysis of PDAC cell lines for relevant model selection

As a first step, we evaluated the spheroid-forming capacity of four commonly used epithelial PDAC cell lines (BxPC-1, HPAF-II, Capan-1, Capan-2) in parallel with PANC-1, one of the most widely used models for PDAC research but classified as quasi-mesenchymal or mesenchymal, according to different sources.[341,352,353] Following the goal to establish an epithelial baseline from which EMT dynamics could be meaningfully assessed, spheroids were generated and systematically assessed for morphological parameters, including size, roundness, circularity, solidity as well as texture features (variance in grey/mean grey & relative grey = mean grey/background grey) (Figure 3.1 A).

For this, single-cell suspensions from all five cell lines in parallel were seeded into non-adhesive agarose-micromolded 6-well plates (approximately 2000 microwells/well) at 3 different concentrations: $2.5x10^5$ cells/mL (Figure 3.1), $5x10^5$ cells/mL (Figure 3.S1) and $1x10^6$ cells/mL (Figure 3.S2) with a total of 1 mL per well resulting in roughly 125, 250 and 500 cells/microwell (spheroid) respectively. Following the seeding, spheroid formation was

monitored with a plate reader via bright field imaging on days 0, 1, 2, 3 and 4 (Figure 3.1 B).

It can be observed from Figure 3.1 B that spheroid formation varies drastically amongst cell lines in shape, size, time required for cell cohesion, and apparent density, among the others. Indeed, the reference mesenchymal cell line PANC-1 struggled to form spheroids over 4 days with some aggregation taking place at D4, however, largely remaining as single cells that fail to form cohesive structures with minimal changes in shape or texture-related features (Figure 3.1 B-C). In contrast, BxPC-3 and HPAF-II cell lines demonstrated excellent spheroid formation within the first 24 hours post seeding, forming more cohesive, compact and dense structures over the next days. Indeed, these two cell lines are the only ones that presented a drastic drop in spheroids' area as compared to D0 (Figure 3.1 C) due to rapid cell aggregation and cohesion as well as an increase in circularity, roundness and solidity. In addition, both of their textural features were reduced most and fastest, indicating formation of texturally more heterogeneous and dense spheroids as compared to other cell lines. Interestingly, HPAF-II-generated spheroids continued to augment in size from D1 to D4, forming characteristic budding that slightly alters further shape-related measurements despite maintaining high spheroid homogeneity and density, while BxPC-3 seemed to reach a plateau in their development within the first 24-48 hours following the seeding.

On the other hand, Capan-1 and Capan-2 cells were the least consistent in spheroid formation over time. Not only were these cell types unable to form cohesive spheroidal structures over 4 days, but in some cases, they escaped/fell back into the microwells, as can be observed with Capan-2 cell line from D1-D2-D3 (Figure 3.1 B), further complicating spheroid aggregation. This could be attributed to a distinct, potentially lower density and surface tension of these cells as well as thicker glycocalyx due to increased mucin expression.[354,355] Along with size variations, this resulted in variable shape and textural characteristics of these cell clusters, which is consistent with the hallmarks of these cells, being the most highly differentiated PDAC cell lines, prone to form duct-like structures.[341,356]

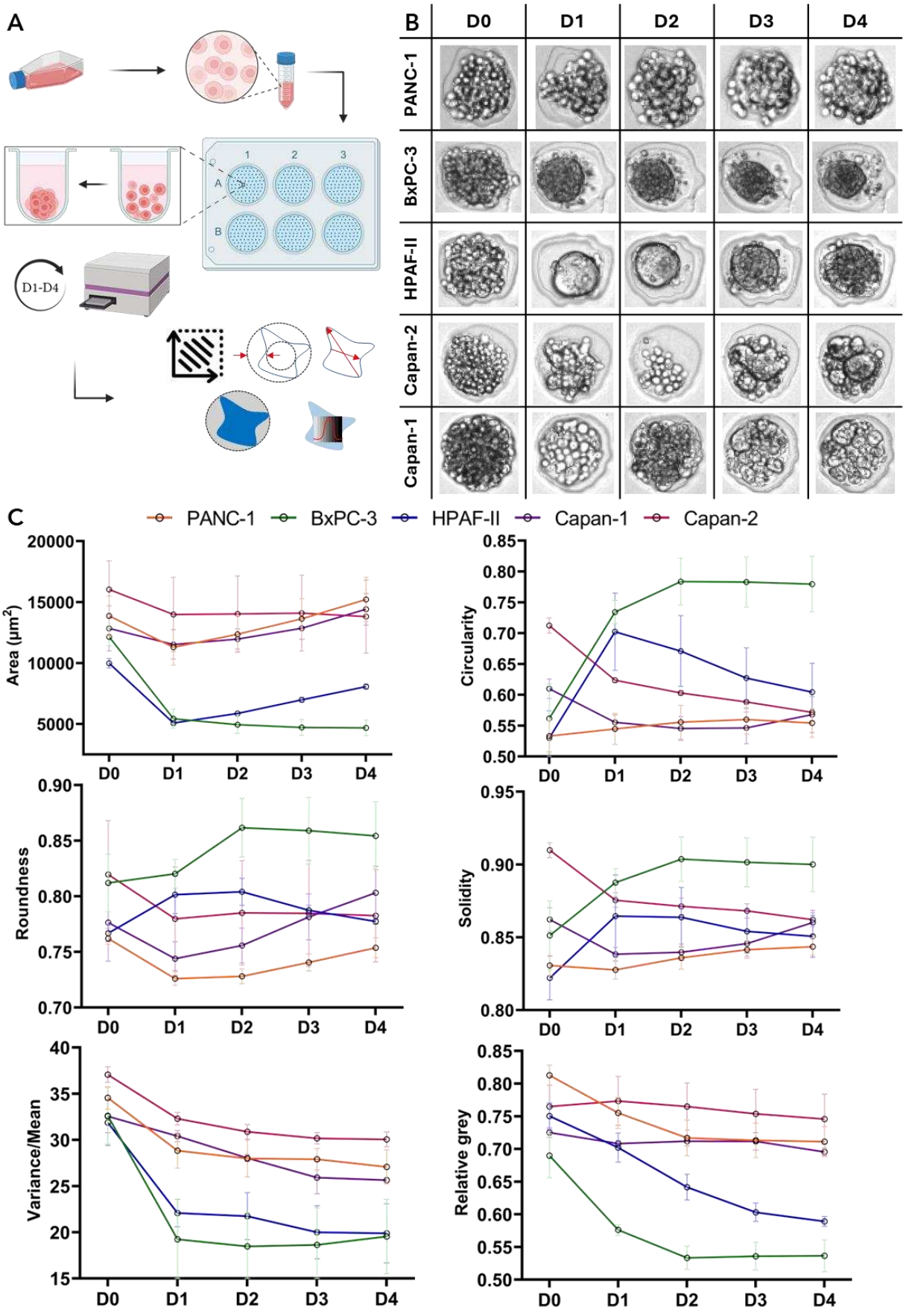


Figure 3.1: **Comparative analysis of spheroid features from five PDAC cell lines. A.** Schematic representation of the procedure of spheroid formation from single cells, monitoring and

characterization over 4 days. **B.** Bright field imaging of spheroids generated from 5 cell lines over 4 days. Microwell diameter = 200µm. **C.** Characterization of spheroids (125 cells/microwell) through computation of area, circularity, roundness, solidity, variance/mean grey and relative grey values. (N≥3 for each cell line, n≥1000 spheroids).

To validate the phenotypical profile of the four epithelial cell lines studied, immunofluorescent imaging of the spheroids was performed for the key EMT-related markers, E-cadherin and Vimentin, on D4 post-seeding (Figure 3.2 A). As expected, all four cell lines strongly expressed E-cadherin cell-cell adhesion protein with little-to-no Vimentin expression, indicating pronounced epithelial cell characteristics and high spheroid cohesiveness. Notably, Capan-1 cells failed to yield cohesive spheroids, as discussed earlier, which limited the microwell extraction and immunofluorescent imaging to much smaller cell clusters, as compared to other cell lines (Figure 3.2 A).

In addition, to confirm spheroid viability post formation and feasibility with microfluidic 3D culture, spheroids of each cell line were collected on D4 of formation and seeded in collagen type I (6 mg/mL) on a chip, similarly to as reported previously.[293] Live/dead assay was performed 3 days after seeding on chip, validating high viability of spheroids independently of the cell line (Figure 3.2 B). Exceptionally, while all the cell lines have shown some degree of interaction with the surrounding collagen fibers (typically, by pulling on them), Capan-1 cells have completely contracted the collagen-based ECM within the chip, forming a dense fused spheroid-collagen tissue, thereby losing the distinctive spheroid structures (Figure 3.2 C). Being the most highly differentiated PDAC cell line, Capan-1 was reported to strongly express integrin-β1, which is a key receptor for collagen type I.[357,358] In addition, due to Capan-1 cells forming smaller structures over 4 days of spheroid formation rather than larger cohesive spheroids like other cell lines, the exposure of collagen fibers to integrin receptors might be higher.

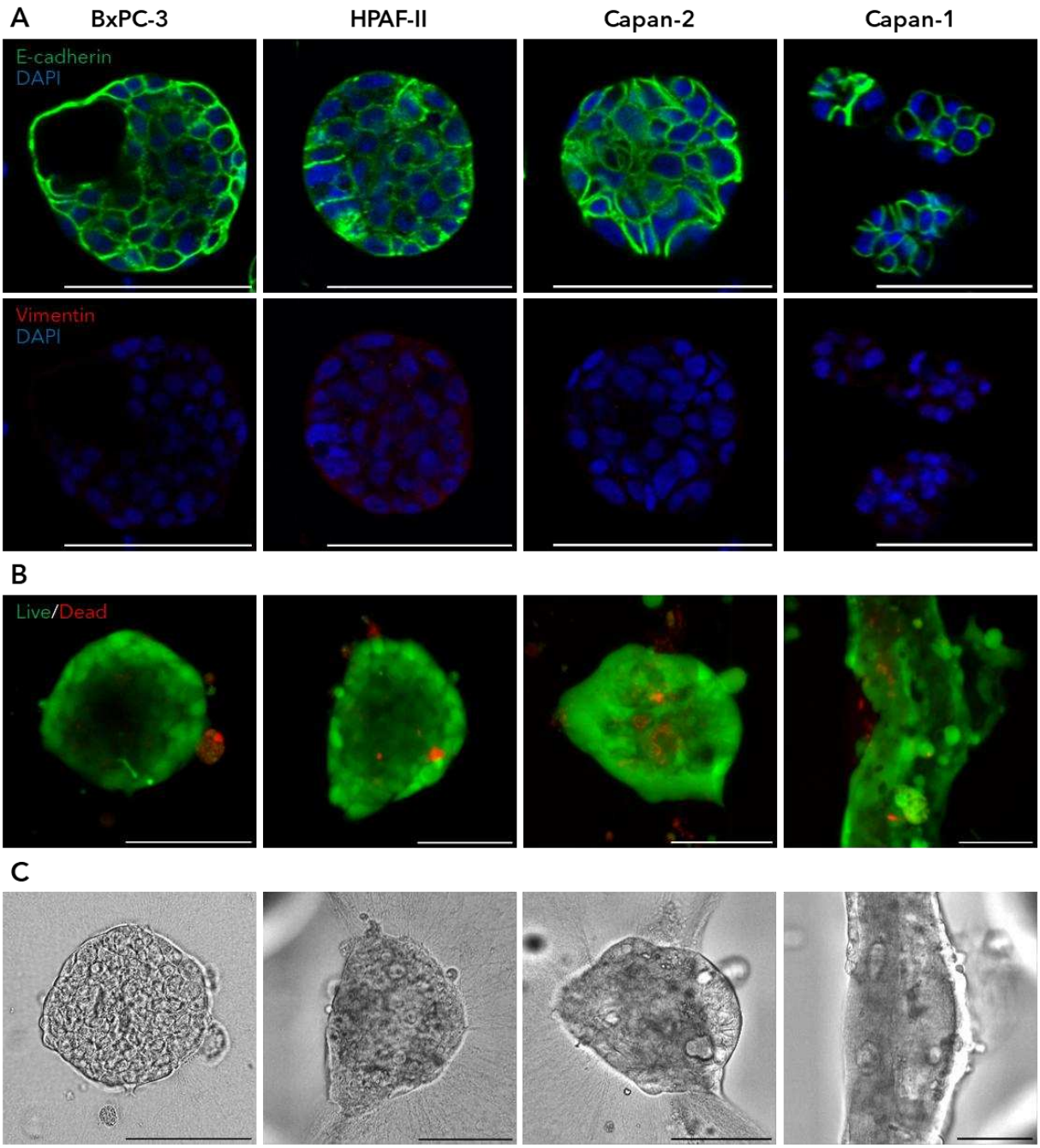


Figure 3.2: **EMT marker expression and on-chip viability assessment of epithelial cell line-spheroids. A.** Confocal imaging of spheroids in suspension extracted on D4 post seeding immunostained for E-cadherin (green), Vimentin (red) and DAPI (blue). **B.** Spheroid viability assessment at D3 in collagen I (6 mg/mL) on chip with confocal microscopy imaging (3D z-projection, sum slices method), live/dead (Calcein Green/Texas Red) assay. **C.** Bright field imaging with enhanced contrast, highlighting the spheroid-collagen fibers interactions. Scale bar = 100μm.

Out of the four highly epithelial cell lines analyzed in this study, Capan-1 and Capan-2 cell lines represent the most differentiated PDAC cell lines with longest doubling time reported, forming complex irregular structures resembling ductal differentiation.[341,356,359] BxPC-3 cell line, while being moderately-to-poorly differentiated, yields reproducible spheroids within the shortest period of time. However, BxPC-3 cell line lacks the

characteristic KRAS mutation present in over 90% of PDAC cases, hence limiting this model's relevance for PDAC research. HPAF-II cell line, in turn, while possessing all four most prominent PDAC mutations (KRAS, CDKN2A, p53 and SMAD4), generates consistent spheroidal structures in a short period of time, and was therefore selected as the cell model for the following investigation.

2. Mid, but not low, molecular weight HA enhances CD44 expression in cancer spheroids on chip when incorporated at single-cell stage

Having established HPAF-II as the most suitable cell line for the present study, the next step consisted in investigation of hyaluronic acid (HA), a key stromal matrix component in PDAC, contribution to epithelial-mesenchymal plasticity in the PDAC-on-chip model. While the overarching objective is to evaluate the EMT-related changes associated with HA, we first focused on the expression of the principal HA receptor and well-recognized mediator of HA-driven signaling, CD44, as initial readout of HA-cancer cell interactions. Interacting with CD44, a transmembrane glycoprotein implicated in diverse physiological and pathological processes including development, inflammation, immune regulation, and cancer progression, HA modulates cellular behavior.[142,360] Binding of HA to CD44 has shown to enhance mesenchymal signaling, stemness, and chemoresistance, with high CD44 expression correlating with epithelial-mesenchymal plasticity.[115,360]

Evidence suggests that low MW HA often exerts tumor-promoting functions, whereas high MW HA may have tumor-suppressive effects; however, this dichotomy remains controversial and context-dependent.[120–122,361] Adding further complexity, MW classification of HA varies across studies.[114,120] In this work, we adopted the definitions proposed by Monslow et al., which specify high MW HA as 1000-6000 kDa, mid as 250-1000 kDa and low as 10-250 kDa.[111] Given the rapid HA turnover in tissues, where homeostasis is tightly regulated by a dynamic metabolic network of biosynthesis, degradation, and clearance, the balance of which varies across cell types, tissue environments, and pathological states,[112,362,363] prior to incorporating the HA into PDAC-on-chip, we first evaluated the presence of HA of three different MWs (low, mid and high) in collagen I matrix as a function of time, concentration and molecular weight (Figure 3.S3). Briefly, HA was introduced into collagen gel mixture (6 mg/mL) in a soluble, non-crosslinked form at concentrations ranging from 0 to 25% w/w (25% HA corresponding to 2 mg/mL of HA and 6 mg/mL of collagen) and analyzed via Alcian Blue staining at D0, 1, 2, 3, 7 for low, mid and high MW HA. Substantial HA diffusion from the collagen matrix was observed, with ~80% loss by D3 across all MWs even at the highest proportion of 25% (Figure 3.S3 A), although

residual HA remained detectable within the collagen matrix. To counteract this depletion, HA was also supplemented in the culture medium (1 mg/mL, refreshed daily), which markedly increased long term HA concentration in the collagen matrix, regardless of the initial content (Figure 3.S3 C-D). Notably, while low and mid MW HA was homogeneously integrated, high MW exhibited uneven distribution and dense aggregates, most likely stemming from an increased viscosity and homogenization difficulty attributed to the longer molecular chain length (Figure 3.S3 B). Based on these findings, 25% w/w matrices supplied with HA-dissolved media (1 mg/mL) were chosen for subsequent experiments to maximize HA content in the system, with mid MW HA prioritized as a less explored form, and low MW retained as a comparator due to its reported pro-tumoral effects.

To evaluate the effect of HA incorporation into our PDAC-on-chip system, HPAF-II spheroids were formed in agarose microwells over 24h starting with ~125 cell/microwell, as described previously, and then embedded in collagen I (6 mg/mL) matrix on chip, with HA integrated through three different strategies: (i) HA polymerization into the collagen hydrogel (2 mg/mL HA, 6 mg/mL collagen) + HA supplemented in culture medium (1 mg/mL) (ECM + media condition, done only with Mid MW HA), (ii) HA addition only during spheroid formation in agarose microwells (1 mg/mL) (HAS condition), or a combination of the two strategies (MAX condition) (Figure 3.3 A).

Figure 3.3 B evidences an increase in CD44 expression in the samples, incorporated with mid MW HA. Indeed, the quantitative analysis (Figure 3.3 C) demonstrated a significant increase in the number of CD44 positive cells per spheroid in the samples treated with mid HA at D6. While the trend of CD44 expression increase in respective D3 samples resembled that of D6, it was not significant compared to control D3, suggesting that a more marked cell response to HA presence may require longer exposure times and higher concentrations. Interestingly, the incorporation method of HA (HAS vs MAX) did not show any impact on CD44 expression, indicating that integration of HA at the stage of spheroid formation may play a key role in cell response to HA presence. This is further supported by the absence of effect on CD44 expression when HA is incorporated solely in ECM + media but not in the spheroids (Figure 3.3 C). This may stem from the fact that during spheroid formation exposure to HA takes place at a single-cell level, maximizing the interactions of individual cells with HA molecules, as compared to coherent spheroids, where only the peripheral cells are exposed.

In contrast, low MW HA integration had no observable impact on CD44 expression in cancer cells. This may be attributed to the shorter molecular chain length of the molecule,

resulting in its faster degradation which did not allow to induce any detectable effects at this concentration and exposure time.

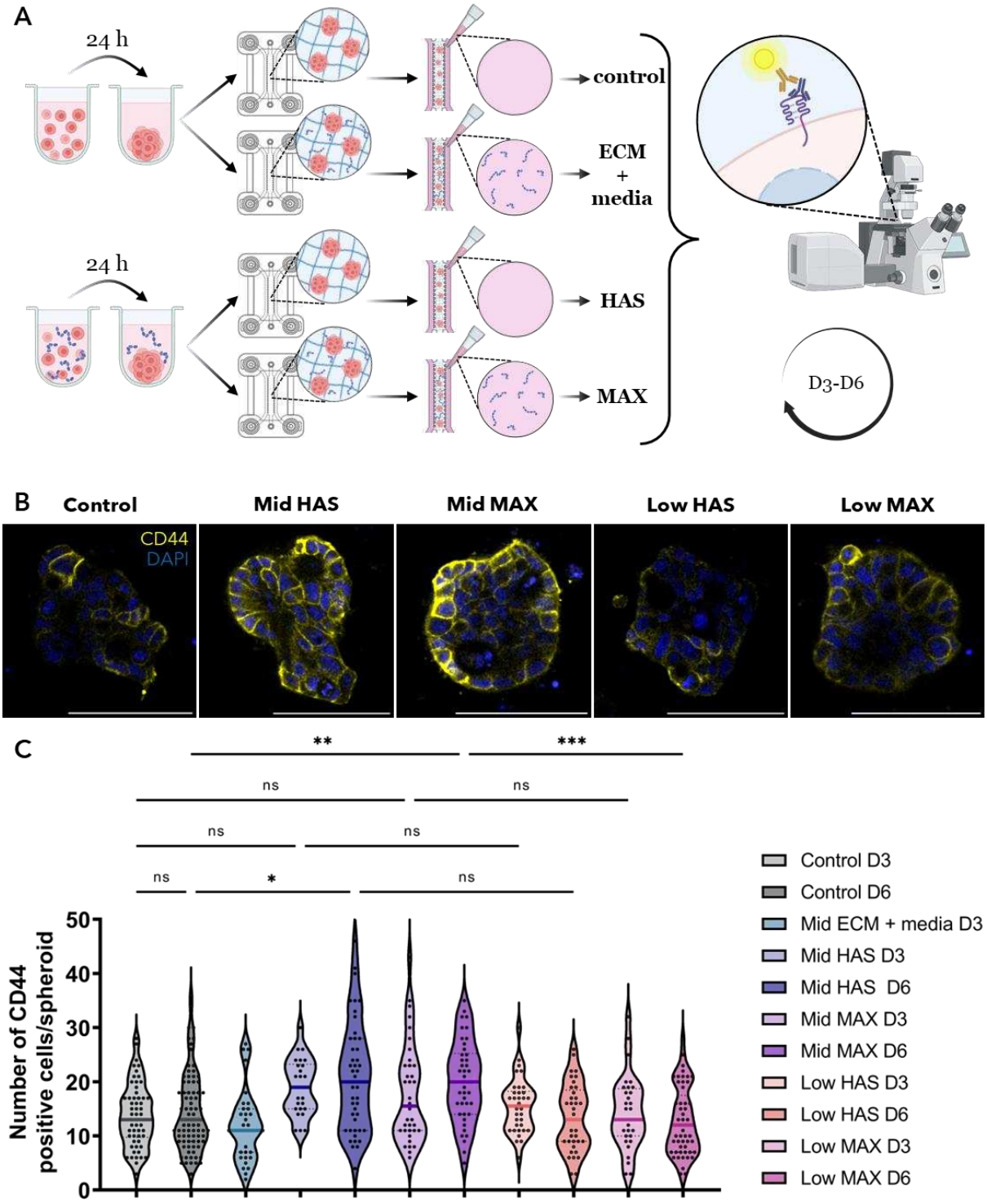


Figure 3.3: **Impact of hyaluronic acid (HA) on CD44 expression in PDAC-on-chip as a function of molecular weight, time and incorporation method. A.** Schematic representation of the HA incorporation analysis strategy and conditions: control (spheroids in collagen 6 mg/mL matrix on chip supplied with culture media), ECM + media (spheroids in collagen 6 mg/mL + HA matrix on chip supplied with culture media + HA), HAS (spheroids, formed with HA in cell suspension, in collagen 6 mg/mL matrix on chip supplied with culture media) and MAX (spheroids, formed with HA in cell suspension, in collagen 6 mg/mL + HA matrix on chip supplied with culture media + HA); samples

were immunostained for CD44 and imaged with confocal microscope at D0 (control only), D3, D6. **B.** Representative confocal images (section of 3D image) of samples at D6 immunostained for CD44 (yellow) and DAPI (blue). Scale bar = 100 µm. **C.** Quantitative analysis of the number of CD44 positive cells/spheroid as a function of time, HA molecular weight and incorporation method. Data are presented as violin plot including all experimental data points (>4 independent experiments for each condition, ≥10 spheroids per experiment). *p< 0,1; **p< 0,01; ***p< 0,001; ****p< 0,0001.

Overall, these results suggest that mid, but not low, MW HA can induce CD44 overexpression within cancer spheroids embedded in collagen matrix on chip, with initial single-cell exposure to HA molecules being key to this effect. These findings indicate active PDAC cell sensing and adaptation to matrix composition, reinforcing the central role of HA-CD44 signaling in shaping tumor-stroma interactions. In addition, HA-driven upregulation of CD44 is particularly relevant given CD44's established role as one of the key mediators of EMT initiation and progression in PDAC.

3. Incorporation of mid molecular weight HA in PDAC-on-chip is associated with a moderate EMT shift

We next investigated the link between the presence of HA within our PDAC-on-chip model and epithelial-mesenchymal cancer cell plasticity. The same experimental setup was applied, and spheroids cultured under different HA MWs and integration strategies were analyzed for the canonical EMT marker expression E-cadherin (epithelial) and Vimentin (mesenchymal) at days 3 and 6 (Figure 3.4 A).

Consistent with the CD44 data, conditions incorporating mid MW HA on-chip induced a shift toward a more mesenchymal phenotype via both apparent E-cadherin downregulation and Vimentin upregulation in the cells of cancer spheroids as soon as at D3 (Figure 3.4 B). Indeed, quantitative analysis demonstrated an increase in the number of Vimentin-positive cells per spheroid for mid HAS D3, mid MAX D3 & D6, as compared to control (Figure 3.4 C). A similar trend was observed for reduced E-cadherin expression, although this decrease was not statistically significant as most of the cells within cancer spheroid remained largely E-cadherin-positive, potentially pointing to a partial EMT phenotype. Similarly, these changes appear independent of whether HA was present solely during spheroids formation or maximized through the different steps of on-chip culture, as observed at D3 (Figure 3.4 C), underlining the importance of HA integration early in the model. Interestingly, mid HAS D6 condition did not show any detectable EMT shift in cancer spheroids as compared to control D6 samples, and both the number of Vimentin-positive and E-cadherin negative cells was smaller than at D3 of the same condition. These results suggest that in absence of HA supplementation the intrinsically epithelial profile of these cancer cells allows them to recover their epithelial characteristics over time, contrary to

CD44 expression discussed before. This is confirmed by the significant EMT shift observed in mid MAX conditions at D6, where HA is resupplied in the model over time, while it is still lower than the respective condition at D3, indicating potential cell preference for their epithelial characteristics as spheroids compact in 3D matrix. Indeed, in control samples the number of E-cadherin negative cells drastically decreased from D3 to D6, indicating increasing spheroid cohesion and cell-cell junctions over time, thus, acquiring a highly epithelial phenotype upon on-chip collagen culture. A similar trend was observed within mid HA samples, with MAX condition better sustaining the EMT shift at D6.

In contrast, incorporation of low MW HA did not produce any consistent changes in EMT markers across conditions. The difference of the effect between low and mid MW HA likely reflects their distinct stability and biological activities within the system, with low HA being more rapidly degraded and therefore, less effective at sustaining EMT modulation under the conditions tested. Together, these HA MW-dependent outcomes also reflect on the current debate on the implications of HA molecular properties in PDAC TME.[120–122,361]

It is worth noting that HA presence in the system did not seem to impact spheroid size (Figure 3.S4), which could potentially bias the positive cell count per spheroid. Indeed, projected area of the spheroids across conditions was not different within the same day of culture. Importantly, changes in spheroid area over time did not appear to impact the number of E-cadherin- or Vimentin-positive cells, allowing expression dynamics to be assessed independently of size. For example, in control spheroids, despite a moderate increase in area (Figure 3.S4), the number of E-cadherin negative cells decreased further, while the number of Vimentin-positive cells remained unchanged (Figure 3.4 C).

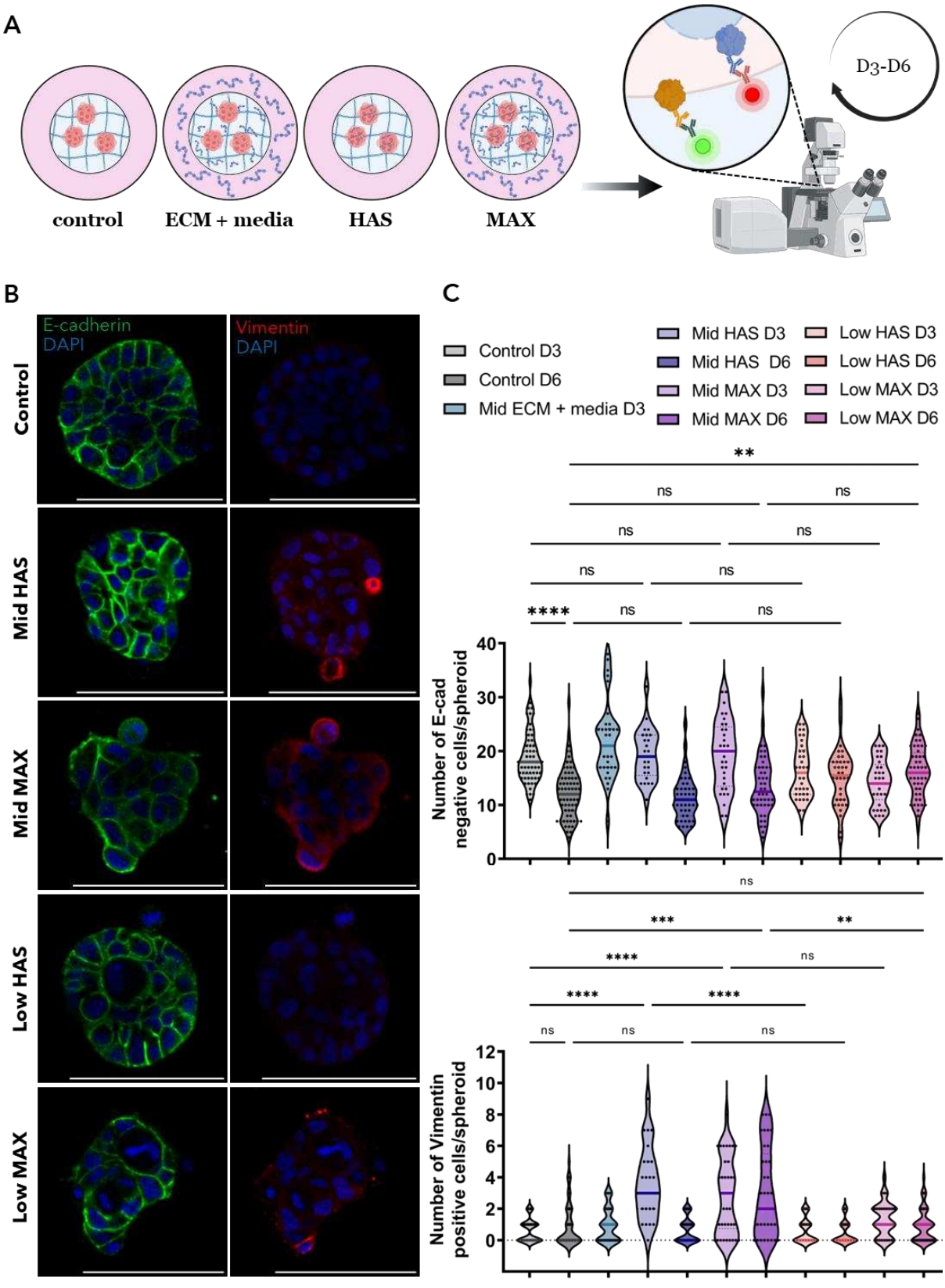


Figure 3.4: **Impact of hyaluronic acid (HA) on EMT marker expression in PDAC-on-chip as a function of molecular weight, time and incorporation method. A.** Schematic representation of the analysis of HA impact on EMT marker expression as a function of incorporation strategy. **B.** Representative confocal images (section of 3D image) of samples at D3 immunostained for E-cadherin (green), Vimentin (red) and DAPI (blue). Scale bar = 100 µm. **C.** Quantitative analysis of the number of E-cadherin negative and Vimentin positive cells/spheroid as a function of time, HA

molecular weight and incorporation method. Data are presented as violin plot including all experimental data points (>4 independent experiments for each condition, ≥10 spheroids per experiment). *p< 0,1; **p< 0,01; ***p< 0,001; ****p< 0,0001.

Altogether, the findings indicate that the presence of mid MW HA in the PDAC-on-chip system promotes and sustains an EMT shift in cancer spheroids over time, preventing the conversion toward a more epithelial phenotype, as observed in control samples. Notably, among the mid HA conditions, only the mid HAS D6 samples failed to maintain EMT marker expression, suggesting that initial HA exposure during spheroid formation is insufficient to sustain EMT in the absence of continued HA supplementation, contrary to CD44 expression that was maintained over time. Thus, mid MW HA appears to stabilize EMT-like features in PDAC-on-chip, underscoring its potential as a critical component for developing *in vivo*-relevant PDAC-on-chip models.

4. Stromal conditioned media, but not direct single-CAF co-culture, drives EMT in PDAC-on-chip

Given that HA alone only partially drives EMT, we next investigated the contribution of stromal factors, focusing on soluble cues derived from two distinct sources of tumor-associated fibroblasts to modulate EMT marker expression in this model. These included primary human pancreatic stellate cells (HPaSteCs), isolated from a healthy pancreas and known precursors of CAFs within TME, and primary pancreatic CAFs (P-CAFs), isolated directly from pancreatic tumor tissue. While the molecular and phenotypic distinctions between these two cell types remain incompletely defined, their comparison provides insight into potential differences in stromal signaling relevant to EMT. Similarly, HPAF-II spheroids were generated in agarose microwells for 24h and subsequently cultured on-chip, adopting two experimental strategies: (i) co-culture with dispersed stromal cells (HPaSteCs or P-CAFs) and (ii) culture in stromal conditioned media (CM) obtained from the same cell sources (Figure 3.5 A). EMT was assessed by immunostaining for E-cadherin and Vimentin expressions at days 3 and 6.

As a result, initial co-culture with single stromal cells until D3 did not alter EMT marker expression compared to controls (Figure 3.5 B). This lack of effect is likely explained by the relatively low stromal-to-cancer cell ratio achievable in the chip (1:1), resulting in insufficient direct contact and local concentrations of secreted factors to influence PDAC spheroids. To overcome this limitation, cultures were next supplemented with CM, which provides a concentrated source of stromal-derived soluble signals.

Strikingly, CM exposure had a clear impact on EMT as soon as at D3 of culture

(Figure 3.5 B). In spheroids formed in CM and maintained with daily refreshed CM on-chip, both HPaSteC- and P-CAF-derived media induced a significant increase in Vimentin-positive and E-cadherin-negative cells at D3 (Figure 3.5 C). While these changes became slightly more pronounced by D6 with HPaSteC CM, CAF CM induced a more significant shift from D3 to D6, as shown by an increase in Vimentin-positive cells. Overall, however, no significant differences were observed between cell phenotypic changes driven by CM derived from HPaSteC or CAFs, indicating that both stromal sources secrete factors sufficient to trigger EMT in this model.

Importantly, similar to previous observations, in control conditions the number of E-cadherin-negative cells per spheroid decreased from D3 to D6, indicating progressive increase in spheroid epithelial characteristics with time, consistent with the intrinsic epithelial nature of the cell model. Therefore, to address whether sustained exposure was necessary to maintain the EMT phenotypic shift over time, we next compared conditions where CM was supplied only until D3 and then replaced with standard media, with spheroids maintained until and analyzed at D6. For both HPaSteC- and CAF-CM, transient exposure did not significantly differ from continuous D6 CM exposure, suggesting that early CM exposure is sufficient to initiate EMT, while sustained exposure is not strictly required to maintain it.

Together, these results underscore the central role of stromal-derived paracrine signals in promoting EMT in PDAC spheroids on chip. Incorporating CM into the PDAC-on-chip system thus provides an effective means to capture stromal-tumor interactions and enhances the physiological relevance of the platform while dissecting EMT dynamics.

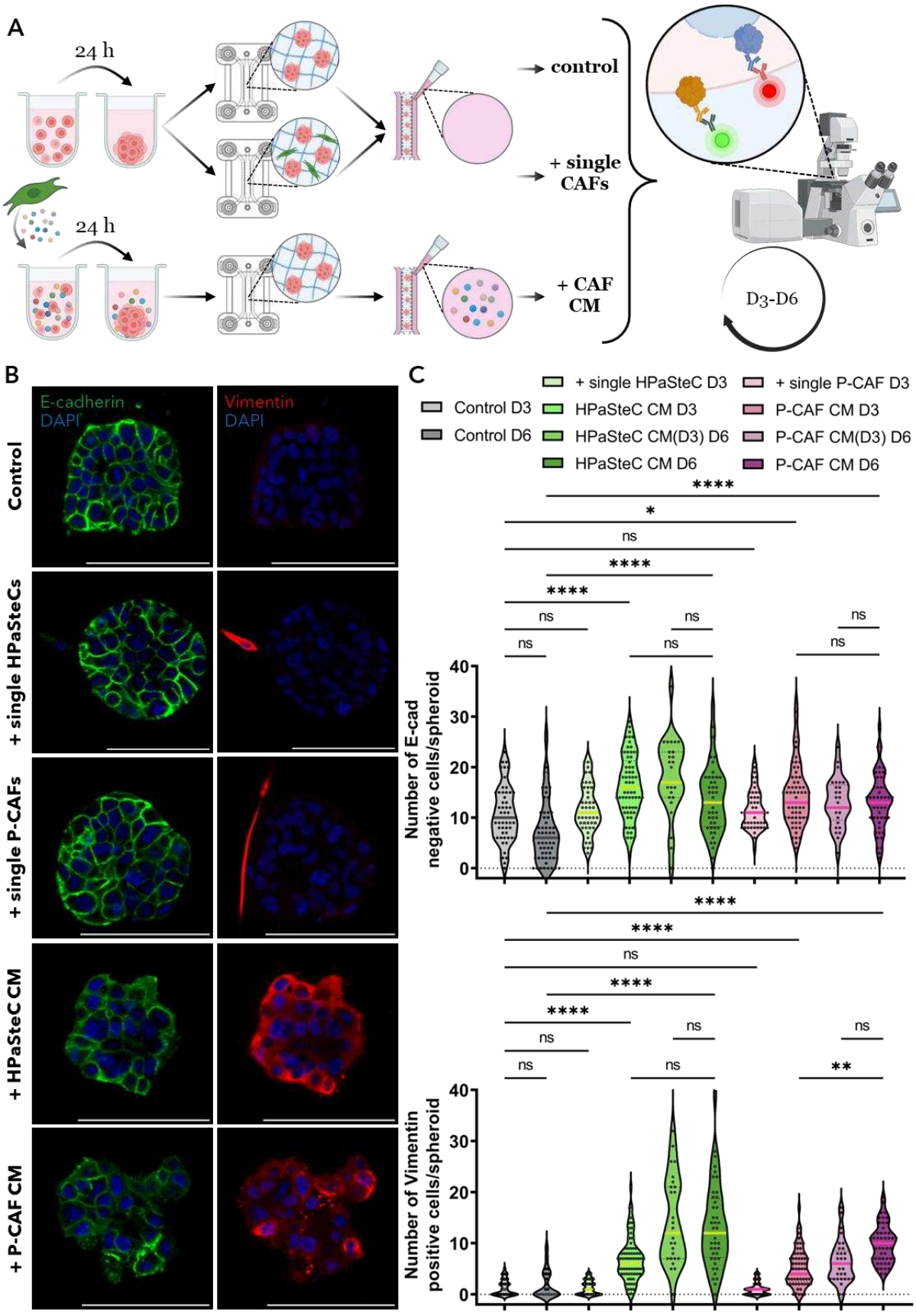


Figure 3.5: **Impact of CAF-derived stromal factors on EMT marker expression in PDAC-on-chip as a function of time and exposure method. A.** Schematic representation of the CAF incorporation analysis strategy and conditions: control (spheroids in collagen 6 mg/mL matrix on chip supplied with culture media), + single CAFs (co-culture of spheroids in collagen 6 mg/mL with single CAFs), + CAF

CM (spheroids, formed with CAF CM in single cell suspension, seeded in collagen 6 mg/mL matrix on chip supplied with CAF CM daily); samples were immunostained for E-cadherin and Vimentin and imaged with confocal microscope at D0 (control only), D3, D6. **B.** Representative confocal images (section of 3D image) of samples at D3 immunostained for E-cadherin (green), Vimentin (red) and DAPI (blue). Scale bar = 100 µm. **C.** Quantitative analysis of the number of E-cadherin negative and Vimentin positive cells/spheroid as a function of time and CAF factors exposure method. Data are presented as violin plot including all experimental data points (>4 independent experiments for each condition, ≥10 spheroids per experiment). *p< 0,1; **p< 0,01; ***p< 0,001; ****p< 0,0001.

III. DISCUSSION

Although the molecular circuitry underlying EMT in PDAC is increasingly well characterized, its integration within complex 3D microfluidic *in vitro* models is critical not only for capturing how the TME regulates this process but also for developing more physiologically relevant *in vitro* systems. Several PDAC-on-chip systems have attempted to incorporate stromal elements, but their ability to capture EMT dynamics is still limited. Most platforms have positioned fibroblasts or stellate cells in parallel channels separated from tumor aggregates, restricting direct interactions and reducing the paracrine concentration gradients that are critical for EMT induction.[269,270,272–274,277,282,283,286,349] Others have relied predominantly on mesenchymal-like PDAC cell lines such as PANC-1, making it difficult to resolve EMT with fidelity.[269,270,272–277] Even when epithelial cell lines or organoids were used, EMT was most often assessed qualitatively or indirectly (e.g., via monitoring invasion distances).[263,278] Furthermore, the ECM in such models is typically restricted to collagen I or Matrigel, overlooking stromal components such as HA, that is abundant in PDAC tissue since early stages of cancer development and known to modulate EMT signaling.

In this study, we used a modular PDAC-on-chip platform to dissect the contributions of ECM components and stromal signals to EMT in pancreatic cancer spheroids. By combining HPAF-II spheroids with controlled HA integration and stromal factors exposure from either pancreatic stellate cells or CAFs, we systematically evaluated how biochemical and cellular microenvironmental cues influence EMT in a physiologically relevant 3D context.

Our results revealed that not only HA presence is important but also its molecular properties, like its MW. Mid MW HA can induce EMT, particularly when cells are exposed at the single-cell stage, before the spheroid formation, which maximizes direct interactions with HA molecules. This is evidenced by increased CD44 expression and modest shifts in Vimentin-positive and E-cadherin-negative cell numbers per cancer spheroid. However, unlike CD44 expression, the EMT phenotype shift effect was transient when HA supplementation was limited to spheroid formation, underscoring that sustained ECM-

derived cues are necessary to maintain mesenchymal features in a highly epithelial PDAC model. Although the precise molecular mechanisms of CD44 function remain incompletely understood, its strong association with cancer invasion and metastasis has recently made it a clinical target. Accordingly, HA and CD44 are under active investigation in both preclinical and clinical contexts, underscoring their dual role in shaping PDAC EMT through ECM remodeling and direct receptor-mediated signaling.[142,360] Importantly, these observations mirror what happens in the *in vivo* situation, where HA is continuously synthesized and degraded by both tumor and stromal cells, creating a dynamic turnover that shapes local signaling rather than a static HA reservoir.[111] These findings also extend previous reports by highlighting that HA molecular weight, integration strategy, and exposure timing critically modulate EMT dynamics in a 3D microenvironment. Notably, they also align with the ongoing debate on HA's dual role, as low MW fragments are frequently described as tumor-promoting, while high MW HA has in some contexts been associated with tumor-restrictive effects, though contradictory reports highlight that this dichotomy remains unresolved in PDAC.[111,350,364,365]

In contrast to HA alone, stromal CM robustly induced EMT, with both stellate cells- and CAF-derived CM triggering significant Vimentin upregulation and E-cadherin downregulation already by day 3 of culture. This suggests that, within our model, stromal cues from two different cell sources converge to common pathways driving EMT. In addition, early, transient exposure to CM was sufficient to oppose the intrinsic increase in epithelial characteristics of cancer spheroids over time for both CAFs and stellate cells, demonstrating that stromal paracrine signals can induce a partial EMT state even in the absence of continuous stimulation. Moreover, our results suggest the possibility of a competitive interaction between spheroid epithelial features and EMT induction over time under both HA and stromal cell sues incorporation. This is supported by the observation of marker expression that remained elevated but stable between D3 and D6 under sustained integration of these factors, whereas controls exhibited increased epithelial traits over the same period of time. Such findings are consistent with some of the prior studies on this cell line that reported seemingly conflicting phenotypic changes, potentially reflecting the simultaneous emergence of opposing phenotypes.[366,367] In comparison, direct co-culture with dispersed single stromal cells had negligible effect, likely due to low stromal-to-tumor ratios in the microfluidic chip, highlighting that soluble factor concentration and distribution are critical determinants of effective EMT induction.

The integration of HA and CM in this model offers a unique opportunity to

approximate *in vivo*-like tumor-stroma interactions. In PDAC tumors, ECM components and stromal fibroblasts act synergistically to shape the tumor microenvironment and maintain partial or reversible EMT states that drive tumor dissemination. Our findings suggest that combining HA with stromal CM in PDAC-on-chip models could more faithfully recapitulate this complexity, providing physiologically relevant platform for the study of tumor-stroma crosstalk and therapeutic development.

Despite these advances, several limitations should be acknowledged. Firstly, this study was conducted using a single epithelial PDAC cell line, which, while providing reproducibility and a clear baseline for EMT induction, may not fully capture the heterogeneity of patient tumors. Incorporating additional cell lines or patient-derived organoids would be beneficial to enhance translational relevance. Secondly, although HA (along with collagen I) are one of the key players in PDAC aggressiveness, other ECM components such as various collagens, laminin, or fibronectin, as well as matrix stiffness, are known modulators of PDAC cell plasticity and could be incorporated into the model to increase its physiological fidelity. Lastly, the current platform lacks immune and endothelial compartments, which may further influence EMT and stromal interactions, as observed *in vivo*.[168,351]

Future directions should focus on combining HA and stromal CM within a single system to explore potential synergistic effects on EMT induction and maintenance. Additional refinements should include incorporation of other ECM components and stromal subtypes, as well as implementation of dynamic gradients of soluble factors to better mimic the *in vivo* TME. While such enhancements would enhance physiological relevance of *in vitro* models, it remains equally important to preserve the ability to dissect individual contributions in a controlled manner. This stepwise integration of complexity, exemplified by the modular approach taken in this study, represents a key advantage of PDAC-on-chip platforms.

In conclusion, our study identifies some of the key microenvironmental components that should be incorporated into PDAC-on-chip systems to faithfully reproduce *in vivo*-relevant EMT dynamics. We demonstrated that stromal-derived soluble factors act as potent inducers of EMT in PDAC spheroids, while hyaluronan contributes to modulating this process, particularly when cells encounter it at the single-cell stage and under sustained exposure. By systematically dissecting these influences, our work highlights the necessity of integrating both matrix and paracrine stromal cues into future PDAC-on-chip models. Such an approach not only enhances physiological relevance but also preserves the mechanistic

resolutions required to disentangle the specific drivers of tumor cell plasticity.

IV. EXPERIMENTAL PROCEDURES

Cell lines & culture

Human pancreatic cancer cell lines HPAF-II (ATCC, CRL-1997TM), BxPC-3 (ATCC, CRL-1687), Capan-1 (ATCC, HTB-79), Capan-2 (ATCC, HTB-80), PANC-1 (ATCC, CRL-1469) were used. For stromal cell component, primary human pancreatic stellate cells (HPaSteC, ScienCell, 3830-SC) and human pancreatic adenocarcinoma cancer-associated fibroblasts (P-CAF, Vitro Biopharma, CAF08) were used. Cells were continuously cultured in 2D in T75 flasks in a humidified incubator at 37°C, 5% CO2 with the appropriate media: EMEM media (ATCC, 30-2003 TM) supplemented with 1% of penicillin-streptomycin (P/S) (Gibco 15140-122), and 10% fetal bovine serum (FBS) (Gibco 10270-106) for HPAF-II cells, high glucose DMEM medium (Gibco 61965-026, GlutaMAX™) supplemented with 1% of P/S and 10% FBS for PANC-1, RPMI 1640 (Gibco 11875-093) supplemented with 1% of P/S and 10% FBS for BxPC-3, Iscove's Modified Dulbecco's Medium (IMDM, ATCC, 30-2005) supplemented with 1% of P/S and 20% FBS for Capan-1, McCoy's 5a Medium Modified (ATCC, 30-2007) supplemented with 1% of P/S and 10% FBS for Capan-2, high glucose DMEM media with stellate cell growth supplement (SteCGS, Cat. #5352), 1% P/S, 10% FBS for HPaSteC, and pancreatic stellate CAFs maintenance media (MSC-GRO™, PC00B5) for P-CAF cells. Culture flasks for HPaSteC were pre-coated with 0.15% poly-lysine in sterile Milli-Q water. Each passage took place at 80-90% confluence level and proceeded from passage 2 to 15.

Conditioned media (CM)

Conditioned media (CM) was collected from confluent stromal cell cultures (HPaSteC or P-CAFs) maintained in T75 flasks. Once cells reached 80-95% confluency, culture media was left in contact with the cells for 48 h before collection. The supernatant was harvested and passed through a 0.22 µm filter. CM was then mixed with HPAF-II culture media at a 2:1 ratio (CM:HPAF-II media) prior to use. For on-chip experiments, media was refreshed daily until fixation (D3 or D6), using either freshly collected CM or CM obtained the day before.

Cancer cell spheroid formation

Cancer spheroids were generated by cell aggregation in non-adhesive agarose microwells. Briefly, a 1% agarose solution was prepared and heated until fully dissolved. Microfabricated molds (200 µm diameter) were used to stamp the agarose and produce uniform-sized microwells (~ 2000 microwells/well) in 6-well plates, as described previously.[368] After polymerization at 4°C, microwells were sterilized with UV light for 45 min and stored in PBS at 4°C for up to one week. Before seeding, wells were pre-humidified with

culture medium. For spheroid formation, 1 mL of cell suspension (2.5 x 10^5 cell/mL) was added to each well; after 1 h, an additional 1 mL of media was added. Where indicated, hyaluronic acid (HA) (1 mg/mL, low molecular weight: 150–300 kDa (ref 750044); mid: 750–1000 kDa (ref 53163); high: 1750–2000 kDa (ref 02737), sodium hyaluronate from Streptococcus equi, Sigma-Aldrich) or conditioned media (CM) was incorporated into the culture medium during cell seeding. After 24 h, spheroids were recovered by flushing media.

Spheroid seeding on chip

Commercially available microfluidic devices suitable for 3D cell culture (DAX-1, idenTx 3, AIM Biotech, Singapore) were used, Individual chips were separated by cutting plates of three devices and sterilized under UV light for 30 min prior to use.

To recreate PDAC microenvironment, HPAF-II spheroids were embedded in the central chamber within collagen type I matrix, with or without stromal cells (HPaSteC or P-CAF) and with or without HA, depending on the experimental condition. The collagen mixture was prepared using high-concentration rat tail collagen type I (Corning, USA, 354249), combined with 10X PBS, 1 M NaOH, and Milli-Q water (HPAF-II culture medium when spheroids/HA were included), following the manufacturer's instructions. Final collagen concentration was 6 mg/mL with pH 6.5-7.5. For HA-containing conditions, hyaluronan was dissolved in HPAF-II media at 8 mg/mL and mixed with collagen I solution at a final mass ration of 1:3 (HA:collagen). For HA delivered in culture media, hyaluronan was dissolved in HPAF-II media at 1 mg/mL and refreshed daily.

Spheroids were formed as described above and collected by flushing from agarose microwells into a 2 mL Eppendorf tube, followed by centrifugation at 1000 rpm for 2 min to form a pellet. Each pellet contained spheroids from 2 microwells (~ 2000 spheroids/microwell), with spheroids composed of ~125 cells each. After accounting for processing losses, this corresponded to 10-30 spheroids per chip, or 1250-3750 cancer cells per chip. For co-culture conditions, stromal cells were harvested from culture flasks and mixed with the spheroid pellet at a final concentration of 250 000 cells/mL, yielding ~2500 cells per chip and an average cancer-to-stromal ration of 1:1.

The total collagen-cell mixture volume was 200 µL, with ~ 10 µL loaded per chip. All steps involving collagen handling were performed at 4°C to prevent premature polymerization. After seeding, gels were polymerized at 37°C and 5% CO_2 for 1 h. Chips were flipped every 5 min during the first 15 min of incubation to prevent spheroids

sedimentation and ensure uniform 3D distribution. Following polymerization, appropriate media was introduced through side channels, and chips were maintained under standard culture conditions (37°C, 5% CO_2) for subsequent experiments.

Alcian Blue staining

Alcian Blue staining was used to assess hyaluronan (HA) incorporation and retention in collagen I/HA matrices of varying molecular weights (low 150–300 kDa; mid 750–1000 kDa; high 1750–2000 kDa). Polymerized collagen I/HA gels (~ 50 µL) were cast in 24-well plates at HA mass fractions of 0%, 2.5%, 5%, 10%, 15%, 20%, and 25% (relative to total HA + collagen protein content). Matrices were analyzed at days 0, 1, 3 and 7. For time points beyond day 0, gels were maintained in HPAF-II culture medium under standard conditions (37 °C, 5% CO_2), with or without additional HA supplementation (1 mg/mL) depending on the experimental group.

A staining solution consisting of 10% Alcian Blue (Sigma Aldrich, 41116130) and 3% acetic acid (Fluka, purity ≥ 99.8%) in ultrapure water was prepared. Each gel was first washed with 500 µL of 3% acetic acid for ~ 10 min, followed by incubation overnight at RT with 500 µL of Alcian Blue solution. Excess dye was removed the following day by washing with 1mL of 3% acetic acid for 1 h, followed by two rinses in 1 mL ultrapure water: first for 1 h and then overnight, to minimize background staining.

Gels were imaged under standard lighting conditions using a smartphone camera. Staining intensity was quantified with ImageJ. For baseline comparisons, all conditions were normalized to the average intensity of HA-free (control) matrices at day 0. For experiments with HA-supplemented media, normalization was performed against the matched HA-free matrix cultured under the same media condition. Data were represented as boxplots, with each dot corresponding to the average intensity of one independent collagen mix (x2 technical replicates per condition).

LIVE/DEAD assay and immunofluorescence staining

Cell viability of spheroids in chips was assessed using the LIVE/DEAD™ Cell Imaging Kit (Invitrogen™, R37601), prepared according to the manufacturer's protocol. Samples were incubated with the staining solution for 30min at 37°C in 5% CO_2 and imaged using Leica DMi8 confocal microscope with a 40x water-immersion objective. Calcein Green was used to detect live cells and Texas Red for dead cells.

For immunofluorescence analysis, samples were fixed at three time points Day 0 (1 h after collagen polymerization), Day 3 and Day 6. Fixation was performed with 4%

paraformaldehyde (PFA) in PBA for 45 min at room temperature (RT), followed by PBS washes. Permeabilization was carried out using 0.1% Triton X-100 in PBS for 20min at RT. Samples were then blocked for 2.5 h at RT in 4% bovine serum albumin (BSA) with 0.1% Triton X-100 in PBS. Primary antibody incubation was performed overnight at RT with mouse anti-E-cadherin (1:200, Invitrogen SHE78-7), guinea pig anti-Vimentin (1:200, ProGen GP53), and rat anti-CD44 (1:200, Abcam ab119348) diluted in blocking buffer.

Following 3x1 h PBS washes, samples were incubated with secondary antibodies overnight at RT: Alexa Fluor 488-conjugated goat anti-mouse IgG (H+L) (1:500, ThermoFisher A11029), Alexa Fluor 647-conjugated donkey anti-guinea pig IgG (H+L) (1:500, ThermoFisher A21450), and Alexa Fluor 555-conjugated goat anti-rat IgG (H+L) (1:500, ThermoFisher A21434). DAPI (300 nM, Invitrogen D3571) was added at a 1:400 dilution during secondary incubation. Prior to imaging, three additional PBS washes of 1 h each were performed.

Imaging was conducted on a Leica DMi8 inverted confocal microscope (Leica Microsystems) with a 40x water immersion objective. Z-stacks were acquired at 2 µm intervals using bidirectional scanning and a line average of 3, with image resolution set to 1024 x 1024 pixels. For each condition, two chips (technical replicates) were images, with at least five spheroids imaged per chip. Excitation was sequentially performed with four lasers: 452 nm for DAPI (intensity 3.7%, detector gain 500%), 488 nm for Alexa Fluor 488 (intensity 1%, gain 100%), 552 nm for Alexa Fluor 555 (intensity 0.4%, gain 50%), and 638 nm for Alexa Fluor 647 (intensity 1%, gain 100%).

Image analysis & Quantification

Spheroid formation over time in 6-well plates were analyzed using a plate reader (Perkin-Elmer Ensight Multimode Plate Reader) in bright-field mode, with several images obtained/plane. Image analysis was performed using ImageJ and Python. Images were pre-processed by autofocus correction (maximum entropy method), cropping and exclusion of wells located at plate edges. Spheroid segmentation was performed by training Ilastik pixel classifier (probability threshold: 0.7), followed by morphological filtering to exclude outside-of-microwell objects, noise and artifacts. Watershed segmentation (BioVoxxel library) was applied to separate adjacent structures, and spheroids were further filtered based on size, shape (aspect ratio < 2), position within the field of view, and illumination quality. Only isolated spheroids within well-centered regions were retained for downstream analyses. Quantitative features including spheroid area, perimeter, circularity ($\frac{4 \cdot \pi \cdot Area}{Perimeter^2}$),

aspect ratio, Feret diameter, roundness ($\frac{4 \cdot Area}{\pi \cdot Feret\ d^2}$), and solidity ($\frac{Area}{Convex\ Area}$) were extracted with a custom Python code, along with intensity-based metrics such as mean spheroid grey value, variance, skewness, and kurtosis. Spheroid texture characteristics were then estimated through relative grey measure ($\frac{Spheroid\ mean}{Background\ mean}$) and Variance/Mean ($\frac{Mean\ variance}{Backgroudn\ mean}$) as an approximation for spheroid's density and heterogeneity respectively.

Immunofluorescence confocal z-stack images of spheroids were processed and analyzed manually to quantify marker expression. Image stacks were inspected plane by plane using ImageJ software, and individual cells were identified based on DAPI nuclear staining. Marker expression was evaluated by visual assessment of fluorescent intensity, following the adjustment in brightness & contrast of the image to reveal the over or under expressing cells from the bulk of the spheroid. For each spheroid, the number of cells positive for Vimentin, negative for E-cadherin, and positive for CD44 were recorded. Marker positivity or negativity was determined using consistent intensity thresholds across all image sets, established from negative controls and applied uniformly throughout the analysis. A minimum of 10 spheroids/experiment were analyzed with a minimum of 4 independent experiments performed per condition.

Data representation and statistical analysis

For graphical representation, violin plots were used with individual spheroids were plotted as dots and line representing the median. Data distributions were tested for normality and homogeneity using D'Agostino & Pearson and Shapiro-Wilk tests ($\alpha = 0.05$). As the data were partially non-normally distributed, nonparametric statistical tests were used. Comparisons across multiple groups were performed using Kruskal-Wallis tests, and pairwise comparisons with two factors were conducted using two-tailed Mann-Whitney tests ($\alpha = 0.05$). Statistical significance is indicated as *$p < 0.05$, **$p < 0.01$, ***$p < 0.001$, and ****$p < 0.0001$. All analyses and data visualization were performed using GraphPad Prism version 9 and each condition was tested in more than four independent experiments.

V. SUPPLEMENTARY INFORMATION

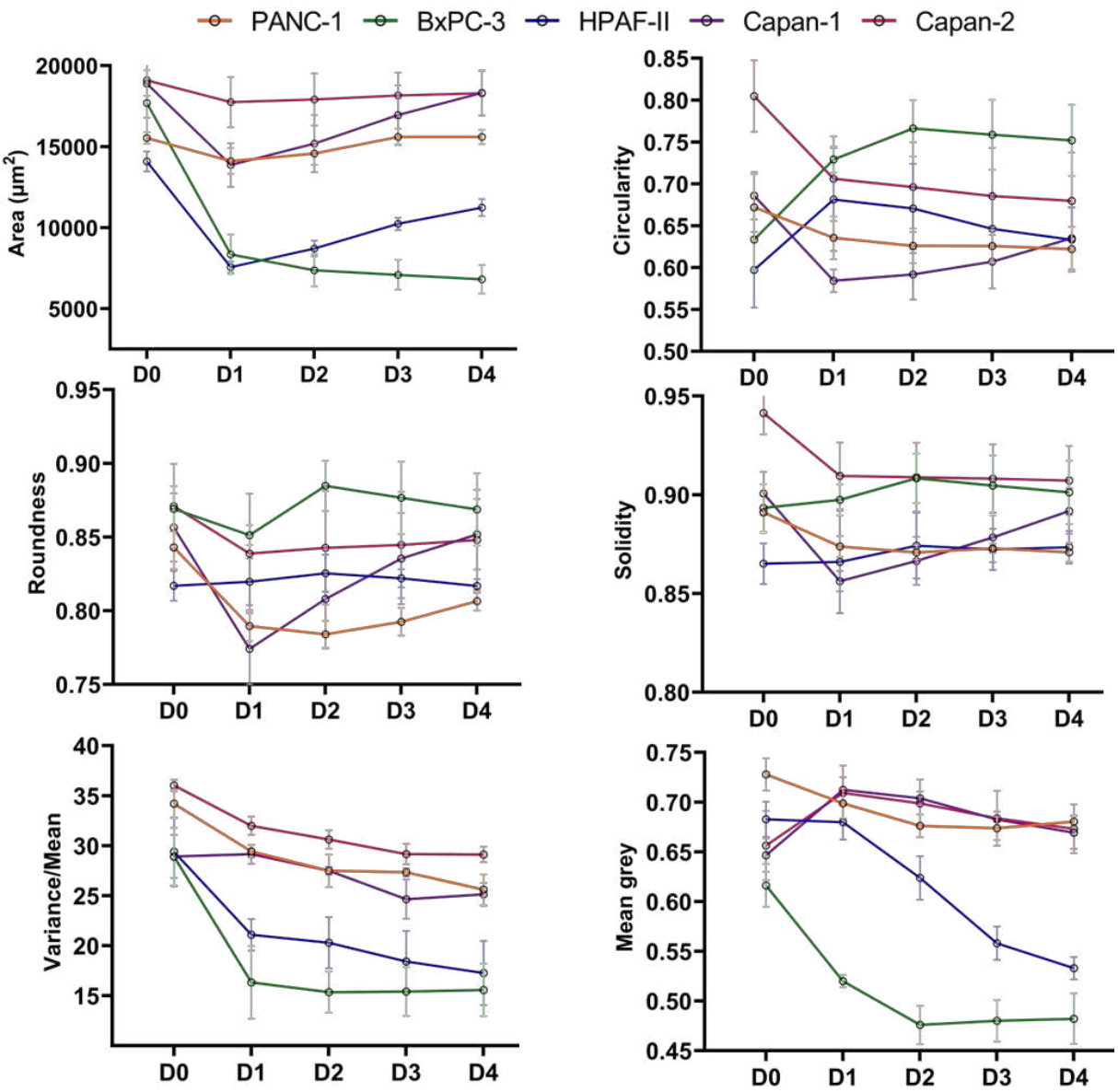


Figure 3.S1: **Comparative analysis of spheroid formation from five PDAC cell lines in agarose micromolded 6-well plates, 5x10^5 cell/well.** Characterization of spheroids (250 cells/microwell) through computation of area, circularity, roundness, solidity, variance/mean grey and relative grey values. (N≥3 for each cell line, n≥1000 spheroids).

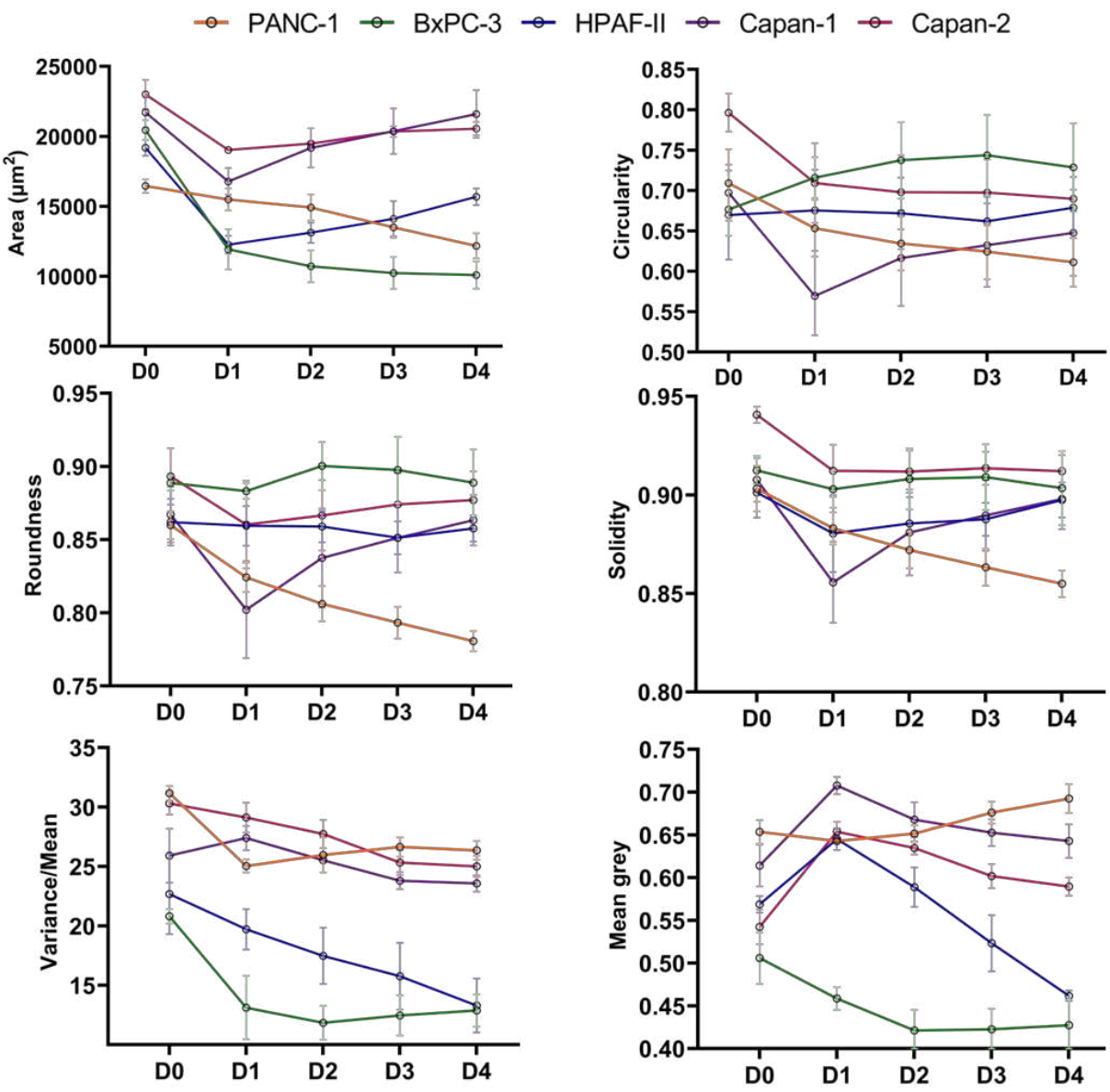


Figure 3.S2: **Comparative analysis of spheroid formation from five PDAC cell lines in agarose micromolded 6-well plates, 1x10⁶ cell/well.** Characterization of spheroids (500 cells/microwell) through computation of area, circularity, roundness, solidity, variance/mean grey and relative grey values. (N≥3 for each cell line, n≥1000 spheroids).

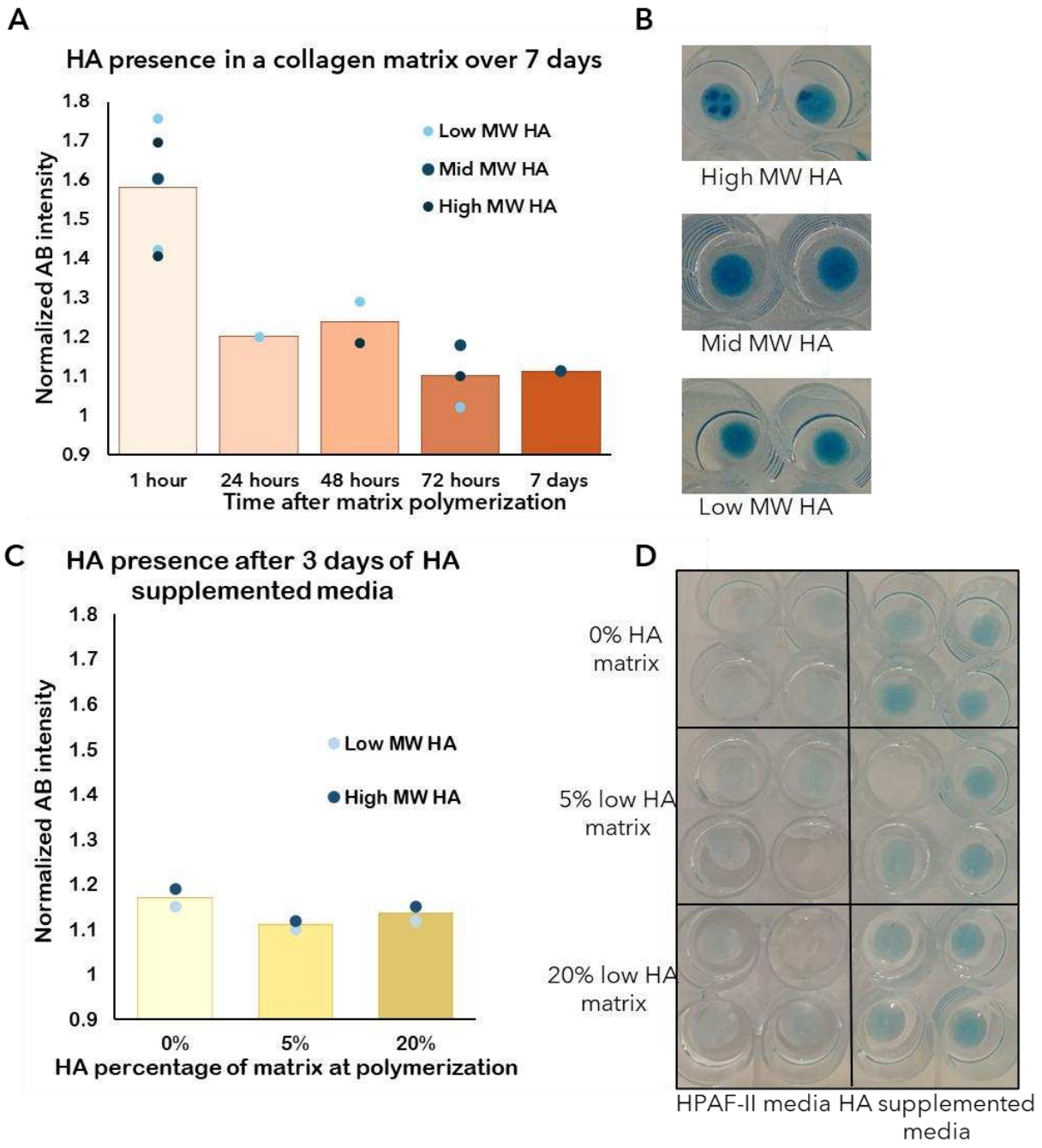


Figure 3.S3: **Alcian blue staining to quantify HA presence change in a collagen matrix over 7 days. A**. HA presence after 0, 1, 2, 3, and 7 days in a 25% HA collagen matrix. HA content was quantified via Alcian blue staining intensity, normalized to that of a collagen matrix devoid of HA (0% HA). **B**. Representative Alcian blue-stained images of 25% HA collagen matrices formulated using high, mid, or low MW HA, imaged at 1 hour post-polymerization. Two technical replicates per condition are shown. Increased Alcian blue intensity corresponds to elevated HA content, with darker blue regions indicating localized HA accumulation, particularly in matrices containing high MW HA. **C.** Quantification of HA content at 72 hours in 0%, 5%, or 20% HA collagen matrices, with daily supplementation of HA-enriched media. Alcian blue staining intensity was normalized to that of non-supplemented counterparts for each HA concentration. **D**. Representative image illustrating HA distribution in matrices supplemented with HA-containing media, used for intensity quantification shown in panel C. In panels A and C, each data point represents the mean staining intensity of two technical replicates derived from a single collagen preparation. The percentage of HA in the collagen matrices refers to the mass percentage of HA initially added to the collagen matrix.

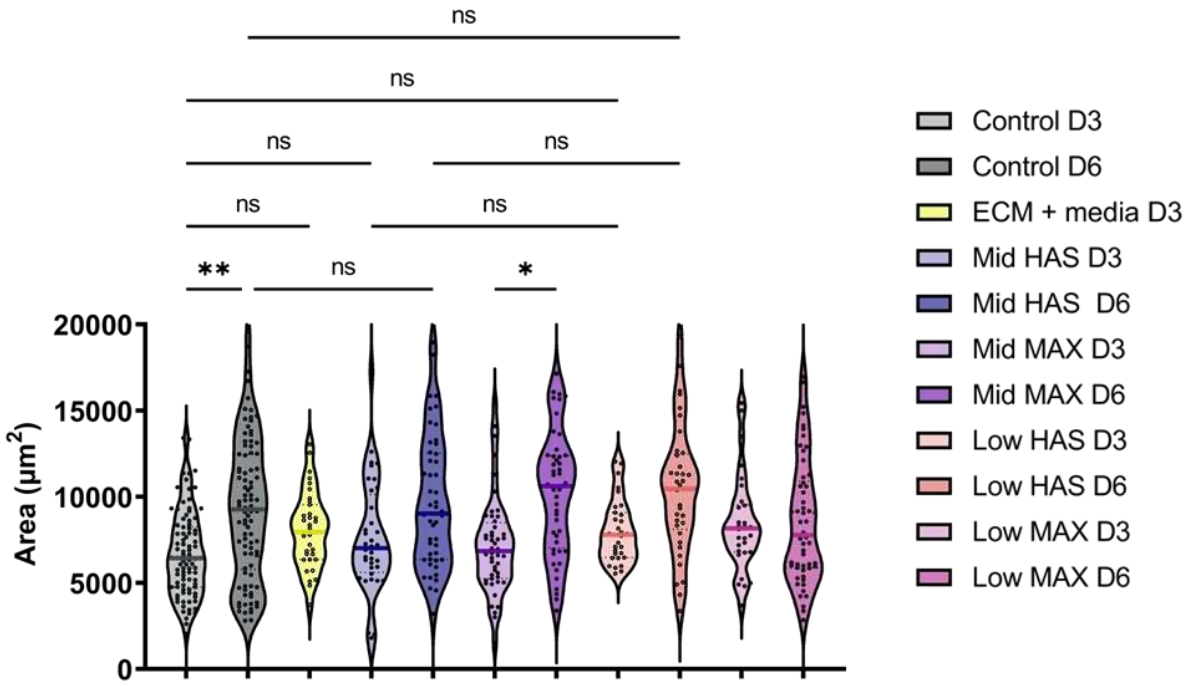


Figure 3.S4: **Evolution of spheroids' area in PDAC-on-chip.** Quantitative analysis of the spheroid 3D z-projected area as a function of time, HA molecular weight and incorporation method. Data are presented as violin plot including all experimental data points (>4 independent experiments for each condition, ≥10 spheroids per experiment). *p< 0,1; **p< 0,01; ***p< 0,001; ****p< 0,0001.

Challenges, limitations & future directions

In this section, I reflect on experimental approaches that did not yield expected outcomes, particularly immunofluorescence ***image processing*** pipeline, and explain how these were adapted during the course of the study. I also discuss ***additional analyses*** that could complement the present findings and outline ***directions for future work*** to further advance this line of research.

Image analysis & quantification

Initially, the key data of the study — fluorescent EMT marker expression — was analyzed with a custom-developed ImageJ and Python programming pipeline that included extensive, automated image processing to quantify fluorescence of 3D confocal images across conditions.

For this, the four fluorescence channels (DAPI, E-cadherin, Vimentin, CD44 (experiments with HA) or mCherry (nuclei of HPAF-II cells were transfected for experiments with stromal cells to differentiate between two cell types in co-culture) were first separated into individual z-stack files. Nuclear regions were identified by generating a mask from the DAPI channel, and the mean DAPI intensity was computed for each z-slice to be then used for marker normalization in z imaging direction due to signal attenuation in z direction of 3D confocal images. For protein-specific quantification, masks were generated for each channel (Vimentin, E-cadherin, CD44) to exclude background signal. Pixel intensities within each slice were normalized to the corresponding DAPI intensity. Final normalized protein intensity for each spheroid was obtained by averaging marker expression intensity across slices. In addition, for conditions with stromal cells present, to exclude the signal coming from the stromal cells, mCherry fluorescence (restricted to cancer spheroids) was used to create distinct masks to isolate the signal coming from the cancer spheroids.

However, this analytical methodology did not yield any significant results across conditions, including both studies with stromal cues as well as hyaluronan integration, as can be observed in Figure 3.SS1 with the example of stromal cues analysis that showed the strongest results following manual analysis in the paper draft presented above.

While a few of trends were still captured, such as increased E-cadherin intensity from D3 to D6 and its decrease in HPaSteC CM at D6, the majority of observations evident in the source were not captured with this analytical platform. Hence, we ultimately resorted to manual image analysis and quantification, which are presented in the main results of this chapter, to focus on discrete cells overexpressing the given marker rather average marker

expression within a spheroid. In the following section, we discuss potential reasons behind the failure of the described image analysis methodology.

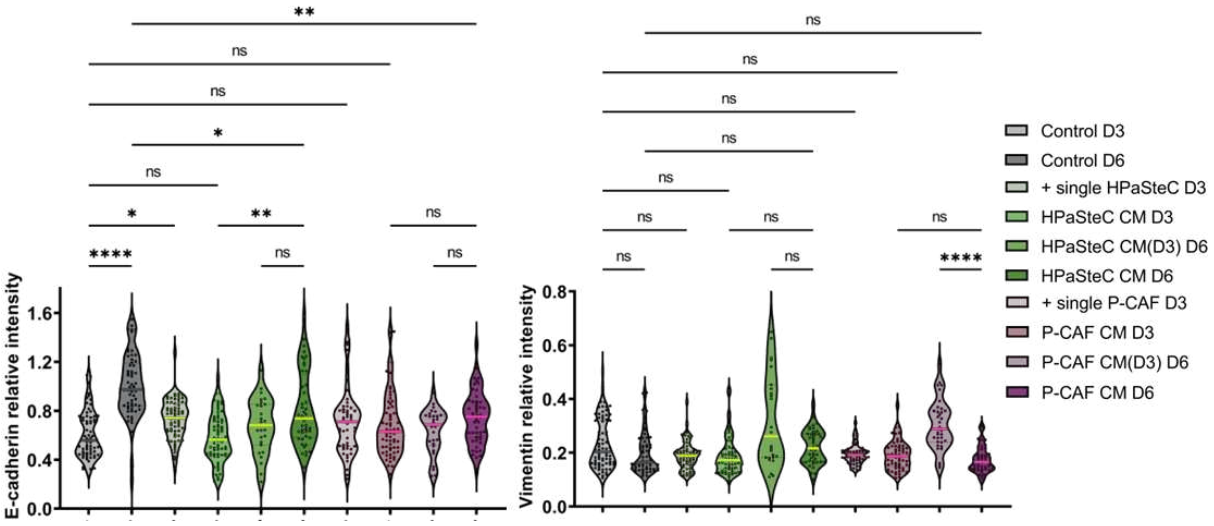


Figure 3.SS1: **Impact of CAF-derived stromal factors on EMT marker expression in PDAC-on-chip as a function of time and exposure method.** Automatized quantitative analysis of the relative E-cadherin and Vimentin fluorescent intensities across 3D confocal images as a function of time and CAF factors exposure method. Data are presented as violin plot including all experimental data points (>4 independent experiments for each condition, ≥10 spheroids per experiment). *p< 0,1; **p< 0,01; ***p< 0,001; ****p< 0,0001.

First of all, the effects induced via various conditions typically took place in several individual cells of the cancer spheroids rather than in the entirety of the cell aggregate, as could also be observed both qualitatively and quantitatively in the figures of the paper draft. Therefore, it can be supposed that due to bulk image analysis of 3D spheroids composed of at least 125 cells, where marker expression is calculated as an averaged value across the spheroid, individual cell expression changes might be obscured. At the same time, stricter thresholding to single out the activated cells could result in a loss of valuable signal, since protein expression changes as well as signal to noise ratio are not always the same not only between different experiments but also between the different technical replicates of the same experiment, and even spheroids within the same chip, while immunostaining and imaging conditions remain constant (Figure 3.SS2 A-B).

Marker-specific signal contribute to the bias in the automated image processing pipeline. Vimentin is a perinuclear protein, typically localized around the cells' nuclei. While the automated image analysis was focused on protein intensity levels, some conditions have presented higher levels of background noise without necessarily corresponding to the perinuclear cell's signal (Figure 3.SS2 B), thus yielding to higher intensity measurements and results bias. However, under different conditions this same intensity may correspond to the valid perinuclear Vimentin signal (Figure 3.SS2 A) and hence, cannot be effectively filtered

out.

Due to the nature of E-cadherin signal, it can also introduce significant bias into intensity-based analytical strategies. While only a few cells may almost completely lose E-cadherin expression within a cancer spheroid (Figure 3.SS2 C), a more common event is the redistribution of E-cadherin from the membrane to the cytoplasm, that is reported as an acknowledged marker of EMT.[369] In cases of complete E-cadherin cytoplasmic relocation this effect could be captured with intensity-assessing algorithm (since cytoplasmic E-cadherin is much less intense and blurrier, yielding lower overall intensity measurement). However, Figure 3.SS2 D illustrates what typically occurs: only a minority of cells show complete cytoplasmic E-cadherin, while most of cells display dual E-cadherin expression both with a more intense signal in the membrane and less intense, blurry cytoplasmic expression. Indeed, a competition between epithelial and mesenchymal phenotypes was observed in spheroids, where conditions presenting an EMT shift at D3 through cytoplasmic E-cadherin relocalization, by D6 presented both cytoplasmic E-cadherin and increased membrane signal, indicating that two opposing events might be happening at the same time. While this should on average still yield lower intensity values, uniform thresholding methods that include both membrane and cytoplasmic E-cadherin expression would lead to bias in the conditions where cells do not undergo EMT (such as control) and thus, do not express cytoplasmic E-cadherin, as inclusion of background cytoplasmic areas would subsequently lower the intensity measurements.

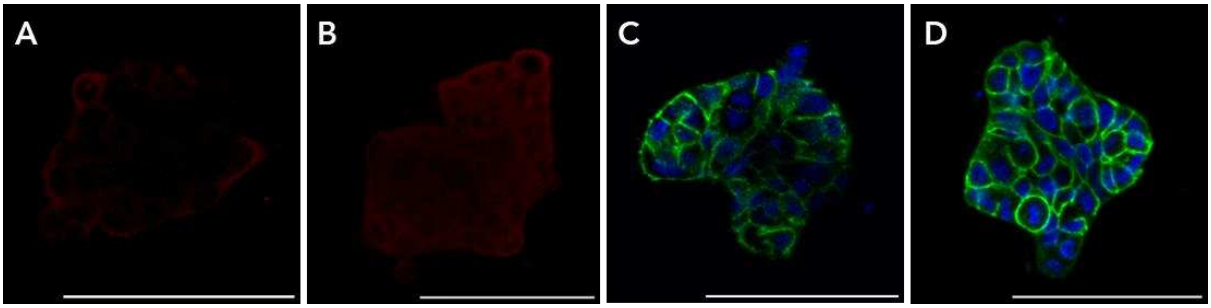


Figure 3.SS2: **Examples of E-cadherin and Vimentin markers imaging that may induce inconsistencies in automatized image processing algorithms. A.** Vimentin staining with average signal-to-noise ratio, where Vimentin-positive cells' intensity is significantly higher than that of the background spheroids fluorescence. **B.** Low signal-to-noise ratio Vimentin fluorescence image, where background fluorescence is as high as that of Vimentin-positive cells in other conditions. **C.** E-cadherin fluorescent image, with 2 budding cells without E-cadherin expression. **D.** Representative E-cadherin fluorescent image that includes few cells with complete internalization of E-cadherin, some cells fully positive for E-cadherin and some cells sharing both intense membrane E-cadherin signal and blurry internalized E-cadherin. Scale bar = 100 μm.

As a result, in order to address the aforementioned issues stemming from biological, diffusion and distribution variabilities as well as particular characteristics of EMT markers

expressions in 3D spheroid structures, more advanced image analysis strategies should be developed, that could potentially include differential segmentation techniques, more complex noise recognition methods and local intensity assessment. Alternatively, other immunostaining markers, imaging modalities or EMT analytical approaches could be explored, some of which will be addressed further; however, broader possibilities largely remain beyond the scope of this discussion.

Nevertheless, in an attempt to extract finer expression changes, we exploited other analytical readouts beyond average relative intensity measurements, particularly by evaluating potential co-localization of CD44 and E-cadherin expressions (for the study with HA) via two complementary analyses of pixel-wise correlation and pixel-wise overexpression (Figure 3.SS3). This approach leverages the co-localized membrane expression of these markers to assess the potential of their anti-correlation.

Following the imaging of HA-incorporated conditions, we observed some events of anti-correlation of E-cadherin and CD44 signals in the membranes of individual cells of the spheroid. Therefore, through correlation analysis, pixel intensities of normalized CD44 and E-cadherin signals were compared using the formula: $\left(2\,x\,\frac{Ecad}{255}-1\right)x\,\left(2\,x\,\frac{CD44}{255}-1\right)$, yielding values from –1 (strong anti-correlation) to +1 (strong correlation). Fractions of strongly correlated (>0.5) and anti-correlated (-0.5) pixels were computed relative to total pixel number (Figure 3.SS3 A-B). It is important to note that correlation and anti-correlation measurements are therefore not inverse measurements of one another. In addition, CD44 overexpression analysis was performed by generating difference images: subtracting intensity-normalized E-cadherin from CD44 images to identify the regions where CD44>E-cadherin and compute the CD44 overexpression ratio as the fraction of pixels where CD44 signal exceeded E-cadherin signal relative to the total count of pixels in both channels (Figure 3.SS3 C).

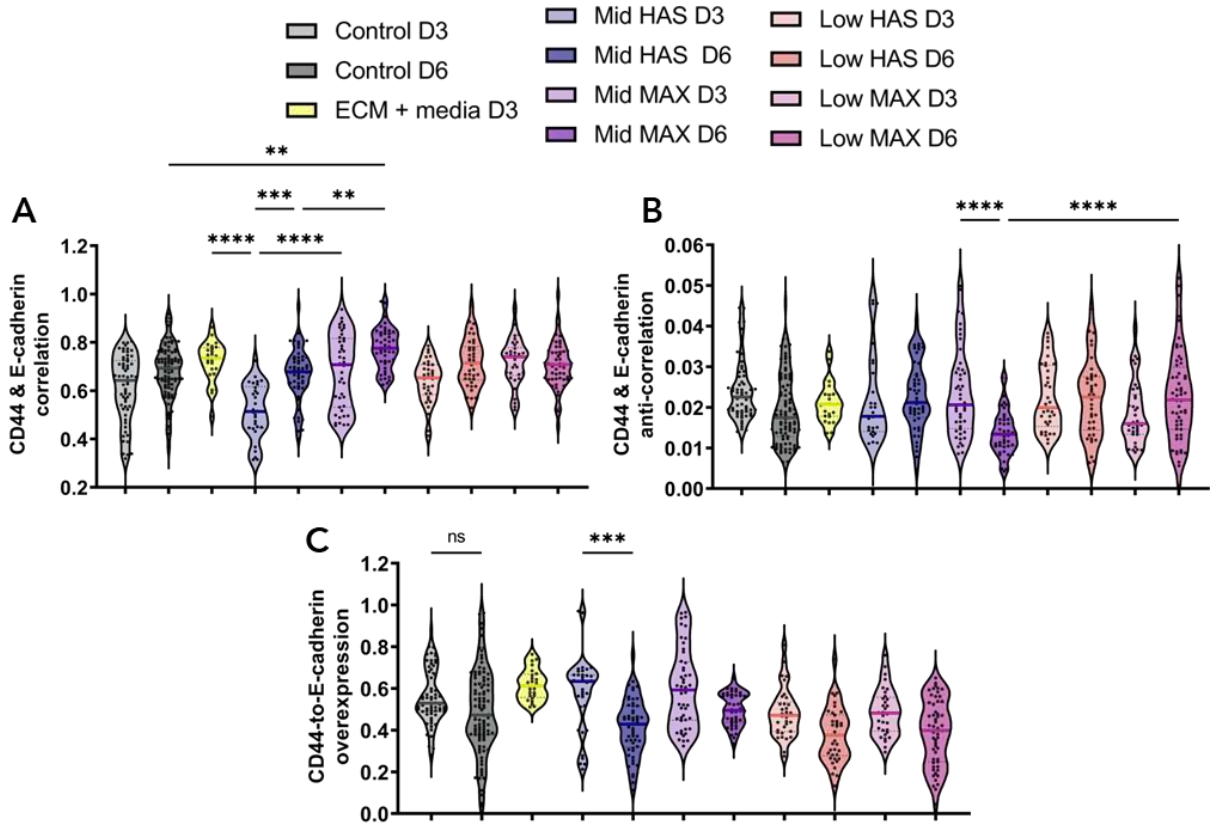


Figure 3.SS3: **Impact of hyaluronan on spheroid CD44 & E-cadherin marker correlation and CD44 overexpression in PDAC-on-chip as a function of time and exposure method.** Automatized quantitative analysis of CD44 vs E-cadherin pixel-wise correlation (**A**), anti-correlation (**B**) and CD44 pixel-wise overexpression as compared to E-cadherin (**C**). Data are presented as violin plot including all experimental data points (>4 independent experiments for each condition, ≥10 spheroids per experiment). *p< 0,1; **p< 0,01; ***p< 0,001; ****p< 0,0001. All other comparisons are non-significant.

As a result, while a few trends were consistent with the conclusions discussed in this chapter, such as decrease in E-cadherin and CD44 correlation at D3 of mid MW HAS condition, indicating potential loss of E-cadherin and gain of CD44 as well as increasing CD44 overexpression trends with mid MW HA at D3 condition, most results remained non-conclusive and statistically insignificant. The absence of pronounced trends even with more sensitive automatized image analysis tools, combined with the results presented in the paper draft suggests that the overall shifts in PDAC spheroids' phenotype were moderate under the conditions investigated. To further validate the conclusions presented in this chapter, additional analysis should be included.

Overall, it is important to acknowledge the limitations of large-scale image analyses that rely on averaging across big amounts of imaging data. In our model, EMT-associated changes appear to occur only in a subset of cells, which is consistent with the predominantly epithelial phenotype of the cell line and possibly also reflects the nature of EMT induction. While these approaches do reveal measurable effects, the extent to which we mimic *in vivo*

concentrations and exposure times remains uncertain, as is often the case in the field. Under such non-binary conditions, conventional automated image analyses, and even more refined computational methods, such as correlation/anti-correlation-based profiling, may fail to capture biologically relevant heterogeneity. This underscores the value of careful, detailed data observation and image inspection, and in some cases, the necessity to prioritize direct visualization of phenotypes over complex image analysis strategies to avoid overlooking subtle but meaningful cellular responses.

Additional analytical tools

The next step to validate and extend the findings would be to perform transcriptomic profiling (e.g., RNA sequencing) of PDAC spheroids exposed to HA and/or stromal CM (*currently ongoing*), to capture the breadth of EMT-related pathways and identify additional regulatory networks beyond E-cadherin and Vimentin. This work has been initiated during the last period, and the samples are soon to be sent for sequencing.

Complementary analysis of the stromal cell-specific secretome through proteomics or cytokine array will be performed next to pinpoint the soluble mediators responsible for driving EMT in this system, such as TGF-β, IL-6, or CXCL12.

Quantitative monitoring of HA concentration and turnover within the matrix and media as well as mechanical properties of the ECM over time would be critical to better correlate HA availability with cellular responses. In parallel, validation of protein-level changes in EMT regulators (e.g., Snail, Slug, ZEB1) by immunostaining or targeted mass spectrometry would provide additional molecular confirmation of EMT induction. Together, these approaches would strengthen the mechanistic understanding of stromal-tumor-matrix interactions in PDAC-on-chip models.

Current model considerations

The choice of HPAF-II as an epithelial PDAC model in this study revealed important limitations, as these cells appeared relatively resistant to undergoing a robust EMT response. This resistance may, at least in part, be attributable to their metastatic origin and strong epithelial differentiation state, which could constrain epithelial plasticity. However, identifying alternative epithelial PDAC models remains challenging. Capan-1 and Capan-2, while harboring key mutations, are among the most highly differentiated PDAC cell lines, and are therefore unlikely to undergo substantial EMT. BxPC-3 readily forms spheroids and exhibits intermediate differentiation but lack the canonical KRAS mutation that drives more than 90% of PDAC cases, limiting its translational relevance. In contrast, widely used cell

lines such as PANC-1, MIA PaCa-2, or AsPC-1 are already quasi-mesenchymal or mesenchymal, and thus unsuitable for modeling EMT induction. This limitation underscores the need to consider more complex systems for this study, such as patient-derived organoids or primary tumor samples to better capture EMT dynamics. Such models retain the mutational, phenotypic, and architectural complexity of the original tumors, offering a more physiologically relevant platform. However, they often come with high inter-patient variability and limited scalability, compared to cell lines among the others and may therefore pose challenges for systematic analyses. Incorporating such models into PDAC-on-chip systems would therefore come with clear advantages in biological relevance, but also with trade-offs in standardization and reproducibility. In this regard, we have initiated a collaboration with the team of clinical researcher, Cindy Neuzillet, to incorporate patient-derived PDAC samples on-chip, yielding first encouraging results and highlighting a promising direction for future studies, extending findings presented here.

Future directions

Building upon the findings, challenges and limitations presented in this chapter, several future directions emerge to refine the PDAC-on-chip platform and to expand its application to novel treatment testing, in particular nanoparticle-mediated photothermia (NP-PTT).

One of the first steps to further advance the PDAC-on-chip platform will be to integrate hyaluronic acid (HA) with the stromal cues in the same system. While these factors have been explored separately, their combined influence more faithfully reflects the *in vivo* situation, where ECM composition and stromal signaling jointly orchestrate EMT and therapy resistance. By varying HA molecular weight, concentration, exposure time, and delivery mode in conjunction with stromal conditioned media and/or stromal cells, it will be possible to capture synergistic or antagonistic effects that remain obscured in single-factor experiments. To ensure that observed phenotypes can be mechanistically interpreted, complementary assays will be required to monitor HA turnover and distribution within the matrix, as we as fine cell molecular processes, thereby linking microenvironmental changes with cellular outcomes.

Another possible avenue involves reinforcing direct cancer-CAF interactions. Our current findings suggest that dispersed CAFs in co-culture are insufficient to induce robust EMT, likely because their concentration and proximity to cancer cells remain too low. Increasing CAF density within spheroids, or retaining them in close association with cancer aggregates, could enhance contact-drive signaling and better capture mechanical

remodeling effects. In that regard, we have tested hybrid spheroid formation by seeding a mixture of cancer cells and stromal cells (HPAF-II:HPaSteC 1:5) and assessing their EMT marker expression over time (Figure 3.SS4). HPAF-II cells used were stably transfected for nuclear mCherry expression for their easier differentiation from the stromal cells. As a result, we observed that initially, 24h after seeding, the HPaSteC cells were successfully integrated into the spheroid, as observed by solely DAPI nuclear signal (no HPAF-associated mCherry) and their strong Vimentin expression, characteristic of fibroblast-like cells (Figure 3.SS4 D1). However, not only was their location primarily in the center of the spheroid rather than at the periphery, with time we observed their gradual escape from the spheroid and domination of cancer cells. Indeed, at D4 to D8 only few HPaSteC cells were present, and the spheroid appeared to be dominated by the cancer cells, as observed by a prevailing overlap of DAPI and mCherry signals as well as strong E-cadherin expression (Figure 3.SS4 D4-D8). To revisit this strategy in the future, stepwise coating approach could be considered, whereby stromal cells are seeded in successive rounds onto preformed cancer spheroids and stabilized with thin matrix layers to encourage self-organization around the cancer core.

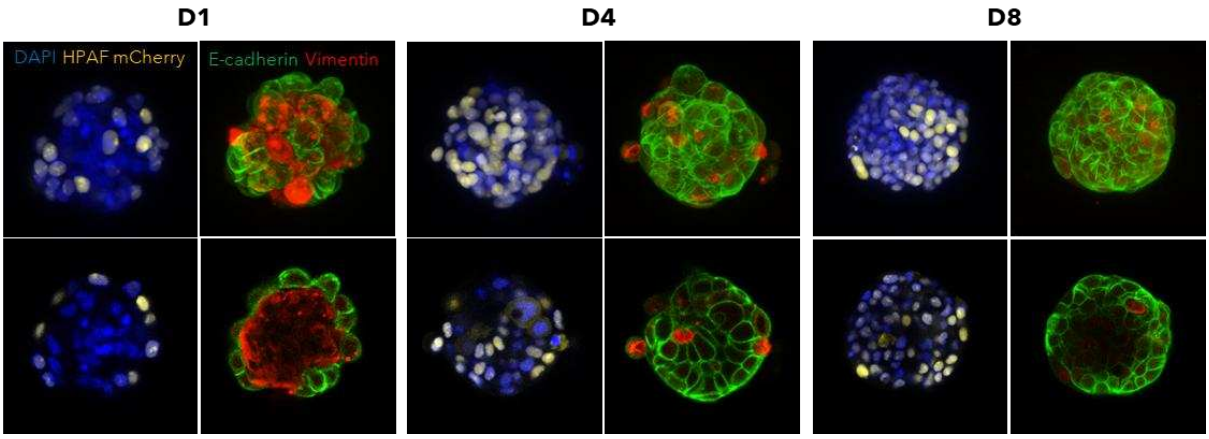


Figure 3.SS4: **Hybrid spheroid (HPAF:HPaSteC 1:5) monitoring for EMT markers over time.** Spheroids formed in agarose microwells monitored at D1-D4-D8 post seeding through immunostaining for E-cadherin (green) and Vimentin (red) as well as fluorescent for DAPI (blue) and nuclear mCherry (HPAF-II cells only, yellow) and imaged with confocal microscope. Top panel: 3D image z-projection, standard deviation method. Bottom panel: representative slice (2D) of the 3D image.

Another promising avenue could lie in the chip redesign, where concentric geometries could be exploited to spatially confine CAFs in annular chambers around central spheroids. Such an architecture not only maximizes the surface of direct cancer-stroma contact but may also leverage the intrinsic contractility of CAFs to compact the surrounding matrix, thereby increasing their effective concentration immediately adjacent to tumor cells. These developments are currently being pursued by Juliette Jin (1st-year PhD) in the team,

and the first experiments using HPAF-II and CAFs seem very promising. These refinements would substantially increase the model's ability to recapitulate CAF-driven EMT and matrix remodeling.

In parallel, NP-PTT should be systematically tested across progressive steps of model complexification. Starting from simple spheroid mono-cultures and gradually incorporating HA, stromal cell conditioned media, stromal cell co-culture, and ultimately multicellular constructs, this approach will provide a unique opportunity to map how each element of the TME alters NP distribution, heat dissipation, and biological responses. Such a stepwise approach is particularly well suited for the PDAC-on-chip, where microenvironmental conditions can be finely tuned and monitored in real time. Beyond spheroid viability and EMT marker expression, more granular readouts should be incorporated, including matrix denaturation dynamics, NP localization, and stromal cell survival or activation.

Our preliminary NP-PTT experiments suggest intriguing, yet incompletely understood, effects of stromal cells on heat dissipation. Specifically, HPAF-generated spheroids co-cultured with single stromal cells in collagen I (6 mg/mL) on chip reached higher bulk temperatures under identical NP and irradiation conditions compared to cancer spheroid-only controls. This could be driven by increased NP retention or aggregation within stromal cells or reduced convective cooling due to CAF-mediated compaction of the matrix. Clarifying these mechanisms will require precise quantification of NP distribution and local thermal properties. While this could implicate higher NP-PTT efficacy in stroma-rich contexts, this effect must be balanced against the possibility of protecting residual stromal cells that survive treatment.

This leads directly to our observation that cancer spheroids and CAFs display differential sensitivity to NP-induced heating. While cancer spheroids exhibited widespread death at temperatures above 42°C heating (Figure 3.SS5 B-D), CAFs remained visibly viable even at temperatures up to 45°C (Figure 3.SS5 D). Such resistance may derive from robust stress response mechanisms of fibroblasts, including upregulation of heat shock proteins and antioxidant defenses, or differences in NP uptake. From a therapeutic perspective, selective killing of cancer cells while sparing CAFs could be a double-edged sword. On the one hand, surviving CAFs may maintain structural barriers and secrete pro-tumorigenic factors that promote recurrence. On the other hand, preservation of CAF subtypes with tumor-restraining properties could contribute to improved long-term outcomes. Further work is therefore required to dissect the functional consequences of differential survival, including characterization of stress responses, secretome changes, and invasive capacity of

surviving CAFs after NP-PTT.

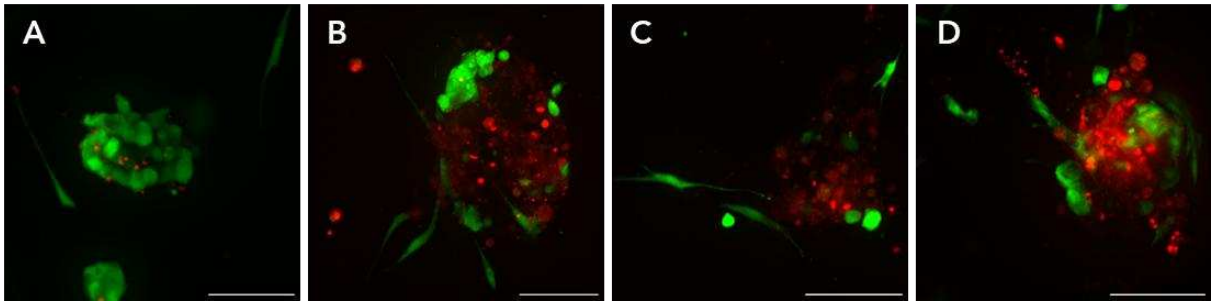


Figure 3.SS5: Viability of PDAC spheroids co-cultured with single CAFs in collagen on chip 24h following NP-PTT exposure. Representative confocal microscopy images (Z projection, SD type) control (**A**), 42°C (**B**), 43-44°C (**C**) and 45°C (**D**); live/dead (Calcein Green/Texas Red) viability assay. Scale bar = 100µm.

Future platform iterations should incorporate high-resolution readouts to more precisely link NP-PTT with biological outcomes. Local thermometry will enable precise mapping of thermal exposures, NP quantification will clarify effective intratumoral doses, and live imaging with apoptosis or ROS reporters, combined with ECM mechanical characterization, will provide dynamics views of tumor-stroma remodeling. Molecular and secretome profiling — including RNA sequencing, proteomics, and cytokine arrays — will complement this data and uncover pathways driving EMT, therapy resistance, or stromal activation, guiding potential therapeutic combinations.

Model complexity should also be expanded to include stromal heterogeneity and immune components. Distinct CAF subtypes and immune cells such as macrophages or T cells may either amplify or mitigate NP-PTT outcomes, depending on their phenotype. Their stepwise incorporation will allow assessment of NP-PTT both as a tumor-debulking strategy and as a modulator of stromal and immune responses.

Collectively, these efforts would advance the PDAC-on-chip platform from a proof-of-concept model toward a versatile and translationally relevant tool, bridging mechanistic understanding with therapeutic optimization.

GENERAL CONCLUSION

This thesis was set out to bridge two complementary but interconnected streams in PDAC research: (i) the development of physiologically relevant, controllable *in vitro* models, and (ii) mechanistic evaluation and optimization of nanoparticle-mediated photothermal therapy (NP-PTT) in the context of the tumor microenvironment. Across three integrated chapters — a comprehensive bibliographical review and rationale (Chapter 1), a proof-of-concept study applying magnetite NP-PTT in a PDAC-on-chip (Chapter 2), and a systematic model complexification study probing stromal and matrix drivers of EMT (Chapter 3) — the work delivered methodological advances, new experimental data, and practical recommendations to improve translational relevance for both PDAC-on-chip systems and nano-mediated therapeutic strategies.

The first chapter established the clinical and biological rationale for this work. By synthesizing current understanding of PDAC pathophysiology — including desmoplasia, stromal heterogeneity, HA enrichment, CAF diversity, and EMT-associated therapy resistance — and critically examining existing preclinical models, it became clear that a gap remains between highly controlled *in vitro* approaches and the need to capture essential microenvironmental drivers of PDAC progression. This motivated the central hypothesis of the thesis: combining advanced PDAC-on-chip models with NP-PTT would allow mechanistic, high-resolution interrogation of both tumor and stromal responses, thereby accelerating rational therapy design.

Building on this foundation, Chapter 2 presented a peer-reviewed study that demonstrated the integration of magnetite nanoparticles for PTT within a PDAC-on-chip platform. This work showed that localized NP-PTT induces targeted cytotoxicity while simultaneously remodeling the surrounding ECM. Importantly, it identified thermal thresholds for collagen denaturation and for incomplete but biologically relevant levels of cancer cell killing, underscoring the dual action of NP-PTT on both tumor cells and their microenvironment. At the same time, the study revealed several translational challenges, notably the difficulty in accurately quantifying effective NP dose due to complex matrix and cell diffusion phenomenon and aggregation, and variability in ECM organization. These findings not only provided proof-of-concept but also highlighted the need for more refined model systems capable of disentangling microenvironmental response to treatment.

To address part of these challenges, Chapter 3 extended the platform through stepwise introduction of stromal complexity, focusing on how hyaluronic acid (HA) and

stromal fibroblasts regulate EMT. By systematically incorporating HA of different molecular weights and delivery strategies, and by comparing the effects of pancreatic stellate cells and primary CAFs, either delivered directly or via conditioned media, this study showed that stromal factors exert a powerful influence on EMT marker expression. Mid-molecular weight HA was found to upregulate CD44 and sustain EMT-associated phenotypes when integrated early in the system and under maintained exposure, while conditioned media from both stromal sources induced rapid and robust EMT signatures. Interestingly, these effects were transient or sustained depending on the stromal source and exposure time, providing insight into the plasticity of tumor-stroma interactions. Beyond these biological findings, the study also underscored both methodological and model-related challenges, pointing to the need for more advanced single-cell and spatial analysis tools in 3D microfluidic systems as well as careful model interpretation.

Taken together, this work illustrates how PDAC-on-chip models can be strategically expanded from simplified tumor spheroid cultures to more complex and clinically relevant systems that capture essential stromal influences, while also documenting the practical tradeoffs to be considered — between model fidelity and experimental tractability, between bulk readouts and the need for single-cell resolution, and between proof-of-concept NP-PTT efficacy and clinical translatability. Within this framework, this thesis makes three main contributions: (i) it provides experimental evidence that NP-PTT exerts dual actions on both cancer cells and their microenvironment, establishing a physiologically relevant foundation for optimizing treatment strategies; (ii) it develops a refined toolkit for probing stromal drivers of EMT, including HA incorporation protocols, stromal conditioned media paradigms, and rationale for cell model selection, thereby offering methods transferable to broader research contexts; (iii) and it identifies key analytical blind spots while proposing clear methodological advances that will be essential to fully capture tumor-stroma-therapy interactions and guide future refinements.

In conclusion, this thesis highlights the potential of organ-on-chip technologies as powerful platforms to unravel interactions between tumor cells, stromal drivers, and nanomedicine-based therapies. It discusses both current possibilities and technical limitations while outlining a roadmap for their resolution. Looking forward, integrating patient-derived samples, immune components, and spatially resolved multiomic readouts into systematically NP-PTT-tested PDAC-on-chip would generate more predictive data to guide mechanism-aware strategies against one of the most lethal and treatment-refractory cancers.

REFERENCES

(1) International Agency for Research on Cancer. *GLOBOCAN 2022: Estimated Cancer Incidence, Mortality and Prevalence Worldwide*; World Health Organization, 2022. https://gco.iarc.fr/today (accessed 2025-08-20).
(2) Cai, J.; Chen, H.; Lu, M.; Zhang, Y.; Lu, B.; You, L.; Zhang, T.; Dai, M.; Zhao, Y. Advances in the Epidemiology of Pancreatic Cancer: Trends, Risk Factors, Screening, and Prognosis. *Cancer Lett.* **2021**, *520*, 1–11.
(3) Zhang, L.; Sanagapalli, S.; Stoita, A. Challenges in Diagnosis of Pancreatic Cancer. *World J. Gastroenterol.* **2018**, *24* (19), 2047–2047.
(4) American Cancer Society. Pancreatic Cancer Early Detection, Diagnosis, and Staging. **2024**.
(5) Heller, M.; Mann, D. A.; Katona, B. W. Current Approaches of Pancreatic Cancer Surveillance in High-Risk Individuals. *J. Gastrointest. Cancer* **2025**, *56* (1), 1–16.
(6) Blackford, A. L.; Canto, M. I.; Dbouk, M.; Hruban, R. H.; Katona, B. W.; Chak, A.; Brand, R. E.; Syngal, S.; Farrell, J.; Kastrinos, F. Pancreatic Cancer Surveillance and Survival of High-Risk Individuals. *JAMA Oncol.* **2024**, *10* (8), 1087–1096.
(7) Leung, P. S.; Leung, P. S. Overview of the Pancreas. *Renin-Angiotensin Syst. Curr. Res. Prog. Pancreas RAS Pancreas* **2010**, 3–12.
(8) Marstrand-Daucé, L.; Lorenzo, D.; Chassac, A.; Nicole, P.; Couvelard, A.; Haumaitre, C. Acinar-to-Ductal Metaplasia (ADM): On the Road to Pancreatic Intraepithelial Neoplasia (PanIN) and Pancreatic Cancer. *Int. J. Mol. Sci.* **2023**, *24* (12), 9946–9946.
(9) Pian, L.; Song, M.; Wang, T.; Qi, L.; Peng, T.; Xie, K. Identification and Analysis of Pancreatic Intraepithelial Neoplasia: Opportunities and Challenges. *Front. Endocrinol.* **2025**, *15*, 1401829–1401829.
(10) Kamisawa, T.; Wood, L. D.; Itoi, T.; Takaori, K. Pancreatic Cancer. *The Lancet* **2016**, *388* (10039), 73–85.
(11) Bailey, P.; Chang, D. K.; Nones, K.; Johns, A. L.; Patch, A.-M.; Gingras, M.-C.; Miller, D. K.; Christ, A. N.; Bruxner, T. J.; Quinn, M. C. Genomic Analyses Identify Molecular Subtypes of Pancreatic Cancer. *Nature* **2016**, *531* (7592), 47–52.
(12) Torres, C.; Grippo, P. J. Pancreatic Cancer Subtypes: A Roadmap for Precision Medicine. *Ann. Med.* **2018**, *50* (4), 277–287.
(13) Taherian, M.; Wang, H.; Wang, H. Pancreatic Ductal Adenocarcinoma: Molecular Pathology and Predictive Biomarkers. *Cells* **2022**, *11* (19), 3068.
(14) Fan, Z.; Xiao, Y.; Du, Y.; Zhang, Y.; Zhou, W. Pancreatic Cancer Subtyping-the Keystone of Precision Treatment. *Front. Immunol.* **2025**, *16*, 1563725.
(15) Espiau-Romera, P.; Courtois, S.; Parejo-Alonso, B.; Sancho, P. Molecular and Metabolic Subtypes Correspondence for Pancreatic Ductal Adenocarcinoma Classification. *J. Clin. Med.* **2020**, *9* (12), 4128.
(16) Schneider, A. T.; Koppe, C.; Crouchet, E.; Papargyriou, A.; Singer, M. T.; Büttner, V.; Keysberg, L.; Szydlowska, M.; Jühling, F.; Moehlin, J.; Chen, M.-C.; Leone, V.; Mueller, S.; Neuß, T.; Castoldi, M.; Lesina, M.; Bergmann, F.; Hackert, T.; Steiger, K.; Knoefel, W. T.; Zaufel, A.; Kather, J. N.; Esposito, I.; Gaida, M. M.; Ghallab, A.; Hengstler, J. G.; Einwächter, H.; Unger, K.; Algül, H.; Gassler, N.; Schmid, R. M.; Rad, R.; Baumert, T. F.; Reichert, M.; Heikenwalder, M.; Kondylis, V.; Vucur, M.; Luedde, T. A Decision Point between Transdifferentiation and Programmed Cell Death Priming Controls KRAS-Dependent Pancreatic Cancer Development. *Nat. Commun.* **2025**, *16* (1), 1765. https://doi.org/10.1038/s41467-025-56493-7.
(17) Chuvin, N.; Vincent, D. F.; Pommier, R. M.; Alcaraz, L. B.; Gout, J.; Caligaris, C.; Yacoub, K.; Cardot, V.; Roger, E.; Kaniewski, B. Acinar-to-Ductal Metaplasia Induced by Transforming Growth Factor Beta Facilitates KRASG12D-Driven

Pancreatic Tumorigenesis. *Cell. Mol. Gastroenterol. Hepatol.* **2017**, *4* (2), 263–282.
(18) Iacobuzio-Donahue, C. A.; Velculescu, V. E.; Wolfgang, C. L.; Hruban, R. H. Genetic Basis of Pancreas Cancer Development and Progression: Insights from Whole-Exome and Whole-Genome Sequencing. *Clin. Cancer Res.* **2012**, *18* (16), 4257–4265.
(19) Heinrich, M. A.; Mostafa, A. M. R. H.; Morton, J. P.; Hawinkels, L. J. A. C.; Prakash, J. Translating Complexity and Heterogeneity of Pancreatic Tumor: 3D in Vitro to in Vivo Models. *Adv. Drug Deliv. Rev.* **2021**, *174*, 265–293.
(20) Vincent, A.; Herman, J.; Schulick, R.; Hruban, R. H.; Goggins, M. Pancreatic Cancer. *The lancet* **2011**, *378* (9791), 607–620.
(21) Borrero, L. J. H.; El-Deiry, W. S. Tumor Suppressor P53: Biology, Signaling Pathways, and Therapeutic Targeting. *Biochim. Biophys. Acta BBA-Rev. Cancer* **2021**, *1876* (1), 188556–188556.
(22) Makohon-Moore, A.; Iacobuzio-Donahue, C. A. Pancreatic Cancer Biology and Genetics from an Evolutionary Perspective. *Nat. Rev. Cancer* **2016**, *16* (9), 553–565.
(23) Sasaki, K.; Takahashi, S.; Ouchi, K.; Otsuki, Y.; Wakayama, S.; Ishioka, C. Different Impacts of TP53 Mutations on Cell Cycle-Related Gene Expression among Cancer Types. *Sci. Rep.* **2023**, *13* (1), 4868–4868.
(24) Iovanna, J.; Fraunhoffer, N.; Urrutia, R.; Dusetti, N. Understanding the Heterogeneity of Pancreatic Ductal Adenocarcinoma. *Transl. Oncol.* **2025**, *60*, 102479. https://doi.org/10.1016/j.tranon.2025.102479.
(25) García-Gareta, E.; Calderón-Villalba, A.; Alamán-Díez, P.; Costa, C. G.; Guerrero, P. E.; Mur, C.; Flores, A. R.; Jurjo, N. O.; Sancho, P.; Pérez, M. Á.; García-Aznar, J. M. Physico-Chemical Characterization of the Tumour Microenvironment of Pancreatic Ductal Adenocarcinoma. *Eur. J. Cell Biol.* **2024**, *103* (2), 151396. https://doi.org/10.1016/j.ejcb.2024.151396.
(26) Myo Min, K. K.; Ffrench, C. B.; Jessup, C. F.; Shepherdson, M.; Barreto, S. G.; Bonder, C. S. Overcoming the Fibrotic Fortress in Pancreatic Ductal Adenocarcinoma: Challenges and Opportunities. *Cancers* **2023**, *15* (8), 2354. https://doi.org/10.3390/cancers15082354.
(27) Rasheed, Z. A.; Matsui, W.; Maitra, A. Pathology of Pancreatic Stroma in PDAC. **2012**.
(28) Opitz, F. V.; Haeberle, L.; Daum, A.; Esposito, I. Tumor Microenvironment in Pancreatic Intraepithelial Neoplasia. *Cancers* **2021**, *13* (24), 6188. https://doi.org/10.3390/cancers13246188.
(29) Apte, M. V.; Haber, P. S.; Darby, S. J.; Rodgers, S. C.; McCaughan, G. W.; Korsten, M. A.; Pirola, R. C.; Wilson, J. S. Pancreatic Stellate Cells Are Activated by Proinflammatory Cytokines: Implications for Pancreatic Fibrogenesis. *Gut* **1999**, *44* (4), 534–541.
(30) Erkan, M.; Hausmann, S.; Michalski, C. W.; Fingerle, A. A.; Dobritz, M.; Kleeff, J.; Friess, H. The Role of Stroma in Pancreatic Cancer: Diagnostic and Therapeutic Implications. *Nat. Rev. Gastroenterol. Hepatol.* **2012**, *9* (8), 454–467.
(31) Erkan, M. The Role of Pancreatic Stellate Cells in Pancreatic Cancer. *Pancreatology* **2013**, *13* (2), 106–109.
(32) Wang, Z.; He, R.; Dong, S.; Zhou, W. Pancreatic Stellate Cells in Pancreatic Cancer: As Potential Targets for Future Therapy. *Front. Oncol.* **2023**, *13*, 1185093–1185093.
(33) Mekapogu, A.; Pothula, S.; Pirola, R.; Wilson, J.; Apte, M. Pancreatic Stellate Cells in Health and Disease. *Pancreapedia Exocrine Pancreas Knowl. Base* **2020**.
(34) Ferdek, P. E.; Jakubowska, M. A. Biology of Pancreatic Stellate Cells—More

than Just Pancreatic Cancer. *Pflüg. Arch. - Eur. J. Physiol.* **2017**, *469* (9), 1039–1050. https://doi.org/10.1007/s00424-017-1968-0.

(35) Hrabak, P.; Kalousova, M.; Krechler, T.; Zima, T. Pancreatic Stellate Cells-Rising Stars in Pancreatic Pathologies. *Physiol. Res.* **2021**, *70* (Suppl 4), S597–S597.

(36) Mekapogu, A. R.; Pothula, S. P.; Pirola, R. C.; Wilson, J. S.; Apte, M. V. Multifunctional Role of Pancreatic Stellate Cells in Pancreatic Cancer. *Ann. Pancreat. Cancer* **2019**, *2*, 10–10. https://doi.org/10.21037/apc.2019.05.02.

(37) Wu, Y.; Zhang, C.; Jiang, K.; Werner, J.; Bazhin, A. V.; D'Haese, J. G. The Role of Stellate Cells in Pancreatic Ductal Adenocarcinoma: Targeting Perspectives. *Front. Oncol.* **2021**, *10*, 621937–621937.

(38) Jin, G.; Hong, W.; Guo, Y.; Bai, Y.; Chen, B. Molecular Mechanism of Pancreatic Stellate Cells Activation in Chronic Pancreatitis and Pancreatic Cancer. *J. Cancer* **2020**, *11* (6), 1505–1505.

(39) Wang, Z.; Dong, S.; Zhou, W. Pancreatic Stellate Cells: Key Players in Pancreatic Health and Diseases. *Mol. Med. Rep.* **2024**, *30* (1), 109–109.

(40) Wang, S.; Zheng, Y.; Yang, F.; Zhu, L.; Zhu, X.-Q.; Wang, Z.-F.; Wu, X.-L.; Zhou, C.-H.; Yan, J.-Y.; Hu, B.-Y.; Kong, B.; Fu, D.-L.; Bruns, C.; Zhao, Y.; Qin, L.-X.; Dong, Q.-Z. The Molecular Biology of Pancreatic Adenocarcinoma: Translational Challenges and Clinical Perspectives. *Signal Transduct. Target. Ther.* **2021**, *6* (1), 249. https://doi.org/10.1038/s41392-021-00659-4.

(41) Hamada, S.; Matsumoto, R.; Masamune, A. Pancreatic Stellate Cells and Metabolic Alteration: Physiology and Pathophysiology. *Front. Physiol.* **2022**, *13*, 865105–865105.

(42) Kusiak, A. A.; Jakubowska, M. A.; Stopa, K. B.; Zhang, X.; Huang, W.; Gerasimenko, J. V.; Gerasimenko, O. V.; Sutton, R.; Petersen, O. H.; Ferdek, P. E. Activation of Pancreatic Stellate Cells Attenuates Intracellular Ca2+ Signals Due to Downregulation of TRPA1 and Protects against Cell Death Induced by Alcohol Metabolites. *Cell Death Dis.* **2022**, *13* (8), 744–744.

(43) Yang, D.; Liu, J.; Qian, H.; Zhuang, Q. Cancer-Associated Fibroblasts: From Basic Science to Anticancer Therapy. *Exp. Mol. Med.* **2023**, *55* (7), 1322–1332.

(44) Murray, E. R.; Menezes, S.; Henry, J. C.; Williams, J. L.; Alba-Castellon, L.; Baskaran, P.; Quetier, I.; Desai, A.; Marshall, J. J. T.; Rosewell, I. Disruption of Pancreatic Stellate Cell Myofibroblast Phenotype Promotes Pancreatic Tumor Invasion. *Cell Rep.* **2022**, *38* (4).

(45) Öhlund, D.; Handly-Santana, A.; Biffi, G.; Elyada, E.; Almeida, A. S.; Ponz-Sarvise, M.; Corbo, V.; Oni, T. E.; Hearn, S. A.; Lee, E. J. Distinct Populations of Inflammatory Fibroblasts and Myofibroblasts in Pancreatic Cancer. *J. Exp. Med.* **2017**, *214* (3), 579–596.

(46) Manoukian, P.; Bijlsma, M.; Van Laarhoven, H. The Cellular Origins of Cancer-Associated Fibroblasts and Their Opposing Contributions to Pancreatic Cancer Growth. *Front. Cell Dev. Biol.* **2021**, *9*, 743907–743907.

(47) Zhang, T.; Ren, Y.; Yang, P.; Wang, J.; Zhou, H. Cancer-Associated Fibroblasts in Pancreatic Ductal Adenocarcinoma. *Cell Death Dis.* **2022**, *13* (10), 897–897.

(48) Helms, E. J.; Berry, M. W.; Chaw, R. C.; DuFort, C. C.; Sun, D.; Onate, M. K.; Oon, C.; Bhattacharyya, S.; Sanford-Crane, H.; Horton, W. Mesenchymal Lineage Heterogeneity Underlies Nonredundant Functions of Pancreatic Cancer–Associated Fibroblasts. *Cancer Discov.* **2022**, *12* (2), 484–501.

(49) Garcia, P. E.; Adoumie, M.; Kim, E. C.; Zhang, Y.; Scales, M. K.; El-Tawil, Y. S.; Shaikh, A. Z.; Wen, H.-J.; Bednar, F.; Allen, B. L. Differential Contribution of Pancreatic Fibroblast Subsets to the Pancreatic Cancer Stroma. *Cell. Mol. Gastroenterol. Hepatol.* **2020**, *10* (3), 581–599.

(50) Miyazaki, Y.; Oda, T.; Mori, N.; Kida, Y. S. Adipose-derived Mesenchymal Stem Cells Differentiate into Pancreatic Cancer-associated Fibroblasts in Vitro. *FEBS*

Open Bio **2020**, *10* (11), 2268–2281.
(51) Han, L.; Wu, Y.; Fang, K.; Sweeney, S.; Roesner, U. K.; Parrish, M.; Patel, K.; Walter, T.; Piermattei, J.; Trimboli, A. The Splanchnic Mesenchyme Is the Tissue of Origin for Pancreatic Fibroblasts during Homeostasis and Tumorigenesis. *Nat. Commun.* **2023**, *14* (1), 1–1.
(52) Clere, N.; Renault, S.; Corre, I. Endothelial-to-Mesenchymal Transition in Cancer. *Front. Cell Dev. Biol.* **2020**, *8*, 747–747.
(53) Fan, C.-S.; Chen, L.-L.; Hsu, T.-A.; Chen, C.-C.; Chua, K. V.; Li, C.-P.; Huang, T.-S. Endothelial-Mesenchymal Transition Harnesses HSP90α-Secreting M2-Macrophages to Exacerbate Pancreatic Ductal Adenocarcinoma. *J. Hematol. Oncol.J Hematol Oncol* **2019**, *12* (1), 138–138.
(54) Adjuto-Saccone, M.; Soubeyran, P.; Garcia, J.; Audebert, S.; Camoin, L.; Rubis, M.; Roques, J.; Binétruy, B.; Iovanna, J. L.; Tournaire, R. TNF-α Induces Endothelial–Mesenchymal Transition Promoting Stromal Development of Pancreatic Adenocarcinoma. *Cell Death Dis.* **2021**, *12* (7), 649–649.
(55) Huang, H.; Wang, Z.; Zhang, Y.; Pradhan, R. N.; Ganguly, D.; Chandra, R.; Murimwa, G.; Wright, S.; Gu, X.; Maddipati, R. Mesothelial Cell-Derived Antigen-Presenting Cancer-Associated Fibroblasts Induce Expansion of Regulatory T Cells in Pancreatic Cancer. *Cancer Cell* **2022**, *40* (6), 656–673.
(56) Cords, L.; Tietscher, S.; Anzeneder, T.; Langwieder, C.; Rees, M.; de Souza, N.; Bodenmiller, B. Cancer-Associated Fibroblast Classification in Single-Cell and Spatial Proteomics Data. *Nat. Commun.* **2023**, *14* (1), 4294–4294.
(57) Helms, E.; Onate, M. K.; Sherman, M. H. Fibroblast Heterogeneity in the Pancreatic Tumor Microenvironment. *Cancer Discov.* **2020**, *10* (5), 648–656.
(58) Elyada, E.; Bolisetty, M.; Laise, P.; Flynn, W. F.; Courtois, E. T.; Burkhart, R. A.; Teinor, J. A.; Belleau, P.; Biffi, G.; Lucito, M. S.; Sivajothi, S.; Armstrong, T. D.; Engle, D. D.; Yu, K. H.; Hao, Y.; Wolfgang, C. L.; Park, Y.; Preall, J.; Jaffee, E. M.; Califano, A.; Robson, P.; Tuveson, D. A. Cross-Species Single-Cell Analysis of Pancreatic Ductal Adenocarcinoma Reveals Antigen-Presenting Cancer-Associated Fibroblasts. *Cancer Discov.* **2019**, *9* (8), 1102–1123. https://doi.org/10.1158/2159-8290.CD-19-0094.
(59) Sousa, C. M.; Biancur, D. E.; Wang, X.; Halbrook, C. J.; Sherman, M. H.; Zhang, L.; Kremer, D.; Hwang, R. F.; Witkiewicz, A. K.; Ying, H.; Asara, J. M.; Evans, R. M.; Cantley, L. C.; Lyssiotis, C. A.; Kimmelman, A. C. Pancreatic Stellate Cells Support Tumour Metabolism through Autophagic Alanine Secretion. *Nature* **2016**, *536* (7617), 479–483. https://doi.org/10.1038/nature19084.
(60) Dosch, A. R.; Singh, S.; Dai, X.; Mehra, S.; Silva, I. D. C.; Bianchi, A.; Srinivasan, S.; Gao, Z.; Ban, Y.; Chen, X. Targeting Tumor–Stromal IL6/STAT3 Signaling through IL1 Receptor Inhibition in Pancreatic Cancer. *Mol. Cancer Ther.* **2021**, *20* (11), 2280–2290.
(61) Hu, B.; Wu, C.; Mao, H.; Gu, H.; Dong, H.; Yan, J.; Qi, Z.; Yuan, L.; Dong, Q.; Long, J. Subpopulations of Cancer-Associated Fibroblasts Link the Prognosis and Metabolic Features of Pancreatic Ductal Adenocarcinoma. *Ann. Transl. Med.* **2022**, *10* (5), 262–262. https://doi.org/10.21037/atm-22-407.
(62) Coursier, D.; Calvo, F. CAFs vs. TECs: When Blood Feuds Fuel Cancer Progression, Dissemination and Therapeutic Resistance. *Cell. Oncol.* **2024**, *47* (4), 1091–1112. https://doi.org/10.1007/s13402-024-00931-z.
(63) Mello, A. M.; Ngodup, T.; Lee, Y.; Donahue, K. L.; Li, J.; Rao, A.; Carpenter, E. S.; Crawford, H. C.; Pasca Di Magliano, M.; Lee, K. E. Hypoxia Promotes an Inflammatory Phenotype of Fibroblasts in Pancreatic Cancer. *Oncogenesis* **2022**, *11* (1), 56. https://doi.org/10.1038/s41389-022-00434-2.
(64) Geng, X.; Chen, H.; Zhao, L.; Hu, J.; Yang, W.; Li, G.; Cheng, C.; Zhao, Z.; Zhang, T.; Li, L. Cancer-Associated Fibroblast (CAF) Heterogeneity and Targeting Therapy of CAFs in Pancreatic Cancer. *Front. Cell Dev. Biol.* **2021**, *9*,

655152–655152.
(65) Masugi, Y. The Desmoplastic Stroma of Pancreatic Cancer: Multilayered Levels of Heterogeneity, Clinical Significance, and Therapeutic Opportunities. *Cancers* **2022**, *14* (13), 3293–3293.
(66) Park, H.; Lee, Y.; Lee, H.; Kim, J.-W.; Hwang, J.-H.; Kim, J.; Yoon, Y.-S.; Han, H.-S.; Kim, H. The Prognostic Significance of Cancer-Associated Fibroblasts in Pancreatic Ductal Adenocarcinoma. *Tumor Biol.* **2017**, *39* (10), 1010428317718403–1010428317718403.
(67) Neuzillet, C.; Tijeras-Raballand, A.; Ragulan, C.; Cros, J.; Patil, Y.; Martinet, M.; Erkan, M.; Kleeff, J.; Wilson, J.; Apte, M. Inter-and Intra-tumoural Heterogeneity in Cancer-associated Fibroblasts of Human Pancreatic Ductal Adenocarcinoma. *J. Pathol.* **2019**, *248* (1), 51–65.
(68) Shinkawa, T.; Ohuchida, K.; Nakamura, M. Heterogeneity of Cancer-Associated Fibroblasts and the Tumor Immune Microenvironment in Pancreatic Cancer. *Cancers* **2022**, *14* (16), 3994. https://doi.org/10.3390/cancers14163994.
(69) Feig, C.; Jones, J. O.; Kraman, M.; Wells, R. J. B.; Deonarine, A.; Chan, D. S.; Connell, C. M.; Roberts, E. W.; Zhao, Q.; Caballero, O. L.; Teichmann, S. A.; Janowitz, T.; Jodrell, D. I.; Tuveson, D. A.; Fearon, D. T. Targeting CXCL12 from FAP-Expressing Carcinoma-Associated Fibroblasts Synergizes with Anti–PD-L1 Immunotherapy in Pancreatic Cancer. *Proc. Natl. Acad. Sci.* **2013**, *110* (50), 20212–20217. https://doi.org/10.1073/pnas.1320318110.
(70) Sandberg, T. P.; Stuart, M. P. M. E.; Oosting, J.; Tollenaar, R. A. E. M.; Sier, C. F. M.; Mesker, W. E. Increased Expression of Cancer-Associated Fibroblast Markers at the Invasive Front and Its Association with Tumor-Stroma Ratio in Colorectal Cancer. *BMC Cancer* **2019**, *19* (1), 284. https://doi.org/10.1186/s12885-019-5462-2.
(71) Krishnamurty, A. T.; Shyer, J. A.; Thai, M.; Gandham, V.; Buechler, M. B.; Yang, Y. A.; Pradhan, R. N.; Wang, A. W.; Sanchez, P. L.; Qu, Y.; Breart, B.; Chalouni, C.; Dunlap, D.; Ziai, J.; Elstrott, J.; Zacharias, N.; Mao, W.; Rowntree, R. K.; Sadowsky, J.; Lewis, G. D.; Pillow, T. H.; Nabet, B. Y.; Banchereau, R.; Tam, L.; Caothien, R.; Bacarro, N.; Roose-Girma, M.; Modrusan, Z.; Mariathasan, S.; Müller, S.; Turley, S. J. LRRC15+ Myofibroblasts Dictate the Stromal Setpoint to Suppress Tumour Immunity. *Nature* **2022**, *611* (7934), 148–154. https://doi.org/10.1038/s41586-022-05272-1.
(72) Mizutani, Y.; Kobayashi, H.; Iida, T.; Asai, N.; Masamune, A.; Hara, A.; Esaki, N.; Ushida, K.; Mii, S.; Shiraki, Y.; Ando, K.; Weng, L.; Ishihara, S.; Ponik, S. M.; Conklin, M. W.; Haga, H.; Nagasaka, A.; Miyata, T.; Matsuyama, M.; Kobayashi, T.; Fujii, T.; Yamada, S.; Yamaguchi, J.; Wang, T.; Woods, S. L.; Worthley, D.; Shimamura, T.; Fujishiro, M.; Hirooka, Y.; Enomoto, A.; Takahashi, M. Meflin-Positive Cancer-Associated Fibroblasts Inhibit Pancreatic Carcinogenesis. *Cancer Res.* **2019**, *79* (20), 5367–5381. https://doi.org/10.1158/0008-5472.CAN-19-0454.
(73) Quemerais, C.; Jean, C.; Brunel, A.; Decaup, E.; Labrousse, G.; Audureau, H.; Raffenne, J.; Belhabib, I.; Cros, J.; Perraud, A.; Dusetti, N.; Nicolle, R.; Mathonnet, M.; Pyronnet, S.; Martineau, Y.; Fanjul, M.; Bousquet, C. Unveiling FKBP7 as an Early Endoplasmic Reticulum Sentinel in Pancreatic Stellate Cell Activation, Collagen Remodeling and Tumor Progression. *Cancer Lett.* **2025**, *614*, 217538. https://doi.org/10.1016/j.canlet.2025.217538.
(74) Croizer, H.; Mhaidly, R.; Kieffer, Y.; Gentric, G.; Djerroudi, L.; Leclere, R.; Pelon, F.; Robley, C.; Bohec, M.; Meng, A.; Meseure, D.; Romano, E.; Baulande, S.; Peltier, A.; Vincent-Salomon, A.; Mechta-Grigoriou, F. Deciphering the Spatial Landscape and Plasticity of Immunosuppressive Fibroblasts in Breast Cancer. *Nat. Commun.* **2024**, *15* (1), 2806. https://doi.org/10.1038/s41467-024-

47068-z.
(75) Melchionna, R.; Trono, P.; Di Carlo, A.; Di Modugno, F.; Nisticò, P. Transcription Factors in Fibroblast Plasticity and CAF Heterogeneity. *J. Exp. Clin. Cancer Res.* **2023**, *42* (1), 347. https://doi.org/10.1186/s13046-023-02934-4.
(76) Peiffer, R.; Boumahd, Y.; Gullo, C.; Crake, R.; Letellier, E.; Bellahcène, A.; Peulen, O. Cancer-Associated Fibroblast Diversity Shapes Tumor Metabolism in Pancreatic Cancer. *Cancers* **2022**, *15* (1), 61. https://doi.org/10.3390/cancers15010061.
(77) Liang, C.; Shi, S.; Meng, Q.; Liang, D.; Ji, S.; Zhang, B.; Qin, Y.; Xu, J.; Ni, Q.; Yu, X. Complex Roles of the Stroma in the Intrinsic Resistance to Gemcitabine in Pancreatic Cancer: Where We Are and Where We Are Going. *Exp. Mol. Med.* **2017**, *49* (12), e406–e406. https://doi.org/10.1038/emm.2017.255.
(78) Brichkina, A.; Polo, P.; Sharma, S. D.; Visestamkul, N.; Lauth, M. A Quick Guide to CAF Subtypes in Pancreatic Cancer. *Cancers* **2023**, *15* (9), 2614. https://doi.org/10.3390/cancers15092614.
(79) Menezes, S.; Okail, M. H.; Jalil, S. M. A.; Kocher, H. M.; Cameron, A. J. M. Cancer-associated Fibroblasts in Pancreatic Cancer: New Subtypes, New Markers, New Targets. *J. Pathol.* **2022**, *257* (4), 526–544. https://doi.org/10.1002/path.5926.
(80) Pfeifer, E.; Burchell, J. M.; Dazzi, F.; Sarker, D.; Beatson, R. Apoptosis in the Pancreatic Cancer Tumor Microenvironment—The Double-Edged Sword of Cancer-Associated Fibroblasts. *Cells* **2021**, *10* (7), 1653–1653.
(81) Rhim, A. D.; Oberstein, P. E.; Thomas, D. H.; Mirek, E. T.; Palermo, C. F.; Sastra, S. A.; Dekleva, E. N.; Saunders, T.; Becerra, C. P.; Tattersall, I. W.; Westphalen, C. B.; Kitajewski, J.; Fernandez-Barrena, M. G.; Fernandez-Zapico, M. E.; Iacobuzio-Donahue, C.; Olive, K. P.; Stanger, B. Z. Stromal Elements Act to Restrain, Rather Than Support, Pancreatic Ductal Adenocarcinoma. *Cancer Cell* **2014**, *25* (6), 735–747. https://doi.org/10.1016/j.ccr.2014.04.021.
(82) Hu, C.; Xia, R.; Zhang, X.; Li, T.; Ye, Y.; Li, G.; He, R.; Li, Z.; Lin, Q.; Zheng, S.; Chen, R. circFARP1 Enables Cancer-Associated Fibroblasts to Promote Gemcitabine Resistance in Pancreatic Cancer via the LIF/STAT3 Axis. *Mol. Cancer* **2022**, *21* (1), 24. https://doi.org/10.1186/s12943-022-01501-3.
(83) Maru, S. Y.; Wetzel, M.; Mitchell, J. T.; Gross, N. E.; Andaloori, L.; Howe, K.; Kartalia, E.; Mo, G.; Leatherman, J.; Ho, W. J.; Fertig, E. J.; Kagohara, L. T.; Pearce, E. J.; Jaffee, E. M. Antigen-Presenting Cancer-Associated Fibroblasts in Murine Pancreatic Tumors Differentially Control Regulatory T Cell Phenotype and Function via CXCL9 and CCL22. Cancer Biology April 1, 2025. https://doi.org/10.1101/2025.03.27.645833.
(84) Wang, D.; Li, Y.; Ge, H.; Ghadban, T.; Reeh, M.; Guengoer, C. The Extracellular Matrix: A Key Accomplice of Cancer Stem Cell Migration, Metastasis Formation, and Drug Resistance in PDAC. *Cancers* **2022**, *14* (16), 3998–3998.
(85) Perez, V. M.; Kearney, J. F.; Yeh, J. J. The PDAC Extracellular Matrix: A Review of the ECM Protein Composition, Tumor Cell Interaction, and Therapeutic Strategies. *Front. Oncol.* **2021**, *11*, 751311–751311.
(86) Tian, C.; Clauser, K. R.; Öhlund, D.; Rickelt, S.; Huang, Y.; Gupta, M.; Mani, D. R.; Carr, S. A.; Tuveson, D. A.; Hynes, R. O. Proteomic Analyses of ECM during Pancreatic Ductal Adenocarcinoma Progression Reveal Different Contributions by Tumor and Stromal Cells. *Proc. Natl. Acad. Sci.* **2019**, *116* (39), 19609–19618. https://doi.org/10.1073/pnas.1908626116.
(87) Zhang, H.; Chen, J.; Hu, X.; Bai, J.; Yin, T. Adjustable Extracellular Matrix Rigidity Tumor Model for Studying Stiffness Dependent Pancreatic Ductal Adenocarcinomas Progression and Tumor Immunosuppression. *Bioeng. Transl.*

Med. **2023**, *8* (3), e10518. https://doi.org/10.1002/btm2.10518.
(88) Huang, H.; Brekken, R. A. Beyond Stiffness. *Am. J. Pathol.* **2020**, *190* (8), 1622–1624. https://doi.org/10.1016/j.ajpath.2020.05.005.
(89) Erkan, M.; Michalski, C. W.; Rieder, S.; Reiser–Erkan, C.; Abiatari, I.; Kolb, A.; Giese, N. A.; Esposito, I.; Friess, H.; Kleeff, J. The Activated Stroma Index Is a Novel and Independent Prognostic Marker in Pancreatic Ductal Adenocarcinoma. *Clin. Gastroenterol. Hepatol.* **2008**, *6* (10), 1155–1161. https://doi.org/10.1016/j.cgh.2008.05.006.
(90) Heger, U.; Martens, A.; Schillings, L.; Walter, B.; Hartmann, D.; Hinz, U.; Pausch, T.; Giese, N.; Michalski, C. W.; Hackert, T. Myofibroblastic CAF Density, Not Activated Stroma Index, Indicates Prognosis after Neoadjuvant Therapy of Pancreatic Carcinoma. *Cancers* **2022**, *14* (16), 3881. https://doi.org/10.3390/cancers14163881.
(91) Mahajan, U. M.; Langhoff, E.; Goni, E.; Costello, E.; Greenhalf, W.; Halloran, C.; Ormanns, S.; Kruger, S.; Boeck, S.; Ribback, S.; Beyer, G.; Dombroswki, F.; Weiss, F.-U.; Neoptolemos, J. P.; Werner, J.; D'Haese, J. G.; Bazhin, A.; Peterhansl, J.; Pichlmeier, S.; Büchler, M. W.; Kleeff, J.; Ganeh, P.; Sendler, M.; Palmer, D. H.; Kohlmann, T.; Rad, R.; Regel, I.; Lerch, M. M.; Mayerle, J. Immune Cell and Stromal Signature Associated With Progression-Free Survival of Patients With Resected Pancreatic Ductal Adenocarcinoma. *Gastroenterology* **2018**, *155* (5), 1625-1639.e2. https://doi.org/10.1053/j.gastro.2018.08.009.
(92) Ogawa, Y.; Masugi, Y.; Abe, T.; Yamazaki, K.; Ueno, A.; Fujii-Nishimura, Y.; Hori, S.; Yagi, H.; Abe, Y.; Kitago, M. Three Distinct Stroma Types in Human Pancreatic Cancer Identified by Image Analysis of Fibroblast Subpopulations and Collagen. *Clin. Cancer Res.* **2021**, *27* (1), 107–119.
(93) Moffitt, R. A.; Marayati, R.; Flate, E. L.; Volmar, K. E.; Loeza, S. G. H.; Hoadley, K. A.; Rashid, N. U.; Williams, L. A.; Eaton, S. C.; Chung, A. H. Virtual Microdissection Identifies Distinct Tumor-and Stroma-Specific Subtypes of Pancreatic Ductal Adenocarcinoma. *Nat. Genet.* **2015**, *47* (10), 1168–1178.
(94) Nabavizadeh, A.; Payen, T.; Iuga, A. C.; Sagalovskiy, I. R.; Desrouilleres, D.; Saharkhiz, N.; Palermo, C. F.; Sastra, S. A.; Oberstein, P. E.; Rosario, V.; Kluger, M. D.; Schrope, B. A.; Chabot, J. A.; Olive, K. P.; Konofagou, E. E. Noninvasive Young's Modulus Visualization of Fibrosis Progression and Delineation of Pancreatic Ductal Adenocarcinoma (PDAC) Tumors Using Harmonic Motion Elastography (HME) *in Vivo*. *Theranostics* **2020**, *10* (10), 4614–4626. https://doi.org/10.7150/thno.37965.
(95) Iglesias-Garcia, J.; De La Iglesia-Garcia, D.; Lariño-Noia, J.; Dominguez-Muñoz, J. E. Endoscopic Ultrasound (EUS) Guided Elastography. *Diagnostics* **2023**, *13* (10), 1686. https://doi.org/10.3390/diagnostics13101686.
(96) Iino, Y.; Maruyama, H.; Mikata, R.; Yasui, S.; Koroki, K.; Nagashima, H.; Awatsu, M.; Shingyoji, A.; Kusakabe, Y.; Kobayashi, K.; Kiyono, S.; Nakamura, M.; Ohyama, H.; Sugiyama, H.; Sakai, Y.; Chiba, T.; Kato, J.; Tsuyuguchi, T.; Kato, N. Percutaneous Two-Dimensional Shear Wave Elastography for Diagnosis of Pancreatic Tumor. *Diagnostics* **2021**, *11* (3), 498. https://doi.org/10.3390/diagnostics11030498.
(97) Vincent, P.; Wang, H.; Nieskoski, M.; Gunn, J. R.; Marra, K.; Hoopes, P. J.; Samkoe, K. S.; Doyley, M. M.; Hasan, T.; Pogue, B. W. High-Resolution *Ex Vivo* Elastography to Characterize Tumor Stromal Heterogeneity In Situ in Pancreatic Adenocarcinoma. *IEEE Trans. Biomed. Eng.* **2020**, *67* (9), 2490–2496. https://doi.org/10.1109/TBME.2019.2963562.
(98) Li, Q.; Yang, C.; Li, J.; Wang, R.; Min, J.; Song, Y.; Su, H. The Type I Collagen Paradox in PDAC Progression: Microenvironmental Protector Turned Tumor Accomplice. *J. Transl. Med.* **2025**, *23* (1), 744. https://doi.org/10.1186/s12967-025-06778-8.

(99) Levental, K. R.; Yu, H.; Kass, L.; Lakins, J. N.; Egeblad, M.; Erler, J. T.; Fong, S. F. T.; Csiszar, K.; Giaccia, A.; Weninger, W.; Yamauchi, M.; Gasser, D. L.; Weaver, V. M. Matrix Crosslinking Forces Tumor Progression by Enhancing Integrin Signaling. *Cell* **2009**, *139* (5), 891–906. https://doi.org/10.1016/j.cell.2009.10.027.

(100) Nieskoski, M. D.; Marra, K.; Gunn, J. R.; Hoopes, P. J.; Doyley, M. M.; Hasan, T.; Trembly, B. S.; Pogue, B. W. Collagen Complexity Spatially Defines Microregions of Total Tissue Pressure in Pancreatic Cancer. *Sci. Rep.* **2017**, *7* (1), 10093. https://doi.org/10.1038/s41598-017-10671-w.

(101) Drifka, C. R.; Loeffler, A. G.; Mathewson, K.; Keikhosravi, A.; Eickhoff, J. C.; Liu, Y.; Weber, S. M.; Kao, W. J.; Eliceiri, K. W. Highly Aligned Stromal Collagen Is a Negative Prognostic Factor Following Pancreatic Ductal Adenocarcinoma Resection. *Oncotarget* **2016**, *7* (46), 76197–76213. https://doi.org/10.18632/oncotarget.12772.

(102) Ferrara, B.; Pignatelli, C.; Cossutta, M.; Citro, A.; Courty, J.; Piemonti, L. The Extracellular Matrix in Pancreatic Cancer: Description of a Complex Network and Promising Therapeutic Options. *Cancers* **2021**, *13* (17), 4442–4442.

(103) Chang, Y.; Lee, J. W. N.; Holle, A. W. The Mechanobiology of Fibroblast Activation in Disease. *APL Bioeng.* **2025**, *9* (2), 021505. https://doi.org/10.1063/5.0272393.

(104) Olivares, O.; Mayers, J. R.; Gouirand, V.; Torrence, M. E.; Gicquel, T.; Borge, L.; Lac, S.; Roques, J.; Lavaut, M.-N.; Berthezène, P.; Rubis, M.; Secq, V.; Garcia, S.; Moutardier, V.; Lombardo, D.; Iovanna, J. L.; Tomasini, R.; Guillaumond, F.; Vander Heiden, M. G.; Vasseur, S. Collagen-Derived Proline Promotes Pancreatic Ductal Adenocarcinoma Cell Survival under Nutrient Limited Conditions. *Nat. Commun.* **2017**, *8* (1), 16031. https://doi.org/10.1038/ncomms16031.

(105) Wu, H.; Fu, M.; Wu, M.; Cao, Z.; Zhang, Q.; Liu, Z. Emerging Mechanisms and Promising Approaches in Pancreatic Cancer Metabolism. *Cell Death Dis.* **2024**, *15* (8), 553. https://doi.org/10.1038/s41419-024-06930-0.

(106) Chitty, J. L.; Yam, M.; Perryman, L.; Parker, A. L.; Skhinas, J. N.; Setargew, Y. F. I.; Mok, E. T. Y.; Tran, E.; Grant, R. D.; Latham, S. L.; Pereira, B. A.; Ritchie, S. C.; Murphy, K. J.; Trpceski, M.; Findlay, A. D.; Melenec, P.; Filipe, E. C.; Nadalini, A.; Velayuthar, S.; Major, G.; Wyllie, K.; Papanicolaou, M.; Ratnaseelan, S.; Phillips, P. A.; Sharbeen, G.; Youkhana, J.; Russo, A.; Blackwell, A.; Hastings, J. F.; Lucas, M. C.; Chambers, C. R.; Reed, D. A.; Stoehr, J.; Vennin, C.; Pidsley, R.; Zaratzian, A.; Da Silva, A. M.; Tayao, M.; Charlton, B.; Herrmann, D.; Nobis, M.; Clark, S. J.; Biankin, A. V.; Johns, A. L.; Croucher, D. R.; Nagrial, A.; Gill, A. J.; Grimmond, S. M.; Australian Pancreatic Cancer Genome Initiative (APGI); Chantrill, L. A.; Chou, A.; Dwarte, T.; Metcalf, X. L.; Jeong, G.; Kenyon, L.; Waddell, N.; Pearson, J. V.; Patch, A.-M.; Nones, K.; Newell, F.; Mukhopadhyay, P.; Addala, V.; Kazakoff, S.; Holmes, O.; Leonard, C.; Wood, S.; Hofmann, O.; Samra, J. S.; Pavlakis, N.; Arena, J.; High, H. A.; Asghari, R.; Merrett, N. D.; Das, A.; Cosman, P. H.; Ismail, K.; Stoita, A.; Williams, D.; Spigellman, A.; McLeo, D.; Kirk, J.; Kench, J. G.; Grimison, P.; Sandroussi, C.; Goodwin, A.; Mead, R. S.; Tucker, K.; Andrews, L.; Texler, M.; Forrest, C.; Ballal, M.; Fletcher, D.; Beilin, M.; Feeney, K.; Epari, K.; Mukhedkar, S.; Zeps, N.; Nguyen, N. Q.; Ruszkiewicz, A. R.; Worthley, C.; Chen, J.; Brooke-Smith, M. E.; Papangelis, V.; Clouston, A. D.; Barbour, A. P.; O'Rourke, T. J.; Fawcett, J. W.; Slater, K.; Hatzifotis, M.; Hodgkinson, P.; Nikfarjam, M.; Eshleman, J. R.; Hruban, R. H.; Wolfgang, C. L.; Scarpa, A.; Lawlor, R. T.; Corbo, V.; Bassi, C.; Jamieson, N. B.; Chang, D. K.; Dreyer, S. B.; Australian Pancreatic Cancer Matrix Atlas (APMA); Abdulkhalek, L.; Schmitz, T.; Lee, V.; Stewart, K. P.; Arshi, M.; Steinmann, A. M.; Pajic, M.; Timpson, P.;

Jarolimek, W.; Cox, T. R. A First-in-Class Pan-Lysyl Oxidase Inhibitor Impairs Stromal Remodeling and Enhances Gemcitabine Response and Survival in Pancreatic Cancer. *Nat. Cancer* **2023**, *4* (9), 1326–1344. https://doi.org/10.1038/s43018-023-00614-y.

(107) Nicolas-Boluda, A.; Vaquero, J.; Vimeux, L.; Guilbert, T.; Barrin, S.; Kantari-Mimoun, C.; Ponzo, M.; Renault, G.; Deptula, P.; Pogoda, K.; Bucki, R.; Cascone, I.; Courty, J.; Fouassier, L.; Gazeau, F.; Donnadieu, E. Tumor Stiffening Reversion through Collagen Crosslinking Inhibition Improves T Cell Migration and Anti-PD-1 Treatment. *eLife* **2021**, *10*, e58688. https://doi.org/10.7554/eLife.58688.

(108) Zhang, S.; Cai, Z.; Jiang, L.; Cai, S.; Weng, Z.; Jiang, S. Targeting Stiff Stroma by Neutralizing LOX-Mediated Matrix Crosslinking in Pancreatic Cancer. *Acta Pharm. Sin. B* **2025**, *15* (5), 2783–2786. https://doi.org/10.1016/j.apsb.2025.03.010.

(109) Chen, Y.; Kim, J.; Yang, S.; Wang, H.; Wu, C.-J.; Sugimoto, H.; LeBleu, V. S.; Kalluri, R. Type I Collagen Deletion in αSMA+ Myofibroblasts Augments Immune Suppression and Accelerates Progression of Pancreatic Cancer. *Cancer Cell* **2021**, *39* (4), 548-565.e6. https://doi.org/10.1016/j.ccell.2021.02.007.

(110) Tian, C.; Huang, Y.; Clauser, K. R.; Rickelt, S.; Lau, A. N.; Carr, S. A.; Vander Heiden, M. G.; Hynes, R. O. Suppression of Pancreatic Ductal Adenocarcinoma Growth and Metastasis by Fibrillar Collagens Produced Selectively by Tumor Cells. *Nat. Commun.* **2021**, *12* (1), 2328. https://doi.org/10.1038/s41467-021-22490-9.

(111) Monslow, J.; Govindaraju, P.; Puré, E. Hyaluronan–a Functional and Structural Sweet Spot in the Tissue Microenvironment. *Front. Immunol.* **2015**, *6*, 231.

(112) Fraser, J. R. E.; Laurent, T. C.; Laurent, U. Hyaluronan: Its Nature, Distribution, Functions and Turnover. *J. Intern. Med.* **1997**, *242* (1), 27–33.

(113) Theocharis, A. D.; Tsara, M. E.; Papageorgacopoulou, N.; Karavias, D. D.; Theocharis, D. A. Pancreatic Carcinoma Is Characterized by Elevated Content of Hyaluronan and Chondroitin Sulfate with Altered Disaccharide Composition. *Biochim. Biophys. Acta BBA - Mol. Basis Dis.* **2000**, *1502* (2), 201–206. https://doi.org/10.1016/S0925-4439(00)00051-X.

(114) Sato, N.; Cheng, X.-B.; Kohi, S.; Koga, A.; Hirata, K. Targeting Hyaluronan for the Treatment of Pancreatic Ductal Adenocarcinoma. *Acta Pharm. Sin. B* **2016**, *6* (2), 101–105. https://doi.org/10.1016/j.apsb.2016.01.002.

(115) Sato, N.; Kohi, S.; Hirata, K.; Goggins, M. Role of Hyaluronan in Pancreatic Cancer Biology and Therapy: Once Again in the Spotlight. *Cancer Sci.* **2016**, *107* (5), 569–575. https://doi.org/10.1111/cas.12913.

(116) Tahkola, K.; Ahtiainen, M.; Mecklin, J.-P.; Kellokumpu, I.; Laukkarinen, J.; Tammi, M.; Tammi, R.; Väyrynen, J. P.; Böhm, J. Stromal Hyaluronan Accumulation Is Associated with Low Immune Response and Poor Prognosis in Pancreatic Cancer. *Sci. Rep.* **2021**, *11* (1), 12216. https://doi.org/10.1038/s41598-021-91796-x.

(117) Kumar, K.; Kanojia, D.; Bentrem, D. J.; Hwang, R. F.; Butchar, J. P.; Tridandapani, S.; Munshi, H. G. Targeting BET Proteins Decreases Hyaluronidase-1 in Pancreatic Cancer. *Cells* **2023**, *12* (11), 1490. https://doi.org/10.3390/cells12111490.

(118) Cheng, X.-B.; Sato, N.; Kohi, S.; Yamaguchi, K. Prognostic Impact of Hyaluronan and Its Regulators in Pancreatic Ductal Adenocarcinoma. *PLoS ONE* **2013**, *8* (11), e80765. https://doi.org/10.1371/journal.pone.0080765.

(119) Yang, C.; Cao, M.; Liu, H.; He, Y.; Xu, J.; Du, Y.; Liu, Y.; Wang, W.; Cui, L.; Hu, J.; Gao, F. The High and Low Molecular Weight Forms of Hyaluronan Have Distinct Effects on CD44 Clustering. *J. Biol. Chem.* **2012**, *287* (51), 43094–43107. https://doi.org/10.1074/jbc.M112.349209.

(120) Cheng, X.-B.; Kohi, S.; Koga, A.; Hirata, K.; Sato, N. Hyaluronan Stimulates Pancreatic Cancer Cell Motility. *Oncotarget* **2016**, *7* (4), 4829–4840. https://doi.org/10.18632/oncotarget.6617.
(121) Yang, Y.; Sun, C.; Wilhelm, M. E.; Fox, L. J.; Zhu, J.; Kaufman, L. J. Influence of Chondroitin Sulfate and Hyaluronic Acid on Structure, Mechanical Properties, and Glioma Invasion of Collagen I Gels. *Biomaterials* **2011**, *32* (31), 7932–7940.
(122) Sapudom, J.; Ullm, F.; Martin, S.; Kalbitzer, L.; Naab, J.; Möller, S.; Schnabelrauch, M.; Anderegg, U.; Schmidt, S.; Pompe, T. Molecular Weight Specific Impact of Soluble and Immobilized Hyaluronan on CD44 Expressing Melanoma Cells in 3D Collagen Matrices. *Acta Biomater.* **2017**, *50*, 259–270.
(123) Junliang, L.; Lili, W.; Xiaolong, L.; Xuguang, L.; Huanwen, W.; Zhiyong, L. High-Molecular-Weight Hyaluronan Produced by Activated Pancreatic Stellate Cells Promotes Pancreatic Cancer Cell Migration via Paracrine Signaling. *Biochem. Biophys. Res. Commun.* **2019**, *515* (3), 493–498. https://doi.org/10.1016/j.bbrc.2019.05.167.
(124) Seufferlein, T.; Ducreux, M.; Hidalgo, M.; Prager, G.; Cutsem, E. V. More than a Gel & Hyaluronic Acid, a Central Component in the Microenvironment of Pancreatic Cancer. *Eur. Oncol. Haematol.* **2018**, *14* (1), 40. https://doi.org/10.17925/EOH.2018.14.1.40.
(125) DuFort, C. C.; DelGiorno, K. E.; Carlson, M. A.; Osgood, R. J.; Zhao, C.; Huang, Z.; Thompson, C. B.; Connor, R. J.; Thanos, C. D.; Scott Brockenbrough, J.; Provenzano, P. P.; Frost, G. I.; Michael Shepard, H.; Hingorani, S. R. Interstitial Pressure in Pancreatic Ductal Adenocarcinoma Is Dominated by a Gel-Fluid Phase. *Biophys. J.* **2016**, *110* (9), 2106–2119. https://doi.org/10.1016/j.bpj.2016.03.040.
(126) DuFort, C. C.; DelGiorno, K. E.; Hingorani, S. R. Mounting Pressure in the Microenvironment: Fluids, Solids, and Cells in Pancreatic Ductal Adenocarcinoma. *Gastroenterology* **2016**, *150* (7), 1545-1557.e2. https://doi.org/10.1053/j.gastro.2016.03.040.
(127) Kim, P. K.; Halbrook, C. J.; Kerk, S. A.; Radyk, M.; Wisner, S.; Kremer, D. M.; Sajjakulnukit, P.; Andren, A.; Hou, S. W.; Trivedi, A.; Thurston, G.; Anand, A.; Yan, L.; Salamanca-Cardona, L.; Welling, S. D.; Zhang, L.; Pratt, M. R.; Keshari, K. R.; Ying, H.; Lyssiotis, C. A. Hyaluronic Acid Fuels Pancreatic Cancer Cell Growth. *eLife* **2021**, *10*, e62645. https://doi.org/10.7554/eLife.62645.
(128) Provenzano, P. P.; Cuevas, C.; Chang, A. E.; Goel, V. K.; Von Hoff, D. D.; Hingorani, S. R. Enzymatic Targeting of the Stroma Ablates Physical Barriers to Treatment of Pancreatic Ductal Adenocarcinoma. *Cancer Cell* **2012**, *21* (3), 418–429. https://doi.org/10.1016/j.ccr.2012.01.007.
(129) Abetamann, V.; Kern, H. F.; Elsässer, H. Differential Expression of the Hyaluronan Receptors CD44 and RHAMM in Human Pancreatic Cancer Cells. *Clin. Cancer Res. Off. J. Am. Assoc. Cancer Res.* **1996**, *2* (9), 1607–1618.
(130) Cirillo, N. The Hyaluronan/CD44 Axis: A Double-Edged Sword in Cancer. *Int. J. Mol. Sci.* **2023**, *24* (21), 15812. https://doi.org/10.3390/ijms242115812.
(131) Zhao, S.; Chen, C.; Chang, K.; Karnad, A.; Jagirdar, J.; Kumar, A. P.; Freeman, J. W. CD44 Expression Level and Isoform Contributes to Pancreatic Cancer Cell Plasticity, Invasiveness, and Response to Therapy. *Clin. Cancer Res.* **2016**, *22* (22), 5592–5604. https://doi.org/10.1158/1078-0432.CCR-15-3115.
(132) Chen, C.; Zhao, S.; Karnad, A.; Freeman, J. W. The Biology and Role of CD44 in Cancer Progression: Therapeutic Implications. *J. Hematol. Oncol.J Hematol Oncol* **2018**, *11* (1), 64. https://doi.org/10.1186/s13045-018-0605-5.
(133) Liu, Y.; Wu, T.; Lu, D.; Zhen, J.; Zhang, L. CD44 Overexpression Related to Lymph Node Metastasis and Poor Prognosis of Pancreatic Cancer. *Int. J. Biol. Markers* **2018**, *33* (3), 308–313. https://doi.org/10.1177/1724600817746951.

(134) Li, X.-P.; Zhang, X.-W.; Zheng, L.-Z.; Guo, W.-J. Expression of CD44 in Pancreatic Cancer and Its Significance. *Int. J. Clin. Exp. Pathol.* **2015**, *8* (6), 6724.
(135) Cheng, X.-B.; Sato, N.; Kohi, S.; Koga, A.; Hirata, K. Receptor for Hyaluronic Acid-Mediated Motility Is Associated with Poor Survival in Pancreatic Ductal Adenocarcinoma. *J. Cancer* **2015**, *6* (11), 1093–1098. https://doi.org/10.7150/jca.12990.
(136) Cheng, X.-B.; Wang, S.; Yang, H.; Tong, H.; Shi, G.; Wu, L.; Shi, L.; Li, H.; Ren, S.; Zhou, Y.; Sato, N. Negative Regulation between the Expression Levels of Receptor for Hyaluronic Acid-mediated Motility and Hyaluronan Leads to Cell Migration in Pancreatic Cancer. *Oncol. Lett.* **2020**, *20* (5), 1–1. https://doi.org/10.3892/ol.2020.12060.
(137) Solipuram, V.; Gopalakrishna, H.; Nair, G.; Mohan, A. Efficacy and Safety of PEGPH20 in Pancreatic Cancer: Systematic Review and Meta-Analysis. *Curr. Cancer Ther. Rev.* **2021**, *17* (4), 255–260. https://doi.org/10.2174/1573394717666210616152341.
(138) Cheng, X.; Sato, N.; Kohi, S.; Koga, A.; Hirata, K. 4-Methylumbelliferone Inhibits Enhanced Hyaluronan Synthesis and Cell Migration in Pancreatic Cancer Cells in Response to Tumor-Stromal Interactions. *Oncol. Lett.* **2018**. https://doi.org/10.3892/ol.2018.8147.
(139) Müller, S.; Cañeque, T.; Solier, S.; Rodriguez, R. Copper and Iron Orchestrate Cell-State Transitions in Cancer and Immunity. *Trends Cell Biol.* **2025**, *35* (2), 105–114.
(140) Solier, S.; Müller, S.; Cañeque, T.; Versini, A.; Mansart, A.; Sindikubwabo, F.; Baron, L.; Emam, L.; Gestraud, P.; Pantoş, G. D. A Druggable Copper-Signalling Pathway That Drives Inflammation. *Nature* **2023**, *617* (7960), 386–394.
(141) Rodriguez, R.; Cañeque, T.; Baron, L.; Müller, S.; Carmona, A.; Colombeau, L.; Versini, A.; Sabatier, M.; Sampaio, J.; Mishima, E. Activation of Lysosomal Iron Triggers Ferroptosis in Cancer. *Res. Sq.* **2024**, rs-3.
(142) Müller, S.; Sindikubwabo, F.; Cañeque, T.; Lafon, A.; Versini, A.; Lombard, B.; Loew, D.; Wu, T.-D.; Ginestier, C.; Charafe-Jauffret, E. CD44 Regulates Epigenetic Plasticity by Mediating Iron Endocytosis. *Nat. Chem.* **2020**, *12* (10), 929–938.
(143) Dardare, J.; Witz, A.; Merlin, J.-L.; Bochnakian, A.; Toussaint, P.; Gilson, P.; Harlé, A. Epithelial to Mesenchymal Transition in Patients with Pancreatic Ductal Adenocarcinoma: State-of-the-Art and Therapeutic Opportunities. *Pharmaceuticals* **2021**, *14* (8), 740–740.
(144) Aiello, N. M.; Maddipati, R.; Norgard, R. J.; Balli, D.; Li, J.; Yuan, S.; Yamazoe, T.; Black, T.; Sahmoud, A.; Furth, E. E.; Bar-Sagi, D.; Stanger, B. Z. EMT Subtype Influences Epithelial Plasticity and Mode of Cell Migration. *Dev. Cell* **2018**, *45* (6), 681-695.e4. https://doi.org/10.1016/j.devcel.2018.05.027.
(145) Masuo, K.; Chen, R.; Yogo, A.; Sugiyama, A.; Fukuda, A.; Masui, T.; Uemoto, S.; Seno, H.; Takaishi, S. SNAIL2 Contributes to Tumorigenicity and Chemotherapy Resistance in Pancreatic Cancer by Regulating IGFBP2. *Cancer Sci.* **2021**, *112* (12), 4987–4999. https://doi.org/10.1111/cas.15162.
(146) Guinn, S.; Perez, B.; Tandurella, J. A.; Ramani, M.; Lee, J. W.; Zabransky, D. J.; Kartalia, E.; Patel, J.; Zlomke, H.; Nicolson, N.; Shin, S.; Barrett, B.; Sun, N.; Hernandez, A.; Coyne, E.; Cannon, C.; Gross, N. E.; Charmsaz, S.; Cho, Y.; Leatherman, J.; Lyman, M.; Mitchell, J.; Kagohara, L. T.; Goggins, M. G.; Lafaro, K. J.; He, J.; Shubert, C.; Burns, W.; Zheng, L.; Fertig, E. J.; Jaffee, E. M.; Burkhart, R. A.; Ho, W. J.; Zimmerman, J. W. Cancer Associated Fibroblasts Drive Epithelial to Mesenchymal Transition and Classical to Basal Change in Pancreatic Ductal Adenocarcinoma Cells with Loss of IL-8 Expression. Cancer Biology January 8, 2025.

https://doi.org/10.1101/2025.01.07.631784.
(147) David, C. J.; Huang, Y.-H.; Chen, M.; Su, J.; Zou, Y.; Bardeesy, N.; Iacobuzio-Donahue, C. A.; Massagué, J. TGF-β Tumor Suppression through a Lethal EMT. *Cell* **2016**, *164* (5), 1015–1030. https://doi.org/10.1016/j.cell.2016.01.009.
(148) Otsuru, T.; Kobayashi, S.; Wada, H.; Takahashi, T.; Gotoh, K.; Iwagami, Y.; Yamada, D.; Noda, T.; Asaoka, T.; Serada, S.; Fujimoto, M.; Eguchi, H.; Mori, M.; Doki, Y.; Naka, T. Epithelial-mesenchymal Transition via Transforming Growth Factor Beta in Pancreatic Cancer Is Potentiated by the Inflammatory Glycoprotein LEUCINE-RICH ALPHA-2 GLYCOPROTEIN. *Cancer Sci.* **2019**, *110* (3), 985–996. https://doi.org/10.1111/cas.13918.
(149) Luo, Q.; Hu, Z.; Zhao, H.; Fan, Y.; Tu, X.; Wang, Y.; Liu, X. The Role of TGF-β in the Tumor Microenvironment of Pancreatic Cancer. *Genes Dis.* **2023**, *10* (4), 1513–1524. https://doi.org/10.1016/j.gendis.2022.10.019.
(150) Thibault, B.; Ramos-Delgado, F.; Pons-Tostivint, E.; Therville, N.; Cintas, C.; Arcucci, S.; Cassant-Sourdy, S.; Reyes-Castellanos, G.; Tosolini, M.; Villard, A. V. Pancreatic Cancer Intrinsic PI3Kα Activity Accelerates Metastasis and Rewires Macrophage Component. *EMBO Mol. Med.* **2021**, *13* (7), e13502.
(151) Baer, R.; Cintas, C.; Dufresne, M.; Cassant-Sourdy, S.; Schönhuber, N.; Planque, L.; Lulka, H.; Couderc, B.; Bousquet, C.; Garmy-Susini, B. Pancreatic Cell Plasticity and Cancer Initiation Induced by Oncogenic Kras Is Completely Dependent on Wild-Type PI 3-Kinase P110α. *Genes Dev.* **2014**, *28* (23), 2621–2635.
(152) Rice, A. J.; Cortes, E.; Lachowski, D.; Cheung, B. C. H.; Karim, S. A.; Morton, J. P.; Del Río Hernández, A. Matrix Stiffness Induces Epithelial–Mesenchymal Transition and Promotes Chemoresistance in Pancreatic Cancer Cells. *Oncogenesis* **2017**, *6* (7), e352–e352. https://doi.org/10.1038/oncsis.2017.54.
(153) Palamaris, K.; Felekouras, E.; Sakellariou, S. Epithelial to Mesenchymal Transition: Key Regulator of Pancreatic Ductal Adenocarcinoma Progression and Chemoresistance. *Cancers* **2021**, *13* (21), 5532. https://doi.org/10.3390/cancers13215532.
(154) Yang, J.; Liu, Y.; Liu, S. The Role of Epithelial-Mesenchymal Transition and Autophagy in Pancreatic Ductal Adenocarcinoma Invasion. *Cell Death Dis.* **2023**, *14* (8), 506. https://doi.org/10.1038/s41419-023-06032-3.
(155) Słodkowski, M.; Wroński, M.; Karkocha, D.; Kraj, L.; Śmigielska, K.; Jachnis, A. Current Approaches for the Curative-Intent Surgical Treatment of Pancreatic Ductal Adenocarcinoma. *Cancers* **2023**, *15* (9), 2584. https://doi.org/10.3390/cancers15092584.
(156) Conroy, T.; Castan, F.; Lopez, A.; Turpin, A.; Ben Abdelghani, M.; Wei, A. C.; Mitry, E.; Biagi, J. J.; Evesque, L.; Artru, P.; Lecomte, T.; Assenat, E.; Bauguion, L.; Ychou, M.; Bouché, O.; Monard, L.; Lambert, A.; Hammel, P.; Canadian Cancer Trials Group and the Unicancer-GI–PRODIGE Group; Francois, E.; Ramee, J.-F.; Castanie, H.; Pracht, M.; Ghiringhelli, F.; Maillard, E.; Couffon, C.; Volet, J.; Bourgeois, V.; Chauvenet, M.; Blanc, J.-F.; Péré-Vergé, D.; De La Fouchardiere, C.; Adenis, A.; El Hajbi, F.; Bennouna, J.; Texereau, P.; Faroux, R.; Miglianico, L.; Platini, C.; Legoux, J.-L.; Caroli-Bosc, F.-X.; Bouhier-Leporrier, K.; Gagnaire, A.; Granger, V.; Lebrun-Ly, V.; Guimbaud, R.; Touchefeu, Y.; Gasmi, M.; Di Fiore, F.; Seitz, J. F.; Etienne, P.-L.; Ligeza Poisson, C.; Rinaldi, Y.; Baba-Hamed, N.; Bachet, J. B.; Aparicio, T.; Chone, L.; Guillet, M.; Forestier, J.; Terrebonne, E.; Hebbar, M.; Breysacher, G.; Andre, T.; Khemissa-Akouz, F.; Hautefeuille, V.; Guerin-Meyer, V.; Hartwig, J.; Becouarn, Y.; Malka, D.; Louvet, C.; Raoul, J.-L.; Cany, L.; Juzina, B.; Jouffroy, C.; Gourgou, S.; Rassouli, M.; Chalchal, H.; Renouf, D.; Wong, R.; Lemay, F.; Aubin, F.; Couture, F.; Mc Whirter, E.; Welch, S.; Kavan, P.; Findlay, B.; Cripps,

C.; Cano, P.; Ahmed, S.; Harb, M.; Pressnail, B.; Dowden, S.; O'Callaghan, C. Five-Year Outcomes of FOLFIRINOX vs Gemcitabine as Adjuvant Therapy for Pancreatic Cancer: A Randomized Clinical Trial. *JAMA Oncol.* **2022**, *8* (11), 1571. https://doi.org/10.1001/jamaoncol.2022.3829.

(157) Li, B.; Zhang, Q.; Castaneda, C.; Cook, S. Targeted Therapies in Pancreatic Cancer: A New Era of Precision Medicine. *Biomedicines* **2024**, *12* (10), 2175. https://doi.org/10.3390/biomedicines12102175.

(158) Lutfi, W.; Talamonti, M. S.; Kantor, O.; Wang, C.-H.; Stocker, S. J.; Bentrem, D. J.; Roggin, K. K.; Winchester, D. J.; Marsh, R.; Prinz, R. A.; Baker, M. S. Neoadjuvant External Beam Radiation Is Associated with No Benefit in Overall Survival for Early Stage Pancreatic Cancer. *Am. J. Surg.* **2017**, *213* (3), 521–525. https://doi.org/10.1016/j.amjsurg.2016.11.039.

(159) Liu, A. K. N.; Lefresne, S. Palliative Radiotherapy in Pancreatic Cancer: A Retrospective Study of 100 Cases and Regional Patterns of Practice. *Ann. Palliat. Med.* **2023**, *12* (5), 89199–89899.

(160) Balachandran, V. P.; Beatty, G. L.; Dougan, S. K. Broadening the Impact of Immunotherapy to Pancreatic Cancer: Challenges and Opportunities. *Gastroenterology* **2019**, *156* (7), 2056–2072. https://doi.org/10.1053/j.gastro.2018.12.038.

(161) Di Federico, A.; Mosca, M.; Pagani, R.; Carloni, R.; Frega, G.; De Giglio, A.; Rizzo, A.; Ricci, D.; Tavolari, S.; Di Marco, M.; Palloni, A.; Brandi, G. Immunotherapy in Pancreatic Cancer: Why Do We Keep Failing? A Focus on Tumor Immune Microenvironment, Predictive Biomarkers and Treatment Outcomes. *Cancers* **2022**, *14* (10), 2429. https://doi.org/10.3390/cancers14102429.

(162) Han, X.; Burrows, M.; Kim, L. C.; Xu, J. P.; Vostrejs, W.; Van Le, T. N.; Poltorack, C.; Jiang, Y.; Cukierman, E.; Stanger, B. Z.; Reiss, K. A.; Shaffer, S. M.; Mesaros, C.; Keith, B.; Simon, M. C. Cancer-Associated Fibroblasts Maintain Critical Pancreatic Cancer Cell Lipid Homeostasis in the Tumor Microenvironment. *Cell Rep.* **2024**, *43* (11), 114972. https://doi.org/10.1016/j.celrep.2024.114972.

(163) Wang, M.; Xue, W.; Yuan, H.; Wang, Z.; Yu, L. Nano-Drug Delivery Systems Targeting CAFs: A Promising Treatment for Pancreatic Cancer. *Int. J. Nanomedicine* **2024**, *Volume 19*, 2823–2849. https://doi.org/10.2147/IJN.S451151.

(164) Yamazaki, M.; Ishimoto, T. Targeting Cancer-Associated Fibroblasts: Eliminate or Reprogram? *Cancer Sci.* **2025**, *116* (3), 613–621. https://doi.org/10.1111/cas.16443.

(165) Hosein, A. N.; Brekken, R. A.; Maitra, A. Pancreatic Cancer Stroma: An Update on Therapeutic Targeting Strategies. *Nat. Rev. Gastroenterol. Hepatol.* **2020**, *17* (8), 487–505.

(166) Tian, C.; Öhlund, D.; Rickelt, S.; Lidström, T.; Huang, Y.; Hao, L.; Zhao, R. T.; Franklin, O.; Bhatia, S. N.; Tuveson, D. A.; Hynes, R. O. Cancer Cell–Derived Matrisome Proteins Promote Metastasis in Pancreatic Ductal Adenocarcinoma. *Cancer Res.* **2020**, *80* (7), 1461–1474. https://doi.org/10.1158/0008-5472.CAN-19-2578.

(167) Elaskalani, O.; Razak, N. B. A.; Falasca, M.; Metharom, P. Epithelial-Mesenchymal Transition as a Therapeutic Target for Overcoming Chemoresistance in Pancreatic Cancer. *World J. Gastrointest. Oncol.* **2017**, *9* (1), 37. https://doi.org/10.4251/wjgo.v9.i1.37.

(168) Gaianigo, N.; Melisi, D.; Carbone, C. EMT and Treatment Resistance in Pancreatic Cancer. *Cancers* **2017**, *9* (9), 122. https://doi.org/10.3390/cancers9090122.

(169) Peura, J.; Johnson, C.; Pitarresi, J. R. To EMT or Not to EMT: Ablation of

Mesenchymal Tumor Cell Lineages Reveals the Essential Role of EMT in Pancreatic Cancer Initiation and Evolution. *Cancer Res.* **2025**, *85* (12), 2146–2148. https://doi.org/10.1158/0008-5472.CAN-25-1443.

(170) Vilas-Boas, V.; Carvalho, F.; Espiña, B. Magnetic Hyperthermia for Cancer Treatment: Main Parameters Affecting the Outcome of In Vitro and In Vivo Studies. *Molecules* **2020**, *25* (12), 2874. https://doi.org/10.3390/molecules25122874.

(171) Behrouzkia, Z.; Joveini, Z.; Keshavarzi, B.; Eyvazzadeh, N.; Aghdam, R. Z. Hyperthermia: How Can It Be Used? *Oman Med. J.* **2016**, *31* (2), 89–97. https://doi.org/10.5001/omj.2016.19.

(172) Elming, P.; Sørensen, B.; Oei, A.; Franken, N.; Crezee, J.; Overgaard, J.; Horsman, M. Hyperthermia: The Optimal Treatment to Overcome Radiation Resistant Hypoxia. *Cancers* **2019**, *11* (1), 60. https://doi.org/10.3390/cancers11010060.

(173) Crezee, J.; Franken, N. A. P.; Oei, A. L. Hyperthermia-Based Anti-Cancer Treatments. *Cancers* **2021**, *13* (6), 1240–1240.

(174) Oei, A. L.; Vriend, L. E. M.; Crezee, J.; Franken, N. A. P.; Krawczyk, P. M. Effects of Hyperthermia on DNA Repair Pathways: One Treatment to Inhibit Them All. *Radiat. Oncol.* **2015**, *10* (1), 165. https://doi.org/10.1186/s13014-015-0462-0.

(175) Yi, G. Y.; Kim, M. J.; Kim, H. I.; Park, J.; Baek, S. H. Hyperthermia Treatment as a Promising Anti-Cancer Strategy: Therapeutic Targets, Perspective Mechanisms and Synergistic Combinations in Experimental Approaches. *Antioxidants* **2022**, *11* (4), 625–625.

(176) Song, C. W.; Park, H.; Griffin, R. J. Improvement of Tumor Oxygenation by Mild Hyperthermia. *Radiat. Res.* **2001**, *155* (4), 515–528. https://doi.org/10.1667/0033-7587(2001)155%255B0515:IOTOBM%255D2.0.CO;2.

(177) Lukácsi, S.; Munkácsy, G.; Győrffy, B. Harnessing Hyperthermia: Molecular, Cellular, and Immunological Insights for Enhanced Anticancer Therapies. *Integr. Cancer Ther.* **2024**, *23*, 15347354241242094. https://doi.org/10.1177/15347354241242094.

(178) Skitzki, J. J.; Repasky, E. A.; Evans, S. S. Hyperthermia as an Immunotherapy Strategy for Cancer. *Curr. Opin. Investig. Drugs Lond. Engl. 2000* **2009**, *10* (6), 550.

(179) Abreu, M. M.; Chocron, A. F.; Smadja, D. M. From Cold to Hot: Mechanisms of Hyperthermia in Modulating Tumor Immunology for Enhanced Immunotherapy. *Front. Immunol.* **2025**, *16*, 1487296. https://doi.org/10.3389/fimmu.2025.1487296.

(180) Piehler, S.; Wucherpfennig, L.; Tansi, F. L.; Berndt, A.; Quaas, R.; Teichgraeber, U.; Hilger, I. Hyperthermia Affects Collagen Fiber Architecture and Induces Apoptosis in Pancreatic and Fibroblast Tumor Hetero-Spheroids in Vitro. *Nanomedicine Nanotechnol. Biol. Med.* **2020**, *28*, 102183. https://doi.org/10.1016/j.nano.2020.102183.

(181) Hirunsai, M.; Srikuea, R.; Yimlamai, T. Heat Stress Promotes Extracellular Matrix Remodelling via TGF- **β** 1 and MMP-2/TIMP-2 Modulation in Tenotomised Soleus and Plantaris Muscles. *Int. J. Hyperthermia* **2015**, *31* (4), 336–348. https://doi.org/10.3109/02656736.2014.1002019.

(182) 竹内晃; 蓮村ひろみ; 関谷巳知秋; 白髭正一; 原山恵美; 琴寄幸子; 竹内隆. Whole-Body-Hyperthermia-Induced Changes Interstitial Collagenase Activity and an Extracellular Matrix Remodeling Theory. *Therm. Med.* **2010**, *26* (4), 109–119.

(183) *Hyperthermia to Treat Cancer - NCI*. https://www.cancer.gov/about-cancer/treatment/types/hyperthermia (accessed 2025-08-21).

(184) *What Is Hyperthermia? | Hyperthermia to Treat Cancer*.

https://www.cancer.org/cancer/managing-cancer/treatment-types/hyperthermia.html (accessed 2025-08-21).
(185) Kok, H. P.; Cressman, E. N. K.; Ceelen, W.; Brace, C. L.; Ivkov, R.; Grüll, H.; Ter Haar, G.; Wust, P.; Crezee, J. Heating Technology for Malignant Tumors: A Review. *Int. J. Hyperthermia* **2020**, *37* (1), 711–741. https://doi.org/10.1080/02656736.2020.1779357.
(186) *BSD 500 Hyperthermia System from BSD Medical*. News-Medical. https://www.news-medical.net/BSD-500-Hyperthermia-System-from-BSD-Medical (accessed 2025-08-21).
(187) ltd, R. and M. *Hyperthermia Cancer Treatment - Global Strategic Business Report*. https://www.researchandmarkets.com/reports/6089499/hyperthermia-cancer-treatment-global-strategic (accessed 2025-08-21).
(188) admin_h99g6f6. *New Oncothermia user clinic in North America - Oncotherm Kft.* https://oncotherm.com/new-oncothermia-user-clinic-in-north-america/ (accessed 2025-08-21).
(189) Bakrin, N.; Bereder, J.-M.; Decullier, E.; Classe, J.-M.; Msika, S.; Lorimier, G.; Abboud, K.; Meeus, P.; Ferron, G.; Quenet, F. Peritoneal Carcinomatosis Treated with Cytoreductive Surgery and Hyperthermic Intraperitoneal Chemotherapy (HIPEC) for Advanced Ovarian Carcinoma: A French Multicentre Retrospective Cohort Study of 566 Patients. *Eur. J. Surg. Oncol. EJSO* **2013**, *39* (12), 1435–1443.
(190) Forika, G.; Kiss, E.; Petovari, G.; Danko, T.; Gellert, A. B.; Krenacs, T. Modulated Electro-Hyperthermia Supports the Effect of Gemcitabine Both in Sensitive and Resistant Pancreas Adenocarcinoma Cell Lines. *Pathol. Oncol. Res.* **2021**, *27*, 1610048. https://doi.org/10.3389/pore.2021.1610048.
(191) Maurici, C. E.; Colenbier, R.; Wylleman, B.; Brancato, L.; van Zwol, E.; Van den Bossche, J.; Timmermans, J.-P.; Giovannetti, E.; Mori da Cunha, M. G. M. C.; Bogers, J. Hyperthermia Enhances Efficacy of Chemotherapeutic Agents in Pancreatic Cancer Cell Lines. *Biomolecules* **2022**, *12* (5), 651–651.
(192) Van Der Horst, A.; Versteijne, E.; Besselink, M. G. H.; Daams, J. G.; Bulle, E. B.; Bijlsma, M. F.; Wilmink, J. W.; Van Delden, O. M.; Van Hooft, J. E.; Franken, N. A. P.; Van Laarhoven, H. W. M.; Crezee, J.; Van Tienhoven, G. The Clinical Benefit of Hyperthermia in Pancreatic Cancer: A Systematic Review. *Int. J. Hyperthermia* **2018**, *34* (7), 969–979. https://doi.org/10.1080/02656736.2017.1401126.
(193) Lambin, T.; Lafon, C.; Drainville, R. A.; Pioche, M.; Prat, F. Locoregional Therapies and Their Effects on the Tumoral Microenvironment of Pancreatic Ductal Adenocarcinoma. *World J. Gastroenterol.* **2022**, *28* (13), 1288–1303. https://doi.org/10.3748/wjg.v28.i13.1288.
(194) Beik, J.; Abed, Z.; Ghoreishi, F. S.; Hosseini-Nami, S.; Mehrzadi, S.; Shakeri-Zadeh, A.; Kamrava, S. K. Nanotechnology in Hyperthermia Cancer Therapy: From Fundamental Principles to Advanced Applications. *J. Controlled Release* **2016**, *235*, 205–221.
(195) Lee, N.; Yoo, D.; Ling, D.; Cho, M. H.; Hyeon, T.; Cheon, J. Iron Oxide Based Nanoparticles for Multimodal Imaging and Magnetoresponsive Therapy. *Chem. Rev.* **2015**, *115* (19), 10637–10689.
(196) Szwed, M.; Marczak, A. Application of Nanoparticles for Magnetic Hyperthermia for Cancer Treatment—the Current State of Knowledge. *Cancers* **2024**, *16* (6), 1156.
(197) Liu, X.; Zhang, Y.; Wang, Y.; Zhu, W.; Li, G.; Ma, X.; Zhang, Y.; Chen, S.; Tiwari, S.; Shi, K.; Zhang, S.; Fan, H. M.; Zhao, Y. X.; Liang, X.-J. Comprehensive Understanding of Magnetic Hyperthermia for Improving Antitumor Therapeutic Efficacy. *Theranostics* **2020**, *10* (8), 3793–3815.

https://doi.org/10.7150/thno.40805.
(198) Chu, S.; Stochaj, U. Exploring Near-Infrared Absorbing Nanocarriers to Overcome Cancer Drug Resistance. *Cancer Drug Resist.* **2020**. https://doi.org/10.20517/cdr.2020.20.
(199) Wu, X.; Suo, Y.; Shi, H.; Liu, R.; Wu, F.; Wang, T.; Ma, L.; Liu, H.; Cheng, Z. Deep-Tissue Photothermal Therapy Using Laser Illumination at NIR-IIa Window. *Nano-Micro Lett.* **2020**, *12* (1), 38. https://doi.org/10.1007/s40820-020-0378-6.
(200) Cao, J.; Zhu, B.; Zheng, K.; He, S.; Meng, L.; Song, J.; Yang, H. Recent Progress in NIR-II Contrast Agent for Biological Imaging. *Front. Bioeng. Biotechnol.* **2020**, *7*, 487. https://doi.org/10.3389/fbioe.2019.00487.
(201) Skinner, W. H.; Salimi, M.; Moran, L.; Blein-Dezayes, I.; Mehta, M.; Mosca, S.; Vaideanu, A.-G.; Gardner, B.; Palombo, F.; Schätzlein, A. G.; Matousek, P.; Harries, T.; Stone, N. Plasmonic Nanoparticles for Photothermal Therapy: Benchmarking of Photothermal Properties and Modeling of Heating at Depth in Human Tissues. *J. Phys. Chem. C* **2025**, *129* (3), 1864–1872. https://doi.org/10.1021/acs.jpcc.4c06381.
(202) Taylor, M. L.; Wilson, R. E.; Amrhein, K. D.; Huang, X. Gold Nanorod-Assisted Photothermal Therapy and Improvement Strategies. *Bioengineering* **2022**, *9* (5), 200. https://doi.org/10.3390/bioengineering9050200.
(203) Riley, R. S.; Day, E. S. Gold Nanoparticle-mediated Photothermal Therapy: Applications and Opportunities for Multimodal Cancer Treatment. *WIREs Nanomedicine Nanobiotechnology* **2017**, *9* (4), e1449. https://doi.org/10.1002/wnan.1449.
(204) Espinosa, A.; Kolosnjaj-Tabi, J.; Abou-Hassan, A.; Plan Sangnier, A.; Curcio, A.; Silva, A. K. A.; Di Corato, R.; Neveu, S.; Pellegrino, T.; Liz-Marzán, L. M. Magnetic (Hyper) Thermia or Photothermia? Progressive Comparison of Iron Oxide and Gold Nanoparticles Heating in Water, in Cells, and in Vivo. *Adv. Funct. Mater.* **2018**, *28* (37), 1803660–1803660.
(205) Sangnier, A. P.; Preveral, S.; Curcio, A.; Silva, A. K. A.; Lefèvre, C. T.; Pignol, D.; Lalatonne, Y.; Wilhelm, C. Targeted Thermal Therapy with Genetically Engineered Magnetite Magnetosomes@ RGD: Photothermia Is Far More Efficient than Magnetic Hyperthermia. *J. Controlled Release* **2018**, *279*, 271–281.
(206) Espinosa, A.; Di Corato, R.; Kolosnjaj-Tabi, J.; Flaud, P.; Pellegrino, T.; Wilhelm, C. Duality of Iron Oxide Nanoparticles in Cancer Therapy: Amplification of Heating Efficiency by Magnetic Hyperthermia and Photothermal Bimodal Treatment. *ACS Nano* **2016**, *10* (2), 2436–2446.
(207) Van de Walle, A.; Figuerola, A.; Espinosa, A.; Abou-Hassan, A.; Estrader, M.; Wilhelm, C. Emergence of Magnetic Nanoparticles in Photothermal and Ferroptotic Therapies. *Mater. Horiz.* **2023**, *10* (11), 4757–4775.
(208) Mazuel, F.; Espinosa, A.; Luciani, N.; Reffay, M.; Le Borgne, R.; Motte, L.; Desboeufs, K.; Michel, A.; Pellegrino, T.; Lalatonne, Y. Massive Intracellular Biodegradation of Iron Oxide Nanoparticles Evidenced Magnetically at Single-Endosome and Tissue Levels. *ACS Nano* **2016**, *10* (8), 7627–7638.
(209) Estelrich, J.; Busquets, M. A. Iron Oxide Nanoparticles in Photothermal Therapy. *Molecules* **2018**, *23* (7), 1567–1567.
(210) Roca, A. G.; López-Barbera, J. F.; Lafuente, A.; Özel, F.; Fantechi, E.; Muro-Cruces, J.; Hémadi, M.; Sepúlveda, B.; Nogués, J. Iron Oxide Nanoparticles (Fe3O4, γ-Fe2O3 and FeO) as Photothermal Heat Mediators in the First, Second and Third Biological Windows. *Phys. Rep.* **2023**, *1043*, 1–35.
(211) Díaz-Riascos, Z. V.; Llaguno-Munive, M.; Lafuente-Gómez, N.; Luengo, Y.; Holmes, S.; Volatron, J.; Ibarrola, O.; Mancilla, S.; Sarno, F.; Aguirre, J. J.; Razafindrakoto, S.; Southern, P.; Terán, F. J.; Keogh, A.; Salas, G.; Prina-Mello,

A.; Lacal, J. C.; Del Pozo, A.; Pankhurst, Q. A.; Hidalgo, M.; Gazeau, F.; Somoza, Á.; Schwartz, S.; Abasolo, I. Preclinical Development of Magnetic Nanoparticles for Hyperthermia Treatment of Pancreatic Cancer. *ACS Appl. Mater. Interfaces* **2025**, *17* (2), 2924–2939. https://doi.org/10.1021/acsami.4c16129.

(212) Henderson, T. A.; Morries, L. Near-Infrared Photonic Energy Penetration: Can Infrared Phototherapy Effectively Reach the Human Brain? *Neuropsychiatr. Dis. Treat.* **2015**, 2191. https://doi.org/10.2147/NDT.S78182.

(213) Chen, K.; Yin, B.; Luo, Q.; Liu, Y.; Wang, Y.; Liao, Y.; Li, Y.; Chen, X.; Sun, B.; Zhou, N.; Liu, H.; Peng, C.; Liu, S.; Cheng, W.; Song, G. Endoscopically Guided Interventional Photodynamic Therapy for Orthotopic Pancreatic Ductal Adenocarcinoma Based on NIR-II Fluorescent Nanoparticles. *Theranostics* **2023**, *13* (13), 4469–4481. https://doi.org/10.7150/thno.84164.

(214) Nomura, S.; Morimoto, Y.; Tsujimoto, H.; Arake, M.; Harada, M.; Saitoh, D.; Hara, I.; Ozeki, E.; Satoh, A.; Takayama, E.; Hase, K.; Kishi, Y.; Ueno, H. Highly Reliable, Targeted Photothermal Cancer Therapy Combined with Thermal Dosimetry Using a near-Infrared Absorbent. *Sci. Rep.* **2020**, *10* (1), 9765. https://doi.org/10.1038/s41598-020-66646-x.

(215) Liu, X.; Zhou, W.; Wang, T.; Miao, S.; Lan, S.; Wei, Z.; Meng, Z.; Dai, Q.; Fan, H. Highly Localized, Efficient, and Rapid Photothermal Therapy Using Gold Nanobipyramids for Liver Cancer Cells Triggered by Femtosecond Laser. *Sci. Rep.* **2023**, *13* (1), 3372. https://doi.org/10.1038/s41598-023-30526-x.

(216) Bianchi, L.; Baroni, S.; Paroni, G.; Violatto, M. B.; Moscatiello, G. Y.; Panini, N.; Russo, L.; Fiordaliso, F.; Colombo, L.; Diomede, L.; Saccomandi, P.; Bigini, P. Thermal Effects and Biological Response of Breast and Pancreatic Cancer Cells Undergoing Gold Nanorod-Assisted Photothermal Therapy. *J. Photochem. Photobiol. B* **2024**, *259*, 112993. https://doi.org/10.1016/j.jphotobiol.2024.112993.

(217) Robert, J.; Chauhan, D. S.; Cherifi, K.; Phan, Q. T.; Sangwan, V.; De Crescenzo, G.; Banquy, X. Hybrid Nanocarrier Delivers Immuno-Photothermal Therapy to Modulate Pancreatic Tumor Microenvironment. *ACS Appl. Bio Mater.* **2025**, *8* (6), 5239–5251. https://doi.org/10.1021/acsabm.5c00562.

(218) Yang, C.; Chan, K. K.; Xu, G.; Yin, M.; Lin, G.; Wang, X.; Lin, W.-J.; Birowosuto, M. D.; Zeng, S.; Ogi, T.; Okuyama, K.; Permatasari, F. A.; Iskandar, F.; Chen, C.-K.; Yong, K.-T. Biodegradable Polymer-Coated Multifunctional Graphene Quantum Dots for Light-Triggered Synergetic Therapy of Pancreatic Cancer. *ACS Appl. Mater. Interfaces* **2019**, *11* (3), 2768–2781. https://doi.org/10.1021/acsami.8b16168.

(219) Wang, M.; Li, Y.; Wang, M.; Liu, K.; Hoover, A. R.; Li, M.; Towner, R. A.; Mukherjee, P.; Zhou, F.; Qu, J.; Chen, W. R. Synergistic Interventional Photothermal Therapy and Immunotherapy Using an Iron Oxide Nanoplatform for the Treatment of Pancreatic Cancer. *Acta Biomater.* **2022**, *138*, 453–462. https://doi.org/10.1016/j.actbio.2021.10.048.

(220) Teng, T.; Lin, R.; Lin, Z.; Ke, K.; Lin, X.; Pan, M.; Zhang, D.; Huang, H. Photothermal Augment Stromal Disrupting Effects for Enhanced Abraxane Synergy Chemotherapy in Pancreatic Cancer PDX Mode. *Biomater. Sci.* **2020**, *8* (12), 3278–3285. https://doi.org/10.1039/D0BM00549E.

(221) Zhang, F.; Hu, Q.; Li, B.; Huang, Y.; Wang, M.; Shao, S.; Tang, H.; Yao, Z.; Ping, Y.; Liang, T. A Biomimetic Nanodrug for Enhanced Chemotherapy of Pancreatic Tumors. *J. Controlled Release* **2023**, *354*, 835–850.

(222) Hu, Y.; Qi, E.; Yun, C.; Li, X.; Liu, F.; Cheng, Z.; Guan, N.; Wang, Q.; Zhao, H.; Xiao, W.; Peng, L.; Yang, J.; Yu, X. Photothermal Therapy Combined with a STING Agonist Induces Pyroptosis, and Gasdermin D Could Be a New Biomarker for Guiding the Treatment of Pancreatic Cancer. *J. Transl. Med.* **2025**, *23* (1), 271. https://doi.org/10.1186/s12967-025-06247-2.

(223) Guo, Y.; Zhang, Z.; Kim, D.-H.; Li, W.; Nicolai, J.; Procissi, D.; Huan, Y.; Han, G.; Omary, R. A.; Larson, A. C. Photothermal Ablation of Pancreatic Cancer Cells with Hybrid Iron-Oxide Core Gold-Shell Nanoparticles. *Int. J. Nanomedicine* **2013**, 3437–3446.
(224) Mocan, L.; Ilie, I.; Tabaran, F. A.; Dana, B.; Zaharie, F.; Zdrehus, C.; Puia, C.; Mocan, T.; Muntean, V.; Teodora, P. Surface Plasmon Resonance-Induced Photoactivation of Gold Nanoparticles as Mitochondria-Targeted Therapeutic Agents for Pancreatic Cancer. *Expert Opin. Ther. Targets* **2013**, *17* (12), 1383–1393.
(225) Mocan, T.; Matea, C. T.; Cojocaru, I.; Ilie, I.; Tabaran, F. A.; Zaharie, F.; Iancu, C.; Bartos, D.; Mocan, L. Photothermal Treatment of Human Pancreatic Cancer Using PEGylated Multi-Walled Carbon Nanotubes Induces Apoptosis by Triggering Mitochondrial Membrane Depolarization Mechanism. *J. Cancer* **2014**, *5* (8), 679.
(226) Joubert, F.; Martin, L.; Perrier, S.; Pasparakis, G. Development of a Gemcitabine-Polymer Conjugate with Prolonged Cytotoxicity against a Pancreatic Cancer Cell Line. *ACS Macro Lett.* **2017**, *6* (5), 535–540. https://doi.org/10.1021/acsmacrolett.7b00160.
(227) Poudel, B. K.; Gupta, B.; Ramasamy, T.; Thapa, R. K.; Pathak, S.; Oh, K. T.; Jeong, J.-H.; Choi, H.-G.; Yong, C. S.; Kim, J. O. PEGylated Thermosensitive Lipid-Coated Hollow Gold Nanoshells for Effective Combinational Chemo-Photothermal Therapy of Pancreatic Cancer. *Colloids Surf. B Biointerfaces* **2017**, *160*, 73–83. https://doi.org/10.1016/j.colsurfb.2017.09.010.
(228) Banstola, A.; Pham, T. T.; Jeong, J.-H.; Yook, S. Polydopamine-Tailored Paclitaxel-Loaded Polymeric Microspheres with Adhered NIR-Controllable Gold Nanoparticles for Chemo-Phototherapy of Pancreatic Cancer. *Drug Deliv.* **2019**, *26* (1), 629–640. https://doi.org/10.1080/10717544.2019.1628118.
(229) Sujai, P. T.; Shamjith, S.; Joseph, M. M.; Maiti, K. K. Elucidating Gold–MnO_2 Core–Shell Nanoenvelope for Real Time SERS-Guided Photothermal Therapy on Pancreatic Cancer Cells. *ACS Appl. Bio Mater.* **2021**, *4* (6), 4962–4972. https://doi.org/10.1021/acsabm.1c00241.
(230) Nedelcu, A.; Mocan, T.; Sabau, L. I.; Matea, C. T.; Tabaran, F.; Pop, T.; Delcea, C.; Mosteanu, O.; Mocan, L. In Vitro Photothermal Therapy of Pancreatic Cancer Mediated by Immunoglobulin G-Functionalized Silver Nanoparticles. *Sci. Rep.* **2024**, *14* (1), 14417. https://doi.org/10.1038/s41598-024-63142-4.
(231) Yılmaz, E.; Kacaroglu, D.; Ozden, A. K.; Aydogan, N. Gold Nanoparticles Decorated FOLFIRINOX Loaded Liposomes for Synergistic Therapy of Pancreatic Cancer. *Int. J. Pharm.* **2025**, *669*, 125067. https://doi.org/10.1016/j.ijpharm.2024.125067.
(232) Wang, S.; Zhang, Q.; Luo, X. F.; Li, J.; He, H.; Yang, F.; Di, Y.; Jin, C.; Jiang, X. G.; Shen, S. Magnetic Graphene-Based Nanotheranostic Agent for Dual-Modality Mapping Guided Photothermal Therapy in Regional Lymph Nodal Metastasis of Pancreatic Cancer. *Biomaterials* **2014**, *35* (35), 9473–9483.
(233) Hu, Y.; Chi, C.; Wang, S.; Wang, L.; Liang, P.; Liu, F.; Shang, W.; Wang, W.; Zhang, F.; Li, S.; Shen, H.; Yu, X.; Liu, H.; Tian, J. A Comparative Study of Clinical Intervention and Interventional Photothermal Therapy for Pancreatic Cancer. *Adv. Mater.* **2017**, *29* (33), 1700448. https://doi.org/10.1002/adma.201700448.
(234) Li, H.; Wang, P.; Deng, Y.; Zeng, M.; Tang, Y.; Zhu, W.-H.; Cheng, Y. Combination of Active Targeting, Enzyme-Triggered Release and Fluorescent Dye into Gold Nanoclusters for Endomicroscopy-Guided Photothermal/Photodynamic Therapy to Pancreatic Ductal Adenocarcinoma. *Biomaterials* **2017**, *139*, 30–38. https://doi.org/10.1016/j.biomaterials.2017.05.030.

(235) Zhao, R.; Han, X.; Li, Y.; Wang, H.; Ji, T.; Zhao, Y.; Nie, G. Photothermal Effect Enhanced Cascade-Targeting Strategy for Improved Pancreatic Cancer Therapy by Gold Nanoshell@ Mesoporous Silica Nanorod. *ACS Nano* **2017**, *11* (8), 8103–8113.

(236) Jiang, T.; Zhang, B.; Shen, S.; Tuo, Y.; Luo, Z.; Hu, Y.; Pang, Z.; Jiang, X. Tumor Microenvironment Modulation by Cyclopamine Improved Photothermal Therapy of Biomimetic Gold Nanorods for Pancreatic Ductal Adenocarcinomas. *ACS Appl. Mater. Interfaces* **2017**, *9* (37), 31497–31508.

(237) Zhang, F.; Han, X.; Hu, Y.; Wang, S.; Liu, S.; Pan, X.; Wang, H.; Ma, J.; Wang, W.; Li, S.; Wu, Q.; Shen, H.; Yu, X.; Yuan, Q.; Liu, H. Interventional Photothermal Therapy Enhanced Brachytherapy: A New Strategy to Fight Deep Pancreatic Cancer. *Adv. Sci.* **2019**, *6* (5), 1801507. https://doi.org/10.1002/advs.201801507.

(238) Lu, G.-H.; Shang, W.-T.; Deng, H.; Han, Z.-Y.; Hu, M.; Liang, X.-Y.; Fang, C.-H.; Zhu, X.-H.; Fan, Y.-F.; Tian, J. Targeting Carbon Nanotubes Based on IGF-1R for Photothermal Therapy of Orthotopic Pancreatic Cancer Guided by Optical Imaging. *Biomaterials* **2019**, *195*, 13–22.

(239) Yu, Q.; Qiu, Y.; Li, J.; Tang, X.; Wang, X.; Cun, X.; Xu, S.; Liu, Y.; Li, M.; Zhang, Z.; He, Q. Targeting Cancer-Associated Fibroblasts by Dual-Responsive Lipid-Albumin Nanoparticles to Enhance Drug Perfusion for Pancreatic Tumor Therapy. *J. Controlled Release* **2020**, *321*, 564–575. https://doi.org/10.1016/j.jconrel.2020.02.040.

(240) Jia, X.; Xu, W.; Ye, Z.; Wang, Y.; Dong, Q.; Wang, E.; Li, D.; Wang, J. Functionalized Graphene@Gold Nanostar/Lipid for Pancreatic Cancer Gene and Photothermal Synergistic Therapy under Photoacoustic/Photothermal Imaging Dual-Modal Guidance. *Small* **2020**, *16* (39), 2003707. https://doi.org/10.1002/smll.202003707.

(241) Wang, Q.; Zhu, X.; Wu, Z.; Sun, T.; Huang, W.; Wang, Z.; Ding, X.; Jiang, C.; Li, F. Theranostic Nanoparticles Enabling the Release of Phosphorylated Gemcitabine for Advanced Pancreatic Cancer Therapy. *J. Mater. Chem. B* **2020**, *8* (12), 2410–2417. https://doi.org/10.1039/D0TB00017E.

(242) Zhan, X.; Nie, X.; Gao, F.; Zhang, C.; You, Y.-Z.; Yu, Y. An NIR-Activated Polymeric Nanoplatform with ROS- and Temperature-Sensitivity for Combined Photothermal Therapy and Chemotherapy of Pancreatic Cancer. *Biomater. Sci.* **2020**, *8* (21), 5931–5940. https://doi.org/10.1039/D0BM01324B.

(243) Shi, X.; Li, Q.; Zhang, C.; Pei, H.; Wang, G.; Zhou, H.; Fan, L.; Yang, K.; Jiang, B.; Wang, F.; Zhu, R. Semiconducting Polymer Nano-Radiopharmaceutical for Combined Radio-Photothermal Therapy of Pancreatic Tumor. *J. Nanobiotechnology* **2021**, *19* (1), 337. https://doi.org/10.1186/s12951-021-01083-0.

(244) Li, S.; Zhang, W.; Xing, R.; Yuan, C.; Xue, H.; Yan, X. Supramolecular Nanofibrils Formed by Coassembly of Clinically Approved Drugs for Tumor Photothermal Immunotherapy. *Adv. Mater.* **2021**, *33* (21), 2100595. https://doi.org/10.1002/adma.202100595.

(245) Sun, J.; Wan, Z.; Xu, J.; Luo, Z.; Ren, P.; Zhang, B.; Diao, D.; Huang, Y.; Li, S. Tumor Size-Dependent Abscopal Effect of Polydopamine-Coated All-in-One Nanoparticles for Immunochemo-Photothermal Therapy of Early- and Late-Stage Metastatic Cancer. *Biomaterials* **2021**, *269*, 120629. https://doi.org/10.1016/j.biomaterials.2020.120629.

(246) Yu, Q.; Tang, X.; Zhao, W.; Qiu, Y.; He, J.; Wan, D.; Li, J.; Wang, X.; He, X.; Liu, Y.; Li, M.; Zhang, Z.; He, Q. Mild Hyperthermia Promotes Immune Checkpoint Blockade-Based Immunotherapy against Metastatic Pancreatic Cancer Using Size-Adjustable Nanoparticles. *Acta Biomater.* **2021**, *133*, 244–256. https://doi.org/10.1016/j.actbio.2021.05.002.

(247) Liu, S.; He, J.; Song, R.; Zhang, M.; Huang, L.; Chen, J.; Wang, M.; Liu, F.; Zhou, F. Fe_2 P Nanorods Based Photothermal Therapy Combined with Immune Checkpoint Inhibitors for Pancreatic Cancer. *Nanophotonics* **2021**, *10* (12), 3267–3278. https://doi.org/10.1515/nanoph-2021-0196.
(248) Yang, X.-Y.; Zhang, J.-G.; Zhou, Q.-M.; Yu, J.-N.; Lu, Y.-F.; Wang, X.-J.; Zhou, J.-P.; Ding, X.-F.; Du, Y.-Z.; Yu, R.-S. Extracellular Matrix Modulating Enzyme Functionalized Biomimetic Au Nanoplatform-Mediated Enhanced Tumor Penetration and Synergistic Antitumor Therapy for Pancreatic Cancer. *J. Nanobiotechnology* **2022**, *20* (1), 524. https://doi.org/10.1186/s12951-022-01738-6.
(249) Tong, S.; Yu, Z.; Yin, F.; Yang, Q.; Chu, J.; Huang, L.; Gao, W.; Qian, M. Manganese-Based Prussian Blue Nanoparticles Inhibit Tumor Proliferation and Migration via the MAPK Pathway in Pancreatic Cancer. *Front. Chem.* **2022**, *10*, 1026924. https://doi.org/10.3389/fchem.2022.1026924.
(250) Hu, Q.; Xu, M.; Feng, J.; Xie, H.; Li, J.; He, Y.; Tang, G.; Guo, B. Hyperthermia-Induced Stellate Cell Deactivation to Enhance Dual Chemo and pH-Responsive Photothermal Therapy for Pancreatic Cancers. *Nanoscale* **2022**, *14* (42), 15735–15748.
(251) Cheng, Y.; Zheng, X.; Zhang, L.; Zhao, J.; Hu, L.; Wang, S. Enhanced Photothermal and Chemotherapy of Pancreatic Tumors by Degrading the Extracellular Matrix. *Colloids Surf. B Biointerfaces* **2023**, *221*, 113010. https://doi.org/10.1016/j.colsurfb.2022.113010.
(252) Liu, L.; Xiao, X.; Guo, J.; Wang, J.; Liu, S.; Wang, M.; Peng, Q.; Jiang, N. Aptamer and Peptide-Engineered Polydopamine Nanospheres for Target Delivery and Tumor Perfusion in Synergistic Chemo-Phototherapy of Pancreatic Cancer. *ACS Appl. Mater. Interfaces* **2023**, *15* (13), 16539–16551. https://doi.org/10.1021/acsami.3c01967.
(253) Xu, L.; Wu, R.; Ni, J.; Jin, L.; Xu, K.; Zhu, Y.; Hong, L.; Chen, C.; Wang, L.; Zhu, L.; Zhou, W.; Shen, W.; Wang, J. Black TiO2-Based Nanoparticles as Toll-like Receptor Stimulator Delivery System for Enhanced Photothermal-Immunotherapy of Pancreatic Cancer. *Cancer Nanotechnol.* **2024**, *15* (1), 27. https://doi.org/10.1186/s12645-024-00266-2.
(254) Yang, Y.; Liu, Y.; Weng, J.; Wen, X.; Liu, Y.; Ye, D. A Carbonic Anhydrase-Targeted NIR-II Fluorescent Cisplatin Theranostic Nanoparticle for Combined Therapy of Pancreatic Tumors. *Biomaterials* **2024**, *305*, 122454. https://doi.org/10.1016/j.biomaterials.2023.122454.
(255) Jin, Y.; Huang, J.; Tang, Y.; Li, Z.; Zhang, A.; Yang, Z.; Song, J.; Huang, X.; Bai, Y.; Sun, C.; Wu, X.; Cheng, J.; Wang, L.; Zhang, Q.; Yao, W. Boosting Ferroptosis by Intervention of Redox Balance and Synergetic with Photothermal/Photodynamic Therapy for Suppression of Pancreatic Cancer. *Chem. Eng. J.* **2024**, *497*, 154569. https://doi.org/10.1016/j.cej.2024.154569.
(256) Meng, Y.; Chen, C.; Lin, R.; Zheng, L.; Fan, Y.; Zhang, M.; Zhang, Z.; Shi, H.; Zheng, X.; Chen, J.; Chen, D.; Teng, T.; Chen, B. Mitochondria-Targeting Virus-Like Gold Nanoparticles Enhance Chemophototherapeutic Efficacy Against Pancreatic Cancer in a Xenograft Mouse Model. *Int. J. Nanomedicine* **2024**, *Volume 19*, 14059–14074. https://doi.org/10.2147/IJN.S497346.
(257) Hickman, J. A.; Graeser, R.; de Hoogt, R.; Vidic, S.; Brito, C.; Gutekunst, M.; van der Kuip, H. Three-dimensional Models of Cancer for Pharmacology and Cancer Cell Biology: Capturing Tumor Complexity in Vitro/Ex Vivo. *Biotechnol. J.* **2014**, *9* (9), 1115–1128.
(258) Trujillo-de Santiago, G.; Flores-Garza, B. G.; Tavares-Negrete, J. A.; Lara-Mayorga, I. M.; González-Gamboa, I.; Zhang, Y. S.; Rojas-Martínez, A.; Ortiz-López, R.; Álvarez, M. M. The Tumor-on-Chip: Recent Advances in the

Development of Microfluidic Systems to Recapitulate the Physiology of Solid Tumors. *Materials* **2019**, *12* (18), 2945.
(259) Rauner, G.; Gupta, P. B.; Kuperwasser, C. From 2D to 3D and beyond: The Evolution and Impact of in Vitro Tumor Models in Cancer Research. *Nat. Methods* **2025**. https://doi.org/10.1038/s41592-025-02769-1.
(260) Thorel, L.; Perréard, M.; Florent, R.; Divoux, J.; Coffy, S.; Vincent, A.; Gaggioli, C.; Guasch, G.; Gidrol, X.; Weiswald, L.-B. Patient-Derived Tumor Organoids: A New Avenue for Preclinical Research and Precision Medicine in Oncology. *Exp. Mol. Med.* **2024**, *56* (7), 1531–1551.
(261) Jouybar, M.; de Winde, C. M.; Wolf, K.; Friedl, P.; Mebius, R. E.; den Toonder, J. M. Cancer-on-Chip Models for Metastasis: Importance of the Tumor Microenvironment. *Trends Biotechnol.* **2024**, *42* (4), 431–448.
(262) Bouquerel, C.; Dubrova, A.; Hofer, I.; Phan, D. T. T.; Bernheim, M.; Ladaigue, S.; Cavaniol, C.; Maddalo, D.; Cabel, L.; Mechta-Grigoriou, F. Bridging the Gap between Tumor-on-Chip and Clinics: A Systematic Review of 15 Years of Studies. *Lab. Chip* **2023**.
(263) Nguyen, D.-H. T.; Lee, E.; Alimperti, S.; Norgard, R. J.; Wong, A.; Lee, J. J.-K.; Eyckmans, J.; Stanger, B. Z.; Chen, C. S. A Biomimetic Pancreatic Cancer On-Chip Reveals Endothelial Ablation via ALK7 Signaling. *Sci. Adv.* **2019**, *5* (8), eaav6789–eaav6789.
(264) Moon, H.; Ozcelikkale, A.; Yang, Y.; Elzey, B. D.; Konieczny, S. F.; Han, B. An Engineered Pancreatic Cancer Model with Intra-Tumoral Heterogeneity of Driver Mutations. *Lab. Chip* **2020**, *20* (20), 3720–3732.
(265) Bradney, M. J.; Venis, S. M.; Yang, Y.; Konieczny, S. F.; Han, B. A Biomimetic Tumor Model of Heterogeneous Invasion in Pancreatic Ductal Adenocarcinoma. *Small* **2020**, *16* (10), 1905500.
(266) Acosta, M. A.; Jiang, X.; Huang, P.-K.; Cutler, K. B.; Grant, C. S.; Walker, G. M.; Gamcsik, M. P. A Microfluidic Device to Study Cancer Metastasis under Chronic and Intermittent Hypoxia. *Biomicrofluidics* **2014**, *8* (5).
(267) Beer, M.; Kuppalu, N.; Stefanini, M.; Becker, H.; Schulz, I.; Manoli, S.; Schuette, J.; Schmees, C.; Casazza, A.; Stelzle, M. A Novel Microfluidic 3D Platform for Culturing Pancreatic Ductal Adenocarcinoma Cells: Comparison with in Vitro Cultures and in Vivo Xenografts. *Sci. Rep.* **2017**, *7* (1), 1325.
(268) Hernández-Hatibi, S.; Guerrero, P. E.; Garcia-Aznar, J. M.; Garcia-Gareta, E. Polydopamine Interfacial Coating for Stable Tumor-on-a-Chip Models: Application for Pancreatic Ductal Adenocarcinoma. *Biomacromolecules* **2024**, *25* (8), 5169–5180.
(269) Drifka, C. R.; Eliceiri, K. W.; Weber, S. M.; Kao, W. J. A Bioengineered Heterotypic Stroma–Cancer Microenvironment Model to Study Pancreatic Ductal Adenocarcinoma. *Lab. Chip* **2013**, *13* (19), 3965–3975.
(270) Lee, J.-H.; Kim, S.-K.; Khawar, I. A.; Jeong, S.-Y.; Chung, S.; Kuh, H.-J. Microfluidic Co-Culture of Pancreatic Tumor Spheroids with Stellate Cells as a Novel 3D Model for Investigation of Stroma-Mediated Cell Motility and Drug Resistance. *J. Exp. Clin. Cancer Res.* **2018**, *37*, 1–12.
(271) Gioeli, D.; Snow, C. J.; Simmers, M. B.; Hoang, S. A.; Figler, R. A.; Allende, J. A.; Roller, D. G.; Parsons, J. T.; Wulfkuhle, J. D.; Petricoin, E. F. Development of a Multicellular Pancreatic Tumor Microenvironment System Using Patient-Derived Tumor Cells. *Lab. Chip* **2019**, *19* (7), 1193–1204.
(272) Jang, S.-D.; Song, J.; Kim, H.-A.; Im, C.-N.; Khawar, I. A.; Park, J. K.; Kuh, H.-J. Anti-Cancer Activity Profiling of Chemotherapeutic Agents in 3D Co-Cultures of Pancreatic Tumor Spheroids with Cancer-Associated Fibroblasts and Macrophages. *Cancers* **2021**, *13* (23), 5955.
(273) Mollica, H.; Teo, Y. J.; Tan, A. S. M.; Tan, D. Z. M.; Decuzzi, P.; Pavesi, A.; Adriani, G. A 3D Pancreatic Tumor Model to Study T Cell Infiltration. *Biomater.*

Sci. **2021**, *9* (22), 7420–7431.
(274) Mohan, M. D.; Latifi, N.; Flick, R.; Simmons, C. A.; Young, E. W. Interrogating Matrix Stiffness and Metabolomics in Pancreatic Ductal Carcinoma Using an Openable Microfluidic Tumor-on-a-Chip. *ACS Appl. Mater. Interfaces* **2024**, *16* (16), 20169–20185.
(275) Kpeglo, D.; Haddrick, M.; Knowles, M. A.; Evans, S. D.; Peyman, S. A. Modelling and Breaking down the Biophysical Barriers to Drug Delivery in Pancreatic Cancer. *Lab. Chip* **2024**, *24* (4), 854–868.
(276) Deipenbrock, A.; Wilmes, B. E.; Sommermann, T.; Abdo, N.; Moustakas, K.; Raasch, M.; Rennert, K.; Teusch, N. E. Modelling of the Multicellular Tumor Microenvironment of Pancreatic Ductal Adenocarcinoma (PDAC) on a Fit-for-Purpose Biochip for Preclinical Drug Discovery. *Lab. Chip* **2025**, *25* (9), 2168–2181.
(277) Pele, K. G.; Calderón-Villalba, A.; Amaveda, H.; Mora, M.; Zhang-Zhou, J.; Pérez, M. Á.; García-Aznar, J. M.; Alamán-Díez, P.; García-Gareta, E. Novel Hydrogel-Based Cancer-on-a-Chip Models for Growth of 3D Multi-Cellular Structures and Investigation of Early Angiogenesis in Pancreatic Ductal Adenocarcinoma. *Colloids Surf. B Biointerfaces* **2025**, 114736.
(278) Haque, M. R.; Wessel, C. R.; Leary, D. D.; Wang, C.; Bhushan, A.; Bishehsari, F. Patient-Derived Pancreatic Cancer-on-a-Chip Recapitulates the Tumor Microenvironment. *Microsyst. Nanoeng.* **2022**, *8* (1), 1–13.
(279) Lai, B. F. L.; Lu, R. X. Z.; Hu, Y.; Davenport Huyer, L.; Dou, W.; Wang, E. Y.; Radulovich, N.; Tsao, M. S.; Sun, Y.; Radisic, M. Recapitulating Pancreatic Tumor Microenvironment through Synergistic Use of Patient Organoids and Organ-on-a-chip Vasculature. *Adv. Funct. Mater.* **2020**, *30* (48), 2000545–2000545.
(280) Song, T.; Zhang, H.; Luo, Z.; Shang, L.; Zhao, Y. Primary Human Pancreatic Cancer Cells Cultivation in Microfluidic Hydrogel Microcapsules for Drug Evaluation. *Adv. Sci.* **2023**, *10* (12), 2206004.
(281) Choi, D.; Gonzalez-Suarez, A. M.; Dumbrava, M. G.; Medlyn, M.; de Hoyos-Vega, J. M.; Cichocki, F.; Miller, J. S.; Ding, L.; Zhu, M.; Stybayeva, G. Microfluidic Organoid Cultures Derived from Pancreatic Cancer Biopsies for Personalized Testing of Chemotherapy and Immunotherapy. *Adv. Sci.* **2024**, *11* (5), 2303088.
(282) Geyer, M.; Schreyer, D.; Gaul, L.-M.; Pfeffer, S.; Pilarsky, C.; Queiroz, K. A Microfluidic-Based PDAC Organoid System Reveals the Impact of Hypoxia in Response to Treatment. *Cell Death Discov.* **2023**, *9* (1), 20–20.
(283) Geyer, M.; Gaul, L.-M.; DAgosto, S. L.; Corbo, V.; Queiroz, K. The Tumor Stroma Influences Immune Cell Distribution and Recruitment in a PDAC-on-a-Chip Model. *Front. Immunol.* **2023**, *14*, 1155085.
(284) Goluba, K.; Parfejevs, V.; Rostoka, E.; Jekabsons, K.; Blake, I.; Neimane, A.; Ule, A. A.; Rimsa, R.; Vangravs, R.; Pcolkins, A. Personalized PDAC Chip with Functional Endothelial Barrier for Tumour Biomarker Detection: A Platform for Precision Medicine Applications. *Mater. Today Bio* **2024**, *29*, 101262.
(285) Kramer, B.; Haan, L. de; Vermeer, M.; Olivier, T.; Hankemeier, T.; Vulto, P.; Joore, J.; Lanz, H. L. Interstitial Flow Recapitulates Gemcitabine Chemoresistance in a 3D Microfluidic Pancreatic Ductal Adenocarcinoma Model by Induction of Multidrug Resistance Proteins. *Int. J. Mol. Sci.* **2019**, *20* (18), 4647.
(286) Sgarminato, V.; Marasso, S. L.; Cocuzza, M.; Scordo, G.; Ballesio, A.; Ciardelli, G.; Tonda-Turo, C. PDAC-on-Chip for in Vitro Modeling of Stromal and Pancreatic Cancer Cell Crosstalk. *Biomater. Sci.* **2023**, *11* (1), 208–224.
(287) Sheng, W.; Ogunwobi, O. O.; Chen, T.; Zhang, J.; George, T. J.; Liu, C.; Fan, Z. H. Capture, Release and Culture of Circulating Tumor Cells from Pancreatic Cancer Patients Using an Enhanced Mixing Chip. *Lab Chip* **2014**, *14* (1), 89–

98. https://doi.org/10.1039/C3LC51017D.
(288) Guiying Wang; Lilin Luo. Detection of Circulating Tumor Cells in Patients with Pancreatic Cancer by Novel Nano Microfluidic Chips and Comprehensive Nursing Intervention. *Cell. Mol. Biol.* **2023**, *69* (14), 121–125. https://doi.org/10.14715/cmb/2023.69.14.19.
(289) Ni, R.; Ge, K.; Luo, Y.; Zhu, T.; Hu, Z.; Li, M.; Tao, P.; Chi, J.; Li, G.; Yuan, H.; Pang, Q.; Gao, W.; Zhang, P.; Zhu, Y. Highly Sensitive Microfluidic Sensor Using Integrated Optical Fiber and Real-Time Single-Cell Raman Spectroscopy for Diagnosis of Pancreatic Cancer. *Biosens. Bioelectron.* **2024**, *264*, 116616. https://doi.org/10.1016/j.bios.2024.116616.
(290) Rahmanian, M.; Hematabad, O. S.; Askari, E.; Shokati, F.; Bakhshi, A.; Moghadam, S.; Olfatbakhsh, A.; Hashemi, E. A. S.; Ahmadi, M. K.; Naghib, S. M. A Micropillar Array-Based Microfluidic Chip for Label-Free Separation of Circulating Tumor Cells: The Best Micropillar Geometry? *J. Adv. Res.* **2023**, *47*, 105–121.
(291) Swayden, M.; Soubeyran, P.; Iovanna, J. Upcoming Revolutionary Paths in Preclinical Modeling of Pancreatic Adenocarcinoma. *Front. Oncol.* **2020**, *9*, 1443. https://doi.org/10.3389/fonc.2019.01443.
(292) Haque, M. R.; Rempert, T. H.; Al-Hilal, T. A.; Wang, C.; Bhushan, A.; Bishehsari, F. Organ-Chip Models: Opportunities for Precision Medicine in Pancreatic Cancer. *Cancers* **2021**, *13* (17), 4487–4487.
(293) Dubrova, A.; Cavaniol, C.; Van de Walle, A.; Mathieu, P.; Fusilier, Z.; Yaacoub, N.; Lalatonne, Y.; Descroix, S.; Wilhelm, C. Magnetite Nanoparticle Photothermal Therapy in a Pancreatic Tumor-on-Chip: A Dual-Action Approach Targeting Cancer Cells and Their Microenvironment. *ACS Nano* **2025**, *19* (21), 19790–19805.
(294) Rawla, P.; Sunkara, T.; Gaduputi, V. Epidemiology of Pancreatic Cancer: Global Trends, Etiology and Risk Factors. *World J. Oncol.* **2019**, *10* (1), 10–10.
(295) Siegel, R. L.; Giaquinto, A. N.; Jemal, A. Cancer Statistics, 2024. *CA. Cancer J. Clin.* **2024**, *74* (1).
(296) Provenzano, P. P.; Hingorani, S. R. Hyaluronan, Fluid Pressure, and Stromal Resistance in Pancreas Cancer. *Br. J. Cancer* **2013**, *108* (1), 1–8.
(297) Weniger, M.; Honselmann, K. C.; Liss, A. S. The Extracellular Matrix and Pancreatic Cancer: A Complex Relationship. *Cancers* **2018**, *10* (9), 316–316.
(298) Rodrigues, H. F.; Capistrano, G.; Bakuzis, A. F. In Vivo Magnetic Nanoparticle Hyperthermia: A Review on Preclinical Studies, Low-Field Nano-Heaters, Noninvasive Thermometry and Computer Simulations for Treatment Planning. *Int. J. Hyperthermia* **2020**, *37* (3), 76–99.
(299) Zhang, J.; Ji, K.; Ning, Y.; Sun, L.; Fan, M.; Shu, C.; Zhang, Z.; Tu, T.; Cao, J.; Gao, F. Biological Hyperthermia-Inducing Nanoparticles for Specific Remodeling of the Extracellular Matrix Microenvironment Enhance pro-Apoptotic Therapy in Fibrosis. *ACS Nano* **2023**, *17* (11), 10113–10128.
(300) Albarqi, H. A.; Wong, L. H.; Schumann, C.; Sabei, F. Y.; Korzun, T.; Li, X.; Hansen, M. N.; Dhagat, P.; Moses, A. S.; Taratula, O. Biocompatible Nanoclusters with High Heating Efficiency for Systemically Delivered Magnetic Hyperthermia. *ACS Nano* **2019**, *13* (6), 6383–6395.
(301) Jose, J.; Kumar, R.; Harilal, S.; Mathew, G. E.; Parambi, D. G. T.; Prabhu, A.; Uddin, M. S.; Aleya, L.; Kim, H.; Mathew, B. Magnetic Nanoparticles for Hyperthermia in Cancer Treatment: An Emerging Tool. *Environ. Sci. Pollut. Res.* **2020**, *27*, 19214–19225.
(302) Huang, H. S.; Hainfeld, J. F. Intravenous Magnetic Nanoparticle Cancer Hyperthermia. *Int. J. Nanomedicine* **2013**, 2521–2532.
(303) Ceelen, W.; Demuytere, J.; de Hingh, I. Hyperthermic Intraperitoneal Chemotherapy: A Critical Review. *Cancers* **2021**, *13* (13), 3114–3114.

(304) Chang, M.; Hou, Z.; Wang, M.; Li, C.; Lin, J. Recent Advances in Hyperthermia Therapy-based Synergistic Immunotherapy. *Adv. Mater.* **2021**, *33* (4), 2004788–2004788.
(305) Pan, J.; Hu, P.; Guo, Y.; Hao, J.; Ni, D.; Xu, Y.; Bao, Q.; Yao, H.; Wei, C.; Wu, Q. Combined Magnetic Hyperthermia and Immune Therapy for Primary and Metastatic Tumor Treatments. *ACS Nano* **2020**, *14* (1), 1033–1044.
(306) Stephen, Z. R.; Zhang, M. Recent Progress in the Synergistic Combination of Nanoparticle-mediated Hyperthermia and Immunotherapy for Treatment of Cancer. *Adv. Healthc. Mater.* **2021**, *10* (2), 2001415–2001415.
(307) Loboda, A.; Smolanka Sr, I.; Orel, V. E.; Syvak, L.; Golovko, T.; Dosenko, I.; Lyashenko, A.; Smolanka Jr, I.; Dasyukevich, O.; Tarasenko, T. Efficacy of Combination Neoadjuvant Chemotherapy and Regional Inductive Moderate Hyperthermia in the Treatment of Patients with Locally Advanced Breast Cancer. *Technol. Cancer Res. Treat.* **2020**, *19*, 1533033820963599–1533033820963599.
(308) Włodarczyk, A.; Gorgoń, S.; Radoń, A.; Bajdak-Rusinek, K. Magnetite Nanoparticles in Magnetic Hyperthermia and Cancer Therapies: Challenges and Perspectives. *Nanomaterials* **2022**, *12* (11), 1807–1807.
(309) Mai, B. T.; Fernandez-Cabada, T.; Conteh, J. S.; Nucci, G. E. P.; Fiorito, S.; Gavilán, H.; Debellis, D.; Gjurgjaj, L.; Pellegrino, T. Nanoplatforms for Magnetic-Photo-Heating of Thermo-Resistant Tumor Cells: Singular Synergic Therapeutic Effects at Mild Temperature. *Small* **2024**, *20* (51), 2310522–2310522.
(310) Mazuel, F.; Espinosa, A.; Radtke, G.; Bugnet, M.; Neveu, S.; Lalatonne, Y.; Botton, G. A.; Abou-Hassan, A.; Wilhelm, C. Magneto-thermal Metrics Can Mirror the Long-term Intracellular Fate of Magneto-plasmonic Nanohybrids and Reveal the Remarkable Shielding Effect of Gold. *Adv. Funct. Mater.* **2017**, *27* (9), 1605997–1605997.
(311) Zeng, W.; Li, Z.; Huang, Q.; Ding, C.; Yang, L.; Wang, W.; Shi, Z.; Yang, Y.; Chen, H.; Mei, L. Multifunctional Mesoporous Polydopamine-based Systematic Delivery of STING Agonist for Enhanced Synergistic Photothermal-immunotherapy. *Adv. Funct. Mater.* **2024**, *34* (1), 2307241–2307241.
(312) Ou, M.; Lin, C.; Wang, Y.; Lu, Y.; Wang, W.; Li, Z.; Zeng, W.; Zeng, X.; Ji, X.; Mei, L. Heterojunction Engineered Bioactive Chlorella for Cascade Promoted Cancer Therapy. *J. Controlled Release* **2022**, *345*, 755–769.
(313) Shi, Z.; Luo, M.; Huang, Q.; Ding, C.; Wang, W.; Wu, Y.; Luo, J.; Lin, C.; Chen, T.; Zeng, X. NIR-Dye Bridged Human Serum Albumin Reassemblies for Effective Photothermal Therapy of Tumor. *Nat. Commun.* **2023**, *14* (1), 6567–6567.
(314) Bertuit, E.; Benassai, E.; Mériguet, G.; Greneche, J.-M.; Baptiste, B.; Neveu, S.; Wilhelm, C.; Abou-Hassan, A. Structure–Property–Function Relationships of Iron Oxide Multicore Nanoflowers in Magnetic Hyperthermia and Photothermia. *ACS Nano* **2021**, *16* (1), 271–284.
(315) Cabana, S.; Curcio, A.; Michel, A.; Wilhelm, C.; Abou-Hassan, A. Iron Oxide Mediated Photothermal Therapy in the Second Biological Window: A Comparative Study between Magnetite/Maghemite Nanospheres and Nanoflowers. *Nanomaterials* **2020**, *10* (8), 1548–1548.
(316) Rastinehad, A. R.; Anastos, H.; Wajswol, E.; Winoker, J. S.; Sfakianos, J. P.; Doppalapudi, S. K.; Carrick, M. R.; Knauer, C. J.; Taouli, B.; Lewis, S. C. Gold Nanoshell-Localized Photothermal Ablation of Prostate Tumors in a Clinical Pilot Device Study. *Proc. Natl. Acad. Sci.* **2019**, *116* (37), 18590–18596.
(317) Han, H. S.; Choi, K. Y. Advances in Nanomaterial-Mediated Photothermal Cancer Therapies: Toward Clinical Applications. *Biomedicines* **2021**, *9* (3), 305–305.
(318) Zeng, S.; Pöttler, M.; Lan, B.; Grützmann, R.; Pilarsky, C.; Yang, H. Chemoresistance in Pancreatic Cancer. *Int. J. Mol. Sci.* **2019**, *20* (18), 4504–

4504.
(319) Sherman, M. H.; Beatty, G. L. Tumor Microenvironment in Pancreatic Cancer Pathogenesis and Therapeutic Resistance. *Annu. Rev. Pathol. Mech. Dis.* **2023**, *18* (1), 123–148.
(320) Carvalho, T. M. A.; Di Molfetta, D.; Greco, M. R.; Koltai, T.; Alfarouk, K. O.; Reshkin, S. J.; Cardone, R. A. Tumor Microenvironment Features and Chemoresistance in Pancreatic Ductal Adenocarcinoma: Insights into Targeting Physicochemical Barriers and Metabolism as Therapeutic Approaches. *Cancers* **2021**, *13* (23), 6135–6135.
(321) Palacio-Castañeda, V.; Dumas, S.; Albrecht, P.; Wijgers, T. J.; Descroix, S.; Verdurmen, W. P. R. A Hybrid in Silico and Tumor-on-a-Chip Approach to Model Targeted Protein Behavior in 3D Microenvironments. *Cancers* **2021**, *13* (10), 2461–2461.
(322) Giannitelli, S. M.; Peluzzi, V.; Raniolo, S.; Roscilli, G.; Trombetta, M.; Mozetic, P.; Rainer, A. On-Chip Recapitulation of the Tumor Microenvironment: A Decade of Progress. *Biomaterials* **2024**, 122482–122482.
(323) Del Piccolo, N.; Shirure, V. S.; Bi, Y.; Goedegebuure, S. P.; Gholami, S.; Hughes, C. C. W.; Fields, R. C.; George, S. C. Tumor-on-Chip Modeling of Organ-Specific Cancer and Metastasis. *Adv. Drug Deliv. Rev.* **2021**, *175*, 113798–113798.
(324) Nguyen, M.; De Ninno, A.; Mencattini, A.; Mermet-Meillon, F.; Fornabaio, G.; Evans, S. S.; Cossutta, M.; Khira, Y.; Han, W.; Sirven, P. Dissecting Effects of Anti-Cancer Drugs and Cancer-Associated Fibroblasts by on-Chip Reconstitution of Immunocompetent Tumor Microenvironments. *Cell Rep.* **2018**, *25* (13), 3884–3893.
(325) Bouquerel, C.; César, W.; Barthod, L.; Arrak, S.; Battistella, A.; Gropplero, G.; Mechta-Grigoriou, F.; Zalcman, G.; Parrini, M. C.; Verhulsel, M. Precise and Fast Control of the Dissolved Oxygen Level for Tumor-on-Chip. *Lab. Chip* **2022**, *22* (22), 4443–4455.
(326) Alamdari, S. G.; Amini, M.; Jalilzadeh, N.; Baradaran, B.; Mohammadzadeh, R.; Mokhtarzadeh, A.; Oroojalian, F. Recent Advances in Nanoparticle-Based Photothermal Therapy for Breast Cancer. *J. Controlled Release* **2022**, *349*, 269–303.
(327) Tang, J.; Myers, M.; Bosnick, K. A.; Brus, L. E. Magnetite Fe3O4 Nanocrystals: Spectroscopic Observation of Aqueous Oxidation Kinetics. *J. Phys. Chem. B* **2003**, *107* (30), 7501–7506.
(328) Bertuit, E.; Menguy, N.; Wilhelm, C.; Rollet, A.-L.; Abou-Hassan, A. Angular Orientation between the Cores of Iron Oxide Nanoclusters Controls Their Magneto–Optical Properties and Magnetic Heating Functions. *Commun. Chem.* **2022**, *5* (1), 164–164.
(329) Fromain, A.; Perez, J. E.; Van de Walle, A.; Lalatonne, Y.; Wilhelm, C. Photothermia at the Nanoscale Induces Ferroptosis via Nanoparticle Degradation. *Nat. Commun.* **2023**, *14* (1), 4637–4637.
(330) Sangnier, A. P.; Van de Walle, A. B.; Curcio, A.; Le Borgne, R.; Motte, L.; Lalatonne, Y.; Wilhelm, C. Impact of Magnetic Nanoparticle Surface Coating on Their Long-Term Intracellular Biodegradation in Stem Cells. *Nanoscale* **2019**, *11* (35), 16488–16498.
(331) Santoyo Salazar, J.; Perez, L.; De Abril, O.; Truong Phuoc, L.; Ihiawakrim, D.; Vazquez, M.; Greneche, J.-M.; Begin-Colin, S.; Pourroy, G. Magnetic Iron Oxide Nanoparticles in 10− 40 Nm Range: Composition in Terms of Magnetite/Maghemite Ratio and Effect on the Magnetic Properties. *Chem. Mater.* **2011**, *23* (6), 1379–1386.
(332) Bennink, L. L.; Li, Y.; Kim, B.; Shin, I. J.; San, B. H.; Zangari, M.; Yoon, D.; Yu, S. M. Visualizing Collagen Proteolysis by Peptide Hybridization: From 3D Cell Culture to in Vivo Imaging. *Biomaterials* **2018**, *183*, 67–76.

(333) Dai, J.; Xing, Y.; Xiao, L.; Li, J.; Cao, R.; He, Y.; Fang, H.; Periasamy, A.; Oberhozler, J.; Jin, L. Microfluidic Disc-on-a-Chip Device for Mouse Intervertebral Disc—Pitching a next-Generation Research Platform to Study Disc Degeneration. *ACS Biomater. Sci. Eng.* **2019**, *5* (4), 2041–2051.
(334) Hwang, J.; San, B. H.; Turner, N. J.; White, L. J.; Faulk, D. M.; Badylak, S. F.; Li, Y.; Yu, S. M. Molecular Assessment of Collagen Denaturation in Decellularized Tissues Using a Collagen Hybridizing Peptide. *Acta Biomater.* **2017**, *53*, 268–278.
(335) Sun, Y.; Chen, W.-L.; Lin, S.-J.; Jee, S.-H.; Chen, Y.-F.; Lin, L.-C.; So, P. T. C.; Dong, C.-Y. Investigating Mechanisms of Collagen Thermal Denaturation by High Resolution Second-Harmonic Generation Imaging. *Biophys. J.* **2006**, *91* (7), 2620–2625.
(336) Ozcelikkale, A.; Han, B. Thermal Destabilization of Collagen Matrix Hierarchical Structure by Freeze/Thaw. *PLoS One* **2016**, *11* (1), e0146660–e0146660.
(337) Wright, N. T.; Humphrey, J. D. Denaturation of Collagen via Heating: An Irreversible Rate Process. *Annu. Rev. Biomed. Eng.* **2002**, *4* (1), 109–128.
(338) Zhang, X.; Xu, S.; Shen, L.; Li, G. Factors Affecting Thermal Stability of Collagen from the Aspects of Extraction, Processing and Modification. *J. Leather Sci. Eng.* **2020**, *2*, 1–29.
(339) Liu, Y.; Liu, L.; Chen, M.; Zhang, Q. Double Thermal Transitions of Type I Collagen in Acidic Solution. *J. Biomol. Struct. Dyn.* **2013**, *31* (8), 862–873.
(340) Minami, F.; Sasaki, N.; Shichi, Y.; Gomi, F.; Michishita, M.; Ohkusu-Tsukada, K.; Toyoda, M.; Takahashi, K.; Ishiwata, T. Morphofunctional Analysis of Human Pancreatic Cancer Cell Lines in 2-and 3-Dimensional Cultures. *Sci. Rep.* **2021**, *11* (1), 6775–6775.
(341) Shichi, Y.; Gomi, F.; Sasaki, N.; Nonaka, K.; Arai, T.; Ishiwata, T. Epithelial and Mesenchymal Features of Pancreatic Ductal Adenocarcinoma Cell Lines in Two- and Three-Dimensional Cultures. *J. Pers. Med.* **2022**, *12* (5), 746–746.
(342) Tarannum, M.; Vivero-Escoto, J. L. Nanoparticle-Based Therapeutic Strategies Targeting Major Clinical Challenges in Pancreatic Cancer Treatment. *Adv. Drug Deliv. Rev.* **2022**, *187*, 114357–114357.
(343) Sanhaji, M.; Göring, J.; Couleaud, P.; Aires, A.; Cortajarena, A. L.; Courty, J.; Prina-Mello, A.; Stapf, M.; Ludwig, R.; Volkov, Y. The Phenotype of Target Pancreatic Cancer Cells Influences Cell Death by Magnetic Hyperthermia with Nanoparticles Carrying Gemicitabine and the Pseudo-Peptide NucAnt. *Nanomedicine Nanotechnol. Biol. Med.* **2019**, *20*, 101983–101983.
(344) Logghe, T.; van Zwol, E.; Immordino, B.; Van den Cruys, K.; Peeters, M.; Giovannetti, E.; Bogers, J. Hyperthermia in Combination with Emerging Targeted and Immunotherapies as a New Approach in Cancer Treatment. *Cancers* **2024**, *16* (3), 505–505.
(345) Zheng, X.; Carstens, J. L.; Kim, J.; Scheible, M.; Kaye, J.; Sugimoto, H.; Wu, C.-C.; LeBleu, V. S.; Kalluri, R. Epithelial-to-Mesenchymal Transition Is Dispensable for Metastasis but Induces Chemoresistance in Pancreatic Cancer. *Nature* **2015**, *527* (7579), 525–530.
(346) Rajagopal, M. U.; Bansal, S.; Kaur, P.; Jain, S. K.; Altadil, T.; Hinzman, C. P.; Li, Y.; Moulton, J.; Singh, B.; Bansal, S. TGFβ Drives Metabolic Perturbations during Epithelial Mesenchymal Transition in Pancreatic Cancer: TGFβ Induced EMT in PDAC. *Cancers* **2021**, *13* (24), 6204.
(347) Suri, R.; Zimmerman, J. W.; Burkhart, R. A. Modeling Human Pancreatic Ductal Adenocarcinoma for Translational Research: Current Options, Challenges, and Prospective Directions. *Ann. Pancreat. Cancer* **2020**, *3*, 17.
(348) Krempley, B. D.; Kenneth, H. Y. Preclinical Models of Pancreatic Ductal Adenocarcinoma. *Chin. Clin. Oncol.* **2017**, *6* (3), 25–25.
(349) Kim, S.-K.; Jang, S. D.; Kim, H.; Chung, S.; Park, J. K.; Kuh, H.-J. Phenotypic

Heterogeneity and Plasticity of Cancer Cell Migration in a Pancreatic Tumor Three-Dimensional Culture Model. *Cancers* **2020**, *12* (5), 1305–1305.
(350) Kultti, A.; Zhao, C.; Singha, N. C.; Zimmerman, S.; Osgood, R. J.; Symons, R.; Jiang, P.; Li, X.; Thompson, C. B.; Infante, J. R. Accumulation of Extracellular Hyaluronan by Hyaluronan Synthase 3 Promotes Tumor Growth and Modulates the Pancreatic Cancer Microenvironment. *BioMed Res. Int.* **2014**, *2014* (1), 817613.
(351) Bulle, A.; Lim, K.-H. Beyond Just a Tight Fortress: Contribution of Stroma to Epithelial-Mesenchymal Transition in Pancreatic Cancer. *Signal Transduct. Target. Ther.* **2020**, *5* (1), 249.
(352) Deer, E. L.; González-Hernández, J.; Coursen, J. D.; Shea, J. E.; Ngatia, J.; Scaife, C. L.; Firpo, M. A.; Mulvihill, S. J. Phenotype and Genotype of Pancreatic Cancer Cell Lines. *Pancreas* **2010**, *39* (4), 425–435.
(353) Ungefroren, H.; Thürling, I.; Färber, B.; Kowalke, T.; Fischer, T.; De Assis, L. V. M.; Braun, R.; Castven, D.; Oster, H.; Konukiewitz, B. The Quasimesenchymal Pancreatic Ductal Epithelial Cell Line PANC-1—a Useful Model to Study Clonal Heterogeneity and EMT Subtype Shifting. *Cancers* **2022**, *14* (9), 2057.
(354) Nath, S.; Daneshvar, K.; Roy, L. D.; Grover, P.; Kidiyoor, A.; Mosley, L.; Sahraei, M.; Mukherjee, P. MUC1 Induces Drug Resistance in Pancreatic Cancer Cells via Upregulation of Multidrug Resistance Genes. *Oncogenesis* **2013**, *2* (6), e51–e51.
(355) Jonckheere, N.; Skrypek, N.; Merlin, J.; Dessein, A. F.; Dumont, P.; Leteurtre, E.; Harris, A.; Desseyn, J.-L.; Susini, C.; Frenois, F. The Mucin MUC4 and Its Membrane Partner ErbB2 Regulate Biological Properties of Human CAPAN-2 Pancreatic Cancer Cells via Different Signalling Pathways. *PLoS One* **2012**, *7* (2), e32232.
(356) Sipos, B.; Möser, S.; Kalthoff, H.; Török, V.; Löhr, M.; Klöppel, G. A Comprehensive Characterization of Pancreatic Ductal Carcinoma Cell Lines: Towards the Establishment of an in Vitro Research Platform. *Virchows Arch.* **2003**, *442* (5), 444–452.
(357) Shirk, A. J.; Kuver, R. Epidermal Growth Factor Mediates Detachment from and Invasion through Collagen I and Matrigel in Capan-1 Pancreatic Cancer Cells. *BMC Gastroenterol.* **2005**, *5* (1), 12.
(358) Li, J.; Peng, L.; Chen, Q.; Ye, Z.; Zhao, T.; Hou, S.; Gu, J.; Hang, Q. Integrin B1 in Pancreatic Cancer: Expressions, Functions, and Clinical Implications. *Cancers* **2022**, *14* (14), 3377.
(359) Ware, M. J.; Keshishian, V.; Law, J. J.; Ho, J. C.; Favela, C. A.; Rees, P.; Smith, B.; Mohammad, S.; Hwang, R. F.; Rajapakshe, K. Generation of an in Vitro 3D PDAC Stroma Rich Spheroid Model. *Biomaterials* **2016**, *108*, 129–142.
(360) Koltai, T.; Reshkin, S. J.; Carvalho, T. M.; Cardone, R. A. Targeting the Stromal Pro-Tumoral Hyaluronan-CD44 Pathway in Pancreatic Cancer. *Int. J. Mol. Sci.* **2021**, *22* (8), 3953.
(361) Veettil, S. R. U.; Hwang, D.; Correia, J.; Bartlett, M. D.; Schneider, I. C. Cancer Cell Migration in Collagen-Hyaluronan Composite Extracellular Matrices. *Acta Biomater.* **2021**, *130*, 183–198.
(362) Tammi, M. I.; Day, A. J.; Turley, E. A. Hyaluronan and Homeostasis: A Balancing Act. *J. Biol. Chem.* **2002**, *277* (7), 4581–4584.
(363) Fraser, J.; Laurent, T. Turnover and Metabolism of Hyaluronan; Wiley Online Library, 2007; pp 41–59.
(364) Nagy, N.; Kuipers, H. F.; Marshall, P. L.; Wang, E.; Kaber, G.; Bollyky, P. L. Hyaluronan in Immune Dysregulation and Autoimmune Diseases. *Matrix Biol.* **2019**, *78*, 292–313.
(365) Toole, B. P. Hyaluronan: From Extracellular Glue to Pericellular Cue. *Nat. Rev. Cancer* **2004**, *4* (7), 528–539.

(366) Gagliano, N.; Celesti, G.; Tacchini, L.; Pluchino, S.; Sforza, C.; Rasile, M.; Valerio, V.; Laghi, L.; Conte, V.; Procacci, P. Epithelial-to-Mesenchymal Transition in Pancreatic Ductal Adenocarcinoma: Characterization in a 3D-Cell Culture Model. *World J. Gastroenterol.* **2016**, *22* (18), 4466–4466.

(367) Nicoletta Gagliano, Chiarella Sforza, Michele Sommariva , Alessandra Menon, Vincenzo Conte, Patrizia Sartori, Patrizia Procacci. 3D-Spheroids: What Can They Tell Us about Pancreatic Ductal Adenocarcinoma Cell Phenotype? *Exp. Cell Res.* **2017**, *357* (2), 299–309. https://doi.org/10.1016/j.yexcr.2017.05.027.

(368) Thouvenot, E.; Charnay, L.; Burshtein, N.; Guigner, J.; Dec, L.; Loew, D.; Silva, A. K.; Lindner, A.; Wilhelm, C. High-Yield Bioproduction of Extracellular Vesicles from Stem Cell Spheroids via Millifluidic Vortex Transport. *Adv. Mater.* **2025**, *37* (20), 2412498.

(369) Loh, C.-Y.; Chai, J. Y.; Tang, T. F.; Wong, W. F.; Sethi, G.; Shanmugam, M. K.; Chong, P. P.; Looi, C. Y. The E-Cadherin and N-Cadherin Switch in Epithelial-to-Mesenchymal Transition: Signaling, Therapeutic Implications, and Challenges. *Cells* **2019**, *8* (10), 1118.

ANNEX A

Lab on a Chip

ROYAL SOCIETY OF CHEMISTRY

CRITICAL REVIEW

View Article Online
View Journal | View Issue

Bridging the gap between tumor-on-chip and clinics: a systematic review of 15 years of studies†

Charlotte Bouquerel, [abc] Anastasiia Dubrova,[a] Isabella Hofer,[b] Duc T. T. Phan,[d] Moencopi Bernheim,[a] Ségolène Ladaigue,[b] Charles Cavaniol, [a] Danilo Maddalo, [e] Luc Cabel,[f] Fatima Mechta-Grigoriou,[b] Claire Wilhelm,[a] Gérard Zalcman,[bg] Maria Carla Parrini[b] and Stéphanie Descroix *[a]

Cite this: *Lab Chip*, 2023, 23, 3906

Over the past 15 years, the field of oncology research has witnessed significant progress in the development of new cell culture models, such as tumor-on-chip (ToC) systems. In this comprehensive overview, we present a multidisciplinary perspective by bringing together physicists, biologists, clinicians, and experts from pharmaceutical companies to highlight the current state of ToC research, its unique features, and the challenges it faces. To offer readers a clear and quantitative understanding of the ToC field, we conducted an extensive systematic analysis of more than 300 publications related to ToC from 2005 to 2022. ToC offer key advantages over other *in vitro* models by enabling precise control over various parameters. These parameters include the properties of the extracellular matrix, mechanical forces exerted on cells, the physico-chemical environment, cell composition, and the architecture of the tumor microenvironment. Such fine control allows ToC to closely replicate the complex microenvironment and interactions within tumors, facilitating the study of cancer progression and therapeutic responses in a highly representative manner. Importantly, by incorporating patient-derived cells or tumor xenografts, ToC models have demonstrated promising results in terms of clinical validation. We also examined the potential of ToC for pharmaceutical industries in which ToC adoption is expected to occur gradually. Looking ahead, given the high failure rate of clinical trials and the increasing emphasis on the 3Rs principles (replacement, reduction, refinement of animal experimentation), ToC models hold immense potential for cancer research. In the next decade, data generated from ToC models could potentially be employed for discovering new therapeutic targets, contributing to regulatory purposes, refining preclinical drug testing and reducing reliance on animal models.

Received 16th June 2023,
Accepted 31st July 2023

DOI: 10.1039/d3lc00531c

rsc.li/loc

1. Introduction

For almost one century, scientists have been developing and improving cell culture models to increase their resemblance to human *in vivo* conditions and relevance for clinical transition. In a similar vein, novel tumor-on-a-chip (ToC) technology has developed tremendously over the past decade and holds great promise for clinical applications in oncology. The present review focuses on the quantitative analysis of the tumor on chip field up to date and offers a clear outlook of the subject in terms of both, engineering and application approaches. We have brought together academic researchers (physicists and biologists), clinicians as well as pharmaceutical companies' research experts to offer a multifaceted point of view that reflects the diversity of the actors of the field.

Nowadays in Europe, the yearly number of newly diagnosed people with cancer is about 3.5 million. In 2021, the EU Cancer Mission outlined that if no further action is taken, this number will dramatically increase to more than 4.3 million by 2035. In the fight against cancer, the better understanding of cancer mechanisms and the development of more effective anti-cancer drugs still remain highly challenging. Although conventional and well-established

[a] *Macromolécules et Microsystèmes en Biologie et Médecine, UMR 168, Institut Curie, Institut Pierre Gilles de Gennes, 6 rue Jean Calvin, 75005, Paris, France*
[b] *Stress and Cancer Laboratory, Inserm, U830, Institut Curie, PSL Research University, 26 rue d'Ulm, 75005, Paris, France*
[c] *Fluigent, 67 avenue de Fontainebleau, 94270, Le Kremlin-Bicêtre, France*
[d] *Biomedicine Design, Pfizer Inc., San Diego, CA, USA*
[e] *Department of Translational Oncology, Genentech, Inc., South San Francisco, CA 94080, USA*
[f] *Institut Curie, Department of Medical Oncology, 26 rue d'Ulm, 75005, Paris, France*
[g] *Université Paris Cité, Thoracic Oncology Department, INSERM CIC1425, Bichat Hospital, Cancer Institute AP-HP. Nord, Paris, France.*
E-mail: stephanie.descroix@curie.fr

† Electronic supplementary information (ESI) available. See DOI: https://doi.org/10.1039/d3lc00531c

treatments, such as chemotherapies, face many failures, the development of new therapeutic strategies, such as immunotherapies and targeted therapies, raises new hopes. Since 2015, the U.S. Food and Drug Administration (FDA) has approved more than 80 novel cancer drugs, illustrating a historically high level of successful clinical trials in oncology.[1] However, it is also worth mentioning that only 4 to 7% of potential anticancer drugs obtain final clinical approval[2] compared to 10 to 15% for other diseases.[3] Such low success rates call into question the preclinical studies whose aim is to predict the effect of therapeutic agents in terms of efficacy, safety and dosage. The analysis of clinical trial data (from 2010 to 2017) has shown that the two main reasons for these failures are the unmanageable toxicity and lack of clinical efficacy.[4] Preclinical toxicity studies are mainly assessed by animal testing. However, it is now established that animals are not always suitable models for human toxicity prediction as shown in the meta-analysis of Atkins *et al.*[5] that compares preclinical and clinical toxicity profiles of 108 anti-cancer drugs in animal models and humans. They highlighted that the main unpredictable toxicities are of neurologic/psychiatric, cutaneous, respiratory, and cardiovascular nature. Another reason for the low success rates of anti-cancer drug development is related to intrinsic drug efficacy. Recent studies have also shown that current *in vitro* and *in vivo* models are poor predictors of drug efficacy.[6] The dramatic failure rate of clinical trials not only challenges our ability to design and develop new drugs, but also the use of animal models for basic research. Common *in vivo* models include patient-derived xenografts in mice (PDX), which share several important characteristics with human tumors (*i.e.*, vascularization, 3D structure and metabolism). However, PDX models also lack some crucial features such as human stroma and pharmacokinetics as well as an intact autologous immune system since such models often consist of immune deficient mice to allow efficient engrafting.[7] It is also worth mentioning that syngeneic animal models will be even less predictive for novel anti-cancer therapies such as biologics, gene- and cell-based therapies, since these drugs are either mainly specific to human targeting molecular sequences or involved the human immune system.[8] Very recently, the FDA has removed the requirement of animal testing before human trials ("Modernization Act 2.0"). This FDA statement is an excellent opportunity as well as a strong responsibility for the scientific community to develop and share innovative *in vitro* models that would faithfully reproduce disease mechanisms while improving predictive power.

Within the past decades, researchers have developed more adequate 3D *in vitro* models such as spheroids and organoids. They can incorporate different cell types to better mimic the complex tumor microenvironment (TME) compared to conventional 2D cell cultures. While the use of spheroids for *in vitro* drug testing is popular due to their relative ease of handling, they still exhibit a low degree of structural complexity.[9] Organoids, cultured from embryonic, adult stem cells or induced pluripotent stem cells are better in mimicking the TME[10,11] and several studies have evidenced that they are relatively good predictors of chemotherapy response in patients.[12] However, the establishment of patient-derived organoids generally requires 1 to 3 months,[10] and thereby limits their application in clinics as a diagnostic tool to support the choice of a specific treatment. Organoids and spheroid cultures are also associated with some major limitations: (a) they are static models which can lead to the accumulation of biochemical waste within the cell aggregate, (b) they do not fully reproduce the immune response, presence of fibroblasts and vascularization, (c) they do not reproduce the mechanical properties of tumors which can influence drug response.[13]

New *in vitro* models for oncology research are required for both basic and preclinical research. These models should especially consider that tumors are complex ecosystems dynamically evolving over time. Indeed, the TME not only contains cancer cells, the surrounding extracellular matrix (ECM) with varying mechanical and physico-chemical properties, but also a variety of other cell types such as immune lymphoid and myeloid cells, cancer-associated fibroblasts (CAFs), pericytes and endothelial cells with specific spatial organization. All before mentioned TME components have been shown to play a significant role in tumor progression, metastasis development, and resistance to treatment.[14] Microfluidic technologies, and organ-on-chip approaches in particular have an enormous potential for the development of a new generation of 3D *in vitro* tumor models. ToC contains several features which make them highly attractive for both basic and translational research: (a) the capacity to control the cellular, mechanical and physicochemical conditions on-chip, (b) the compatibility with a wide range of analytical methods including transcriptomic analysis and live imaging, (c) the possibility to produce human and/or immunocompetent models, and (d) the relatively short experimental time of several days as compared to other 3D cancer models such as PDX or organoids, allowing clinical decision.

In this review, we conducted a systematic analysis of the publications related to ToC between 2005 and 2022 to provide the reader with a clear and quantitative vision of the emerging ToC field. Altogether, over 300 publications were identified using PubMed, Google Scholar and looking directly into key journals as shown Fig. S1.† In this systematic review, we identify crucial subject parameters and extracted percentages of each occurrence. We discuss the added values of ToC as well as the scope of possible applications: drug screening, cellular mechanisms understanding and personalized- and nano-medicine. The success of ToC for clinical applications will be determined by its ability to detect and validate new therapeutic targets as well as to guide the definition of the delicate balance between clinical dose, efficacy and safety.

2. Material and methods

We used several databases (such as Pubmed, Google Scholar) and searched for combinations of the following key words in the title and abstract (Fig. S1†): "tumor", "cancer", "microfluidic", "chip". We also searched directly for relevant publications in specific journals such as Lab On Chip. Publications with only computational approaches, as well as reviews were excluded during the first screen (titles and abstract). We screened references of more than 10 reviews to list all the ToC publications. During the second step, a qualitative analysis of all the publications results was performed and only studies including cell culture on chip were included (for example CTC sorting methods were excluded). For the purpose of the analysis, we created a table with information related to the most relevant aspects of OoC devices: a) cellular components: type (cell line, primary cells, freshly resected tumor, IPS cells, organoids), organ (breast, lung, pancreas, prostate, ovary/uterus, colorectal/intestine, liver, brain), spheroids (yes/no); b) physico-chemical control: flow, oxygen control, extracellular matrix; (c) applications: anti-cancer drug, readouts. Excel was used to count occurrence of these key points in all the publications. Over 300 publications were analysed.

3. Tumor-on-chip allows to control the reconstituted tumor micro-environment

Cancer is not defined solely by cancer cells but by the whole TME, including cellular and molecular components, ECM, as well as their complex interplay. Tumors have many biomechanical abnormalities such as elevated solid stress, interstitial pressure, and stiffness.[13] One beauty of the ToC approach is the possibility to finely control and thus dissect the role of each parameter of the reconstituted TME. Particularly, this includes the different cell types and their spatial organization, the ECM properties, the on-chip generation of biochemical gradients, the control of the gaseous environment or even the different mechanical forces at play.

3.1. Controlling physico-chemical properties of the TME

A. Features of the tumor extracellular matrix. The ECM is a complex compartment composed of matrix proteins (*e.g.* collagens and elastin), glycoproteins (*e.g.* fibronectin), glycosaminoglycans (*e.g.* heparan sulfate, hyaluronic acid), proteoglycans (*e.g.* perlecan, syndecan) as well as ECM-sequestered growth factors such as transforming growth factor-β, vascular endothelial growth factor or platelet-derived growth factor and other secreted proteins (*e.g.* proteolytic enzymes and protease inhibitors).[15] The ECM composition varies according to the organ nature and state[16,17] and confers the tissue certain porosity, permeability, stiffness and elasticity. These ECM properties are often altered during pathological conditions such as tumor growth.[18,19] Those dynamic changes affect cell differentiation, proliferation, survival, migration, and adhesion.[15] ECM composition along with its physical properties can also influence cell response to drugs by either enhancing drug efficacy or promoting drug resistance.[20] More precisely, changes in the ECM composition may influence drug response by modifying the expression of drug targets, or by changing the cellular defence mechanisms such as DNA repair upon nucleic acids damage or cell apoptosis.[15] For instance, it has been shown that adhesion to the ECM may contribute to drug resistance by activating several pro-survival pathways such as PI3K/Akt, p53 or ERK/MAPK cascade.[21] Cells can be affected not only by the biochemical composition of the ECM but also by its mechanical properties. Among the different mechanical characteristics, ECM stiffness has proven to be an important parameter, influencing cell division, signalling, migration, gene expression, ultimately leading to cell-mediated ECM remodelling.[15] Tumors are usually stiffer than the surrounding healthy tissue due to the ECM production by stromal cancer-associated fibroblasts, the increase of interstitial pressure and the unorganized microvasculature.[21]

Given the complexity and dynamic alterations of the ECM, one of the key points of ToC is the ability to properly select and design biomaterials to reconstitute the extracellular matrix *in vitro*. Here, we focused on ToC with extracellular matrix, but excluded articles dealing with hydrogel coating for 2D cell monolayers. Collagen I is the main ECM component *in vivo* and is by far the most used hydrogel in ToC being used in half of the ToC publications) (Fig. 1). Collagen I contains the tripeptide RGD (Arg–Gly–Asp) which is a very common motif in humans and animals responsible for cell adhesion.[22] Another important advantage of collagen is its stiffness, which can be adjusted easily through its concentration or by covalent crosslinking *via* non-enzymatic glycation.[23] The second most common ToC hydrogel is Matrigel which is a solubilized basement membrane matrix secreted by Engelbreth–Holm–Swarm mouse sarcoma cells. Nevertheless, it has been suggested that results based on Matrigel-cultured cells should be interpreted with caution[24] due to its influence on gene expression[25] as well as the lack of some human peptide motifs.[22] It is worth noticing that both collagen and Matrigel can vary highly between different batches or manufacturers which can affect ToC reproducibility. Besides Matrigel and collagen, there is a wide range of hydrogels available for ToC development such as fibrin, gelatin and agarose (Fig. 1). Another less common approach relies on *in vivo* extracted matrix. Romero-López *et al.* used a decellularized ECM extracted from both healthy and cancerous colon tissues and prepared hydrogels through enzymatic digestion.[26] However, variability in ECM extraction protocols could introduce further alterations in hydrogels, which may lead to inconsistent results.

Hybrid hydrogels are made up of building blocks that include biologically active peptides, proteins or synthetic structures. Hybrid hydrogels can be used to obtain desirable

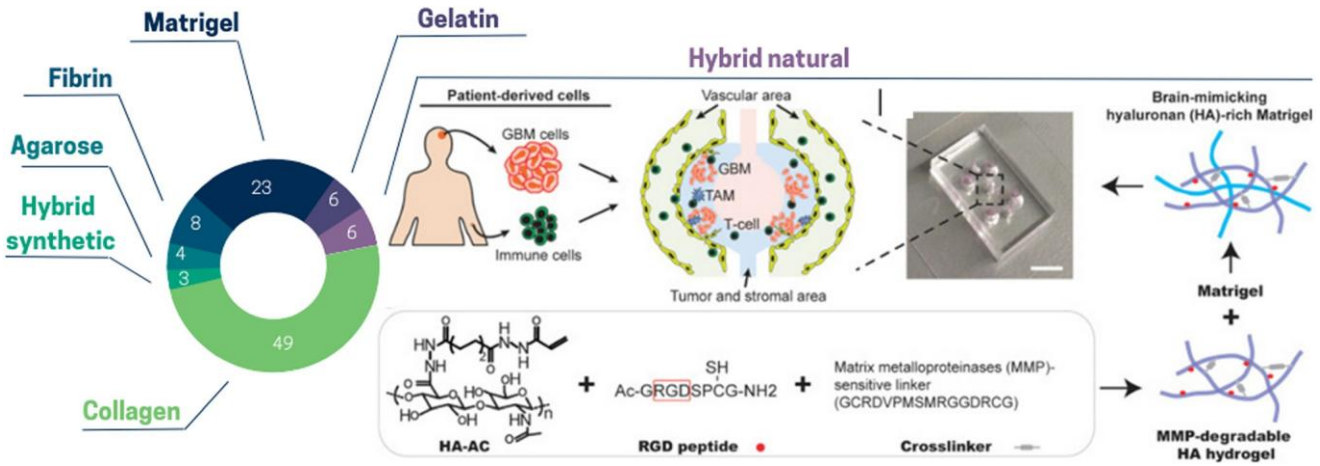


Fig. 1 Pie chart illustrating the proportion of the different extracellular matrix types used in ToC: collagen 49%, Matrigel 23%, fibrin 8%, gelatin 6%, hybrid natural 6%, agarose 4%, hybrid synthetic 3%. (Right panel) Hybrid natural: hydrogels can be created by interpenetrating growth-factor-reduced Matrigel matrix with MMP-degradable ha hydrogel for brain tissue-mimicking extracellular matrix. RGD peptides are conjugated onto acrylated hyaluronic acid (HA–AC) and crosslinked with MMP-degradable crosslinker.[27]

mechanical and biochemical characteristics *via* their functionalization with defined proteolytic sites and encapsulation of growth factors. Nevertheless, given that the ECM alone comprises more than 300 biochemical constituents,[28] this remains a daunting task. Among hybrid hydrogels in ToC, natural ones comprise alginate, fibrinogen, hyaluronan (HA), chitosan, and synthetic ones include poly-ethylene glycol (PEG), poly-caprolactone (PCL) and poly(lactic-*co*-glycolyc) acid (PLGA). Currently, these hydrogels have not been widely adopted. Cui *et al.*[27] used a hybrid brain tissue-mimicking hydrogel with RGD peptides conjugated onto acrylated hyaluronic acid (HA–AC) and crosslinked with MMP-degradable crosslinker (Fig. 1). With the combination of ToC and hybrid hydrogels, it is possible to not only control the ECM chemical composition and stiffness, but also to choose their spatial location. In a breast cancer model, Peela *et al.*[29] proposed a two-step photolithography approach to create an array of cells embedded in circular constructs, with a high stiffness matrix center surrounded by low stiffness matrix. They encapsulated three cell types separately to investigate cell migratory behavior, viability, and morphology. Importantly, cells migrating through the high stiffness circular constructs exhibited different invasive behaviors compared to those migrating through the surrounding matrix. They formed morphologically accurate structures without the addition of any biochemical stimuli, illustrating the versatility of ToC in creating a biomimetic tumor microenvironment.

There are still many challenges to define and improve ECM in order to mimic accurately *in vivo* conditions.[28] Due to the high heterogeneity between different cancer sub-types and even within the same TME, one single type of hydrogel cannot accurately recapitulate the 3D environment experienced by cells *in vivo*. A major challenge is still to synthesize hydrogel matrices that closely mimic the properties of the ECM components specific to each cancer subtype with properties controllable spatially and temporally. It should also be mentioned that fibroblasts and perivascular cells will be key in the future development of ToC as they also contribute to ECM production.

B. Mechanical forces at play. Another important parameter of the TME is the mechanical forces cells experience and convert into mechanical transduction pathways.[30] Among those forces, compressive stress and interstitial fluid pressure[31] are major players. Compressive stress results from the expansion of the solid tumor, but also from changes of the matrix stiffness. This can alter cancer cell properties such as cell cycle regulation[32] and drug resistance.[33] Leaky blood vessels and badly functioning lymphatic vessels can give rise to interstitial fluid pressure.[31] This drives interstitial flow in the tumor, exposing cells to shear stress, which in turn can strongly affect cancer cell migration, endothelial sprouting and even fibroblasts activation.[13] Apart from the mechanical forces at play in the tumor, stretching forces due to the tissue's function such as in uterus, intestine or lung can also impact the tumor development.[30]

Recent tools have been implemented to reproduce these tumor mechanical forces in ToC. To mimic compressive stress, Onal *et al.*[34] developed a chip with an integrated gas pressure micro-piston, applying dynamic compression on ovarian cancer cells. They studied the impact of cyclic stress on the cell nucleus, which is a mechanosensitive organelle, and demonstrated that the circularity of the cell nuclei was significantly less in compressed cells than in control. So far only a few ToC studies integrate controllable compressive stress, but this work highlighted that ToC constitutes a promising tool for studies of cell-mechanical force interaction.

In order to reproduce the interstitial fluid pressure and shear stress, fluidic control in ToC is made possible thanks to conventional fluid controllers also used for seeding cells, refreshing and controlling the cell culture media composition

over time. This fluidic control is mostly performed with syringe pumps[35–37] (half of ToC publications), peristaltic pumps[38–44] or tilted rocking platform[45] while the second half of the ToC studies does not report any flow control (Fig. S2†). Kocal *et al.*[35] investigated how shear stress affects the epithelial to mesenchymal transition of oesophageal cancer cells in a 2D ToC. From the third day of culture under flow, cancer cells experienced a phenotypic switch with a significant decrease in cell–cell adhesion (decrease in E-cadherin expression) as well as an increase of transendothelial migration capacity (increased expression of N-cadherin). Moreover, some ToC studies showed that shear stress can also affect cancer stem cell states. Ip *et al.*[46] found that spheroids grown under shear stress exhibited higher expression of stem cell markers Oct-4, c-Kit (CD117), efflux pumps ABCG2 and P-gp in contrast to static conditions. In clinical settings, a poor prognosis is associated with these factors, highlighting the link between shear stress applied on cancer cells and chemoresistance.[47]

Apart from cancer cells, shear stress can also have a high impact on normal endothelial cells. Several ToC studies showed that shear stress induced an elongated endothelial cell morphology as well as modified junctional protein expression[48] which can facilitate the extravasation of cancer cells. Kim *et al.*[49] demonstrated that the interstitial flow direction can also regulate the direction of capillary sprouting, suggesting angiogenesis occurs in the opposite direction of flow.

Among the mechanical forces experienced by cells *in vivo* is also peristalsis, which is the progression of coordinated muscle contractions. These forces are at play in the gut, oesophagi, uterus and many other organs. Only a few ToC devices have implemented physiological mechanical tissue deformation. Fang *et al.*[50] developed a microfluidic chip allowing high-throughput culture under peristalsis of human colon tumoroids to screen nanomedicines. They observed an increase of stem cell markers (Lgr5) and proliferation markers (Ki67) which could be linked to a peristalsis-induced high interstitial fluid pressure and suggested that peristalsis is also involved in the reduced nanoparticle internalization *via* clathrin-dependent endocytosis. In a recent study, Strelez *et al.* studied colon metastatic spreading in a peristalsis-tunable chip using colorectal cancer (CRC) cells from patients and showed a peristalsis-induced increase of tumor cell invasion.[51] Ao *et al.*[52] evidenced that mechanical stretching of prostatic normal tissue-associated fibroblasts (NAFs) alters the structure of secreted fibronectin. They suggested that mechanical stress is one of the critical factors in NAF activation into cancer associated fibroblasts (CAFs).

There is growing evidence that a wide range of mechanical stresses can alter tumor and stromal cells behavior and ToC appears to be a powerful and innovative technological tool to decipher the role of these various mechanical forces.

C. Tumor oxygen environment. In tumors, leaky and unorganized vascular networks contribute to an unstable oxygenation of microregions.[14] Low oxygen concentration areas named hypoxic zones, develop approximately 100 μm away from blood vessels range from 70 to 200 μm.[53] This is due to the combination of oxygen diffusion limitations and rapid consumption by proliferative cells. These hypoxic micro-regions are heterogeneously distributed within the tumor and lead to oxygen gradients. Hypoxia emerges as a pivotal factor in tumor progression and treatment resistance, through a response mainly ascribed to hypoxia-inducible factors (HIFs)[54] HIF activation in tumors can have several significant consequences: promoting the formation of new blood vessels, metabolic adaptation of cancer cells, enhancing invasiveness and metastasis.[54] Workstation and hypoxic chamber culture systems are the most common methods to create a hypoxic environment. However, they present major limitations: (a) they do not provide oxygen gradients as found *in vivo*, (b) they equilibrate slowly, (c) they only provide gaseous control without any control of dissolved oxygen, (d) they are not easily compatible with live-cell imaging. Several reviews detailed the various methods to control oxygen on-chip[55–57] but studies containing oxygen control in ToC are still rare. The main methods to control oxygen on chip are (Fig. 2): hypoxic incubator, inclusion of a side gas-channel, chemical induction and cell consumption in a low-gas permeable chip. The "gaseous channel" method relies on O_2 diffusion from a gaseous source channel to a channel containing cells across a thin, gas-permeable PDMS membrane. Koens *et al.*[58] described a double-layer microfluidic device (Fig. 2 bottom panel), where two parallel gas channels were located above the cell culture media and gel channels to enhance gas exchange. In addition, a gas-impermeable polycarbonate film was embedded in the device to prevent the diffusion of atmospheric oxygen. With this configuration, an oxygen gradient was established by supplying gas with 0% and 21% O_2 on each side of the gel channel (gradient from 3% to 17% O_2 across the gel). 3D migration trajectories of breast cancer cells inside the gel channel were assessed, and demonstrated that a lower oxygen concentration increases cell migration speed. Despite interesting performances, the main disadvantage of the "gas channel" approach remains that low O_2 concentrations (~0–1%) remain difficult to achieve. It also requires complex microfabrication and the evaporation of culture media can be accelerated by the flow of dry gas through the diffusion membrane. For ToC studies using "chemical induction", oxygen is modulated by on-chip chemical reactions that either generate or consume oxygen. Chang *et al.*[59] exploited the reduction of pyrogallol as oxygen scavenger. The device contains 4 sets of parallel-arranged serpentine channels with identical geometries to generate 6 different concentrations across the width of the channel. The oxygen level was decreased to 1% at the inlet and gradually increased to approximately 16% at the outlet. The device was exploited to perform drug testing on lung cancer cells with varying drug concentrations and under different oxygen pressures. Drug-induced death was assessed on a gradient of tirapazamine (TPZ), which is an original drug metabolized to a toxic radical (only at very low levels of oxygen), where it can exert an anti-

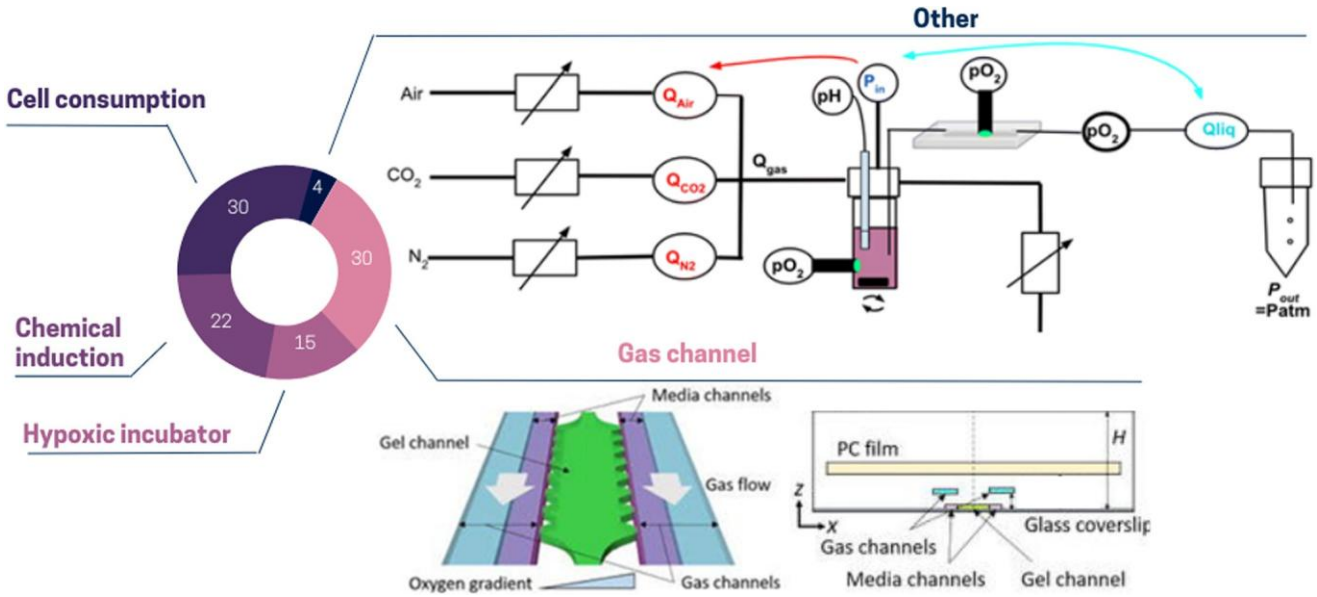


Fig. 2 Pie chart illustrating the proportion of different oxygen control strategies used in ToC: cell consumption 30%, gas channel 30%, chemical induction 22%, hypoxic incubator 15%, other 4%. (Top panel) Other: the dissolved oxygen level can be regulated by modulating pneumatic valves opening. This method simultaneously changes the gas composition and the pressure-driven flow.[62] (Bottom panel) Gas channel: to control dissolved oxygen levels in the media and gel channels, gas mixtures can be supplied to the two separated gas channels. To prevent from atmospheric oxygen diffusion, a polycarbonate film is embedded on top of the gas channels.[58]

cancer effect. This method has the advantage of eliminating the need for pressurized gas tanks, although it generally requires syringe pumps to continuously deliver the reagents. One third of the ToC studies reported oxygen concentration control by simple cell consumption of oxygen in a static chip fabricated with low gas permeable materials.[60] Oxygen consumption by cells can also be combined with constant flow of fresh media to modulate oxygen concentration on chip.[61] Despite simple implementation, this method suffers from major drawbacks, particularly its strong dependency on cell density and metabolic rate. We recently proposed an innovative method for on-chip oxygen control (Fig. 2 top panel)[62] called Oxalis (OXygen ALImentation System) that overcomes most of the cited limitations of current methods. Oxalis regulates simultaneously the gas composition and inlet reservoir pressure by modulating a pneumatic valve opening. Using this dual regulation, both the pressure-driven liquid flow-rate and the level of oxygen dissolved in the chip can be independently controlled. Oxalis offers unprecedented features such as an oxygen equilibration time lower than 3 minutes and accuracy of 3 mmHg. These performances can be reached for chip perfusion flow as low as 1 μL min^{-1}. This approach could thus be used in the future to generate oxygen gradients in ToC.

Reproducing the intricate gaseous environment of the tumor *in vitro* presents considerable challenges, but it holds immense importance as it offers the opportunity to capture spatial metabolic and phenotypic heterogeneity. Significantly, Ayuso *et al.*[63] demonstrated that cells situated farther from the lumen, where nutrients and oxygen originate, displayed upregulated genes associated with apoptosis resistance (*e.g.*, BIRC3), DNA damage induced by starvation (*e.g.*, GADD45G), and stress response (*e.g.*, ADM).

3.2. Controlling the cellular complexity on ToC

A. Cellular composition of the tumor microenvironment. The cellular composition of the TME varies between tumor subtypes. However, besides cancer cells the main cell types found in tumors include endothelial cells, immune cells and cancer associated fibroblasts (CAFs).[64] Tumor blood vessels are disorganized and are bigger in diameter (up to 225 μm) in contrast to physiological ones (up to 100 μm). Tumor blood vessels present an abnormal basement membrane, altered pericyte/endothelial cells ratios, and are highly permeable.[65] The TME contains a variety of immune cells including: different lymphocytes subtypes, tumor-associated macrophages (TAM), natural killer cells, dendritic cells, cancer associated neutrophils. Altogether, they play a major role in response to anti-cancer treatment. CAFs are a key component of the TME, with diverse functions such as matrix deposition and remodeling.[14] Moreover, CAFs are a highly heterogeneous cell population in primary tumors. Costa *et al.*[66] and Pelon *et al.*[67] identified four CAF subpopulations (CAF-S1-S4) in different breast cancer subtypes and metastatic lymph nodes (LN). In particular, the CAF-S1 are linked to an immunosuppressive environment, while both CAF-S1 and CAF-S4 promote cancer invasion and metastasis but with different mechanisms: CAF-S1 stimulate cancer cell

migration and initiate epithelial-to-mesenchymal transition through CXCL12 and TGFβ secretion, while highly contractile CAF-S4 induce cancer cell invasion *via* NOTCH signaling.

Cancer cell lines remain the primary tool for studying biological processes since decades due to their cost-effectiveness, ease of use, and ability to provide an unlimited number of consistent samples. As shown in Fig. 3, about 70% of ToC studies use predominantly cell lines. Most of these cell lines are part of the US National Cancer Institute (NCI) 60 human tumor cell lines anticancer drug screen (NCI60), which have been extensively characterized on a molecular level: exome sequence, DNA methylation, mRNA expression, protein levels and modifications, enzyme activity, and metabolomic profiling.[68] These cell lines theoretically allow an easy comparison between the results obtained inside ToC *versus* other *in vitro* models. However, it is also well-known and accepted that cell lines do not completely represent relevant models of *in vivo* tumors, since indeterminate transcriptomic, epigenetic, genetic and phenotype changes may occur during cell immortalization. Moreover, cells that have been cultured for several years and across different laboratories can present major differences as compared to primary cells and even to the initial source of such cell lines.[69] The use of cell lines therefore raises important questions. Is it essential for the scientific community to agree on the use of specific cell lines for every clinical cancer subtype? Which specific and standardized characterization methods should be performed to confirm genomic or phenotypic drifts or cell–cell contaminations? And at last, to which extent should cell-based models represent the *in vivo* pathology in terms of underlying biological mechanisms and response to treatment?

A more faithful approach to reconstitute the *in vivo* TME includes the use of primary cells directly extracted from fresh tissues or fluids with subsequent *ex vivo* culture. Since primary cells are only cultivated for a low number of passages, they are thought to display most of the differentiated properties of their tissue of origin.[69] Only one third of ToC incorporate primary cells mainly human peripheral blood mononuclear cells (PBMC), CAFs or endothelial cells (*e.g.* HUVECs). PBMCs include lymphocytes mostly T-cells, B cells including rare plasmocytes, NK cells, monocytes, rare dendritic cells and basophils. Numerous ToC studies use PBMCs, such as Boussomier-Calleja *et al.*[70] who studied the effect of monocytes on cancer cell extravasation at different stages of their life cycle. However, since PBMCs are extracted from healthy donors, they cannot be fully considered to perfectly mimic tumor immune cell infiltration. Here, the use of autologous cells offers the possibility to avoid recognition of non-self cells. This is especially crucial for testing immuno-oncology drugs, such as immune checkpoint inhibitors (ICI) that function by unleashing the cytotoxic activity of T-cells.

Among the endothelial cells, HUVECs were by far the most well-represented source of ECs in vascularized ToC models. Only a few studies used micro-vascular ECs from specialized tissues in ToC.[71,72] One major limitation of HUVECs and of most ECs is their non-tumoral origin. On the other hand, tumoral endothelial cells (TECs) are constrained by the isolation, availability, and viability challenges. Matsuda *et al.*[48] estimated that TECs represent around 2% of the overall cells in the tumor. As such, novel and more efficient isolation protocols need to be established to design fully patient-derived vascularized ToC models. Isolation of ECs from peri-tumor areas could consist of a reasonable compromise allowing isolation of tumor cells, immune cells, fibroblasts, and ECs from the same patient. Notably, some ToC integrate human induced pluripotent stem cell-derived endothelial cells (iPSC-EC).[73] In contrast to cell lines, iPSCs achieve immortality by inducing pluripotency rather than by transformation. For ToC development, iPSCs offer interesting advantages due to their ability to be reprogrammed into different types of tissues but their use in ToC remains scarce (only 1% of ToC publications). Lee *et al.*[74] integrated iPSC-derived cardiac cells in a heart-breast ToC. Fibrotic stages of

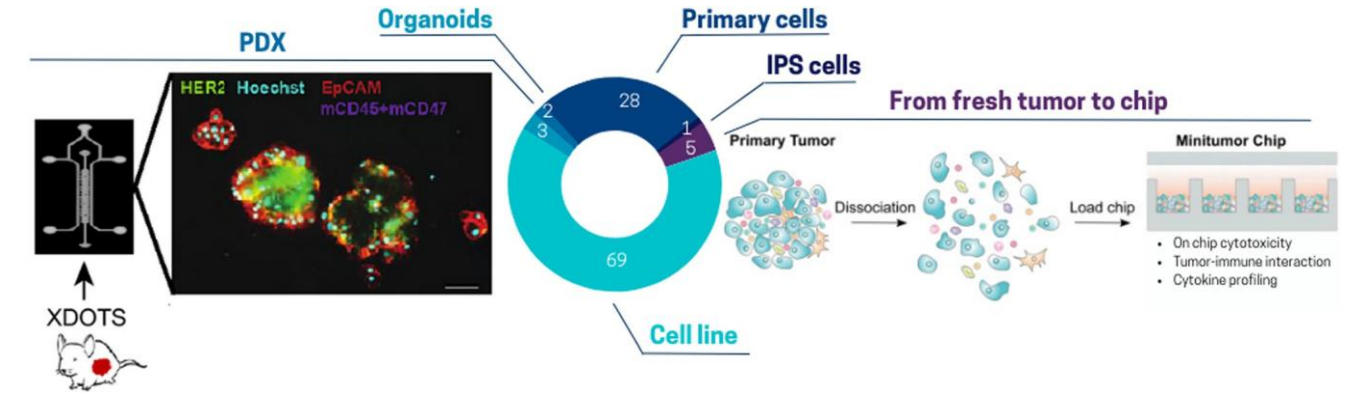


Fig. 3 Pie chart illustrating the proportion of different cell sources used for ToC: cell line 69%, primary cells (HUVECs, PBMCs, primary fibroblasts) 28%, PDX 3%, from fresh tumor to chip (freshly resected tumor, CTCs), IPS cells 1%, organoids 2%. (Left panel) Tumors are harvested from PDXs. After dissociation and filtration isolation, spheroids are produced in ultra-low attachment plate and seeded in the toc.[85] (Right panel) Freshly resected primary tumors can be subjected to tumor digestion using a human primary tumor dissociation kit and then seeded in a micro-well array ToC.[89]

iPSC-derived cardiac tissues have been promoted to assess the differential functionality in healthy and fibrotic cardiac tissues after treatment with chemotherapy. iPSCs also offer the possibility to design multi-organ platforms composed of various tissues from the same donor. For example, cardiomyocytes derived from iPSCs from patients with breast cancer were shown to model at the cellular level the doxorubicin-induced cardiotoxicity observed in some patients.[75]

Other studies used more complex cellular models (although it is still a minority among ToC publications) such as organoids,[76–79] PDX[80–88] or fresh surgical tumor sample.[82–87,90–96] The category "fresh surgical tumor sample" encompasses various form since there is diversity in patient tumor samples including slices, micro-dissected tumor tissues and even single cells. For instance, organotypic slices of PDX breast and prostate tumors were successfully cultured in chips with 6-well plate design for up to 14 days with an accurate prediction of cell death with conventional treatments.[86] Ivanova *et al.*[85] established a PDX ToC system for drug screening (Fig. 3 left panel). Several studies have also demonstrated the feasibility of growing circulating tumor cells (CTCs) isolated from blood samples.[96–98] Often proliferation of primary cells was limited to a few days or weeks but was sufficient for drug screenings.[96] ToC also indicated promising results for the maintenance of fresh surgical tumor samples in culture. Dorrigiv *et al.*[82] demonstrated that oxygen-permeability of microfluidic devices reduces the extent of hypoxia in tissue slices in comparison to 96-well plates. In addition, Chakrabarty *et al.*[86] reported maintaining proliferation in tissue slices for 14 days in ToC *versus* only 7 days with standard plates. Apart from tissue slices, diverse solid tumor types can be included on chip such as primary lesions, lymphadenectomy specimens, pleural effusions, ascites fluid, or resected metastases. Parsian *et al.*[95] fabricated a device with three PDMS layers, where the middle layer accommodates the tissue slices, and the top/bottom layers are perfused with media. Similarly, a study by Ao *et al.*[89] highlights the feasibility of integrating fresh tumor cells directly into microfluidic chips (Fig. 3 right panel). However, this model still lacks several features such as tumor-matching extracellular matrix, which has been demonstrated to affect several key processes, including tumor growth, immune infiltration and drug responses.[15] Alternatively, it is also possible to include micro-dissections of tumors.[81] Growing fresh tumor samples in 3D on ToC including its ECM could pave the way to a closer reflection of the *in vivo* tumor therapeutic response. However, standardized procedures still need to be developed to integrate cell populations isolated from fresh tumors.

B. Tumor cellular architecture. *In vivo*, drug response is influenced by different cell types of the TME through cell–cell interactions or biochemical and cytokines secretions. ToC can reproduce the cellular architecture complexity with great flexibility (varying geometries, positioning of each cell type, *etc.*). During the last 10 years, ToC have integrated cells in mono-, bi-, tri-culture or even more (Fig. 9A). Every cell type has *in vivo*-like organization within the tumor: endothelial cells form perfusable networks, fibroblasts and cancer cells are mixed in a 3D scaffold. About two third of ToC studies included isolated cells while one third used 3D cell aggregates such as spheroids. Spheroids have an organized cellular architecture and present more physiological cell–cell and cell-ECM interactions as compared to 2D cell culture.[99] Furthermore, they exhibit intrinsic metabolic gradients (nutrients, O_2, CO_2) that result in the formation of a multilayer structure: an external layer of proliferative cells, an intermediate layer of quiescent T-cells, and an inner layer consisting of necrotic cells. Despite these convincing features, spheroids generally still lack vascularization that provides cells with essential nutrients and growth factors.

In ToC, cellular architecture can be controlled using various microfabrication approaches. We classified ToC designs, inspired by Sleeboom *et al.*[100] according to five categories (Fig. 4): (a) compartmentalized chip, (b) micro-wells array, (c) 2D chip, (d) membrane chip, (e) lumen chip, and (f) others. Such classification does not cover the whole spectrum of published studies, but highlights the predominant strategies currently employed in the field of tumor-on-chip research. In turn, this classification does not completely capture the diversity and complexity of ToC approaches and some configurations can be a combination of several before mentioned categories.

Almost half of the ToC belong to the "compartmentalized chips" category.[76,101–109] Compartmentalization of cells embedded in hydrogels can be achieved by various physical means. Several studies use co-flow patterning flowing side by side to two different hydrogel solutions. Using this method, Jeong *et al.*[110] co-cultured mammary epithelial cells with human mammary fibroblasts and studied *in vitro* the transition from ductal carcinoma to invasive ductal carcinoma. Compartmentalization can also be created in a more reproducible way by playing with capillary forces.[108] Properly designed pillars induce surface tension to hold the hydrogels in a given area of the chip, while nutrients are supplied through media in adjacent channels. Adjei-Sowah *et al.*[109] (Fig. 4 top left panel) developed a tri-culture of endothelial cells, astrocytes and glioma stem cells utilizing a pillar compartmentalized chip and focused on the identification of ligand-receptor pairs. Compartmentalized chips are very versatile as different types of hydrogel can be arranged in a controlled manner. However, some applications require a fully free interface, while pillars can hinder homogeneous diffusion of the solute. Venzac *et al.* described a new method of compartmentalized chip, where rigid or semi-rigid structures – sliding walls – were inserted into a guiding channel open in the PDMS microfluidic chip sides.[111] The advantage of this method is the possibility to create channels of any size, independently of the hydrogel solutions properties.

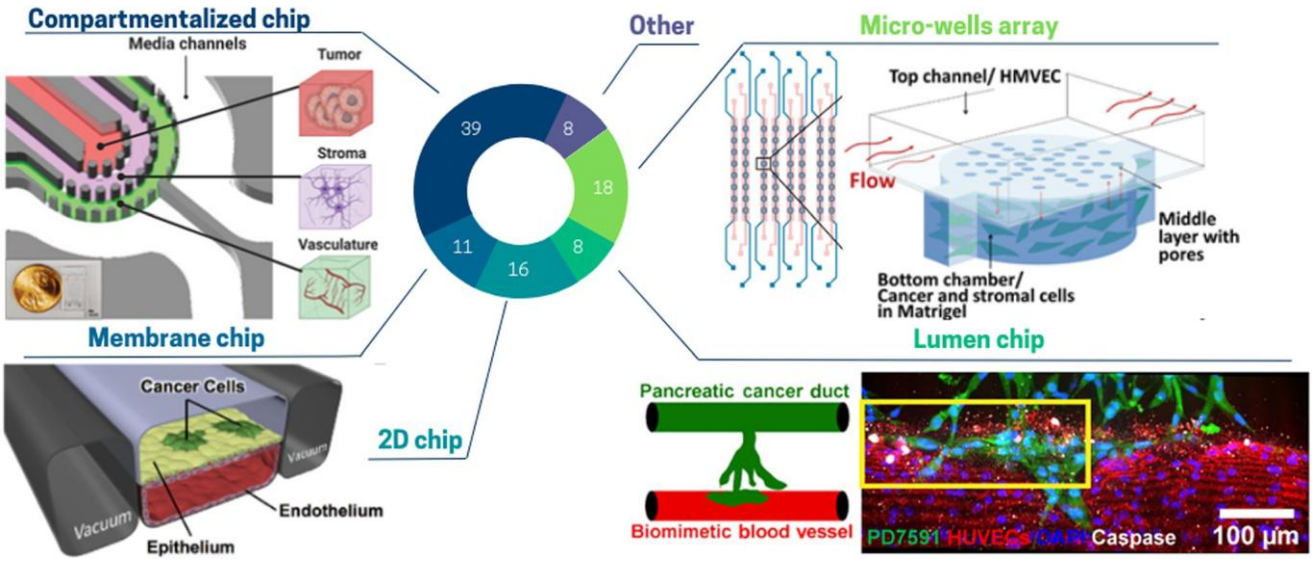


Fig. 4 Pie chart illustrating the proportion of different toc designs used to mimic cell architecture: compartmentalized chip 39%, micro-wells array 18%, 2D chip 16%, membrane chip 11%, lumen chip 8%, other 8%. (Top left panel) The glioblastoma toc model is a compartmentalized chip with three concentric cell culture regions separated by pillars: namely, the vasculature, stroma, and tumor regions surrounded by media channels.[109] (Top right) In this micro-well array ToC, cancer and stromal cells are encapsulated in Matrigel and seeded into the bottom layer, while flow is applied in the top layer.[116] (Bottom left panel) The 2-channel membrane toc contains human lung epithelial cells and a low density of lung cancer cells cultured on the upper surface of a porous ECM-coated membrane. Human lung microvascular endothelial cells are cultured on all four walls of the lower channel, forming a hollow vascular lumen.[71] (Bottom right panel) The lumen ToC is composed of two cylindrical channels embedded within a 3D collagen matrix. One channel is covered with endothelial cells to form a perfusable biomimetic blood vessel, and the other channel is covered with pancreatic cancer cells to form a pancreatic cancer duct.[129]

Another category is the "micro-wells array" which allows studying multiple and/or replicated conditions but often at the price of a limited cell complexity. This category addresses the need for multiplexing ToC studies.[89,112–115] Chi *et al.* (Fig. 4 top right panel) achieved an elevated reconstruction of the *in vivo* TME combined with high throughput screening.[116] They developed a three-layered ToC containing a tumor microvasculature and tumor–stromal microenvironment, along with high throughput screening capability (8 lines of 8 wells). This platform allowed studying the function of the endothelial barrier in drug response and resistance mediated by CAFs.

The "2D chip" approach includes all different designs containing cell cultures as monolayers These 2D models do not display *in vivo* stromal characteristics because their key point is to focus on technological advances, for instance, automation,[117] control of oxygen[62] or shear stress.[35] Kamei *et al.*[117] developed an integrated heart ToC containing three sets of artificial blood circulation loops thanks to the integration of pneumatic valves and a peristaltic pump. This chip allows to automatically perform the following sequence: Matrigel coating, cell introduction, flow circulation and cell staining. 2D chips can also be used to study cell migration. Agliari *et al.*[118] reproduced the interactions between cancer and immune cells and investigated the motility of spleen cells.

"Membrane chips", are composed of microchannels separated by a porous membrane.[41,52,71,79,86,119–121] Although cells are cultured as a monolayer on the membrane, such chips are not to be categorized as 2D chips as cells can migrate through the membrane pores. Membrane chips were originally developed by Huh *et al.*[121] A key feature of this device is the possibility to obtain an air–liquid interface (allowing respiratory epithelial cell differentiation) as well as to apply both controlled peristalsis and shear stress (respiratory lung motion). Although membrane chips were not often used for cancer studies, they are extensively in use for other physiological and pathological models (*e.g.* infection-induced recruitment of immune cells, breathing-induced absorption of nanoparticles).[122] In 2017, Hassell *et al.*[71] (Fig. 4 bottom left panel) created a ToC such membrane-based device. They seeded human lung cancer cells on a monolayer of primary alveolar cells on the same membrane chip, thus recapitulating a lung adenocarcinoma growth.

The category "lumen chip" consists of ToC in which a critical element is used to form lumen in hydrogels.[36,39,49,73,94,123–132] This design is typically used to model blood vessels in tumors or to tightly pack cells in a cylindrical compartment. Nguyen *et al.*[129] (Fig. 4 bottom right panel) describes a chip in which a biomimetic ductal channel containing pancreatic cancer cells is juxtaposed to a blood vessel consisting of an endothelialized perfused lumen. To build these lumen channels, acupuncture needles were withdrawn after collagen polymerization and endothelial cells or pancreatic cancer cells were seeded into each channel. They observed that pancreatic tumor cells invaded and occupied the lumen of the biomimetic blood vessel, resulting in apoptotic

endothelial cells in proximity to cancer cells. On the contrary, endothelial cells in the biomimetic blood vessels in absence of tumor cells invasion did not exhibit apoptotic activity. These data supported the notion that the "lumen chip" model, although being rather simple, allows for complex phenomena to be modelled and studied.

The incorporation of these diverse spatial TME architectures on chip has already provided valuable opportunities to investigate various tumoral mechanisms. Nevertheless, considering the advancements of biological technologies and knowledge, it is obvious that our technologies must evolve accordingly. The emergence of spatial transcriptomics has offered new and insightful perspectives into the architecture and functions of the TME. Consequently, there arises a necessity to further enhance the reconstituted TME on chip to mimic the *in vivo* spatial organization more faithfully. Compared to other cell types found in the TME, the 3D architecture of endothelial cells has been more deeply reproduced in ToC due to its specific organization of perfusable networks. Several *in vitro* approaches exist to replicate the vascular compartment, offering various levels of complexity of ECs arrangement (Fig. 5): patterned microchannel, sacrificial mold and self-assembling. The most straightforward method involves creating a 2D patterned microchannel lined with a monolayer of endothelial cells. This can be achieved by utilizing a membrane configuration, wherein the endothelial cells are seeded onto a porous membrane. The membrane serves to separate the main chamber into two compartments, while additional side channels allow for cyclic stretching of the porous membrane. This configuration is very well suited to study drug penetration of cancer cells extravasation under mechanical stresses. This configuration has been exploited by, Hassell *et al.*[71] to generate a lung ToC model with an air/liquid interface using a 3D endothelial vessel in the basal compartment seeded with lung microvascular ECs. Despite interesting features especially regarding the application of mechanical forces, this approach remains a simplified model of vascularization: geometries are square-shaped and sizes are highly different from tumor vessel networks *in vivo*. 3D blood vessel models with tubular structure have been created *via* several approaches such as bioprinting or guiding needles, called here as "sacrificial molds" and associated with the category of "lumen chips". In this configuration, the endothelial channel can be made in a wide range of hydrogels.[133,134] Miller *et al.*[128] used a commercial chip to incorporate patient derived tumor clusters into a 3D matrix crossed by a vessel mimicking lumen channel (Fig. 5 left panel). Key features include a controlled rate of directional media flow through the cellularized lumen. Although this strategy does not always produce complex geometries, the advantage lies in its full tunability in terms of cell input, perfusion, and 3D matrix. Finally, the most complex ECs organization consists of perfusable and self-assembling microvascular networks (MVNs),[101,135,136] which *in vivo* require interactions with pericytes or fibroblasts. Chen *et al.*[138] studied self-organizing perfusable human microvascular networks (Fig. 5 right panel). Self-assembly is usually restricted to the use of fibrin hydrogel, the only matrix allowing endothelial vessel sprouting, ramification and self-organization.[138] Recently this approach has been exploited by the group of R. Kamm.[38,108,137,139–141] They sequentially added fibroblasts to preform tumor spheroid.[38] They showed that this sequential approach could enhance vascularization and that the vessels close to the tumor spheroid surrounded by fibroblasts made are more perfusable.[38] All these methods have already allowed the study of several important tumoral or therapeutic mechanisms. However, other approaches are currently highly promising; especially photoablation, which could enable the generation of complex vascular networks while avoiding the use of fibrin.[142,143] Besides it is also worth mentioning that there are also room for improvement on the biological aspects of the reconstituted vascular compartment of the TME. *In vitro* replication of the vessel structure remains limited as tumor vascularization is known to be unorganized

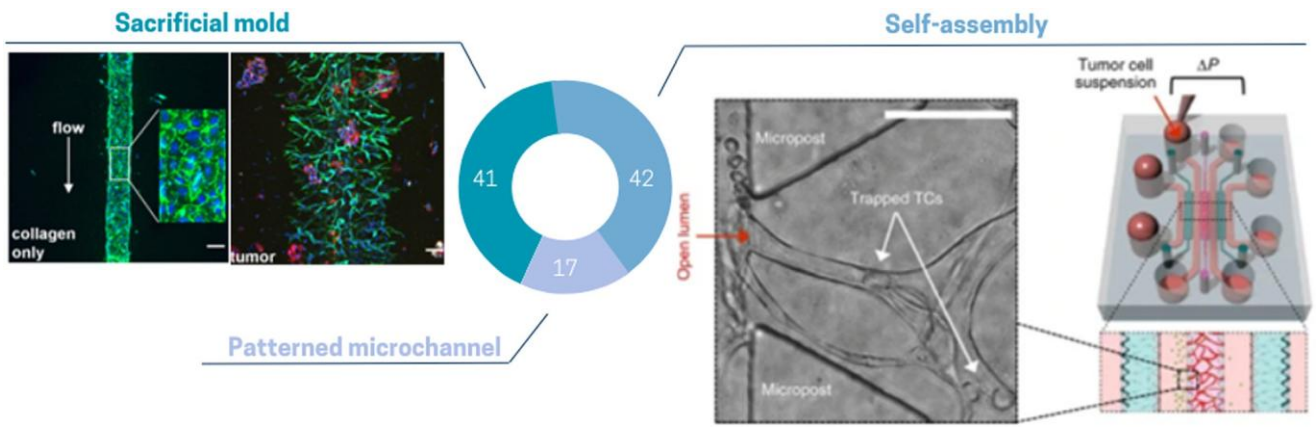


Fig. 5 Pie chart illustrating the proportion of different vascularization methods used in ToC: self-assembly 42%, sacrificial mold 41%, patterned microchannel 17%. (Left panel) Lumen can be formed by removing a retaining rod from collagen and further cellularizing with endothelial cells.[128] (Right panel) Endothelial cells elongate, form vacuoles and subsequently self-assemble into interconnected perfusable vascular networks.[137]

and tortuous, with a lack of pericyte coverage and fenestrated ECs, while most current models mainly focus on accurate perfusion and structural stability. Thus, the development of more accurate *in vivo* mimicking vascularized TME on a chip model remains a challenge.

Tumor-on-chip platforms offer a promising approach to replicate the complexity of tumors *in vivo* within controlled *in vitro* settings. These models provide a unique opportunity to mimic the intricate tumor microenvironment, encompassing factors like extracellular matrix, oxygen gradients, nutrient supply, cell architecture and cell–cell interactions.

4. Applications of ToC for pre-clinical studies for cancer treatment

4.1. A wealth of new information can be extracted from tumor-on-chip

There is a large variety of information which can be extracted from ToC studies. Considering ToC studies of the past 15 years, the most common readouts used in ToC are drug-induced cell death (52% of ToC publications), followed by proteomic (23%), transcriptomic (14%) and secretome (8%) analysis (Fig. 6). Additionally, more readouts such as imaging of hydrogel fibers, diffusion of a compound through the matrix, vessel permeability,[141] cell migration can also be obtained from ToC studies. This classification does not cover the whole spectrum but focuses on the most represented analytical readouts used on ToC; the analytical potential of ToC being continuously expanding.

The high proportion of ToC studies measuring drug-induced death emphasizes the potential of on-chip applications for drug screening. Very recently, Jun Ye Ong *et al.*, proposed an array device to culture PDX-derived spheroids combined with a drug concentration gradient to generate high throughput dose–response.[80] This work was the first to demonstrate a quantitative correlation between drug efficacies estimated on ToC with *in vivo* data. Protein-based studies are conducted in about one fourth of ToC studies and mostly rely on flow cytometry, western blot and immunostaining as for example the work Boussomier-Calleja *et al.*, which analyzed in ToC the expression of macrophage-like markers to characterize monocyte differentiation.[70] Transcriptomics performed on ToC have been used to decipher the impact of several TME parameters, such as oxygen levels, matrix stiffness, cell subsets identity or gene expression. The majority of these studies used RT-qPCR, although some studies performed bulk RNA-seq. Ayuso *et al.*, analyzed a panel of selected immunity-related genes to study stress-induced exhaustion of NK cells in co-culture with breast cancer spheroids.[123] They demonstrated that NK cells in bi-culture exhibited a different transcriptomic profile, dominated by exhaustion markers, as compared to naïve NK cells. Recent studies emphasized the feasibility of single cell RNA-sequencing (scRNA-seq) of ToC derived cells. In the work of Shirure *et al.*, several cell types (cancer cells, endothelial cells, fibroblasts, macrophages) were successfully recovered from chip devices and analyzed by scRNA-seq.[104] The authors identified macrophages to dramatically impact gene expression in both endothelial cells and fibroblasts. Importantly, they were able to identify two distinct endothelial cell phenotypes as a consequence of M1/M2 macrophages and tumor cells co-culture. Several clinical applications could emerge from integrating fresh patient-derived tumors on chip in combination with scRNA-seq. For example, this approach can enable the detection of rare malignant and/or chemo-resistant cancer cells, and provide supporting evidence for further suitable treatment approaches. Analysis of secreted molecules by cells – secretome – can also offer crucial information about the functional responses of the tumor ecosystem. Ligand binding assays (LBA), such as ELISA or Meso Scale Discovery (MSD) platforms can be used to measure such secreted molecules. In Jenkins *et al.*, profiles of secreted cytokines from 3D microfluidic cultures of tumor spheroids were used to screen for the response of murine models and patient tumor samples to immune checkpoint blockade therapy (anti PD-1).[144] Although cytokine analysis is fairly simple and very classical in conventional *in vitro* models, it is still not often used in ToC experiments.[145] Recently, metabolic alterations have been shown to play a role in the sensitivity of cancer cells to drug and rewired metabolism is linked to rapid

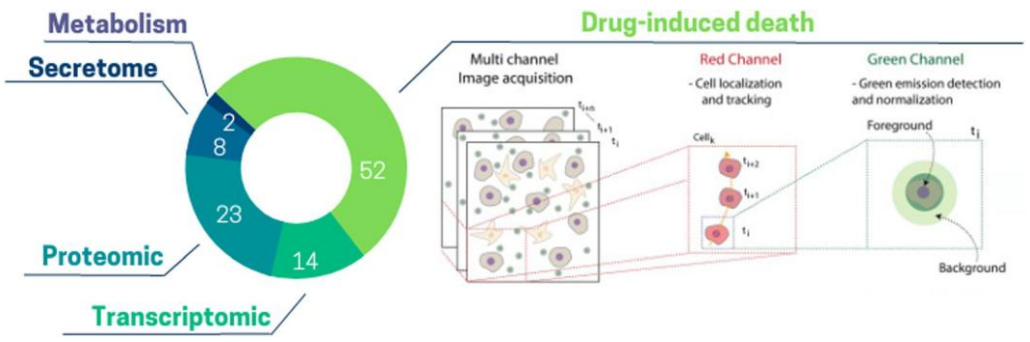


Fig. 6 Pie chart illustrating the proportion of different information extracted from ToC: drug-induced death 52%, proteomic 23%, transcriptomic 14%, secretome 8%, metabolism 2%. (Right panel) Drug-induced death: open-source computational method can be used to extract the temporal kinetics and the spatial maps of cancer death.[150]

tumor growth and proliferation.[146] Only a few ToC studies (2%) focused on cancer cells metabolism highlighting that this field remains to be further explored. Hou *et al.*[147] used ultra-performance liquid chromatography coupled with mass spectrometry (UPLC-MS) to detect metabolites such as 5′-deoxy-5-fluorocytidine or 5-fluorouridine, to study metabolism-induced anticancer bioactivity. Additionally, only a low number of studies apply live markers of metabolism such as pH, hypoxia or ROS, providing both temporal and spatial information[61] which are highly complementary to metabolic endpoint analysis. Among the new analyses that could be performed on ToC, it is worth citing the Assay-Guidance Manual published by the NIH Chemical Genomics Center.[148] It describes guidelines for robust assay development and recommends cell proliferation and cytotoxicity assays including[149] tetrazolium reduction, resazurin reduction, protease markers, and ATP detection, which are not commonly used on ToC up to date. Efforts could also be made to improve the compatibility of ToC with conventional analytical formats (*e.g.*, the plate reader) to be able to use conventional kits and standardized assessment protocols.

To our best knowledge, ToC studies pursuing genomic analysis are rare (only 1 study was identified among the over 300 reviewed in the current article). Zhang *et al.*[98] expanded circulating tumor cells (CTC) isolated from early-stage lung cancer patients with fibroblasts on a co-culture chip. Next-generation sequencing of 124 cancer-related genes revealed matched mutations between the primary tumor and cultured CTCs in 3 out of 8 paired CTC-tumor samples (CASP8, APC, TP53 and ERBB4 genes). Such studies suggest that the combination of ToC with next-generation sequencing could help revealing the genetic and epigenetic underpinnings of cancer, as well as help to redefine treatment paradigms.

In addition to the aforementioned readouts, the compatibility of ToC devices with high resolution imaging is also a major asset. ToC can be continuously imaged with automated video-microscopes which can additionally provide information about cell dynamics (*e.g.*, motility, cell–cell interactions, *etc.*) and cellular activities (*e.g.* death, division, pathway activation, *etc.*), at single-cell resolution. Novel types of information can be deciphered by looking at the behaviors of dynamic 3D microenvironments. However, a major bottleneck is the conception and development of appropriate computer tools to process and extract the richness of biological information encrypted in on-chip images and videos. New findings can be obtained by spying tumor ecosystem dynamics within ToC in the framework of interdisciplinary collaborations between biologists and computer scientists, taking advantage also of the great power of artificial intelligence (AI) tools. For instance, a computational method, named SpatioTemporal Apoptosis MaPper (STAMP), has been developed to extract the temporal kinetics and spatial maps of cancer cell death from ToC[150] (Fig. 6 right panel). STAMP revealed that cancer cells death induced by chemotherapy is transmissible, meaning dying cells promote apoptosis of cancer cells in proximity. Recently, ToC devices are also exploited to track immune cells activity around many individual cancer spheroids simultaneously at high spatiotemporal resolution. Ronteix *et al.*[151] combined parallel imaging of T-cells behavior with probabilistic modelling to investigate the rules governing T-cells recruitment. Additionally, imaging techniques may also be used to visualize intravasation and extravasation processes, which remains a challenge for *in vitro* models. ToC allows studying metastatic processes in a stepwise manner.[152] It enables investigating the impact of each parameter such as the presence of a specific cell type on cancer cell migration, intravasation or extravasation. ToC has been used to study the effect of monocytes, at different stages of their life cycle, on cancer cell extravasation in a 3D vascularized microfluidic model.[70] Boussommier-Calleja *et al.* showed that breast cancer cells are less prone to extravasation in the presence of monocytes highlighting the role of monocytes in metastatic progression.[70]

The next step will be to apply these analysis tools for evaluation of patient-derived ToC for clinical application such as patient stratification and drug response prediction. The use of 'personalized' ToC composed of primary cells isolated from fresh tumors will open the possibility to conceive novel diagnostic tools that exploit AI-based analysis on *ex vivo* live-cell biomarkers. Some recent proof-of-concept studies support this concept. For example, morphodynamic biomarkers of primary cancer cells cultured on chips were used to predict post-surgical risks of relapse in operated breast and prostate cancer patients with high accuracy using machine-learning algorithms.[153] Another study showed that a deep learning approach was able to correctly identify responding breast ToC cancer-immune co-cultures treated with a targeted therapy drug (trastuzumab) by using an atlas of immune cell trajectories.[154] This suggested the feasibility of the methodology to predict drug responses using the information hidden in cell ecosystem dynamics. In the future, it will be essential to intensively pursue and to greatly expand the interdisciplinary collaboration efforts between cancer biologists, clinicians and computer scientists in order to fully take advantage of a large number of hidden information that could be extracted from ToC experiments. The combination of ToC live imaging and advanced computational image analysis, involving AI, thus provide immense opportunities to characterize the behaviors governing tumor ecosystems and to understand their responses to anti-cancer treatments.

4.2. Testing the efficacy of chemotherapies

The TME composition has a profound effect on drug efficacy and deciphering the effect this complex environment is critical.[155] Since ToC allows mimicking the TME, it is a powerful platform to study drug effect as well as the dynamics of cell death in presence of drugs (Fig. 6). According to our analysis, the main anti-cancer treatments

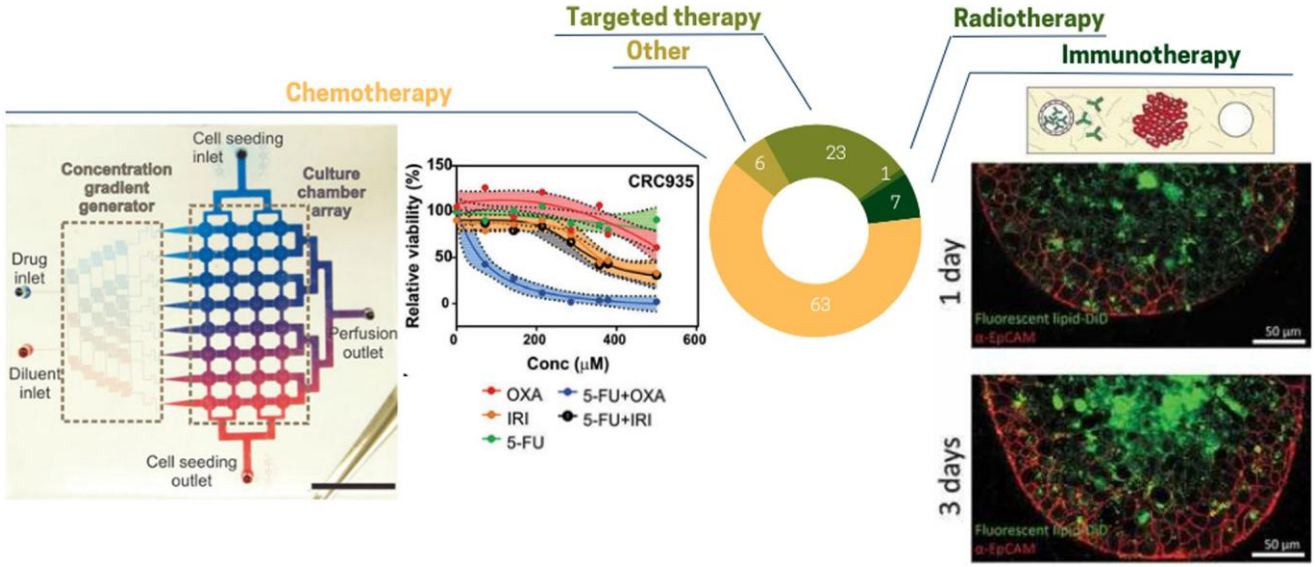


Fig. 7 Pie chart illustrating the proportion of different treatments tested in ToC: chemotherapy 63%, targeted therapy 23%, immunotherapy 7%, other 6%, radiotherapy 1% (right panel) concentration gradient generator to test different drug combinations.[80] (Left panel) Diffusion of antibody inside MCF7 spheroid.[124]

studied in ToC were chemotherapy (63% of ToC publications), targeted therapy (23%) and immunotherapy (7%) (Fig. 7).

Chemotherapy remains the frontline treatment for advanced-stage or metastatic malignancies for which loco-regional treatments, *i.e.* surgery and/or radiation therapy are not useful due to the dissemination of cancer cells in the whole body.[156] Chemotherapies tested in ToC are mostly taxol, doxorubicin, carboplatin or cisplatin,[35,77,106,110,116,117,120,145,157–160] in agreement with clinical practice. These treatments have been mostly applied to common cell lines such as lung cancer A549, breast cancer MCF7 or MDA-MB231. Using an on-chip co-culture of cell lines (cancer cells, CAFs, stem cells and an endothelial monolayer) Chi *et al.*[116] showed that the co-culture with CAF delayed the response of the TME to doxorubicin in comparison to the co-culture with normal fibroblasts. Apart from cell lines, ToC also enables the *in vitro* culture of patient samples for chemotherapy testing.[160] Chakrabarty *et al.*[86] tested the response to cisplatin using cisplatin-sensitive and cisplatin-resistant breast cancer PDX tumors. Interestingly, breast PDX cultured in the ToC platform showed a stronger response to cisplatin treatment than the conventional *ex vivo* culture method (6-well standard plates on an orbital shaker), suggesting that the ToC platform provides with a more optimal drug delivery into the tumor slices than the *ex vivo* culture method. Haque *et al.*[79] developed a ToC incorporating patient derived organoids (PDO) and stromal cells (pancreatic stellate cells and macrophages). They showed that targeting stroma cells (stellate cells by all-*trans* retinoic acid or macrophages by Clodrosome®) improved therapeutic effect of gemcitabine on cancer cells. Conversely, in a ToC model of breast cancer metastasis to bone,[161] including osteoblast-like cells seeded on a 3D-printed biomimetic bone scaffold, the sensitivity to cisplatin of PDX-derived triple-negative breast cancer (TNBC) cells was reduced with respect to conventional 3D cultures in Matrigel, which is consistent with the clinical observations that chemotherapy often failed to completely eliminate TNBC cells colonizing the bone.

Tumor chemosensitivity assays (TCAs) with conventional methods have been gaining attention over the past few decades. They provide a satisfactory negative predictive value (showing the possibility of drug resistance), however they only have a moderate positive predictive value (showing the possibility of drug sensitivity).[156] In this context, ToC appears as a future powerful tool for TCAs with the possibility to evaluate multiple drugs and multiple doses.[156]

4.3. Targeted therapy developments

Over the past two decades, there has been a tremendous shift in cancer treatment from chemo- to targeted therapy in cancer patients' subsets.[156] Targeted therapies often aim to deliver drugs to cells with molecular genetic alterations specific to cancer cells (gain of function, oncogene mutation or gene amplification).[162] Most of these targeted drugs have a much higher affinity for altered proteins in cancer cells than their normal counterparts in normal cells, which explains their lower toxicity (favorable therapeutic index). Targeted therapies can be roughly classified into two categories: small molecules (0.1–1 kDa) and macromolecules (greater than 1 kDa, also called biologics). Biologics are relatively complex molecules derived from living cells or through biological processes, such as monoclonal antibodies or antibody–drug conjugates.[163] Despite the recent interest and success of biologics, small molecules, which are made *via* chemical synthesis, are still in the picture of innovative drug research and development.

About one fourth of drug testing in ToC focused on targeted therapy. Targeted therapies exploring a wide range of targets have been tested on chip, among them kinase inhibitors (Tarceva, erlotinib),[71,164] HER2 inhibitors (trastuzumab),[165] CXC chemokine receptor inhibitors,[73] EGFR inhibitors (cetuximab).[165]

Nguyen *et al.* studied the effect of trastuzumab, a monoclonal antibody directed against the HER2 receptor, on breast cancer cells presenting HER2 amplification.[166] Trastuzumab alone or immune cells (PBMC) alone had mild effects on HER2+ cancer cells, but their combination induced a massive cancer cell apoptosis, exquisitely recapitulating on ToC a complex immune behavior, namely an anti-tumoral antibody-dependent cell cytotoxicity (ADCC). Live imaging combined with advanced cell tracking algorithms allowed to measure the number and the duration time of interactions between cancer and immune cells. In this HER2+ breast ToC, addition of trastuzumab specifically promotes long cancer–immune interactions (>50 min). Moreover, the presence of CAF (CAF-S1 sub-type) abolished this trastuzumab-dependent stimulation of cancer–immune interactions, suggesting that CAF-S1 cells may contribute to trastuzumab resistance by participating in immunomodulation.[166] Other targeted therapies such as anti-angiogenic drugs have been tested in vascularized patient-derived ToC vessels.[94] For different drug concentrations and different targets, the authors quantified vessel permeability as well as vessel sprouting and confluency.

Targeted therapies have already demonstrated their potential in clinics for different cancer subtypes and still holds great promise in particular with the recent emergence of the ADC drugs coupling targeting and chemotherapy precision delivery. However, small-molecule targeted anti-cancer drugs, despite high response rates and rare primary resistance, still face many challenges with the emergence of resistant clones.[162] Drug resistance could be linked to several mechanisms, including gene mutation or amplification, leading to parallel signalling pathway activation, apoptosis or autophagy dysregulation, *etc.*[167] We envision that the ability of ToC to recapitulate the cellular complexity of the tumor will be a strong asset for testing new targeted therapy testing, and we anticipate an increase of the anti-cancer drug application in ToC.

4.4. Pre-clinical studies on tumor-on-chip for immunotherapies

As ToC can include diverse immune cell types, it is emerging as a powerful model for immunotherapy testing. Immune system within the tumor microenvironment consists of adaptive and innate components[168] that are interdependent. The innate system is the first defense mechanism against tumor-specific or tumor-associated antigens, and it generates short-lived responses of antigen-specific immune cells such as monocytes, macrophages, dendritic cells and natural killer (NK) cells. On the other hand, the adaptive system can generate immune memory producing long-lasting responses through T-cells and B cells.[169] In turn, it has been shown that the presence of immune cells in the TME affects tumor progression, explaining why some of the on-going and very promising ToC strategies are focused on immunotherapy development.

Immunotherapies are innovative anti-cancer treatments that have revolutionized anticancer therapy since the early 2000s through unleashing the immune anti-cancer response.[170] Immune checkpoints are receptors expressed by immune cells that enable dynamic regulation of immune homeostasis and are particularly relevant to T-cell functionality.[171] Most immune check-point inhibitors (ICI) have been focusing on reinvigorating CD8+ T-cells to target cancer cells. While their success was originally thought to be dependent on local T-cell abundance, or on the cancer cell abundance of immune checkpoint targets, favorable responses to these therapies are still largely variable, particularly in solid tumors, where T-cell infiltration is highly variable and does not necessarily correlate with therapeutic efficacy.[172] Recent evidence suggested that there is more to be understood about the immune cell component within the TME and how to exploit them for therapeutic purposes. A major challenge to study tumor–immune interactions and develop therapies is the lack of effective and representative models. It is well established that the innate and adaptive immune systems of animal models, like rodents, are different from those of humans.[173] Consequently, syngeneic mouse tumor models, allowing for the participation of the native rodent immune system, rarely mimic human cancer behaviors and their applicability remains limited. PDX models are by nature immune-deficient models and are not suitable for studying immune checkpoint inhibitors targeting human T-cells. Humanized mice models could be used but such mouse humanization is still a highly variable, costly and time-consuming technology. Moreover, the approaches to investigate cancer cell escape from immune surveillance are limited to intravital microscopy in mouse models or observations of tissue slices from human tumor samples. This has motivated the development of ToC as a unique technological approach to reproduce the multiple layers of complexity of cancer–immune system crosstalk.[174–176]

Less than one tenth of the ToC studies focused on immunotherapies[27,38,83,89,123,177–180] but interestingly, the types of immunotherapy (alone or in combination) tested are broad, including immune checkpoint inhibitors (ICI), oncolytic viruses, and T-cell therapies. Parlato *et al.* reported that IFN-α-conditioned dendritic cells (DCs), grown in co-cultured ToC, exhibited remarkable migration and phagocytotic activity against colorectal cancer cells pre-treated with IFN-α and romidepsin, a histone deacetylase (HDAC) inhibitor.[177] In this model, DCs were cultured in the central chamber while both untreated and treated cancer cells were embedded in collagen I gel in the two adjacent chambers to evaluate DCs behavior in the extracellular matrix. An increase in DC migration toward pretreated colorectal cancer cells in this model was driven by

the CXCR4/CCL12 signaling axis, consistent with the DC responses *in vivo*. Most interestingly, by labeling DCs and SW620 with fluorescent dyes, cancer phagocytotic activity was captured in real-time using confocal microscopy, making this model more advantageous than *in vivo* models, where real-time monitoring of DC phagocytotic activity is not possible. Ayuso *et al.* developed a 3D microfluidic model that incorporated NK cells, endothelial channels (HUVECs), and MCF7 spheroids (Fig. 7 right panel). The authors studied antibody penetration into the spheroids, NK cell migration and antibody-dependent cell cytotoxicity (ADCC).[124] The dynamics of ADCC shown in this model *via* live imaging was remarkable. NK cells were able to directly penetrate deep into the spheroid core and destroy the cancer cells in a matter of hours, without first killing the outer layer of the tumor. Such studies highlight the power of ToC to pave the way for new studies which were not feasible with classical cell culture models. Indeed, ToC could enable researchers to focus on antibody dynamics and study the impact of various parameters separately such as endothelial permeability, tumor penetration or antibody clearance by tumor cells. A very recent study from Bi *et al.* interrogated the role of macrophages in tumor progression using a ToC device and downstream single cell RNA-seq. They introduced M1 or M2 macrophages into a 3D tumor-on-chip model to investigate tumor behaviors in response to these macrophage subsets.[104] In this model, M1 macrophages exhibited anti-tumor properties, whereas M2 macrophages showed significant pro-tumor effects, which is consistent with the current understanding of tumor-associated macrophages. However, to date, most ToC that incorporate immune cells do not allow for high-throughput testing. To address this limitation, Ronteix *et al.* recently introduced a platform for the parallel formation, manipulation and multiplexed observation of hundreds of tumor spheroids within stationary microfluidic droplets, in the presence of antigen-specific cytotoxic T lymphocytes.[151] Exploiting mathematical probabilistic models, the quantity and quality of spatiotemporally resolved data allowed to establish that the first recruited T-cells initiate a positive feedback loop to accelerate further recruitment to the spheroid, confirming the cooperation between T-cells in the tumor killing process.[151]

Injecting oncolytic vaccinia viruses (OVV) directly into the tumor microenvironment is an alternative to improve tumor antigen recognition and to strengthen T cell responses.[181] In a lung ToC model, infection by OVV was shown to increase cancer–immune interaction times leading to cooperative antitumoral activity of immune cells and OVV.[154] Proof-of-concept studies also illustrate the feasibility to exploit ToC models for innovative immunotherapies such as Chimeric Antigen Receptor (CAR)-T-cells. In the model developed by Pavesi *et al.*, human T-cells engineered to express tumor-specific T cell receptors (TCR-T-cells) were added into the adjacent channels to investigate the ability of the modified immune cells to migrate and kill the tumor target and their secreted soluble factors.[182] A recent work by Wan *et al.*[38] presented a vascularized *in vitro* model which can be used to evaluate CAR-T cell recruitment, killing capacity, and inflammatory response. After 96 h of perfusion, higher densities of both T-cells and dead cells were found in the CAR-T cell containing ToCs as compared to the control T-cell containing ToC in both co-mixed and sequential tumor spheroids.

Although ToC models offer a powerful experimental setting to quickly test immunotherapies, the vast majority of the immune-competent ToC models are so far based on cell lines and allogeneic immune cells, *i.e.* immune cells not coming from the same individual (mainly PBMC), exhibiting the obstacle of human leukocyte antigen (HLA) incompatibility. Immunotherapy testing requires the use of autologous cytotoxic T-cells to avoid the risk of allogeneic reactions, which, however, would require longer time than the few days needed for ToC experiences. We envision that one of the upcoming challenges in the field will be the development of patient-derived ToC for immunotherapy testing. Some latest works have shown the feasibility of such an approach. For example, a recent work reported the use of a glioblastoma-on-a-chip model to dissect a reconstituted immunosuppressive tumor microenvironment (composed of tumor-associated macrophages (TAM) and cytotoxic CD8+ T-cells) and its response to programmed cell death protein-1 (PD-1) checkpoint blockade. Interestingly, different glioblastoma subtypes displayed distinct CD8+ T-cells behaviors (extravasation, tissue infiltration, cytotoxic activities) as well as cytokine profiles. Moreover, co-targeting of PD-1 immune checkpoint and TAM-associated CSF-1R signaling improved therapeutic efficacy on-chip. However, again, human CD8+ T-cells were allogeneic, sorted from PBMCs, limiting the clinical significance.[27]

Even though immunotherapies can produce impressive and long-term responses in some cancer patients (*e.g.*, 20 to 40% of lung cancer patients), their clinical benefits remain unsatisfactory because the majority of cancer patients are non-responder.[170] What remains to be explored in these tumor–immune models is the incorporation of the adaptive immune cell component, in particular, autologous T-cells, as well as the integration of an *in vitro* immune organ, namely bone marrow- or lymph node-on-chip, to further understand tumor immunity and develop new therapeutics. Most models utilize a variety of cell sources, both immortal and primary cells in combination, making it difficult to study the adaptive immune response. A good metric of ToC would be to evaluate how deeply they are able to reproduce the *in vivo* functional readouts such as cytokine release, phagocytosis, IgM/IgG class switching.

Finally, immunotherapy is a fast-evolving field, and one of the further challenges in immunotherapy is the development of bispecific antibodies (BsAbs) that can directly target two different antigens on immune cells and/or tumors (tumor-associated antigens), synergistically engaging T-cells onto cancer cells, thereby increasing cytotoxic activity.[170] We anticipate that in the near future ToC technology will be able,

by reproducing the complexity of cancer–immune system crosstalk, to help the development of novel therapy exhibiting multiple cell interactions such as bispecific antibodies.

4.5. Drug combination in ToC

Over the years, the concept of combination therapy, which relies on combining two or more therapeutic agents, with different modes of action, has been introduced to overcome cancer treatment resistance. Such combination is either synergistic or additive, and therefore, a lower therapeutic dosage of each individual drug can be required, which also spares the cumulative toxicity.[183] Combination therapy exhibits numerous benefits, such as the ability to target multiple oncogenic pathways, to improve and prolong therapeutic responses while reducing the likelihood of therapeutic resistance.[184] This can include the combination of chemo- and radiotherapy, chemo- and immunotherapy, or chemotherapy and targeted agents.

In contrast to conventional cell culture, fluidic control in ToC allows for creating precise drug mixing and variations over time. Ong *et al.*[80] introduced a ToC with a concentration gradient generator (Fig. 7 left panel). This configuration allowed assessment of 8 drug concentrations and 5 different drug combinations. They showed that tumors did not respond to single-agent Oxaliplatin (OXA) and 5-fluorouracil (5-FU) treatments, but conversely had improved sensitivities when both drugs were combined (5-FU + OXA). This work represents a great illustration of the ToC potential for drug testing. Recent publications highlighted the possibility to test combined therapies on fresh surgical tumor[81] or PDX.[85] For example, Ivanova *et al.*[85] tested drug combinations in breast cancer patient xenograft-derived organotypic spheroids. They identified that neratinib and trastuzumab combination was more effective compared to each agent alone, and was associated with more robust inhibition of HER2. Importantly, Eduati *et al.*[91] presented a plug-based microfluidics platform for functional screening of drug combinations (56 different conditions with at least 20 replicates each). They suggested a novel drug combination for pancreatic cancer cell lines: PHT-427 and MK-2206, which consist of two serine/threonine kinase AKT inhibitors acting through different sites. This study highlights that the best drug combination can be different for each patient and that high throughput ToC holds a great potential for personalized medicine.

Finally, drug combinations can also include immunotherapies. With a vascularized ToC, Humayun *et al.*[73] demonstrated that by combining immunotherapies inhibiting IL-6, IL-8 and MMP-3, the extravasation events can be reduced. In the near future, ToC could be pivotal to decipher the intricate interplay between ADC and ICI. ADCs can selectively induce death of target-expressing tumor cells and activate tumor-specific adaptive immunity through increase of T-cells infiltration in the tumor microenvironment, whereas ICI reinvigorates exhausted T-cells, enhancing antitumor immune responses.[185]

4.6. Support for nanomedicine innovation

Besides these conventional anti-cancer treatments, recent advancements in nanotechnology have opened new windows for the discovery and development of anti-cancer nanomedicine strategies. Having gone through several generations of nanomedicine drug development, nowadays we are at the verge of multifunctional nanomedicine therapeutics, allowing for targeted drug delivery and stimuli-triggered nanosystems, as well as their combinations. Nanocarriers appear as powerful technologies to release anticancer drugs in a stable and controlled manner. Moreover, the use of stimuli can assist in the controlled release of the drug to ensure specific toxicity to the tumor tissue, while sparing the healthy tissue.[186] A variety of nanotechnology-based treatments have already gone through clinical trials, are marketed and are being currently used for clinical cancer therapy applications.[187] However, the prevailing majority of research on nanomedicine therapies for cancer care is still at the stage of preclinical studies.[188] Nowadays, conventional *in vitro* models for nanomedicine screening as well as *in vivo* animal models are unable to closely replicate human *in vivo* tissue environment which, in turn, significantly impedes adequate nanomedicine development and evaluation. Crucial parameters such as nanoparticles' toxicity, diffusion, internalization, accumulation oftentimes cannot be adequately assessed with conventional models. In regard to these limitations, ToC are gaining interest for the development and evaluation of nano-based therapies in tumors.[189] ToC may allow to finely evaluate these pivotal criteria of evolving nanotherapeutic approaches through precise control of microenvironment, phenotype, dynamic fluid flows and physiological gradients among the others – all of which affect nanomedicine's suitability and progress of preclinical studies.[190,191]

While multiple works in ToC have been focused on the various key aspects of nanomedicine evaluation for clinical applications, such as nanoparticles (NP) toxicity,[192,193] transport,[194,195] uptake,[193,196] accumulation,[197,198] they only represent 13% of reviewed ToC-related studies. For the purposes of this review, we will focus on the investigation of the therapeutic impact of NP-based therapies on tumor tissues, their efficacy and cellular effect readouts in ToC models. Broadly, nanomedicine therapies can be subclassified into drug nanocarriers and stimuli-responsive nano objects that function as a treatment itself upon activation.[187] The former has been mostly explored up to date as they allow to increase loaded conventional drug's stability, solubility, blood circulation time as well as to provide controlled drug delivery to the site of interest.[199] In the scope of ToC, multiple studies have been carried out to demonstrate effective tumor cell death following the nanocarrier drug exposure. Thereby, Liu *et al.* have reported a ToC model of human glioma to study tumor targeting with nanomedicine. They have demonstrated remarkable tumor reduction post-treatment with paclitaxel-loaded folate-

decorated NPs as well as significant cell death due to both apoptosis and necrosis.[200]

However, following the concerns of the high NP concentrations required and high systemic drug toxicity, a new line of research is dedicated to the stimuli-responsive nano objects that can be activated by endogenous or exogenous sources at the site of interest and operate as therapeutic agents themselves. Some of the most common non-invasive, stimulating therapies are exogenous triggering mechanisms such as photodynamic therapy (PDT) and hyperthermia-based therapies (*e.g.*, magnetic hyperthermia, photothermal therapy (PTT), ultrasound, among others).[201] PDT is based on the phototoxic reactions that stem from the photosensitizer activation by light within tumor cells.[201,202] Recently, Flont *et al.* designed a ToC model of ovarian cancer to evaluate the effect of PDT through free *vs.* nanoencapsulated photosensitizer on cancer cells.[203] Their results have demonstrated remarkably higher cytotoxicity of nanoencapsulated photosensitizer as compared to the free one, which was further boosted by the PDT. They also demonstrated that PDT induced ROS generation in cancer cells while having little effect on non-malignant cells. Another ToC study on externally triggered nanoparticles was conducted by Lee *et al.* on a co-culture of breast and glioblastoma cancer cells *via* gold nanorod-mediated PTT.[204] They have demonstrated drastic reduction in cell viability upon PTT exposure as compared to separate conditions with either nanorods presence or PTT, indeed indicating an advantage for the stimuli-induced effect.

Stemming from the beneficial characteristics and therapeutic outcomes presented by the stimuli-responsive nanoobjects, some of the recent strategies in nanomedicine therapies development have focused on the combination of nanocarrier and stimuli-responsive nanosystems, which allow for the dual action with triggered drug release, thus limiting the systemic exposure to the toxic chemotherapy. Agarwal *et al.* using a vascularized ToC model of breast cancer, have shown that nano-encapsulated doxorubicin is significantly more effective for cell death induction than free doxorubicin.[205] Moreover, the Dox release can be controlled *via* NIR irradiation thanks to the photothermal and photodynamic sensitivity of the NPs.[205] Another study involving stimuli-responsive nanocarrier drug delivery was conducted by Zervantonakis *et al.* in which they demonstrated in a ToC model of rat glioblastoma that Dox-loaded thermosensitive liposomes, when heated induce the greatest effect on tumor cell death and proliferation inhibition as compared to the single application of either drug-loaded NPs or heating.[206]

These different examples evidenced that ToC modeling would allow us to better investigate the effect of the new generation of nanomedicine therapies by being able to finely assess their influence on the tumor microenvironment in a human-mimicking tissue, therefore facilitating the transition towards the clinical studies.

5. ToC paths towards pharmaceutical and clinical applications

Classically, from the conception of a new drug to the launch of the product, the drug development process can take up to 15 years (although shorter times have been recently shown for targeted therapies), and cost upwards of $1 billion.[207] To date, the success rate of new anticancer drugs development is very low for two main reasons: the lack of clinical efficacy and the unmanageable toxicity of the drug.[4] One third of drugs fail in clinical phases due to an insufficient therapeutic index, meaning that the efficacious dose and the toxic dose are too close.[208] This number evidences the shortcomings of current preclinical models to accurately predict the right target at the right dose. In order to reduce such attrition between preclinical and clinical research, the FDA has recently requested 5 million US$ to develop a comprehensive strategy on alternative testing methods.

Among the different *in vitro* preclinical models, patient-derived cancer organoids (PDO) appear as a powerful new model. A recent review, including 60 studies, indicated that organoid cultures are faithful predictors of patient response to chemotherapy for different types of cancer.[12] However, the establishment of PDO is not equally effective for all solid cancers and cancer organoids still lack some cells component of the TME, including stromal cells, immune cells, and endothelial cells. Moreover, a big challenge of organoids is to align the timescales of model establishment (1–6 months) to those of clinical decision-making. ToC by combining a short establishment time and a high control of several TME features are expected to better predict patient's treatment response.[12] ToC has the potential to complement conventional preclinical models and the global ToC market size is projected to reach 110 million dollars by 2030.[209]

To make ToC seamlessly integrated into the drug discovery and development process, three main aspects must be considered: standardization, reproducibility, and throughput. Since ToC are still in the early-development stage, consistency and standardization are still lacking, and there is often variability in materials, device fabrication and operating conditions.[210] The US IQ MPS workshop 2022 and the European ORCHID project have clearly identified standardization as a fundamental pillar of the advancement of MPS technologies. However, until now, there are currently no specific standards that have been agreed upon. To meet these standards, ToC will have to be independently validated by third-party testing centers. In line with these requirements, the NIH/NCATS and its Tissue Chip Consortium has been working on the establishment of the Tissue Chip Testing Center program dedicated to organ on chip validation. This independent validation is a stepping stone for the MPS field to provide more confidence for industry to onboard this new technology. Beyond standardization, reproducibility is also

an important challenge from industry perspective; future studies would also be needed to properly assess the ToC reproducibility.

Another important consideration is related to the ability of this new technology to achieve the level of multiplexing that would allow rapid and efficient drug discovery at a large scale. So far, only few ToC studies were able to process samples at high throughput (*i.e.* custom micro-well arrays). High-throughput ToC would be a real breakthrough as it would allow for testing multiple compounds, and multiple concentrations in a complex and controlled reconstituted TME. Some studies recently showed the feasibility to automate ToC operations, such as media changes, pH testing, compounds monitoring (oxygen, lactate, glucose), or drug injection.[91] On chip flow control can be used to refresh cell culture medium preventing medium acidification and O_2 decrease.[211] Flow control of ToC should include a partial and controlled recirculation of cell medium to balance nutrients refreshing and cell secretions dilution. The automation of ToC models would considerably improve their ease of use and therefore their reproducibility then supporting regulatory and quality standards.[212] We believe a final goal would be to have automated high-throughput ToC with monitoring and feedback loop for a variety of key parameters (such as pH, oxygen and key functional metabolites).

Some pharmaceutical industries have already taken the step towards ToC tests in their pre-clinical studies. A recent review reported[213] collaborations between several MPS manufacturers (Mimetas, TissUse, Emulate) and pharmaceutical industries (Astrazeneca, Galapagos, Janssen, Novo Nordisk, Bayer and Roche) at different steps of drug discovery: target identification and validation, discovery, pharmacokinetics and pharmacodynamics, preclinical safety and clinical developments. These early adopter studies will provide a better understanding of how the technology is deployed. Gaining the confidence of more Research Contract Organizations (CROs) could also help increase ToC use at the target identification and validation steps.[214] In this section, we aim at providing insights on how ToC can bring added values for companies in their anti-cancer drug development process. We focus on three main aspects of this process:[215] (i) "trust in target" which identifies the right biological target and understand its role, (ii) "trust in targeted patient population" that defines the right patient population with any needed stratification strategies and (iii) "trust in therapeutic index" which identifies the right molecule that delivers the right exposure at the target site of action without compromising patient safety.

5.1. Trust in target

The development of a new drug starts with target identification and validation.[207] During this pre-discovery phase, high-throughput screening (HTS) campaigns are initiated to screen 10^3 to 10^6 potential drugs (called "hit") on cell lines. After screening, the "hits" identified are further evaluated through different methods (*e.g.* dose–response curves). Then, during the hit-to-lead stage, "lead" development candidates are synthesized and their efficacy is estimated. An increasing amount of evidence has established that while extremely informative, screens performed with 2D cell culture often do not recapitulate key information such as drug response and sensitivity. As a result, many targets have been likely missed by hit identification experiments. In this context, ToC offers a great advantage because of both increased complexity and versatility, to allow fit-for-purpose implementations for each disease. ToC can be set up with various degrees of complexity selected based on the specific need to be addressed. Moreover, ToC are compatible with a wide range of readouts such as genomics, proteomics and transcriptomics, which could allow the identification of new targets in presence of the TME. The combination of ToC with *in vivo* imaging technology would be tremendously useful for target identification and validation as it would allow to identify molecules capable of eliciting the desired effect with phenotypic live monitoring. Once ToC reaches higher throughput level, it will appear as a new high-content screening (HCS) tool allowing for multiparametric phenotypic outputs that can be used for more comprehensive drug screens.

5.2. Trust in targeted population

Personalized medicine aims to move apart for the "one-size fits all approach", by providing the most suitable medicine, at the right dose, for the right person, at the right time, at a reasonable cost.[216] This definition encompasses two ideas: (a) finding the most effective drug for an individual patient by testing different drugs on his/her tumor sample in the lab, (b) defining subpopulations of patients based on biomarkers to anticipate the efficient drug which should be chosen for an individual patient. Several prognostic and predictive markers have been identified (*e.g.*, somatic or germline mutations) to determine individual profile of each patient and tumor.[217] ToC could be a powerful tool in this field by combining functional testing on patient sample and biomarkers discovery during pre-clinical phases.[218]

Given the heterogeneity of primary tumor tissues, these ToC could be employed to assess the degree of heterogeneity in drug response according to various clinical characteristics, or genetically similar subgroups. The combination of ToC personalized medicine with artificial intelligence paves the way to digital/*in vitro* twins for the development of predictive responders and non-responders models.[219] The combination of patient ToC functional cytotoxicity assays with specific mathematical models could allow to predict the clinical response. For example, using conventional cell culture methods, Silva *et al.* developed a novel tool capable of predicting within 5 days the clinical response of multiple myeloma patients to 31 drugs over months, using fresh bone marrow aspirates.[220] They implemented a parametric model in which the likelihood of cell death depends on drug

concentration and exposure time. Importantly, the algorithm output is not only limited to a dichotomized response/no-response or depth of response, but can also predict the trajectories of clinical response during the first 3 months of treatment. The combination of mathematical algorithms with ToC could provide precise clinical insights on treatment efficacy in a timely manner and assist oncologists in practicing truly personalized management. The current challenge is to provide robust clinical validations of ToC-based predictions by performing rigorous correlations between *ex vivo* ToC responses and *in vivo* patient responses. This requires close collaborations with clinicians and establishment of appropriate patient cohorts.

5.3. Trust in therapeutic index

One of the main translational goals in drug development is the prediction of adverse events. Current toxicity regulations require testing first on a rodent and then on a larger mammal (pig, rabbit, dog, monkey) in order to identify the human dose prediction (HDP). However, very often animals tolerate higher dose than humans. For example, Chou *et al.*[221] used Emulate chips to create an *in vitro* preclinical model of human hematopoiesis that recapitulates many clinically relevant features of bone marrow pathophysiology in response to drugs and ionizing radiation. The bone-marrow-on-a-chip may serve as a human-specific alternative to animal testing for the study of bone-marrow pathophysiology.

A major drawback of conventional *in vitro* cancer models is that drugs are commonly delivered in fixed concentrations. However, this does not accurately simulate the pharmacokinetic (PK) concentration changes experienced *in vivo* due to drug metabolism and clearance mechanisms, and therefore reduces the predictive value of the data.

To solve this problem perfusion in ToC can be employed to simulate the liver's metabolism by changing the concentration over time, *i.e.*, a rise in blood concentration followed by a decrease. Recent work[222] reproduced *in vivo* PK profiles of different anti-cancer drugs over multi-week experiments, both as single-agent therapy or drug combinations. Interestingly, the authors compared the effects on tumor cell efficacy *in vitro* with efficacy seen in *in vivo* xenograft models. They reported that the incorporation of PK into ToC could improve *in vitro–in vivo* translation understanding for early therapeutic insight. Petreus *et al.*[223] designed a pump-driven microfluidic platform capable of mimicking *in vivo* anti-cancer drug pharmacokinetic profiles in ToC. Tumor xenografts were subcutaneously implanted in mice and subjected to the same treatment schedules as the spheroids in the chip and demonstrated that such microfluidic ToC platforms can successfully predict the efficacy. Incorporating flow into ToC could thus assist with the understanding of how different sequencing (continuous, intermittent, gapped schedules) of the drugs affect their efficacy, thereby guiding the design of confirmatory *in vivo* studies.

Physiologically based pharmacokinetic and pharmacodynamic (PK/PD) models could also be proceeded with multi-organ co-culture. Particularly, as liver and kidney play a big role in drug metabolism and clearance, there is a need to connect liver/kidney models to cancer tissue for the study of small molecules. In the case of biologics larger than 45 kDa, there is less interest in such systems because they are cleared from the system mainly by endocytosis.[224] McAleer *et al.*[225] described a multi-organ device with a PK/PD profiling of tamoxifen on MCF-7 breast cancer cells in the presence/absence of liver cells. They also simultaneously monitored the effect of tamoxifen on cardiac function. The efficacy of multi-organ MPS to predict human PK/PD was also demonstrated in other studies: for capecitabine, and its 5-fluorouracil metabolite, in a four-organ system, composed

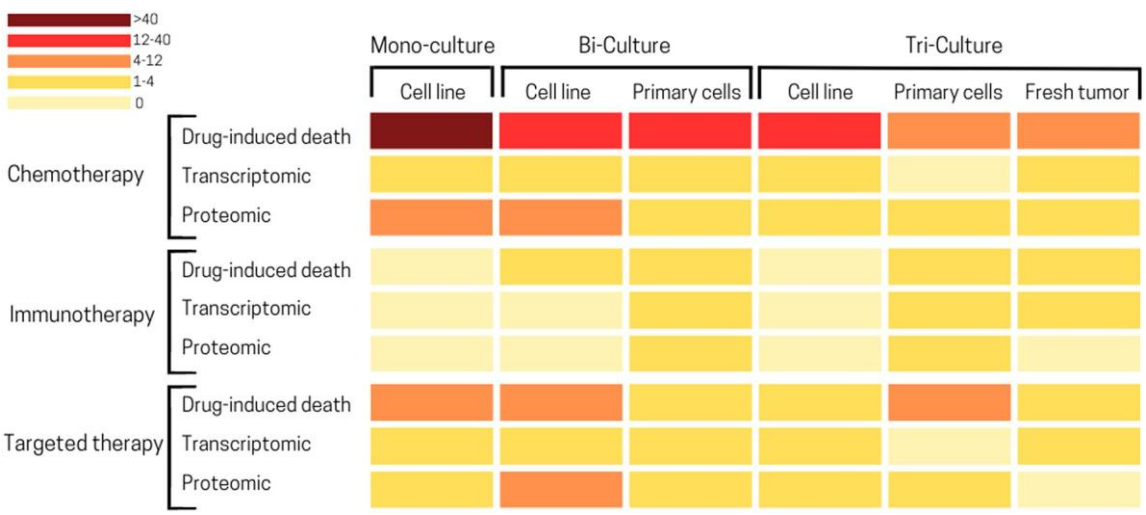


Fig. 8 Heatmap representing the number of publications according to the cellular complexity (mono-culture, bi-culture, tri-culture) with different cell sources (cell line, primary cells or fresh tumor) for different drug treatments (chemotherapy, immunotherapy, targeted therapy) and information extracted (drug-induced death, transcriptomic, proteomic).

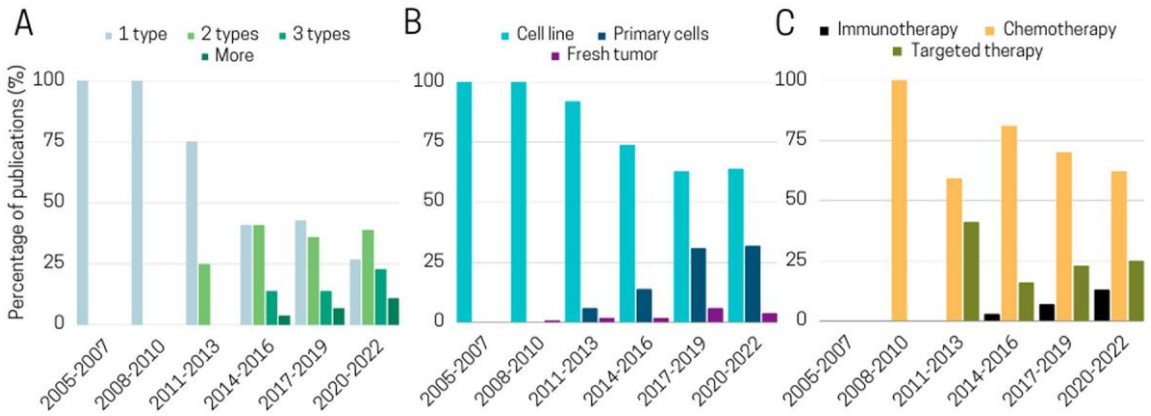


Fig. 9 Evolution of cellular complexity and drug tested over time during the last 15 years of ToC development. Histograms illustrating evolution of A. cell complexity, B. cell source and C. tested therapy in publications.

of intestine, liver, cancer, and connective tissue models;[226] for cisplatin using coupled bone marrow, liver and kidney chips.[227]

6. Conclusion

The past 15 years have witnessed significant advancements in the field of ToC. The microfluidics community in close collaboration with cell biologists and clinicians has actively engaged in this field and achieved impressive milestones. These efforts resulted over the years in an increasing level of complexity on-chip and, consequently, in a better biomimicry of these devices (Fig. 8 and S3†). In this review, our objective was to provide a comprehensive overview of the current state of ToC research and to identify the potential next steps and challenges. To achieve this, we conducted an extensive quantitative analysis of the literature, dissecting the diversity of cell models, drug treatments and extracted information (Fig. 9). Moreover, we highlighted the current promising results of ToC clinical validation.

In this review, we first focused into what sets ToC apart from other *in vitro* models, specifically explaining the various parameters that can be finely controlled in ToC systems. These parameters include the properties of the extracellular matrix, mechanical forces exerted on cells, the physico-chemical environment, cell composition, and the architecture of the tumor microenvironment. ToC ability to precisely and individually manipulate TME parameters enables researchers to dissect the influence of these TME parameters on tumor development, growth, invasion, and response to drugs.

Nevertheless, beyond their interest for basic research, ToC have also the potential to become a transformative technology for clinical and preclinical studies. This potential relies on several factors, notably their compatibility with a wide range of analytical techniques, both conventional and state-of-the-art, such as single-cell-based technologies. Moreover, we believe that the information that can be extracted from ToC remains largely untapped, presenting an avenue for future exploration. Particularly, there is a need to exploit the hidden insights within ToC-generated data, leveraging novel approaches in data analysis. By doing so, as a community, we could be able to unlock a wealth of valuable knowledge and further enhance the capabilities of ToC platforms.

When considering ToC implementation in clinical or preclinical studies, it is also necessary to mention the demonstrated potential and compatibility of ToC devices with a wide range of therapeutic modalities. These modalities encompass chemotherapy, targeted therapy, and more recently, immunotherapy (Fig. 9C). In the field of immunotherapy, ToC hold tremendous importance due to their ability to easily include immune cells, thus, to quite faithfully recapitulate the cell composition of the tumor microenvironment. While promising results have been achieved, significant challenges remain in working with autologous patient cells or incorporating adaptive immunity mechanisms into ToC models.

We also examined the potential of ToC for pharmaceutical industries. At this stage, of course ToC cannot replace all existing *in vitro* and *in vivo* models, and the future landscape will likely involve a combination of animals, organoids, and organ-on-chip platforms. Nevertheless, considering the high failure rate of clinical trials and the increasing emphasis on the 3Rs (replacement, reduction, refinement) principles by regulatory agencies worldwide, we envision that data generated through ToC models could be employed for regulatory purposes within the next decade. While ToC models are generally more costly than conventional cultures, their adoption is expected to occur gradually by identifying applications that will overcome existing barriers in the pharmaceutical industry. A survey conducted among pharmaceutical companies estimated that microphysiological systems could potentially save the industry up to approximately 25% in research and development expenses.[8]

Hence, ToC has the potential to significantly enhance the efficiency and cost-effectiveness of the drug discovery process especially by defining the delicate balance between clinical

dose, efficacy and safety. And the success of ToC for clinical applications will be determined by its ability to detect and validate new therapeutic targets as well as to help the clinicians to define the best therapeutic choices and sequences for patients.

Author contributions

This review was written by a consortium of engineers (CB, AD, SD, CC, CW), biologists (MB, IH, SL, MCP, FMG), clinicians (LC, GZ) and pharmaceutical industries members (DP, DM). Analysis of >300 publications were proceeded by CB and AD. Interviews of pharmaceutical industries and contract research organization were proceeded by CB.

Conflicts of interest

This work was supported by Fluigent and Institut Curie.

Acknowledgements

We would like to acknowledge the financial support from the CNRS, Curie Institute and Fluigent. This work was supported by ANRT, as part of a CIFRE program with the company Fluigent. This work also received the support of "Institut Pierre-Gilles de Gennes" (laboratoire d'excellence, "Investissements d'avenir" program ANR-10-IDEX-0001-02 PSL, ANR-10-EQPX-34 and ANR-10-LABX-31), Fondation ARC pour la Recherche sur le Cancer, PGA12021010002992_3578, INSERM, ITMO N°19CR046-01 and 53712INSERM/ITMO 20-DESCROIX 04/24. We would also like to extend our gratitude to the individuals who were interviewed to contribute to Section 5.

Notes and references

1 P. Webster, A golden era of cancer clinical trials, *Nat. Med.*, 2022, 28, 602–605.
2 C. H. Wong, K. W. Siah and A. W. Lo, Estimation of clinical trial success rates and related parameters, *Biostatistics*, 2019, 20(2), 273–286, DOI: 10.1093/biostatistics/kxx069.
3 M. Hay, D. W. Thomas, J. L. Craighead, C. Economides and J. Rosenthal, Clinical development success rates for investigational drugs, *Nat. Biotechnol.*, 2014, 32, 40–51.
4 D. Sun, W. Gao, H. Hu and S. Zhou, Why 90% of clinical drug development fails and how to improve it?, *Acta Pharm. Sin. B*, 2022, 12(7), 3049–3062, DOI: 10.1016/j.apsb.2022.02.002.
5 J. T. Atkins, G. C. George and K. Hess, *et al.*, Pre-clinical animal models are poor predictors of human toxicities in phase 1 oncology clinical trials, *Br. J. Cancer*, 2020, 123(10), 1496–1501, DOI: 10.1038/s41416-020-01033-x.
6 E. Pan, D. Bogumil, V. Cortessis, S. Yu and J. Nieva, A systematic review of the efficacy of preclinical models of lung cancer drugs, *Front. Oncol.*, 2020, 10, 591, DOI: 10.3389/fonc.2020.00591.
7 J. Komen, S. M. van Neerven, A. van den Berg, L. Vermeulen and A. D. van der Meer, Mimicking and surpassing the xenograft model with cancer-on-chip technology, *EBioMedicine*, 2021, 66, 103303, DOI: 10.1016/j.ebiom.2021.103303.
8 D. E. Ingber, Human organs-on-chips for disease modelling, drug development and personalized medicine, *Nat. Rev. Genet.*, 2022, 23, 467–491, DOI: 10.1038/s41576-022-00466-9.
9 S. Sant and P. A. Johnston, The production of 3D tumor spheroids for cancer drug discovery, *Drug Discovery Today: Technol.*, 2017, 23, 27–36, DOI: 10.1016/j.ddtec.2017.03.002.
10 S. Gunti, A. T. K. Hoke, K. P. Vu and N. R. London, Organoid and spheroid tumor models: Techniques and applications, *Cancers*, 2021, 13(4), 1–18, DOI: 10.3390/cancers13040874.
11 H. Clevers, Modeling Development and Disease with Organoids, *Cell*, 2016, 165(7), 1586–1597, DOI: 10.1016/j.cell.2016.05.082.
12 M. Verduin, A. Hoeben, D. De Ruysscher and M. Vooijs, Patient-Derived Cancer Organoids as Predictors of Treatment Response, *Front. Oncol.*, 2021, 11, 641980, DOI: 10.3389/fonc.2021.641980.
13 H. T. Nia, *et al.*, Physical traits of cancer, *Science*, 2020, 370(6516), eaaz0868, DOI: 10.1126/science.aaz0868.
14 F. R. Balkwill, M. Capasso and T. Hagemann, The tumor microenvironment at a glance, *J. Cell Sci.*, 2012, 125(23), 5591–5596, DOI: 10.1242/jcs.116392.
15 S. A. Langhans, Three-dimensional in vitro cell culture models in drug discovery and drug repositioning, *Front. Pharmacol.*, 2018, 9, 6, DOI: 10.3389/fphar.2018.00006.
16 B. N. Brown, C. A. Barnes, R. T. Kasick, R. Michel, T. W. Gilbert, D. Beer-Stolz, D. G. Castner, B. D. Ratner and S. F. Badylak, Surface Characterization of Extracellular Matrix Scaffolds, *Biomaterials*, 2010, 31(3), 428–437.
17 T. Davidov, Y. Efraim, R. Hayam, J. Oieni, L. Baruch and M. Machluf, Extracellular matrix hydrogels originated from different organs mediate tissue-specific properties and function, *Int. J. Mol. Sci.*, 2021, 22(21), 11624, DOI: 10.3390/ijms222111624.
18 K. S. Kopanska, Y. Alcheikh, R. Staneva, D. Vignjevic and T. Betz, Tensile forces originating from cancer spheroids facilitate tumor invasion, *PLoS One*, 2016, 11(6), 1–23, DOI: 10.1371/journal.pone.0156442.
19 Z. L. Li, Z. J. Wang, G. H. Wei, Y. Yang and X. W. Wang, Changes in extracellular matrix in different stages of colorectal cancer and their effects on proliferation of cancer cells, *World J. Gastrointest. Oncol.*, 2020, 12(3), 267–275, DOI: 10.4251/WJGO.V12.I3.267.
20 C. Bonnans, J. Chou and Z. Werb, Remodelling the extracellular matrix in development and disease, *Nat. Rev. Mol. Cell Biol.*, 2014, 15, 786–801.
21 A. W. Holle, J. L. Young and J. P. Spatz, In vitro cancer cell-ECM interactions inform in vivo cancer treatment, *Adv. Drug Delivery Rev.*, 2016, 97, 270–279, DOI: 10.1016/j.addr.2015.10.007.

22 M. R. Carvalho, D. Lima, R. L. Reis, V. M. Correlo and J. M. Oliveira, Evaluating Biomaterial- and Microfluidic-Based 3D Tumor Models, *Trends Biotechnol.*, 2015, 33(11), 667–678, DOI: 10.1016/j.tibtech.2015.09.009.

23 R. Navneeta, J. Habermehl, M. F. Coté, C. J. Doillon and D. Mantovani, Preparation of ready-to-use, storable and reconstituted type I collagen from rat tail tendon for tissue engineering applications, *Nat. Protoc.*, 2006, 1, 2753–2758.

24 E. A. Aisenbrey and W. L. Murphy, Synthetic alternatives to Matrigel, *Nat. Rev. Mater.*, 2020, 5(7), 539–551, DOI: 10.1038/s41578-020-0199-8.

25 K. J. Price, A. Tsykin and K. M. Giles, *et al.*, Matrigel Basement Membrane Matrix influences expression of microRNAs in cancer cell lines, *Biochem. Biophys. Res. Commun.*, 2012, 427(2), 343–348, DOI: 10.1016/j.bbrc.2012.09.059.

26 M. Romero-López, A. L. Trinh and A. Sobrino, *et al.*, Recapitulating the human tumor microenvironment: Colon tumor-derived extracellular matrix promotes angiogenesis and tumor cell growth, *Biomaterials*, 2017, 116, 118–129, DOI: 10.1016/j.biomaterials.2016.11.034.

27 X. Cui, C. Ma and V. Vasudevaraja, *et al.*, Dissecting the immunosuppressive tumor microenvironments in glioblastoma-on-a-chip for optimized Pd-1 immunotherapy, *eLife*, 2020, 9, 1–21, DOI: 10.7554/ELIFE.52253.

28 B. Yue, Biology of the extracellular matrix: An overview, *J. Glaucoma*, 2014, 23(8), S20–S23, DOI: 10.1097/IJG.0000000000000108.

29 N. Peela, F. S. Sam and W. Christenson, *et al.*, A three dimensional micropatterned tumor model for breast cancer cell migration studies, *Biomaterials*, 2016, 81, 72–83, DOI: 10.1016/j.biomaterials.2015.11.039.

30 F. Gong, Y. Yang, L. Wen, C. Wang, J. Li and J. Dai, An Overview of the Role of Mechanical Stretching in the Progression of Lung Cancer, *Front. Cell Dev. Biol.*, 2021, 9, 781828, DOI: 10.3389/fcell.2021.781828.

31 P. Purkayastha, M. K. Jaiswal and T. P. Lele, Molecular cancer cell responses to solid compressive stress and interstitial fluid pressure, *Cytoskeleton*, 2021, 78(6), 312–322, DOI: 10.1002/cm.21680.

32 M. Delarue, F. Montel, D. Vignjevic, J. Prost, J. F. Joanny and G. Cappello, Compressive stress inhibits proliferation in tumor spheroids through a volume limitation, *Biophys. J.*, 2014, 107(8), 1821–1828, DOI: 10.1016/j.bpj.2014.08.031.

33 I. F. Rizzuti, P. Mascheroni, S. Arcucci, Z. Ben-Mériem, A. Prunet, C. Barentin, C. Rivière, H. Delanoë-Ayari, H. Hatzikirou, J. Guillermet-Guibert and M. Delarue, Mechanical control of cell proliferation increases resistance to chemotherapeutic agents, *Phys. Rev. Lett.*, 2020, 125(12), 128103, DOI: 10.1103/PhysRevLett.125.128103.

34 S. Onal, M. M. Alkaisi and V. Nock, A Flexible Microdevice for Mechanical Cell Stimulation and Compression in Microfluidic Settings, *Front. Phys.*, 2021, 9, DOI: 10.3389/fphy.2021.654918.

35 G. Calibasi Kocal, S. Güven, K. Foygel, A. Goldman, P. Chen, S. Sengupta, R. Paulmurugan, Y. Baskin and U. Demirci, Dynamic Microenvironment Induces Phenotypic Plasticity of Esophageal Cancer Cells under Flow, *Sci. Rep.*, 2016, 6, 38221, DOI: 10.1038/srep38221.

36 A. D. Wong and P. C. Searson, Live-cell imaging of invasion and intravasation in an artificial microvessel platform, *Cancer Res.*, 2014, 74(17), 4937–4945, DOI: 10.1158/0008-5472.CAN-14-1042.

37 L. Zheng, B. Wang and Y. Sun, *et al.*, An Oxygen-Concentration-Controllable Multiorgan Microfluidic Platform for Studying Hypoxia-Induced Lung Cancer-Liver Metastasis and Screening Drugs, *ACS Sens.*, 2021, 6(3), 823–832, DOI: 10.1021/acssensors.0c01846.

38 Z. Wan, M. A. Floryan, M. F. Coughlin, S. Zhang, A. X. Zhong, S. E. Shelton, X. Wang, C. Xu, D. A. Barbie and R. D. Kamm, New Strategy for Promoting Vascularization in Tumor Spheroids in a Microfluidic Assay, *Adv. Healthcare Mater.*, 2023, 12(14), e2201784, DOI: 10.1002/adhm.202201784.

39 X. Y. Wang, Y. Pei and M. Xie, *et al.*, An artificial blood vessel implanted three-dimensional microsystem for modeling transvascular migration of tumor cells, *Lab Chip*, 2015, 15(4), 1178–1187, DOI: 10.1039/c4lc00973h.

40 S. Lu, F. Cuzzucoli and J. Jiang, *et al.*, Development of a biomimetic liver tumor-on-a-chip model based on decellularized liver matrix for toxicity testing, *Lab Chip*, 2018, 18(22), 3379–3392, DOI: 10.1039/C8LC00852C.

41 R. Huang, W. Zheng, W. Liu, W. Zhang, Y. Long and X. Jiang, Investigation of Tumor Cell Behaviors on a Vascular Microenvironment-Mimicking Microfluidic Chip, *Sci. Rep.*, 2015, 5, 17768, DOI: 10.1038/srep17768.

42 R. Fan, T. Emery, Y. Zhang, Y. Xia, J. Sun and J. Wan, Circulatory shear flow alters the viability and proliferation of circulating colon cancer cells, *Sci. Rep.*, 2016, 6, 27073, DOI: 10.1038/srep27073.

43 J. Aleman and A. Skardal, A multi-site metastasis-on-a-chip microphysiological system for assessing metastatic preference of cancer cells, *Biotechnol. Bioeng.*, 2019, 116(4), 936–944, DOI: 10.1002/bit.26871.

44 S. Hao, L. Ha, G. Cheng, Y. Wan, Y. Xia, D. M. Sosnoski, A. M. Mastro and S. Y. Zheng, A Spontaneous 3D Bone-On-a-Chip for Bone Metastasis Study of Breast Cancer Cells, *Small*, 2018, 14(12), e1702787, DOI: 10.1002/smll.201702787.

45 B. Kramer, L. Haan, M. Vermeer, T. Olivier, T. Hankemeier, P. Vulto, J. Joore and H. L. Lanz, Interstitial flow recapitulates gemcitabine chemoresistance in a 3D microfluidic pancreatic ductal adenocarcinoma model by induction of multidrug resistance proteins, *Int. J. Mol. Sci.*, 2019, 20(18), 4647, DOI: 10.3390/ijms20184647.

46 C. K. Ip, S. S. Li, M. Y. Tang, S. K. Sy, Y. Ren, H. C. Shum and A. S. Wong, Stemness and chemoresistance in epithelial ovarian carcinoma cells under shear stress, *Sci. Rep.*, 2016, 6, 26788, DOI: 10.1038/srep26788.

47 S. Parvathy Pillai Babu, S. Venkatabalasubramanian, S. R. Munisankar and A. Thiyagaraj, Cancer stem cell markers interplay with chemoresistance in triple negative breast cancer: A therapeutic perspective, *Bull. Cancer*, 2022, 109(9), 960–971.

48 K. Matsuda, N. Ohga and Y. Hida, *et al.*, Isolated tumor endothelial cells maintain specific character during long-term culture, *Biochem. Biophys. Res. Commun.*, 2010, 394(4), 947–954, DOI: 10.1016/j.bbrc.2010.03.089.

49 D. Kim, K. S. Hwang, E. U. Seo, S. Seo, B. C. Lee, N. Choi, J. Choi and H. N. Kim, Vascularized Lung Cancer Model for Evaluating the Promoted Transport of Anticancer Drugs and Immune Cells in an Engineered Tumor Microenvironment, *Adv. Healthcare Mater.*, 2022, 11(12), e2102581, DOI: 10.1002/adhm.202102581.

50 G. Fang, H. Lu, R. Al-Nakashli, R. Chapman, Y. Zhang, L. A. Ju, G. Lin, M. H. Stenzel and D. Jin, Enabling peristalsis of human colon tumor organoids on microfluidic chips, *Biofabrication*, 2021, 14(1), DOI: 10.1088/1758-5090/ac2ef9.

51 C. Strelez, S. Chilakala and K. Ghaffarian, *et al.*, Human colorectal cancer-on-chip model to study the microenvironmental influence on early metastatic spread, *iScience*, 2021, 24(5), 102509, DOI: 10.1016/j.isci.2021.102509.

52 M. Ao, B. M. Brewer and L. Yang, *et al.*, Stretching fibroblasts remodels fibronectin and alters cancer cell migration, *Sci. Rep.*, 2015, 5, 8334, DOI: 10.1038/srep08334.

53 S. R. McKeown, Defining normoxia, physoxia and hypoxia in tumours - Implications for treatment response, *Br. J. Radiol.*, 2018, 87(1035), 1–12, DOI: 10.1259/bjr.20130676.

54 V. Petrova, M. Annicchiarico-Petruzzelli, G. Melino and I. Amelio, The hypoxic tumour microenvironment, *Oncogenesis*, 2018, 7, 1, DOI: 10.1038/s41389-017-0011-9.

55 M. D. Brennan, M. L. Rexius-Hall, L. J. Elgass and D. T. Eddington, Oxygen control with microfluidics, *Lab Chip*, 2014, 14(22), 4305–4318, DOI: 10.1039/c4lc00853g.

56 M. B. Byrne, M. T. Leslie, H. R. Gaskins and P. J. A. Kenis, Methods to study the tumor microenvironment under controlled oxygen conditions, *Trends Biotechnol.*, 2014, 32(11), 556–563, DOI: 10.1016/j.tibtech.2014.09.006.

57 P. E. Oomen, M. D. Skolimowski and E. Verpoorte, Implementing oxygen control in chip-based cell and tissue culture systems, *Lab Chip*, 2016, 16(18), 3394–3414, DOI: 10.1039/c6lc00772d.

58 R. Koens, Y. Tabata and J. C. Serrano, *et al.*, Microfluidic platform for three-dimensional cell culture under spatiotemporal heterogeneity of oxygen tension, *APL Bioeng.*, 2020, 4(1), 016106, DOI: 10.1063/1.5127069.

59 C. W. Chang, Y. J. Cheng and M. Tu, *et al.*, A polydimethylsiloxane-polycarbonate hybrid microfluidic device capable of generating perpendicular chemical and oxygen gradients for cell culture studies, *Lab Chip*, 2014, 14(19), 3762–3772, DOI: 10.1039/c4lc00732h.

60 V. Palacio-Castañeda, L. Kooijman, B. Venzac, W. P. R. Verdurmen and S Le Gac, Metabolic Switching of Tumor Cells under Hypoxic Conditions in a Tumor-on-a-chip Model, *Micromachines*, 2020, 11(4), 382, DOI: 10.3390/mi11040382.

61 J. M. Ayuso, M. Virumbrales-Muñoz and A. Lacueva, *et al.*, Development and characterization of a microfluidic model of the tumour microenvironment, *Sci. Rep.*, 2016, 6(June), 1–16, DOI: 10.1038/srep36086.

62 C. Bouquerel, W. César and L. Barthod, *et al.*, Precise and fast control of the dissolved oxygen level for tumor-on-chip, *Lab Chip*, 2022, 22(22), 4443–4455, DOI: 10.1039/d2lc00696k.

63 J. M. Ayuso, M. Virumbrales-Munoz and P. H. McMinn, *et al.*, Tumor-on-a-chip: A microfluidic model to study cell response to environmental gradients, *Lab Chip*, 2019, 19(20), 3461–3471, DOI: 10.1039/c9lc00270g.

64 N. M. Anderson and M. C. Simon, The tumor microenvironment, *Curr. Biol.*, 2020, 30(16), R921–R925, DOI: 10.1016/j.cub.2020.06.081.

65 M. B. Schaaf, A. D. Garg and P. Agostinis, Defining the role of the tumor vasculature in antitumor immunity and immunotherapy article, *Cell Death Dis.*, 2018, 9(2), 115, DOI: 10.1038/s41419-017-0061-0.

66 A. Costa, Y. Kieffer and A. Scholer-Dahirel, *et al.*, Fibroblast Heterogeneity and Immunosuppressive Environment in Human Breast Cancer, *Cancer Cell*, 2018, 33(3), 463–479. e10, DOI: 10.1016/j.ccell.2018.01.011.

67 F. Pelon, B. Bourachot, Y. Kieffer, I. Magagna, F. Mermet-Meillon, I. Bonnet, A. Costa, A. M. Givel, Y. Attieh, J. Barbazan, C. Bonneau, L. Fuhrmann, S. Descroix, D. Vignjevic, P. Silberzan, M. C. Parrini, A. Vincent-Salomon and F. Mechta-Grigoriou, Cancer-associated fibroblast heterogeneity in axillary lymph nodes drives metastases in breast cancer through complementary mechanisms, *Nat. Commun.*, 2020, 11(1), 404, DOI: 10.1038/s41467-019-14134-w.

68 D. A. Close, A. X. Wang, S. J. Kochanek, T. Shun, J. L. Eiseman and P. A. Johnston, Implementation of the NCI-60 Human Tumor Cell Line Panel to Screen 2260 Cancer Drug Combinations to Generate >3 Million Data Points Used to Populate a Large Matrix of Anti-Neoplastic Agent Combinations (ALMANAC) Database, *SLAS Discovery*, 2019, 24(3), 242–263, DOI: 10.1177/2472555218812429.

69 M. Richter, O. Piwocka, M. Musielak, I. Piotrowski, W. M. Suchorska and T. Trzeciak, From Donor to the Lab: A Fascinating Journey of Primary Cell Lines, *Front. Cell Dev. Biol.*, 2021, 9, 711381, DOI: 10.3389/fcell.2021.711381.

70 A. Boussommier-Calleja, Y. Atiyas, K. Haase, M. Headley, C. Lewis and R. D. Kamm, The effects of monocytes on tumor cell extravasation in a 3D vascularized microfluidic model, *Biomaterials*, 2019, 198, 180–193, DOI: 10.1016/j.biomaterials.2018.03.005.

71 B. A. Hassell, G. Goyal and E. Lee, *et al.*, Human Organ Chip Models Recapitulate Orthotopic Lung Cancer Growth, Therapeutic Responses, and Tumor Dormancy In Vitro, *Cell Rep.*, 2017, 21(2), 508–516, DOI: 10.1016/j.celrep.2017.09.043.

72 M. Gerigk, H. Bulstrode and H. T. H. Shi, *et al.*, On-chip perivascular niche supporting stemness of patient-derived glioma cells in a serum-free, flowable culture, *Lab Chip*, 2021, 21(12), 2343–2358, DOI: 10.1039/d1lc00271f.

73 M. Humayun, J. M. Ayuso, R. A. Brenneke, M. Virumbrales-Muñoz, K. Lugo-Cintrón, S. Kerr, S. M. Ponik and D. J. Beebe, Elucidating cancer-vascular paracrine signaling

using a human organotypic breast cancer cell extravasation model, *Biomaterials*, 2021, 270, 120640, DOI: 10.1016/j.biomaterials.2020.120640.

74 J. Lee, S. Mehrotra, E. Zare-Eelanjegh, R. O. Rodrigues, A. Akbarinejad, D. Ge, L. Amato, K. Kiaee, Y. Fang, A. Rosenkranz, W. Keung, B. B. Mandal, R. A. Li, T. Zhang, H. Lee, M. R. Dokmeci, Y. S. Zhang, A. Khademhosseini and S. R. Shin, A Heart-Breast Cancer-on-a-Chip Platform for Disease Modeling and Monitoring of Cardiotoxicity Induced by Cancer Chemotherapy, *Small*, 2021, 17(15), e2004258, DOI: 10.1002/smll.202004258.

75 P. W. Burridge, Y. F. Li and E. Matsa, *et al.*, Human induced pluripotent stem cell-derived cardiomyocytes recapitulate the predilection of breast cancer patients to doxorubicin-induced cardiotoxicity, *Nat. Med.*, 2016, 22(5), 547–556, DOI: 10.1038/nm.4087.

76 N. Frenkel, S. Poghosyan and C. Rubio Alarcón, *et al.*, Long-Lived Human Lymphatic Endothelial Cells to Study Lymphatic Biology and Lymphatic Vessel/Tumor Coculture in a 3D Microfluidic Model, *ACS Biomater. Sci. Eng.*, 2021, 7(7), 3030–3042.

77 D. J. Jung, T. H. Shin, M. Kim, C. O. Sung, S. J. Jang and G. S. Jeong, A one-stop microfluidic-based lung cancer organoid culture platform for testing drug sensitivity, *Lab Chip*, 2019, 19(17), 2854–2865, DOI: 10.1039/c9lc00496c.

78 B. Schuster, M. Junkin, S. S. Kashaf, I. Romero-Calvo, K. Kirby, J. Matthews, C. R. Weber, A. Rzhetsky, K. P. White and S. Tay, Automated microfluidic platform for dynamic and combinatorial drug screening of tumor organoids, *Nat. Commun.*, 2020, 11(1), 5271, DOI: 10.1038/s41467-020-19058-4.

79 M. R. Haque, C. R. Wessel, D. D. Leary, C. Wang, A. Bhushan and F. Bishehsari, Patient-derived pancreatic cancer-on-a-chip recapitulates the tumor microenvironment, *Microsyst. Nanoeng.*, 2022, 8(1), 36, DOI: 10.1038/s41378-022-00370-6.

80 L. J. Y. Ong, S. Chia and S. Q. R. Wong, *et al.*, A comparative study of tumour-on-chip models with patient-derived xenografts for predicting chemotherapy efficacy in colorectal cancer patients, *Front. Bioeng. Biotechnol.*, 2022, 10(August), 1–14, DOI: 10.3389/fbioe.2022.952726.

81 M. Astolfi, B. Péant and M. A. Lateef, *et al.*, Micro-dissected tumor tissues on chip: An ex vivo method for drug testing and personalized therapy, *Lab Chip*, 2016, 16(2), 312–325, DOI: 10.1039/c5lc01108f.

82 D. Dorrigiv, K. Simeone, L. Communal, J. Kendall-Dupont, A. St-Georges-Robillard, B. Péant, E. Carmona, A. M. Mes-Masson and T. Gervais, Microdissected tissue vs tissue slices—a comparative study of tumor explant models cultured on-chip and off-chip, *Cancers*, 2021, 13(16), 4208, DOI: 10.3390/cancers13164208.

83 A. R. Aref and M. Campisi, 3D Microfluidic Ex Vivo Culture of Organotypic Tumor Spheroids to Model Immune Checkpoint Blockade, *Physiol. Behav.*, 2018, 18(20), 3129–3143, DOI: 10.1016/j.physbeh.2017.03.040.

84 L. F. Horowitz, A. D. Rodriguez, Z. Dereli-Korkut, R. Lin, K. Castro, A. M. Mikheev, R. J. Monnat Jr, A. Folch and R. C. Rostomily, Multiplexed drug testing of tumor slices using a microfluidic platform, *npj Precis. Oncol.*, 2020, 4, 12, DOI: 10.1038/s41698-020-0117-y.

85 E. Ivanova, M. Kuraguchi and M. Xu, *et al.*, Use of Ex Vivo Patient-Derived Tumor Organotypic Spheroids to Identify Combination Therapies for HER2 Mutant Non–Small Cell Lung Cancer, *Clin. Cancer Res.*, 2020, 26(10), 2393–2403, DOI: 10.1158/1078-0432.CCR-19-1844.

86 S. Chakrabarty, W. F. Quiros-Solano and M. M. P. Kuijten, *et al.*, A Microfluidic Cancer-on-Chip Platform Predicts Drug Response Using Organotypic Tumor Slice Culture, *Cancer Res.*, 2022, 82(3), 510–520, DOI: 10.1158/0008-5472.CAN-21-0799.

87 L. K. Sablatura, K. M. Bircsak, P. Shepherd, M. Bathina, K. Queiroz, M. C. Farach-Carson, R. A. Kittles, P. E. Constantinou, A. Saleh, N. M. Navone and D. A. Harrington, A 3D Perfusable Platform for In Vitro Culture of Patient Derived Xenografts, *Adv. Healthcare Mater.*, 2023, 12(14), e2201434, DOI: 10.1002/adhm.202201434.

88 T. C. Chang, A. M. Mikheev, W. Huynh, R. J. Monnat, R. C. Rostomily and A. Folch, Parallel Microfluidic Chemosensitivity Testing on Individual Slice Cultures, *Lab Chip*, 2014, 14(23), 4540–4551, DOI: 10.1039/b000000x/NIH.

89 Z. Ao, H. Cai and Z. Wu, *et al.*, Evaluation of cancer immunotherapy using mini-tumor chips, *Theranostics*, 2022, 12(8), 3628–3636, DOI: 10.7150/thno.71761.

90 S. M. Hattersley, D. C. Sylvester, C. E. Dyer, N. D. Stafford, S. J. Haswell and J. Greenman, A microfluidic system for testing the responses of head and neck squamous cell carcinoma tissue biopsies to treatment with chemotherapy drugs, *Ann. Biomed. Eng.*, 2012, 40(6), 1277–1288, DOI: 10.1007/s10439-011-0428-9.

91 F. Eduati, R. Utharala and D. Madhavan, *et al.*, A microfluidics platform for combinatorial drug screening on cancer biopsies, *Nat. Commun.*, 2018, 9, 2434, DOI: 10.1038/s41467-018-04919-w.

92 Z. P. Khin, M. L. C. Ribeiro and T. Jacobson, *et al.*, A preclinical assay for chemosensitivity in multiple myeloma, *Cancer Res.*, 2014, 74(1), 56–67, DOI: 10.1158/0008-5472.CAN-13-2397.

93 J. Sun, M. D. Masterman-Smith and N. A. Graham, *et al.*, A microfluidic platform for systems pathology: Multiparameter single-cell signaling measurements of clinical brain tumor specimens, *Cancer Res.*, 2010, 70(15), 6128–6138, DOI: 10.1158/0008-5472.CAN-10-0076.

94 M. Virumbrales-Muñoza, J. Chen, J. Ayuso, M. Lee, J. Abel and D. J. Beebe, Organotypic primary blood vessel models of clear cell renal cell carcinoma for single-patient clinical trials, *Lab Chip*, 2020, 20(23), 4420–4432.

95 M. Parsian, P. Mutlu, E. Yildirim, C. Ildiz, C. Ozen and U. Gunduz, Development of a microfluidic platform to maintain viability of micro-dissected tumor slices in culture, *Biomicrofluidics*, 2022, 16(3), 034103, DOI: 10.1063/5.0087532.

Open Access Article. Published on 18 August 2023. Downloaded on 9/30/2025 10:17:48 AM.
This article is licensed under a Creative Commons Attribution 3.0 Unported Licence.

96 F. D. Schwab, M. C. Scheidmann and L. L. Ozimski, *et al.*, MyCTC chip: microfluidic-based drug screen with patient-derived tumour cells from liquid biopsies, *Microsyst. Nanoeng.*, 2022, 8, 130, DOI: 10.1038/s41378-022-00467-y.

97 B. L. Khoo, G. Grenci, B. Y. Lim, S. C. Lee, J. Han and C. T. Lim, Expansion of patient-derived circulating tumor cells from liquid biopsies using a CTC microfluidic culture device, *Nat. Protoc.*, 2018, 13, 34–58.

98 Z. Zhang, H. Shiratsuchi, J. Lin, G. Chen, R. M. Reddy, E. Azizi, S. Fouladdel, A. C. Chang, L. Lin, H. Jiang, M. Waghray, G. Luker, D. M. Simeone, M. S. Wicha, D. G. Beer, N. Ramnath and S. Nagrath, Expansion of CTCs from early stage lung cancer patients using a microfluidic co-culture model, *Oncotarget*, 2014, 5(23), 12383–12397, DOI: 10.18632/oncotarget.2592.

99 G. Trujillo-de Santiago, B. G. Flores-Garza, J. A. Tavares-Negrete, I. M. Lara-Mayorga, I. González-Gamboa, Y. S. Zhang, A. Rojas-Martínez, R. Ortiz-López and M. M. Álvarez, The Tumor-on-Chip: Recent Advances in the Development of Microfluidic Systems to Recapitulate the Physiology of Solid Tumors, *Materials*, 2019, 12(18), 2945, DOI: 10.3390/ma12182945.

100 J. J. F. Sleeboom, H. Eslami Amirabadi, P. Nair, C. M. Sahlgren and J. M. J. den Toonder, Metastasis in context: Modeling the tumor microenvironment with cancer-on-a-chip approaches, *Dis. Models Mech.*, 2018, 11(3), dmm033100, DOI: 10.1242/dmm.033100.

101 S. Lee, J. Lim, J. Yu, J. Ahn, Y. Lee and N. L. Jeon, Engineering tumor vasculature on an injection-molded plastic array 3D culture (IMPACT) platform, *Lab Chip*, 2019, 19(12), 2071–2080, DOI: 10.1039/c9lc00148d.

102 S. Bersini, J. S. Jeon and G. Dubini, *et al.*, A microfluidic 3D invitro model for specificity of breast cancer metastasis to bone, *Biomaterials*, 2014, 35(8), 2454–2461, DOI: 10.1016/j.biomaterials.2013.11.050.

103 J. Bai, T. Y. Tu, C. Kim, J. P. Thiery and R. D. Kamm, Identification of drugs as single agents or in combination to prevent carcinoma dissemination in a microfluidic 3D environment, *Oncotarget*, 2015, 6(34), 36603–36614, DOI: 10.18632/oncotarget.5464.

104 Y. Bi, V. S. Shirure and R. Liu, *et al.*, Tumor-on-a-chip platform to interrogate the role of macrophages in tumor progression, *Integr. Biol.*, 2020, 12(9), 221–232, DOI: 10.1093/intbio/zyaa017.

105 S. Azadi, M. Tafazzoli Shadpour and M. E. Warkiani, Characterizing the effect of substrate stiffness on the extravasation potential of breast cancer cells using a 3D microfluidic model, *Biotechnol. Bioeng.*, 2021, 118(2), 823–835, DOI: 10.1002/bit.27612.

106 C. R. Drifka, K. W. Eliceiri, S. M. Weber and W. J. Kao, A bioengineered heterotypic stroma-cancer microenvironment model to study pancreatic ductal adenocarcinoma, *Lab Chip*, 2013, 13(19), 3965–3975, DOI: 10.1039/c3lc50487e.

107 W. Han, S. Chen and W. Yuan, *et al.*, Oriented collagen fibers direct tumor cell intravasation, *Proc. Natl. Acad. Sci. U. S. A.*, 2016, 113(40), 11208–11213, DOI: 10.1073/pnas.1610347113.

108 M. Campisi, Y. Shin, T. Osaki, C. Hajal, V. Chiono and R. D. Kamm, 3D self-organized microvascular model of the human blood-brain barrier with endothelial cells, pericytes and astrocytes, *Biomaterials*, 2018, 180, 117–129, DOI: 10.1016/j.biomaterials.2018.07.014.

109 E. A. Adjei-Sowah, S. A. O'Connor, J. Veldhuizen, C. Lo Cascio, C. Plaisier, S. Mehta and M. Nikkhah, Investigating the Interactions of Glioma Stem Cells in the Perivascular Niche at Single-Cell Resolution using a Microfluidic Tumor Microenvironment Model, *Adv. Sci.*, 2022, 9(21), e2201436, DOI: 10.1002/advs.202201436.

110 S. Y. Jeong, J. H. Lee, Y. Shin, S. Chung and H. J. Kuh, Co-Culture of Tumor Spheroids and Fibroblasts in a Collagen Matrix-Incorporated Microfluidic Chip Mimics Reciprocal Activation in Solid Tumor Microenvironment, *PLoS One*, 2016, 11(7), e0159013, DOI: 10.1371/journal.pone.0159013.

111 B. Venzac, Y. Liu, I. Ferrante, P. Vargas, A. Yamada, R. Courson, M. Verhulsel, L. Malaquin, J. L. Viovy and S. Descroix, Sliding walls: a new paradigm for fluidic actuation and protocol implementation in microfluidics, *Microsyst. Nanoeng.*, 2020, 6, 18, DOI: 10.1038/s41378-019-0125-7.

112 X. Jiang, L. Ren, P. Tebon, C. Wang, X. Zhou, M. Qu, J. Zhu, H. Ling, S. Zhang, Y. Xue, Q. Wu, P. Bandaru, J. Lee, H. J. Kim, S. Ahadian, N. Ashammakhi, M. R. Dokmeci, J. Wu, Z. Gu, W. Sun and A. Khademhosseini, Cancer-on-a-Chip for Modeling Immune Checkpoint Inhibitor and Tumor Interactions, *Small*, 2021, 17(7), e2004282, DOI: 10.1002/smll.202004282.

113 D. An, K. Kim and J. Kim, Microfluidic system based high throughput drug screening system for curcumin/TRAIL combinational chemotherapy in human prostate cancer PC3 cells, *Biomol. Ther.*, 2014, 22(4), 355–362, DOI: 10.4062/biomolther.2014.078.

114 N. Azizipour, R. Avazpour, M. H. Weber, M. Sawan, A. Ajji and D. H. Rosenzweig, Uniform Tumor Spheroids on Surface-Optimized Microfluidic Biochips for Reproducible Drug Screening and Personalized Medicine, *Micromachines*, 2022, 13(4), 587, DOI: 10.3390/mi13040587.

115 E. Prince, S. Kheiri, Y. Wang, F. Xu, J. Cruickshank, V. Topolskaia, H. Tao, E. W. K. Young, A. P. McGuigan, D. W. Cescon and E. Kumacheva, Microfluidic Arrays of Breast Tumor Spheroids for Drug Screening and Personalized Cancer Therapies, *Adv. Healthcare Mater.*, 2022, 11(1), e2101085, DOI: 10.1002/adhm.202101085.

116 C. W. Chi, Y. H. Lao, A. H. R. Ahmed, E. C. Benoy, C. Li, Z. Dereli-Korkut, B. M. Fu, K. W. Leong and S. Wang, High-Throughput Tumor-on-a-Chip Platform to Study Tumor–Stroma Interactions and Drug Pharmacokinetics, *Adv. Healthcare Mater.*, 2020, 9(21), e2000880, DOI: 10.1002/adhm.202000880.

117 K. I. Kamei, Y. Kato and Y. Hirai, *et al.*, Integrated heart/cancer on a chip to reproduce the side effects of anti-cancer drugs: In vitro, *RSC Adv.*, 2017, 7(58), 36777–36786, DOI: 10.1039/c7ra07716e.

118 E. Agliari, E. Biselli, A. De Ninno, G. Schiavoni, L. Gabriele, A. Gerardino, F. Mattei, A. Barra and L. Businaro, Cancer-driven dynamics of immune cells in a microfluidic environment, *Sci. Rep.*, 2014, 4, 6639, DOI: 10.1038/srep06639.

119 D. Gioeli, C. J. Snow and M. B. Simmers, *et al.*, Development of a multicellular pancreatic tumor microenvironment system using patient-derived tumor cells, *Lab Chip*, 2019, 19(7), 1193–1204, DOI: 10.1039/c8lc00755a.

120 Y. Choi, E. Hyun and J. Seo, *et al.*, A microengineered pathophysiological model of early-stage breast cancer, *Lab Chip*, 2015, 15(16), 3350–3357, DOI: 10.1039/c5lc00514k.

121 D. Huh, B. D. Matthews, A. Mammoto, M. Montoya-Zavala, H. Yuan Hsin and D. E. Ingber, Reconstituting organ-level lung functions on a chip, *Science*, 2010, 328(5986), 1662–1668, DOI: 10.1126/science.1188302.

122 A. Grassart, V. Malardé and S. Gobba, *et al.*, Bioengineered Human Organ-on-Chip Reveals Intestinal Microenvironment and Mechanical Forces Impacting Shigella Infection, *Cell Host Microbe*, 2019, 26(3), 435–444.e4, DOI: 10.1016/j.chom.2019.08.007.

123 J. M. Ayuso, S. Rehman, M. Virumbrales-Munoz, P. H. McMinn, P. Geiger, C. Fitzgerald, T. Heaster, M. C. Skala and D. J. Beebe, Microfluidic tumor-on-a-chip model to evaluate the role of tumor environmental stress on NK cell exhaustion, *Sci. Adv.*, 2021, 7(8), eabc2331, DOI: 10.1126/sciadv.abc2331.

124 J. M. Ayuso, R. Truttschel and M. M. Gong, *et al.*, Evaluating natural killer cell cytotoxicity against solid tumors using a microfluidic model, *Oncoimmunology*, 2019, 8(3), 1–11, DOI: 10.1080/2162402X.2018.1553477.

125 L. L. Bischel, D. J. Beebe and K. E. Sung, Microfluidic model of ductal carcinoma in situ with 3D, organotypic structure, *BMC Cancer*, 2015, 15(1), 1–10, DOI: 10.1186/s12885-015-1007-5.

126 X. Cao, R. Ashfaq and F. Cheng, *et al.*, A Tumor-on-a-Chip System with Bioprinted Blood and Lymphatic Vessel Pair, *Adv. Funct. Mater.*, 2019, 29(31), 1–13, DOI: 10.1002/adfm.201807173.

127 T. J. Kwak and E. Lee, Rapid multilayer microfabrication for modeling organotropic metastasis in breast cancer, *Biofabrication*, 2020, 13, 015002, DOI: 10.1088/1758-5090/abbd28.

128 C. P. Miller, C. Tsuchida, Y. Zheng, J. Himmelfarb and S. Akilesh, A 3D Human Renal Cell Carcinoma-on-a-Chip for the Study of Tumor Angiogenesis, *Neoplasia*, 2018, 20(6), 610–620, DOI: 10.1016/j.neo.2018.02.011.

129 D. T. Nguyen, E. Lee, S. Alimperti, R. J. Norgard, A. Wong, J. J. Lee, J. Eyckmans, B. Z. Stanger and C. S. Chen, A Biomimetic Pancreatic Cancer On-Chip Reveals Endothelial Ablation via ALK7 Signaling, *Sci. Adv.*, 2019, 5(8), eaav6789, DOI: 10.1126/sciadv.aav6789.

130 D. Nothdurfter, C. Ploner, D. C. Coraça-Huber, D. Wilflingseder, T. Müller, M. Hermann, J. Hagenbuchner and M. J. Ausserlechner, 3D bioprinted, vascularized neuroblastoma tumor environment in fluidic chip devices for precision medicine drug testing, *Biofabrication*, 2022, 14(3), DOI: 10.1088/1758-5090/ac5fb7.

131 S. Pradhan, A. M. Smith, C. J. Garson, I. Hassani, W. J. Seeto, K. Pant, R. D. Arnold, B. Prabhakarpandian and E. A. Lipke, A Microvascularized Tumor-mimetic Platform for Assessing Anti-cancer Drug Efficacy, *Sci. Rep.*, 2018, 8(1), 3171, DOI: 10.1038/s41598-018-21075-9.

132 J. Tien, J. G. Truslow and C. M. Nelson, Modulation of Invasive Phenotype by Interstitial Pressure-Driven Convection in Aggregates of Human Breast Cancer Cells, *PLoS One*, 2012, 7(9), e45191, DOI: 10.1371/journal.pone.0045191.

133 K. A. DiVito, M. A. Daniele, S. A. Roberts, F. S. Ligler and A. A. Adams, Microfabricated blood vessels undergo neoangiogenesis, *Biomaterials*, 2017, 138, 142–152, DOI: 10.1016/j.biomaterials.2017.05.012.

134 L. Yang, S. V. Shridhar, M. Gerwitz and P. Soman, An in vitro vascular chip using 3D printing-enabled hydrogel casting, *Biofabrication*, 2016, 8(3), 035015, DOI: 10.1088/1758-5090/8/3/035015.

135 J. Ko, J. Ahn and S. Kim, *et al.*, Tumor spheroid-on-a-chip: A standardized microfluidic culture platform for investigating tumor angiogenesis, *Lab Chip*, 2019, 19(17), 2822–2833, DOI: 10.1039/c9lc00140a.

136 Y. Kim, J. Ko and N. Shin, *et al.*, All-in-one microfluidic design to integrate vascularized tumor spheroid into high-throughput platform, *Biotechnol. Bioeng.*, 2022, 119(12), 3678–3693, DOI: 10.1002/bit.28221.

137 M. B. Chen, J. A. Whisler, J. Fröse, C. Yu, Y. Shin and R. D. Kamm, On-chip human microvasculature assay for visualization and quantification of tumor cell extravasation dynamics, *Nat. Protoc.*, 2017, 12(5), 865–880, DOI: 10.1038/nprot.2017.018.

138 D. T. T. Phan, X. Wang and B. M. Craver, *et al.*, A vascularized and perfused organ-on-a-chip platform for large-scale drug screening applications, *Lab Chip*, 2017, 17(3), 511–520, DOI: 10.1039/c6lc01422d.

139 C. Hajal, L. Ibrahim, J. C. Serrano, G. S. Offeddu and R. D. Kamm, The effects of luminal and trans-endothelial fluid flows on the extravasation and tissue invasion of tumor cells in a 3D in vitro microvascular platform, *Biomaterials*, 2021, 265, 120470, DOI: 10.1016/j.biomaterials.2020.120470.

140 J. Song, A. Miermont, C. T. Lim and R. D. Kamm, A 3D microvascular network model to study the impact of hypoxia on the extravasation potential of breast cell lines, *Sci. Rep.*, 2018, 8(1), 1–11, DOI: 10.1038/s41598-018-36381-5.

141 K. Haase, G. S. Offeddu, M. R. Gillrie and R. D. Kamm, Endothelial Regulation of Drug Transport in a 3D Vascularized Tumor Model, *Adv. Funct. Mater.*, 2020, 30, 2002444, DOI: 10.1002/adfm.202002444.

142 S. Pradhan, K. A. Keller, J. L. Sperduto and J. H. Slater, Fundamentals of Laser-Based Hydrogel Degradation and Applications in Cell and Tissue Engineering, *Adv. Healthcare Mater.*, 2017, 6(24), DOI: 10.1002/adhm.201700681.

143 O. Sarig-Nadir, N. Livnat, R. Zajdman, S. Shoham and D. Seliktar, Laser photoablation of guidance microchannels into hydrogels directs cell growth in three dimensions, *Biophys. J.*, 2009, 96(11), 4743–4752, DOI: 10.1016/j.bpj.2009.03.019.

144 R. W. Jenkins, A. R. Aref and P. H. Lizotte, *et al.*, Ex vivo profiling of PD-1 blockade using organotypic tumor spheroids, *Cancer Discovery*, 2018, 8(2), 196–215, DOI: 10.1158/2159-8290.CD-17-0833.

145 Z. Du, S. Mi, X. Yi, Y. Xu and W. Sun, Microfluidic system for modelling 3D tumour invasion into surrounding stroma and drug screening, *Biofabrication*, 2018, 10(3), 034102, DOI: 10.1088/1758-5090/aac70c.

146 E. A. Zaal and C. R. Berkers, The influence of metabolism on drug response in cancer, *Front Oncol*, 2018, 8, 500, DOI: 10.3389/fonc.2018.00500.

147 Y. Hou, X. Ai and L. Zhao, *et al.*, An integrated biomimetic array chip for high-throughput co-culture of liver and tumor microtissues for advanced anticancer bioactivity screening, *Lab Chip*, 2020, 20(14), 2482–2494, DOI: 10.1039/d0lc00288g.

148 M. Glicksman, Z. Li and S. Markossian, *et al.*, In Vitro Cell Based Assays, *Assay Guidance Manual*, 2023.

149 T. L. Riss, R. A. Moravec and A. L. Niles, *et al.*, Cell Viability Assays, *Assay Guidance Manual*, 2013.

150 I. Veith, A. Mencattini and V. Picant, *et al.*, Apoptosis mapping in space and time of 3D tumor ecosystems reveals transmissibility of cytotoxic cancer death, *PLoS Comput. Biol.*, 2021, 17(3), 1–23, DOI: 10.1371/JOURNAL.PCBI.1008870.

151 G. Ronteix, S. Jain and C. Angely, *et al.*, High resolution microfluidic assay and probabilistic modeling reveal cooperation between T cells in tumor killing, *Nat. Commun.*, 2022, 13(1), 25–28, DOI: 10.1038/s41467-022-30575-2.

152 Y. S. Zhang, Y. N. Zhang and W. Zhang, Cancer-on-a-chip systems at the frontier of nanomedicine, *Drug Discovery Today*, 2017, 22, 1392–1399.

153 M. S. Manak, J. S. Varsanik and B. J. Hogan, *et al.*, Live-cell phenotypic-biomarker microfluidic assay for the risk stratification of cancer patients via machine learning, *Nat. Biomed. Eng.*, 2018, 47(3), 549–562, DOI: 10.1038/s41551-018-0285-z.Live-cell.

154 A. Mencattini, D. Di Giuseppe and M. C. Comes, *et al.*, Discovering the hidden messages within cell trajectories using a deep learning approach for in vitro evaluation of cancer drug treatments, *Sci. Rep.*, 2020, 10(1), 1–11, DOI: 10.1038/s41598-020-64246-3.

155 F. Klemm and J. A. Joyce, Microenvironmental regulation of therapeutic response in cancer, *Trends Cell Biol.*, 2015, 25(4), 198–213, DOI: 10.1016/j.tcb.2014.11.006.

156 E. Ulukaya, D. Karakas and K. Dimas, Tumor Chemosensitivity Assays Are Helpful for Personalized Cytotoxic Treatments in Cancer Patients, *Medicina*, 2021, 57(6), 636, DOI: 10.3390/medicina57060636.

157 I. Desyatnik, M. Krasner, L. Frolov, M. Ronen, O. Guy, D. Wasserman, A. Tzur, D. Avrahami, E. Barbiro-Michaely and D. Gerber, An Integrated Microfluidics Approach for Personalized Cancer Drug Sensitivity and Resistance Assay, *Adv. Biosyst.*, 2019, 3(11), e1900001, DOI: 10.1002/adbi.201900001.

158 B. Gokce, I. Akcok, A. Cagir and D. Pesen-Okvur, A new drug testing platform based on 3D tri-culture in lab-on-a-chip devices, *Eur. J. Pharm. Sci.*, 2020, 155, 105542, DOI: 10.1016/j.ejps.2020.105542.

159 Y. A. Guerrero, D. Desai, C. Sullivan, E. Kindt, M. E. Spilker, T. S. Maurer, D. E. Solomon and D. W. Bartlett, A Microfluidic Perfusion Platform for In Vitro Analysis of Drug Pharmacokinetic-Pharmacodynamic (PK-PD) Relationships, *AAPS J.*, 2020, 22(2), 53, DOI: 10.1208/s12248-020-0430-y.

160 A. D. Rodriguez and L. F. Horowitz, *et al.*, A microfluidic platform for functional testing of cancer drugs on intact tumor slices, *Lab Chip*, 2020, 20(9), 1658–1675.

161 W. Han, R. El Botty, E. Montaudon, L. Malaquin, F. Deschaseaux, N. Espagnolle, E. Marangoni, P. Cottu, G. Zalcman, M. C. Parrini, F. Assayag, L. Sensebe, P. Silberzan, A. Vincent-Salomon, G. Dutertre, S. Roman-Roman, S. Descroix and J. Camonis, In vitro bone metastasis dwelling in a 3D bioengineered niche, *Biomaterials*, 2021, 269, 120624, DOI: 10.1016/j.biomaterials.2020.120624.

162 V. V. Padma, An overview of targeted cancer therapy, *Biomedicine*, 2015, 5(4), 1–6, DOI: 10.7603/s40681-015-0019-4.

163 F. D. Makurvet, Biologics vs. small molecules: Drug costs and patient access, *Med. Drug Discovery*, 2021, 9, 100075, DOI: 10.1016/j.medidd.2020.100075.

164 Z. Dereli-Korkut, H. D. Akaydin, A. H. R. Ahmed, X. Jiang and S. Wang, Three dimensional microfluidic cell arrays for ex vivo drug screening with mimicked vascular flow, *Anal. Chem.*, 2014, 86(6), 2997–3004, DOI: 10.1021/ac403899j.

165 S. Azadi, E. Mohammadi, M. Tafazzoli-Shadpour and M. Tabatabaei, Effects of chemically EGFR targeting on non-targeted physical cell behaviors in 2D and 3D microfluidic cultures of invasive and non-invasive breast cancer cell lines, *Biochem. Biophys. Res. Commun.*, 2022, 622, 1–7, DOI: 10.1016/j.bbrc.2022.07.013.

166 M. Nguyen, A. De Ninno and A. Mencattini, *et al.*, Dissecting Effects of Anti-cancer Drugs and Cancer-Associated Fibroblasts by On-Chip Reconstitution of Immunocompetent Tumor Microenvironments, *Cell Rep.*, 2018, 25(13), 3884–3893.e3, DOI: 10.1016/j.celrep.2018.12.015.

167 L. Zhong, Y. Li, L. Xiong, W. Wang, M. Wu, T. Yuan, W. Yang, C. Tian, Z. Miao, T. Wang and S. Yang, Small molecules in targeted cancer therapy: advances, challenges, and future perspectives, *Signal Transduction Targeted Ther.*, 2021, 6(1), 201, DOI: 10.1038/s41392-021-00572-w.

168 S. Akkın, G. Varan and E. Bilensoy, A review on cancer immunotherapy and applications of nanotechnology to chemoimmunotherapy of different cancers, *Molecules*, 2021, 26(11), 3382, DOI: 10.3390/molecules26113382.

169 M. Binnewies, E. W. Roberts and K. Kersten, *et al.*, Understanding the tumor immune microenvironment (TIME) for effective therapy, *Nat. Med.*, 2018, 24(5), 541–550, DOI: 10.1038/s41591-018-0014-x.

170 G. You, J. Won, Y. Lee, D. Moon, Y. Park, S. H. Lee and S. W. Lee, Bispecific antibodies: A smart arsenal for cancer immunotherapies, *Vaccines*, 2021, 9(7), 724, DOI: 10.3390/vaccines9070724.

171 D. B. Johnson, C. A. Nebhan, J. J. Moslehi and J. M. Balko, Immune-checkpoint inhibitors: long-term implications of toxicity, *Nat. Rev. Clin. Oncol.*, 2022, 19(4), 254–267, DOI: 10.1038/s41571-022-00600-w.

172 L. Galluzzi, T. A. Chan, G. Kroemer, J. D. Wolchok and A. López-Soto, The hallmarks of successful anticancer immunotherapy, *Sci. Transl. Med.*, 2018, 10(459), 1–15, DOI: 10.1126/scitranslmed.aat7807.

173 J. Mestas and C. C. W. Hughes, Of Mice and Not Men: Differences between Mouse and Human Immunology, *J. Immunol.*, 2004, 172(5), 2731–2738, DOI: 10.4049/jimmunol.172.5.2731.

174 S. Parlato, G. Grisanti, G. Sinibaldi, G. Peruzzi, C. M. Casciola and L. Gabriele, Tumor-on-a-chip platforms to study cancer-immune system crosstalk in the era of immunotherapy, *Lab Chip*, 2021, 21(2), 234–253, DOI: 10.1039/d0lc00799d.

175 T. I. Maulana, E. Kromidas and L. Wallstabe, *et al.*, Immunocompetent cancer-on-chip models to assess immuno-oncology therapy, *Adv. Drug Delivery Rev.*, 2021, 173, 281–305, DOI: 10.1016/j.addr.2021.03.015.

176 M. A. J. Morsink, N. G. A. Willemen, J. Leijten, R. Bansal and S. R. Shin, Immune organs and immune cells on a chip: An overview of biomedical applications, *Micromachines*, 2020, 11(9), 1–25, DOI: 10.3390/MI11090849.

177 S. Parlato, A. De Ninno and R. Molfetta, *et al.*, 3D Microfluidic model for evaluating immunotherapy efficacy by tracking dendritic cell behaviour toward tumor cells, *Sci. Rep.*, 2017, 7(1), 1–16, DOI: 10.1038/s41598-017-01013-x.

178 A. Mencattini, C. Lansche, I. Veith, P. Erbs, J. M. Balloul, E. Quemeneur, S. Descroix, F. Mechta-Grigoriou, G. Zalcman, C. Zaupa, M. C. Parrini and E. Martinelli, Direct imaging and automatic analysis in tumor-on-chip reveal cooperative antitumoral activity of immune cells and oncolytic vaccinia virus, *Biosens. Bioelectron.*, 2022, 215, 114571, DOI: 10.1016/j.bios.2022.114571.

179 A. Pavesi, A. T. Tan, S. Koh, A. Chia, M. Colombo, E. Antonecchia, C. Miccolis, E. Ceccarello, G. Adriani, M. T. Raimondi, R. D. Kamm and A. Bertoletti, A 3D microfluidic model for preclinical evaluation of TCR-engineered T cells against solid tumors, *JCI Insight*, 2017, 2(12), e89762, DOI: 10.1172/jci.insight.89762.

180 M. Chernyavska, C. K. J. C. Hermans and C. Chan, *et al.*, Evaluation of immunotherapies improving macrophage anti-tumor response using a microfluidic model, *Organs-on-a-Chip*, 2022, 4, 100019, DOI: 10.1016/j.ooc.2022.100019.

181 U. Anand, A. Dey, A. K. S. Chandel, R. Sanyal, A. Mishra, D. K. Pandey, V. De Falco, A. Upadhyay, R. Kandimalla, A. Chaudhary, J. K. Dhanjal, S. Dewanjee, J. Vallamkondu and J. M. Pérez de la Lastra, Cancer chemotherapy and beyond: Current status, drug candidates, associated risks and progress in targeted therapeutics, *Genes Dis.*, 2022, 10(4), 1367–1401, DOI: 10.1016/j.gendis.2022.02.007.

182 A. Pavesi, G. Adriani, A. Tay, M. E. Warkiani, W. H. Yeap, S. C. Wong and R. D. Kamm, Engineering a 3D microfluidic culture platform for tumor-treating field application, *Sci. Rep.*, 2016, 6, 26584, DOI: 10.1038/srep26584.

183 R. Bayat Mokhtari, T. S. Homayouni, N. Baluch, E. Morgatskaya, S. Kumar, B. Das and H. Yeger, Combination therapy in combating cancer, *Oncotarget*, 2017, 8(23), 38022–38043, DOI: 10.18632/oncotarget.16723.

184 W. Y. Kong, S. C. Ngai, B. H. Goh, L. H. Lee, T. T. Htar and L. H. Chuah, Is Curcumin the Answer to Future Chemotherapy Cocktail?, *Molecules*, 2021, 26(14), 4329, DOI: 10.3390/molecules26144329.

185 E. Nicolò, F. Giugliano, L. Ascione, P. Tarantino, C. Corti, S. M. Tolaney, M. Cristofanilli and G. Curigliano, Combining antibody-drug conjugates with immunotherapy in solid tumors: current landscape and future perspectives, *Cancer Treat. Rev.*, 2022, 106, 102395, DOI: 10.1016/j.ctrv.2022.102395.

186 S. Tran, P. J. DeGiovanni, B. Piel and P. Rai, Cancer nanomedicine: a review of recent success in drug delivery, *Clin. Transl. Med.*, 2017, 6(1), 44, DOI: 10.1186/s40169-017-0175-0.

187 A. Wicki, D. Witzigmann, V. Balasubramanian and J. Huwyler, Nanomedicine in cancer therapy: Challenges, opportunities, and clinical applications, *J. Controlled Release*, 2015, 200, 138–157, DOI: 10.1016/j.jconrel.2014.12.030.

188 J. K. Patra, G. Das and L. F. Fraceto, *et al.*, Nano based drug delivery systems: Recent developments and future prospects 10 Technology 1007 Nanotechnology 03 Chemical Sciences 0306 Physical Chemistry (incl. Structural) 03 Chemical Sciences 0303 Macromolecular and Materials Chemistry 11 Medical and He, *J. Nanobiotechnol.*, 2018, 16(1), 1–33, DOI: 10.1186/s12951-018-0392-8.

189 H. Zhang, Y. Zhu and Y. Shen, Microfluidics for Cancer Nanomedicine: From Fabrication to Evaluation, *Small*, 2018, 14(28), 1–25, DOI: 10.1002/smll.201800360.

190 N. S. Bhise, J. Ribas and V. Manoharan, *et al.*, Organ-on-a-chip platforms for studying drug delivery systems, *J. Controlled Release*, 2014, 190, 82–93, DOI: 10.1016/j.jconrel.2014.05.004.

191 D. Zhu, Q. Long, Y. Xu and J. Xing, Evaluating Nanoparticles in Preclinical Research Using Microfluidic Systems, *Micromachines*, 2019, 10(6), 414, DOI: 10.3390/mi10060414.

192 O. Mitxelena-Iribarren, J. Zabalo, S. Arana and M. Mujika, Improved microfluidic platform for simultaneous multiple drug screening towards personalized treatment, *Biosens. Bioelectron.*, 2019, 123, 237–243, DOI: 10.1016/j.bios.2018.09.001.

193 J. Wu, H. Li, Q. Chen, X. Lin, W. Liu and J. M. Lin, Statistical single-cell analysis of cell cycle-dependent quantum dot cytotoxicity and cellular uptake using a microfluidic system, *RSC Adv.*, 2014, 4(47), 24929–24934, DOI: 10.1039/c4ra01665c.

194 A. Albanese, A. K. Lam, E. A. Sykes, J. V. Rocheleau and W. C. W. Chan, Tumour-on-a-chip provides an optical window into nanoparticle tissue transport, *Nat. Commun.*, 2013, 4, 1–8, DOI: 10.1038/ncomms3718.

195 B. Kwak, A. Ozcelikkale, C. S. Shin, K. Park and B. Han, Simulation of complex transport of nanoparticles around a tumor using tumor-microenvironment-on-chip, *J. Controlled Release*, 2014, 194, 157–167, DOI: 10.1016/j.jconrel.2014.08.027.

196 C. A. Cunha-Matos, O. R. Millington, A. W. Wark and M. Zagnoni, Real-time assessment of nanoparticle-mediated antigen delivery and cell response, *Lab Chip*, 2016, 16(17), 3374–3381, DOI: 10.1039/c6lc00599c.

197 Y. Tang, F. Soroush, J. B. Sheffield, B. Wang, B. Prabhakarpandian and M. F. Kiani, A Biomimetic Microfluidic Tumor Microenvironment Platform Mimicking the EPR Effect for Rapid Screening of Drug Delivery Systems, *Sci. Rep.*, 2017, 7(1), 1–14, DOI: 10.1038/s41598-017-09815-9.

198 K. Tokarska, M. Bułka and U. Bazylińska, *et al.*, Evaluation of nanoencapsulated verteporfin's cytotoxicity using a microfluidic system, *J. Pharm. Biomed. Anal.*, 2016, 127, 39–48, DOI: 10.1016/j.jpba.2016.02.052.

199 R. Duncan and R. Gaspar, Nanomedicine(s) under the microscope, *Mol. Pharmaceutics*, 2011, 8(6), 2101–2141, DOI: 10.1021/mp200394t.

200 W. Liu, J. C. Wang and J. Wang, Controllable organization and high throughput production of recoverable 3D tumors using pneumatic microfluidics, *Lab Chip*, 2015, 15(4), 1195–1204, DOI: 10.1039/c4lc01242a.

201 M. Chudy, K. Tokarska and E. Jastrzębska, *et al.*, Lab-on-a-chip systems for photodynamic therapy investigations, *Biosens. Bioelectron.*, 2018, 101, 37–51, DOI: 10.1016/j.bios.2017.10.013.

202 A. Dao, R. Kushwaha, A. Kumar, H. Huang and S. Banerjee, Engineered Exosomes as a Photosensitizer Delivery Platform for Cancer Photodynamic Therapy, *ChemMedChem*, 2022, 17(10), e202200119, DOI: 10.1002/cmdc.202200119.

203 M. Flont, E. Jastrz̨ebska and Z. Brzózka, A multilayered cancer-on-a-chip model to analyze the effectiveness of new-generation photosensitizers, *Analyst*, 2020, 145(21), 6937–6947, DOI: 10.1039/d0an00911c.

204 J. M. Lee, H. I. Seo, J. H. Bae and B. G. Chung, Hydrogel microfluidic co-culture device for photothermal therapy and cancer migration, *Electrophoresis*, 2017, 38(9–10), 1318–1324, DOI: 10.1002/elps.201600540.

205 P. Agarwal, H. Wang and M. Sun, *et al.*, Microfluidics Enabled Bottom-Up Engineering of 3D Vascularized Tumor for Drug Discovery, *ACS Nano*, 2017, 11(7), 6691–6702, DOI: 10.1021/acsnano.7b00824.

206 I. K. Zervantonakis and C. D. Arvanitis, Controlled Drug Release and Chemotherapy Response in a Novel Acoustofluidic 3D Tumor Platform, *Small*, 2016, 12(19), 2616–2626, DOI: 10.1002/smll.201503342.

207 J. P. Hughes, S. S. Rees, S. B. Kalindjian and K. L. Philpott, Principles of early drug discovery, *Br. J. Pharmacol.*, 2011, 162(6), 1239–1249, DOI: 10.1111/j.1476-5381.2010.01127.x.

208 A. A. Adjei, What is the right dose? The elusive optimal biologic dose in phase I clinical trials, *J. Clin. Oncol.*, 2006, 24(25), 4054–4055, DOI: 10.1200/JCO.2006.07.4658.

209 K. Sherkar, S. Choudante and O. Sumant, *Organ-Tumor-on-a-Chip Market by Type (Lung Tumor-on-a-Chip, Bone Marrow Tumor-on-a-Chip, Brain Tumor-on-a-Chip, Breast Tumor-on-a-Chip, Urinary System Tumor-on-a-Chip, Intestine Tumor-on-a-Chip, and Liver Tumor-on-a-Chip): Global Opportunity Analysis and Industry Forecast, 2021–2030*, 2021.

210 S. W. Baran, P. C. Brown, A. R. Baudy, S. C. Fitzpatrick, C. Frantz, A. Fullerton, J. Gan, R. N. Hardwick, K. M. Hillgren, A. K. Kopec, J. L. Liras, D. L. Mendrick, R. Nagao, W. R. Proctor, D. Ramsden, A. J. S. Ribeiro, D. Stresser, K. E. Sung, R. Sura, K. Tetsuka, L. Tomlinson, T. Van Vleet, M. P. Wagoner, Q. Wang, S. Y. Arslan, G. Yoder and J. E. Ekert, Perspectives on the evaluation and adoption of complex in vitro models in drug development: Workshop with the FDA and the pharmaceutical industry (IQ MPS Affiliate), *ALTEX*, 2022, 39(2), 297–314, DOI: 10.14573/altex.2112203.

211 R. Baudoin, L. Griscom, J. M. Prot, C. Legallais and E. Leclerc, Behavior of HepG2/C3A cell cultures in a microfluidic bioreactor, *Biochem. Eng. J.*, 2011, 53(2), 172–181, DOI: 10.1016/j.bej.2010.10.007.

212 V. Allwardt, A. J. Ainscough and P. Viswanathan, *et al.*, Translational roadmap for the organs-on-a-chip industry toward broad adoption, *Bioengineering*, 2020, 7(3), 1–27, DOI: 10.3390/bioengineering7030112.

213 P. Vulto and J. Joore, Adoption of organ-on-chip platforms by the pharmaceutical industry, *Nat. Rev. Drug Discovery*, 2021, 20(12), 961–962, DOI: 10.1038/s41573-021-00323-0.

214 G. K. Kiriiri, P. M. Njogu and A. N. Mwangi, Exploring different approaches to improve the success of drug discovery and development projects: a review, *Future J. Pharm. Sci.*, 2020, 6(1), 27, DOI: 10.1186/s43094-020-00047-9.

215 H. Dolgos, M. Trusheim and D. Gross, *et al.*, Translational Medicine Guide transforms drug development processes: The recent Merck experience, *Drug Discovery Today*, 2016, 21(3), 517–526, DOI: 10.1016/j.drudis.2016.01.003.

216 O. Strianese, F. Rizzo and M. Ciccarelli, *et al.*, Precision and personalized medicine: How genomic approach improves the management of cardiovascular and neurodegenerative disease, *Genes*, 2020, 11(7), 1–24, DOI: 10.3390/genes11070747.

217 C. B. M. Du Puch, M. Vanderstraete, S. Giraud, C. Lautrette, N. Christou and M. Mathonnet, Benefits of functional assays in personalized cancer medicine: More than just a proof-of-concept, *Theranostics*, 2021, 11(19), 9538–9556, DOI: 10.7150/THNO.55954.

218 E. L. S. Fong, T. B. Toh, H. Yu and E. K. H. Chow, 3D Culture as a Clinically Relevant Model for Personalized Medicine, *SLAS Technol.*, 2017, 22(3), 245–253, DOI: 10.1177/2472630317697251.

219 T. Hernandez-Boussard, P. Macklin and E. J. Greenspan, *et al.*, Digital twins for predictive oncology will be a paradigm shift for precision cancer care, *Nat. Med.*, 2021, 27(12), 2065–2066, DOI: 10.1038/s41591-021-01558-5.

220 A. Silva, M. C. Silva and P. Sudalagunta, *et al.*, An ex vivo platform for the prediction of clinical response in multiple myeloma, *Cancer Res.*, 2017, 77(12), 3336–3351, DOI: 10.1158/0008-5472.CAN-17-0502.

221 D. B. Chou, V. Frismantas and Y. Milton, *et al.*, On-chip recapitulation of clinical bone marrow toxicities and patient-specific pathophysiology, *Nat. Biomed. Eng.*, 2020, 4(4), 394–406, DOI: 10.1038/s41551-019-0495-z.

222 D. Singh, S. P. Deosarkar, E. Cadogan, V. Flemington, A. Bray, J. Zhang, R. S. Reiserer, D. K. Schaffer, G. B. Gerken, C. M. Britt, E. M. Werner, F. D. Gibbons, T. Kostrzewski, C. E. Chambers, E. J. Davies, A. R. Montoya, J. H. L. Fok, D. Hughes, K. Fabre, M. P. Wagoner, J. P. Wikswo and C. W. Scott, A microfluidic system that replicates pharmacokinetic (PK) profiles in vitro improves prediction of in vivo efficacy in preclinical models, *PLoS Biol.*, 2022, 20(5), e3001624, DOI: 10.1371/journal.pbio.3001624.

223 T. Petreus, E. Cadogan, G. Hughes, A. Smith, V. Pilla Reddy, A. Lau, M. J. O'Connor, S. Critchlow, M. Ashford and L. Oplustil O'Connor, Tumour-on-chip microfluidic platform for assessment of drug pharmacokinetics and treatment response, *Commun. Biol.*, 2021, 4(1), 1001, DOI: 10.1038/s42003-021-02526-y.

224 D. Venturoli and B. Rippe, Ficoll and dextran vs. globular proteins as probes for testing glomerular permselectivity: effects of molecular size, shape, charge, and deformability, *Am. J. Physiol. - Ren. Physiol.*, 2005, 288, 605–613, DOI: 10.1152/ajprenal.00171.2004.-Polydisperse.

225 C. W. McAleer, C. J. Long, D. Elbrecht, T. Sasserath, L. R. Bridges, J. W. Rumsey, C. Martin, M. Schnepper, Y. Wang, F. Schuler, A. B. Roth, C. Funk, M. L. Shuler and J. J. Hickman, Multi-organ system for the evaluation of efficacy and off-target toxicity of anticancer therapeutics, *Sci. Transl. Med.*, 2019, 11(497), eaav1386, DOI: 10.1126/scitranslmed.aav1386.

226 T. Satoh, S. Sugiura and K. Shin, *et al.*, A multi-throughput multi-organ-on-a-chip system on a plate formatted pneumatic pressure-driven medium circulation platform, *Lab Chip*, 2018, 18(1), 115–125, DOI: 10.1039/c7lc00952f.

227 A. Herland, B. M. Maoz and D. Das, *et al.*, Quantitative prediction of human pharmacokinetic responses to drugs via fluidically coupled vascularized organ chips, *Nat. Biomed. Eng.*, 2020, 4(4), 421–436, DOI: 10.1038/s41551-019-0498-9.

ANNEX B

RESEARCH ARTICLE

ADVANCED HEALTHCARE MATERIALS

www.advhealthmat.de

Multiscale Thermal Analysis of Gold Nanostars in 3D Tumor Spheroids: Integrating Cellular-Level Photothermal Effects and Nanothermometry via X-Ray Spectroscopy

Rosalía López-Méndez, Anastasiia Dubrova, Javier Reguera, Rául Magro, Fátima Esteban-Betegón, Ana Parente, Miguel Ángel García, Julio Camarero, Emiliano Fonda, Claire Wilhelm, Álvaro Muñoz-Noval,* and Ana Espinosa**

Check for updates

ADVANCED HEALTHCARE MATERIALS
www.advhealthmat.de

Multiscale Thermal Analysis of Gold Nanostars in 3D Tumor Spheroids: Integrating Cellular-Level Photothermal Effects and Nanothermometry via X-Ray Spectroscopy

Rosalía López-Méndez, Anastasiia Dubrova, Javier Reguera, Rául Magro, Fátima Esteban-Betegón, Ana Parente, Miguel Ángel García, Julio Camarero, Emiliano Fonda, Claire Wilhelm, Álvaro Muñoz-Noval,* and Ana Espinosa**

In the pursuit of enhancing cancer treatment efficacy while minimizing side effects, near-infrared (NIR) photothermal therapy (PTT) has emerged as a promising approach. By using photothermally active nanomaterials, PTT enables localized hyperthermia, effectively eliminating cancer cells with minimal invasiveness and toxicity. Among these nanomaterials, gold nanostars (AuNS) stand out due to their tunable plasmon resonance and efficient light absorption. This study addresses the challenge of measuring nanoscale temperatures during AuNS-mediated PTT by employing X-ray absorption spectroscopy (XAS) within 3D tumor spheroids. It also aims to investigate the heat generated at the nanoscale and the resultant biological damage observed at a larger scale, utilizing confocal microscopy to establish connections between AuNS heat generation, tissue damage, and their impacts on cellular structure. These nanoscale and microscale thermal effects have been compared with macroscopic values obtained from infrared thermography, as part of a multiscale thermal analysis. The findings underscore the efficacy of AuNS in enhancing PTT and provide insights into the spatial distribution of thermal effects within tumor tissues. This research advances the understanding of localized hyperthermia in cancer therapy and underscores the potential of AuNS-based PTT for clinical applications.

1. Introduction

In the quest to address the complexities of cancer and mitigating the risks associated with current treatment modalities, efforts have increasingly focused on enhancing therapeutic efficacy while minimizing safety concerns. Near-infrared (NIR) photothermal therapy (PTT), employing photothermally active nanomaterials, is emerging as a pivotal approach in tumor treatment.[1,2] This method entails the application of highly localized tissue heating, inducing hyperthermia that effectively destroys cancer cells through light-to-heat conversion. This strategy offers inherent advantages, including noninvasiveness, minimal toxicity, increased selectivity, and reduced potential for initiating resistance. Various nanoplatforms have been identified, spanning different compositions, shapes, and structures of metal nanoparticles, including gold and silver,[3–5] carbon nanomaterials and dots,[6–8] graphene

R. López-Méndez, J. Camarero, Á. Muñoz-Noval
IMDEA Nanociencia
c/Faraday, 9, Madrid 28049, Spain
A. Dubrova, C. Wilhelm
Laboratoire Physico Chimie Curie
PCC
CNRS UMR168
Institut Curie
Sorbonne University
PSL University
Paris 75005, France
E-mail: claire.wilhelm@curie.fr
The ORCID identification number(s) for the author(s) of this article can be found under https://doi.org/10.1002/adhm.202403799

© 2024 The Author(s). Advanced Healthcare Materials published by Wiley-VCH GmbH. This is an open access article under the terms of the Creative Commons Attribution-NonCommercial-NoDerivs License, which permits use and distribution in any medium, provided the original work is properly cited, the use is non-commercial and no modifications or adaptations are made.

DOI: 10.1002/adhm.202403799

J. Reguera
BCMaterials, Basque Center Centre for Materials Applications and Nanostructures
UPV/EHU Science Park, Leioa 48940, Spain
J. Reguera
Departamento de Física de la Materia Condensada – GIR Bioforge
Universidad de Valladolid
edificio LUCIA, paseo de Belén 19, Valladolid 47011, Spain
R. Magro, F. Esteban-Betegón, A. Espinosa
Instituto de Ciencia de Materiales de Madrid
ICMM-CSIC
c/ Sor Juana Inés de la Cruz, 3, Madrid 28049, Spain
E-mail: ana.espinosa@csic.es
A. Parente, Á. Muñoz-Noval
Dpto. Física Materiales
Facultad CC. Físicas
Universidad Complutense de Madrid
Madrid 28040, Spain
E-mail: almuno06@ucm.es

oxide,[9] and other inorganic nanoparticles such as silver sulfide,[10] copper sulfide,[11,12] iron oxide[13,14] or MXenes.[15] Among these, NIR-absorbing Au nanomaterials, encompassing Au nanoshells,[16,17] Au nanorods,[18,19] Au nanocages,[20] hollow Au nanospheres,[21,22] and Au nanostars, have emerged as the most prominent and widely studied nanoparticle types. Among the aforementioned NIR-induced gold-based nanoplatforms, Au nanostars (AuNS) stand out as particularly effective for applications in optical biosensing, imaging, and PTT.[23–27] This is largely attributed to their branched morphology which enables high plasmonic resonance within the NIR spectrum, all while maintaining a small nanoparticle size in the 25–75 nm range.[28,29] In contrast, prototype Au nanoshells have diameters typically exceeding 150 nm.[30] One notable feature of AuNSs is their impressive ability to finely tune their localized plasmon resonance spectra and enhance their light absorption efficiency by adjusting parameters like width, length, and spike count.[28,31] Modifying the number and aspect ratio of spikes can be easily accomplished by adjusting the concentration of $HAuCl_4$ and shape-directing agents in the seed-mediated growth process of their chemical synthesis.[27–29] Furthermore, AuNSs facilitate seamless conjugation with a diverse array of bioactive and cancer-targeting agents, thereby paving the way for combination therapies such as PTT alongside drug delivery[32–34] or photodynamic therapy (PDT).[35–37] All this makes it a versatile and effective state-of-the-art PTT agent. Moreover, when internalized by cancer cells and confined in endosomes, even small particles (≈25 nm) exhibit significant absorption in the NIR spectrum due to plasmon coupling between neighboring nanostars.[27,38]

One of the challenges in PTT lies in achieving accurate and precise temperature measurements at the nanoscale within tissues undergoing photothermal treatments. This entails the development of nanothermometric techniques capable of effectively sensing temperature changes in response to localized heating. It also involves addressing factors such as high resolution and the dynamic biological environment. Furthermore, ensuring the compatibility of these nanothermometers with photothermal agents and the targeted cells or tissues introduces complexity to the design and implementation of reliable nanothermometry techniques for hyperthermia. In response to these essential demands for thermal sensing within cellular and tissue contexts, a diverse array of nanothermometers has been created. These solutions harness the potential of luminescent nanoparticles,[39] fluorescent organic dyes,[40] quantum dots,[41,42] nanodiamonds,[43] thermosensitive polymers,[44,45] and metallic nanoparticles.[46] These nanoprobes enable precise temperature measurements within tissue environments and can serve as intracellular temperature indicators for processes involving thermogenesis or thermal therapies. Additionally, nanoscale photothermal effects can be investigated using a recent nanothermometric methodology using X-ray absorption spectroscopy (XAS).[47–49] Gold-iron oxide nanoparticles activated by NIR light exhibited a significantly elevated local heating at the nanoparticle scale both in solid solutions and in tumor cells using this nanothermal method[48,49] compared with overall temperature. Raising the temperature significantly leads to physical harm, including protein denaturation and membrane rupture. This process can elevate oxidative stress, ultimately resulting in coagulative necrosis or apoptosis. These effects are expected to be even more pronounced in the vicinity of nanoparticles, as they are confined within endosomes inside cells.

Due to the significant plasmon-induced thermal gradient observed at the nanoscale within tissue environment,[49] a key concern in PTT treatments is to establish the relationship between induced thermal damage and its spatial extent around the activated heating sources in tumor tissues. Consequently, understanding the biological effects of the localized heat generated in tumor tissues at cellular level still requires further investigation. In this context, 3D tumor models are now preferred for pre-clinical assessment of anti-cancer treatments, striking a balance between the lack of microenvironment in adherent cell cultures and the complexity of in vivo animal models. In spheroids, cancer cells grow as aggregates, promoting cellular proliferation and stimulating extracellular matrix (ECM) production, thereby enhancing cell-cell contact and communication.[50,51] Moreover, the heat produced by thermoexcited nanoparticles within tightly packed cells is not dissipated as rapidly as in 2D cell cultures due to the spheroids' high surface-to-volume ratio, providing a more realistic representation of a heated tumor environment.[50,52–55] The 3D model thus combines features such as coupled capillary and interstitial heat transfer and transport, which are the fundamental mechanisms governing the distribution of heat in nano-based hyperthermic treatments.[56]

Another major challenge lies in fine evaluation of local nanoparticles' hyperthermic effect and resulting cellular tissue damage. To date, confocal microscopy provides one of the most advanced and convenient techniques to precisely evaluate nanoscale impact in live and fixed tissues. It allows for the tracking of temperature changes and thermal damage, including alterations in membrane integrity and protein denaturation, with high-resolution in 3D. Fluorescent probes may serve as optical microprobes to not only assess cell viability post-treatment but gain insight into cellular organization and its associated functions. As such, staining actin filaments that comprise part of the cell cytoskeleton responsible for cell movement can relate to cancer migration, as microfilament disruption has been shown to be associated with its inhibition.[57] In addition, a plethora of cell-cell adhesion complexes, which serve as associated tumor markers, can be observed to assess the potential effect of local hyperthermia on cancer cells. Among those, the cadherin super-

M. Ángel García
Departamento de Electrocerámica
Instituto de Cerámica y Vidrio
ICV-CSIC
Kelsen 5, Madrid 28049, Spain
J. Camarero
Departamento de Física de la Materia Condensada and Instituto 'Nicolás Cabrera'
Universidad Autónoma de Madrid
Madrid 28049, Spain
E. Fonda
Synchrotron SOLEIL
L'Orme des Merisiers – St. Aubin-BP 48
Gif s/Yvette 91192, France
A. Espinosa
Unidad de Nanomateriales Avanzados
IMDEA Nanociencia, Unidad Asociada al CSIC por el ICMM
c/ Faraday 9, Madrid 28049, Spain

© 2024 The Author(s). Advanced Healthcare Materials published by Wiley-VCH GmbH

21922659, 2025, 11, Downloaded from https://advanced.onlinelibrary.wiley.com/doi/10.1002/adhm.202403799 by ESPCI ParisTech, Wiley Online Library on [30/09/2025]. See the Terms and Conditions (https://onlinelibrary.wiley.com/terms-and-conditions) on Wiley Online Library for rules of use; OA articles are governed by the applicable Creative Commons License

family of adherent junctions, and more specifically E-cadherin, is one of the most explored proteins so far, indicative of tissue epitheliality.[58] Therefore, its observed loss or gain following the nanoparticle-localized hyperthermal effect may reveal the respective changes in tissue integrity and hence, its metastatic potential.[59] Targeted visualization of such crucial proteins with confocal microscopy may allow to further detail the extent and distribution of hyperthermic damage and thus, providing insights into the overall efficacy and safety of nanoparticle-based therapies.

This study employs an X-ray spectroscopy-based approach to measure the photothermal heating generated by AuNS within 3D cancer spheroids. Additionally, it explores cellular damage on a larger scale through microscopic analysis of thermal effects and their spatial distribution around activated heating sources. The aim is to establish connections between heat generation, tissue damage, and their effects on cellular structure. Our findings demonstrate that localized temperatures achieved at the nanoscale can exceed those measured at the macroscopic scale, revealing a critical thermal threshold that may indicate the breakdown of cell-cell adhesion. This research emphasizes the importance of accurately assessing nanoscale heating effects to guide the design of more effective photothermal therapies that maximize damage to cancer cells while minimizing harm to healthy tissues.

2. Results

2.1. Characterization of Gold Nanostars in 3D Tumor Spheroids

Gold nanostars (AuNS) were synthesized using seed-mediated protocol following established procedures, employing the polyvinylpyrrolidone/dimethylformamide (PVP/DMF) route synthesis, resulting in a core with a branched structure.[27,28] **Figure 1A** displays representative transmission electron microscopy (TEM) images of AuNS. More TEM images are shown in Figure S1 (Supporting Information). Regarding their optical properties, AuNS exhibited localized surface plasmon resonances (LSPR) within the visible to near-infrared (Vis-NIR) region with a broad band in the 600–900 nm range and a maximum at 735 nm, which is attributed to a tips-core hybridized plasmon mode (see Figure 1B) and a small band in the 500–600 nm region attributed to the core plasmon mode. X-ray diffraction (XRD) patterns, as presented in Figure 1C (upper panel), further confirmed the presence of a crystalline face-centered cubic (fcc) metallic Au phase.

AuNS were incubated with U87 glioblastoma cancer cells for 24 h at an extracellular Au concentration ranging from 12.5 to 100 µM. Figure 1D illustrates the internalization of AuNS with a 58.0 ± 1.4 nm average equivalent diameter (Figure 1E) within cells through TEM, clearly showing the sequestration of these nanoparticles within endosomes, indicating an endocytosis-mediated pathway. The cytotoxicity assessment performed revealed that the AuNS were biocompatible under these incubation conditions (Figure 1F), with cellular uptake ranging from 0.3 to 9.8 pg cell^{-1} of Au (Figure 1G). U87, a glioblastoma cell line representing brain cancer, was employed as a model system to generate aggregates, primarily in the form of spheroids, to replicate the characteristics of tumor tissue. 3D spheroid models not only replicate the complex microenvironment within solid tumors and mimic various tumor characteristics but also facilitate the simulation of a realistic heated tumor mass, accounting for subsequent heat exchange and environmental losses. U87 cells were initially labeled with AuNS at a concentration of 200 µM of Au. Subsequently, ≈300,000 cells were collected to form spheroids. Histological analysis was employed to assess the viability of spheroid-forming cells (Figure 1H). Hematoxylin and eosin-stained histological sections demonstrated viable and compact tissue in labeled cells.

AuNS exhibit a red-shift of the extinction band, moving the peak of their LSPR from 735 to 796 nm due to plasmonic coupling.[27,38] This extends their absorption capability into the broader NIR-I and NIR-II regions. Advanced high brightness X-ray diffraction (XRD) spectroscopy revealed that AuNS inside the cell aggregates exhibit patterns typical of fcc metallic Au (Figure 1C), along with crystals of physiological salts formed within the cells. These findings indicate that AuNS remained unchanged after exposure to the cellular environment, retaining their star-like architecture and crystalline composition.

U87 cells with AuNS formed a compact and homogeneous tumor spheroid of ≈ 300 µm in diameter (Figure 1I). High-resolution confocal microscopy imaging of live/dead assay staining of spheroids revealed maintained high viability of individual cells comprising the aggregates. Confocal immunofluorescence images (Figure 1J) show the structure of the spheroids, including the cell cytoskeleton (actin network) and cell-cell adhesion patterns (E-cadherin). The strengthened E-cadherin bonds indicate the cohesiveness and integrity of the tissue. The 3D spheroid integrity and toxicity of U87 cells were not affected by the presence of internalized AuNS.

2.2. Nanoscale Thermal Probing Inside Cells using X-Ray Absorption Spectroscopy (XAS)

Recent findings have shown that extended X-ray absorption fine structure (EXAFS) spectroscopy can accurately detect local heating in diverse inductively thermal systems.[47,48,60] More recently, we have introduced in situ EXAFS spectroscopy as a precise, versatile, and direct nanothermometric technique at the cellular level within the tumor environment.[49] This approach relies on analyzing the vibrations of structural parameters of heated atoms, such as Au in this case, inferred from fitting the structural Debye-Waller (DW) factor extracted by the EXAFS signal $\chi(k)$ with temperature from a previous study:

$$\chi(k) = \sum_i \frac{\left(N_i S_0^2\right) F_i(k)}{k R_i^2} \sin\left[2kR_i + \delta_i(k)\right] e^{-2\sigma_i^2 k^2} e^{-2R_i/\lambda(k)} \quad (1)$$

where N_i represents the coordination number of atom i, R_i denotes the interatomic distance of each shell, and σ_i^2 is the mean displacement due to thermal motion (DW factor). This factor quantifies the thermal vibrations of atoms and can be modeled according to a correlated Debye model equation. See Supporting Information for more details. At high temperatures, this factor can be expressed as:

$$\sigma_T^2 \approx \frac{A}{\theta_D}\left(\frac{1}{4} + \frac{T}{\theta_D}\right) \quad (2)$$

© 2024 The Author(s). Advanced Healthcare Materials published by Wiley-VCH GmbH

21922659, 2025, 11, Downloaded from https://advanced.onlinelibrary.wiley.com/doi/10.1002/adhm.202403799 by ESPCI ParisTech, Wiley Online Library on [30/09/2025]. See the Terms and Conditions (https://onlinelibrary.wiley.com/terms-and-conditions) on Wiley Online Library for rules of use; OA articles are governed by the applicable Creative Commons License

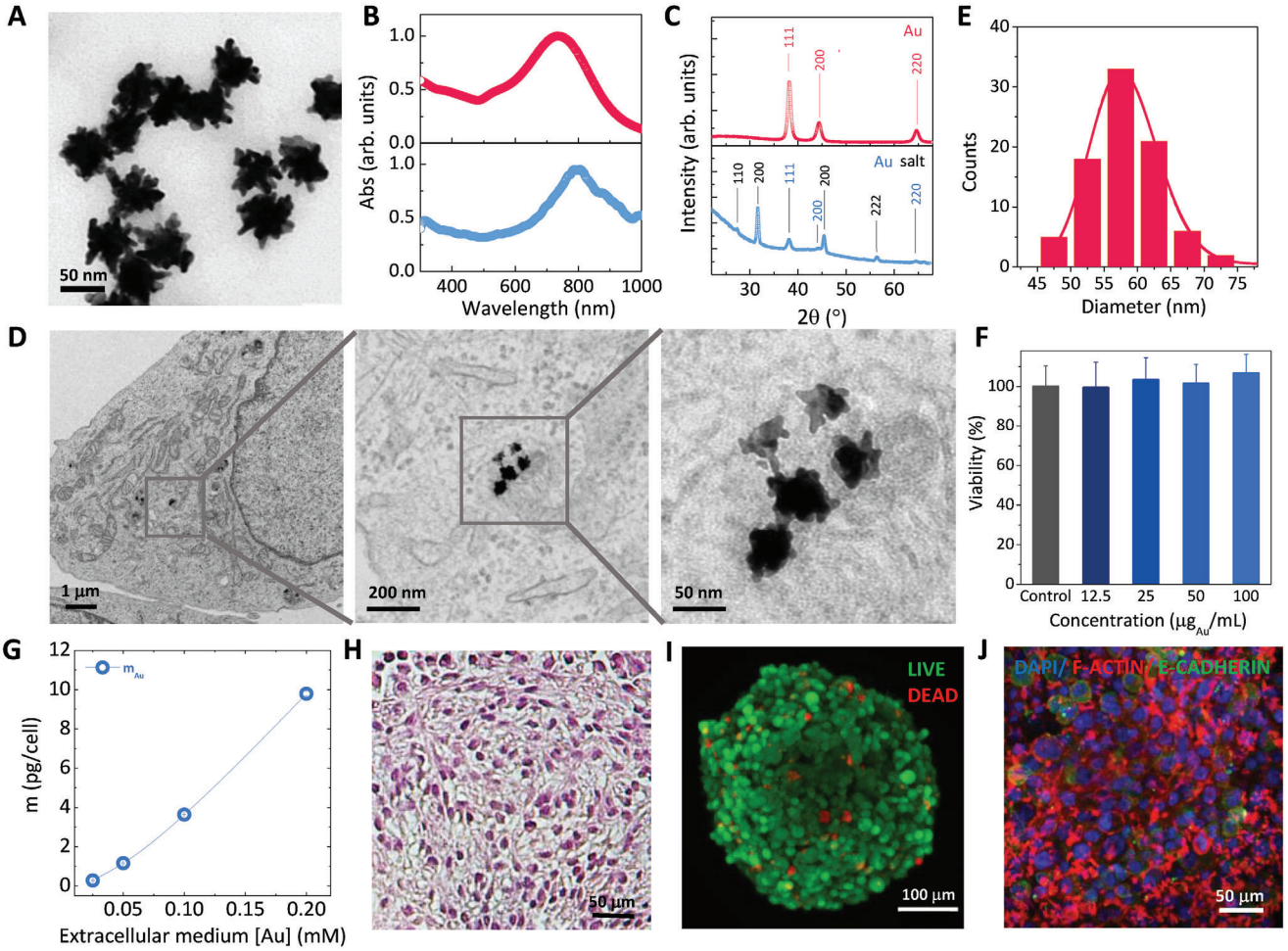


Figure 1. A) TEM image of AuNS (with a diameter of 58.0 ± 1.4 nm). B) UV–Vis–NIR spectra of AuNS in solution (on top) and inside U87 glioblastoma cells (down), both reveal the presence of a plasmon resonance in the near-infrared (NIR) region. C) X-ray diffraction (XRD) pattern of AuNS in solution (on top) and inside U87 cells (down). D) TEM micrographs of AuNS in U87 cells. E) Particle size distribution analysis of the AuNS in water. F) Cell viability of AuNS assessed in U87 cells after 24 h of exposure to different extracellular concentrations (12.5, 25, 50, and 100 μg_{Au} ml^{-1}). G) Cellular internalization of AuNS quantified using inductively coupled plasma optical emission spectroscopy (ICP-OES) in mass of Au per cell after a 24-h incubation at extracellular concentrations ranging from 25 to 200 µM. H) Hematoxylin and eosin staining of a labeled spheroid section. I) 3D reconstructed confocal images of live/dead cells in the formed spheroid with AuNS. Green fluorescent calcein indicates live cells, while red component, iodide, marks dead cells. J) 3D reconstructed confocal images of a spheroid with AuNS stained with F-actin (cytoskeleton, red), E-cadherin (cell junctions, green), and DAPI (nuclei, blue).

where A is a constant containing the reduced mass $M = \frac{m_1 * m_2}{m_1 + m_2}$ of the atom pair, k_B the Boltzmann constant, $\hbar$ is Planck's constant, and θ_D the Debye-Einstein temperature ($A = \frac{3\hbar^2}{Mk_B}$).

XAS measurements were conducted on the SAMBA beamline (SOLEIL synchrotron, France) at the Au L_3-edge in fluorescence mode due to the absorption properties of cell tissue. This method ensures precise and reliable data acquisition, essential for characterizing the local structural and electronic properties of the AuNS in their biological environment. The X-ray absorption near-edge structure (XANES) analysis revealed the electronic structures of metallic Au within cellular environments (**Figure 2A**). The results were benchmarked against reference samples of bulk metallic Au (Au foil) to ensure accuracy. The data confirmed the preservation of the AuNS electronic properties after cellular uptake, demonstrating the stability and integrity of these nanomaterials in biological settings.

A calibration temperature experiment ranging from 100 to 350 K using a helium gas exchange cryostat was first conducted to determine the thermal dependency of σ_i^2 for Au atoms. Two distinct temperature ranges were examined: from 100 to 300 K, with increments of 60–70 K, and above 300 K, with intervals reduced to 25 K to achieve greater precision. The EXAFS signal amplitude is impacted by the thermal motion of atoms as shown in Figure 2B. Fourier transform (FT) of the k^2-weighted EXAFS signals of AuNS within cells is displayed in Figure 2C (non phase-corrected), across various temperatures, using a k-range of 2.5 to 11 $Å^{-1}$. It shows two main peaks associated with the metallic Au-Au bond distances ($R_{Au\text{-}Au}$ = 2.86 Å and assuming a mean coordination number N = 12 for Au metallic bulk). The FT of the

© 2024 The Author(s). Advanced Healthcare Materials published by Wiley-VCH GmbH

21922659, 2025, 11, Downloaded from https://advanced.onlinelibrary.wiley.com/doi/10.1002/adhm.202403799 by ESPCI ParisTech, Wiley Online Library on [30/09/2025]. See the Terms and Conditions (https://onlinelibrary.wiley.com/terms-and-conditions) on Wiley Online Library for rules of use; OA articles are governed by the applicable Creative Commons License

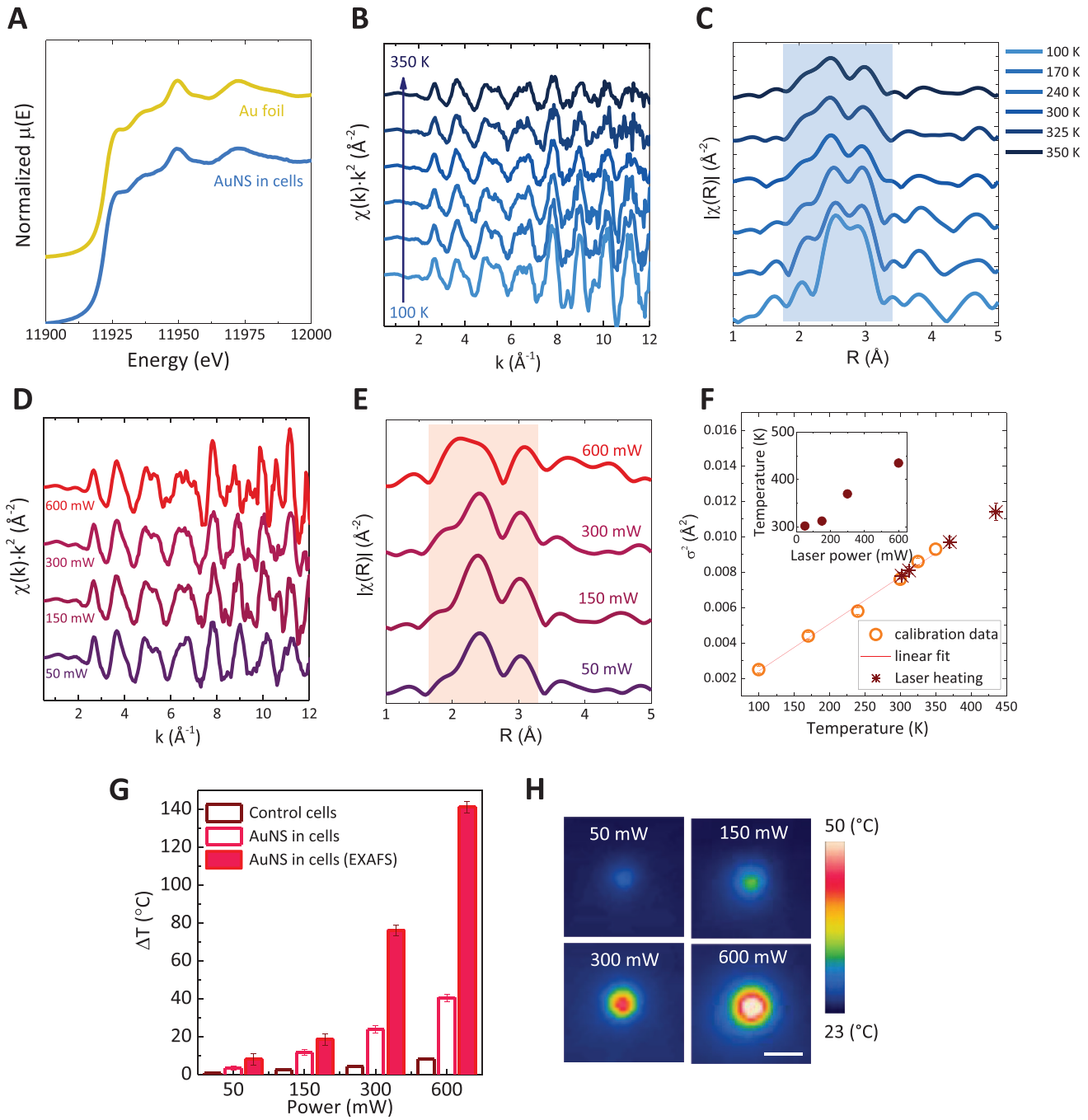


Figure 2. A) X-ray absorption near-edge structure (XANES) at Au L_3-edge (11919 eV) of AuNS in cells compared with Au foil reference at 300 K. Temperature evolution of the B) EXAFS oscillations (k^2-weighted) and C) Fourier Transform (FT) EXAFS signal extracted from Au L_3-edge XAS spectra measured from 100 to 350 K. D) Au L_3-edge EXAFS oscillation functions (k^2-weighted) subjected to photothermal irradiation at different laser powers (0.05–0.6 W). E) FT EXAFS signal under photothermia (0.05–0.6 W). F) Calibration curve of the DW as a function of temperature for AuNS (open symbols). Solid symbols represent calculated values under photothermal excitation. Solid lines depict the fitting based on the Debye-Einstein model in the linear approximation (100–350 K). The inset shows the local temperatures achieved under laser excitation (0.05–0.6 W). G) Average temperature increases of AuNS in cells subjected to various laser powers using EXAFS analysis (local temperature) and an infrared thermal camera (macroscopic). Average temperature elevation of control (unlabeled) cells was also measured under laser excitation. H) Infrared thermal images of AuNS in cells under different laser powers (scale bar: 5 mm).

© 2024 The Author(s). Advanced Healthcare Materials published by Wiley-VCH GmbH

21922659, 2025, 11, Downloaded from https://advanced.onlinelibrary.wiley.com/doi/10.1002/adhm.202403799 by ESPCI ParisTech, Wiley Online Library on [30/09/2025]. See the Terms and Conditions (https://onlinelibrary.wiley.com/terms-and-conditions) on Wiley Online Library for rules of use; OA articles are governed by the applicable Creative Commons License

Table 1. Calibration of AuNS with temperature. Experimental structural parameters, such as coordination number (*N*), average Au–Au bond length (*R*), and the EXAFS Debye–Waller factor (σ^2)) derived from the EXAFS data of the AuNS under different temperatures (K) using a cryostat.

Cryostat temperature (K)	N	R [Å)]	σ^2[Å^2)]
100	10.3 (5)	2.86 (1)	0.0025 (2)
170	10.3 (5)	2.86 (1)	0.0044 (2)
240	10.3 (5)	2.86 (1)	0.0058 (2)
300	10.3 (5)	2.86 (1)	0.0076 (2)
325	10.3 (5)	2.86 (1)	0.0086 (2)
350	10.3 (5)	2.85 (1)	0.0093 (3)

k^2-weighted EXAFS spectra were fitted using theoretical phase and amplitude generated by the FEFF8.1 program[61] and analysis calculations were performed employing Artemis software.[62] The Au–Au nearest-neighbor coordination numbers for AuNS (N = 10.3) are lower than the expected for bulk fcc Au, due to the high surface-to-volume ratio. Analyzing the FT data across various temperatures enabled the determination of σ^2 and facilitated a linear calibration of the temperature-dependent structural parameters for Au atoms (refer to **Table 1**).

For comparison, Figure S2 (Supporting Information) shows that XANES and EXAFS measurements of AuNS synthesized at 300 K confirm the structural presence of fcc Au.

The DW factor calibration with temperature can effectively monitor variations in AuNS temperatures. Subsequently, AuNS in spheroids were subjected to 808 nm laser excitation (with powers ranging from 0.05 to 0.6 W), and identical measurements were conducted to assess the local temperature rise due to photoexcited hyperthermia. Additionally, an infrared thermal camera, positioned in the same setup as used for EXAFS measurements, monitored the macroscopic heating of AuNS in cells over time and with varying laser power. EXAFS spectra and extracted FT were obtained for each laser power as seen in Figure 2D,E. EXAFS fitting parameters and σ^2 values (**Table 2**) were obtained to derive local temperatures based on Au–Au first shell σ^2 values (Figure 2F) from a linear fitting equation (equation S1). Local temperatures ranged from 302 to 435 K under laser powers of 0.05 W to 0.6 W, corresponding to temperature increases (ΔT_{LOCAL}) from 8 to 141 °C (Table 2). Global temperature (ΔT_{GLOBAL}) acquired curves as a function of irradiation time are depicted in Figure S3 (Supporting Information). A comparison of ΔT_{LOCAL} and ΔT_{GLOBAL}, along with the temperature increase in control cells, is depicted in Figure 2G, indicating local thermal increments of 2–3 fold. Thermographic images of global increments are shown in Figure 2H.

Table 2. Experimental structural parameters, such as coordination number (*N*), average Au–Au bond length (*R*), and the EXAFS Debye–Waller factor (σ^2)) derived from the EXAFS data of the AuNS under laser illumination and the obtained local temperatures (T_{LOCAL} (K) and ΔT_{LOCAL} (°C)).

Laser power (mW)	Shell	N	R (Å)	σ^2[Å^2)]	T_{LOCAL} [K]	ΔT_{LOCAL} [°C]
50	Au-Au	10.3 (3)	2.86 (1)	0.0078 (2)	302 (3)	8 (3)
150	Au-Au	10.3 (3)	2.86 (1)	0.0081 (2)	312 (3)	18 (3)
300	Au-Au	10.3 (3)	2.85 (1)	0.0097 (3)	370 (3)	76 (3)
600	Au-Au	10.3 (3)	2.84 (1)	0.0114 (5)	435 (5)	141 (5)

2.3. Localization of Cancer Cell Damage Following Photothermal Treatment using Gold Nanostars in a Tumor Spheroid Model

The 3D multicellular spheroid stands out as a valuable tool for nanotoxicity evaluation and serves as a good model to monitor thermal damage at the cellular level following photothermal treatment in hyperthermic cell-based assays. The same AuNS-labeled spheroids were exposed to various photothermal doses, and 2 h after the treatment live/dead assay was performed and imaged with confocal microscopy, depicting live (green-colored) and dead (red-colored) cells as shown in **Figure 3A**. Observations of heat-induced cell death analysis have shown that increasing thermal doses result in the destabilization (starting from 150 mW, ΔT_{LOCAL} = 18.5 °C) and disintegration of the spheroid, leaving few to no surviving cells at doses ranging from 300 to 600 mW (ΔT_{LOCAL} above 75 °C). The metabolic activity in cell aggregates was assessed using a colorimetric assay with the Alamar Blue reagent (Figure 3B). A clear change in the overall metabolic health and viability of the cell aggregates was detected under 150 mW laser irradiation, with almost no metabolic activity observed at higher laser power doses. This result is in agreement with the percentage of live cells quantified from Figure 3A (see Figure S4, Supporting Information).

To further investigate the impact of local nanoparticle hyperthermia at a finer level of cell structure, spheroids subjected to variable doses of laser power were also fixed following the treatment for subsequent immunostaining. Namely, the changes induced with cell cytoskeleton as well as cell-cell junctions were traced via F-actin and E-cadherin staining, respectively (Figure 3C). As such, F-actin staining revealed that for higher doses of laser power (150 – 300 mW) the hyperthermal treatment induced progressive cytoskeleton damage with little-to-no observable F-actin at the highest laser power of 300 mW. This may be an indicator of cytoskeleton collapse events that, in turn, have been shown to be associated with inhibited cell migration and vast impairing of other cellular functions.[57,63,64] Such an outcome may be beneficial for therapeutic applications in the context of cancer metastasis. On the other hand, we observed an increase in E-cadherin protein fluorescence at 150 and 300 mW laser dosages as compared to the lower laser power, 50 mW, and untreated control. This not only demonstrates that cancer cells did not lose their cell-cell junctions and acquiring a more metastatic phenotype but also suggests a potential stimulation in intercellular adhesions via local hyperthermal treatment. Tumor spheroid cells were also monitored using TEM imaging to investigate potential photothermal-induced AuNS degradation within cells under different thermal doses (Figure 3D). Surprisingly, nanostars were successfully visualized as intact and internalized within cells in spheroids even post higher laser exposure dose (see Figure S5, Supporting Information). This indicates the absence of detrimental impact of photothermal irradiation on either the morphology or integrity of AuNS inside cancer cells, even at 300 mW where nanoparticle spikes are still preserved.

© 2024 The Author(s). Advanced Healthcare Materials published by Wiley-VCH GmbH

21922659, 2025, 11, Downloaded from https://advanced.onlinelibrary.wiley.com/doi/10.1002/adhm.202403799 by ESPCI ParisTech, Wiley Online Library on [30/09/2025]. See the Terms and Conditions (https://onlinelibrary.wiley.com/terms-and-conditions) on Wiley Online Library for rules of use; OA articles are governed by the applicable Creative Commons License

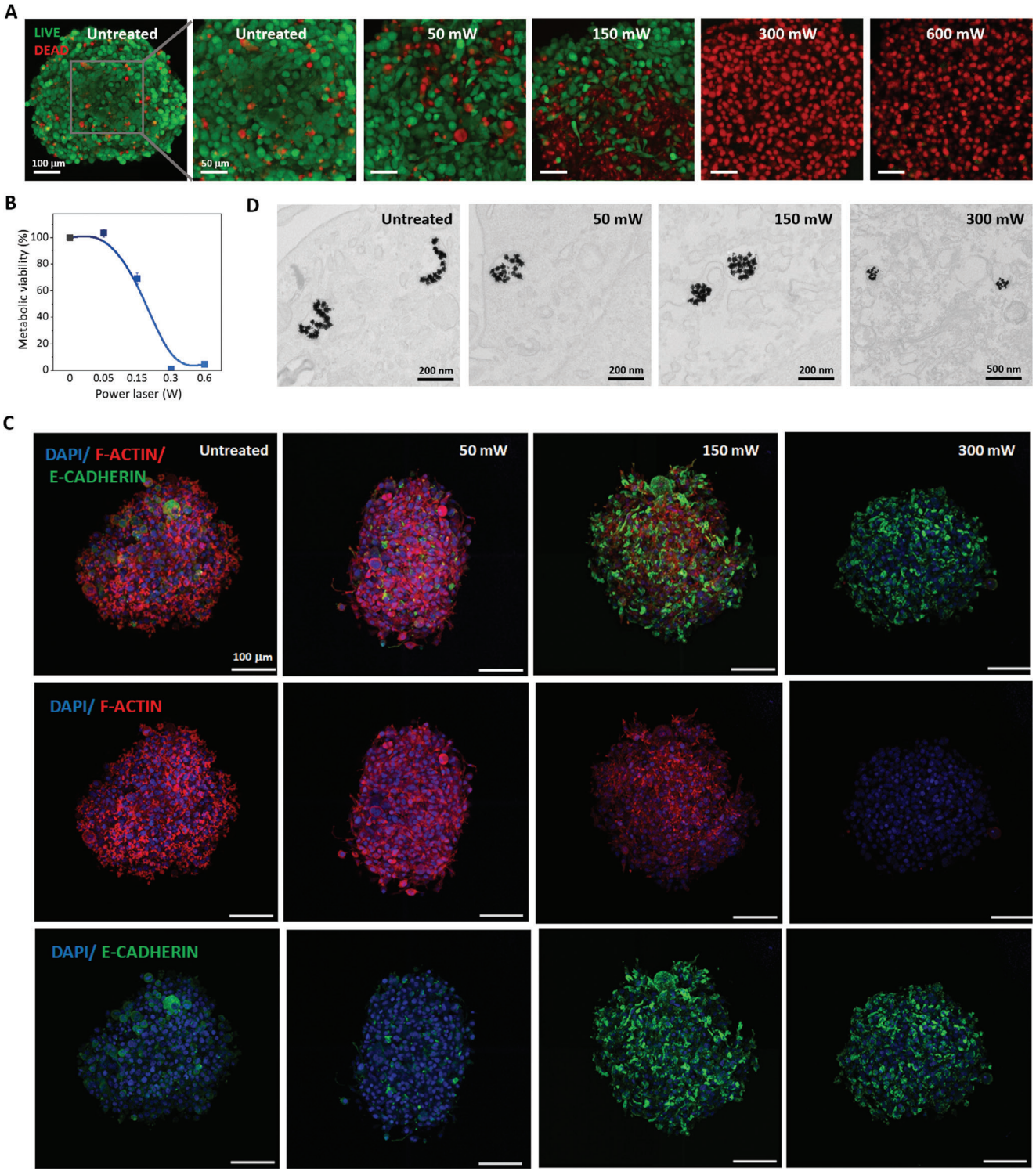


Figure 3. Microscale thermal characterization of spheroids under photothermal effects with microscopy techniques. A) Confocal fluorescence imaging of 3D spheroids labeled with AuNS treated at different photothermal doses (0.05–0.6 W) and stained with Live/Dead solution. B) Metabolic activity in cell spheroids was determined using a colorimetric assay (Alamar Blue). C) 3D rescontructed confocal images of a single spheroid with AuNS stained with F-actin (cytoskeleton, red), E-cadherin (cell juntions, green) and DAPI (nucleus, blue). D) TEM imaging analysis of AuNS internalization inside cells localized in endosomes after photothermal treatments.

© 2024 The Author(s). Advanced Healthcare Materials published by Wiley-VCH GmbH

21922659, 2025, 11, Downloaded from https://advanced.onlinelibrary.wiley.com/doi/10.1002/adhm.202403799 by ESPCI ParisTech, Wiley Online Library on [30/09/2025]. See the Terms and Conditions (https://onlinelibrary.wiley.com/terms-and-conditions) on Wiley Online Library for rules of use; OA articles are governed by the applicable Creative Commons License

3. Discussion

This study successfully demonstrates the integration of high photothermally efficient AuNS into a 3D tumor spheroid model derived from U87 glioblastoma cells. AuNS preserved their crystalline structure, as evidenced by TEM images and XRD, even after cellular uptake, indicating their stability within the biological environment. High cancer spheroid cell viability, cytoskeleton stability, and overall adherent junction integrity, demonstrated via live/dead assays as well as E-cadherin and F-actin protein expression, establish a robust control framework for further photothermal irradiation studies. Similar results in the presence of AuNS within tumor spheroids further underscore their non-toxic nature in 3D cultures—a crucial consideration for potential therapeutic application.

The study explores the potential of state-of-the-art AuNS as both photothermal agents and nanothermometric probes using intracellular XAS. By employing EXAFS analysis, the study demonstrates the ability to monitor local temperature variations at the nanoscale within the tumor spheroid environment during photothermal treatments. Calibrating the Debye-Waller factor (DW) with temperature allows for precise determination of local temperatures, with increases ranging from 13 to 28% in the 300 to 350 K range. The linear response of DW to these temperatures underscores its effectiveness in detecting photoinduced heating in AuNS. The analysis reveals parameter differences in σ^2 up to 25 – 47% under exposure at the highest laser powers. The temperature-dependent EXAFS data provide valuable insights into the thermal behavior of AuNS under various laser powers, offering a detailed framework for assessing photothermal effects in a controlled and quantifiable manner. Moreover, this nanothermometric technique proves reliable and robust in the cellular environment: EXAFS remains stable regardless of concentration and is resilient to changes in pH and viscosity.

As previously observed, gold-based nanomaterials under photoexcitation generate thermal gradients around them.[48] When these nanoparticles are embedded in the cellular matrix, heating is notably amplified, resulting in local temperatures that are significantly higher than global temperature measurements.[49] Specifically, under laser exposure, the local temperatures generated by AuNS in cells are ≈2 to 3 times higher than those recorded macroscopically. This finding aligns with previous experimental and theoretical studies on nanoparticles subjected to magneto- or photo-thermal heating modalities in solution.[44,45,65–68] It is important to note that compared to similar spiky gold-based nanomaterials combined with iron oxide as a hybrid, the thermal gradient is less pronounced in AuNS alone in cells. The iron oxide in hybrid systems acts as a thermal reservoir, moderating the dissipation of the heat generated by the plasmonic gold nanoparticles. While iron oxide (in the form of magnetite) also absorbs NIR light and emits heat, it does so less effectively than the heat produced by the LSPR of Au nanoparticles.[13,14] Various studies have documented large thermal gradients using different nanosystems, highlighting significant temperature variations within small volumes.

The integration of AuNS into the 3D spheroid model also facilitates the in-depth evaluation of photothermal-induced damage at the cellular and subcellular levels and enables correlation with the obtained nanoscale temperature results. Confocal fluorescence imaging and metabolic activity assays reveal a clear correlation between laser power and cell viability, with higher powers leading to an increased cell death and spheroid disintegration. Importantly, the structural integrity of AuNS is maintained even after photothermal treatment, as confirmed by TEM analysis, indicating their resilience and suitability for repeated therapeutic cycles. PTT also has shown to induce cell structural changes, namely, in the cell cytoskeleton (F-actin) and cellular adhesion (E-cadherin) proteins' expression. Adherent junctions and cell cytoskeleton are crucial for tissue integrity and organization preservation with major roles in cell motility, migration, intercellular signaling etc.[58,69] Numerous evidence of these cellular constituents and their functions being involved in cancer cell metastasis has already been brought to attention.[70,72] Nanomaterials-based strategies have been gaining interest over the past years as active actin inhibitors to impede cell migration, with several approaches including nanoparticle-coupled hyperthermal treatments.[73–75] Liu et al. have shown one of the latest achievements via blocking the cancer cell migration through actin cytoskeleton-linked protein targeting with the combination of gold nanorods with mild PTT.[57] Our findings correlate the extent of the thermal gradient generated in the vicinity of nanoparticles with its propagation at different scales, depending on photothermal excitation conditions, and with subtle changes in actin filament organization and cadherin-mediated adhesion. These changes suggest a promising impact on tumorigenesis by disrupting actin filament networks while preserving crucial cell-cell adhesions. In this work, we have demonstrated the potential effects of AuNS-targeted PTT on the cell cytoskeleton and intercellular junctions. When combined with highly precise local measurements of photothermal treatment effect propagation, this approach will allow us to further study the modulation of nanoparticle photothermia response in cancer cells at the subcellular level and its implications for therapeutic applications. Among the various parameters that can be monitored to evaluate cell integrity and the cytoskeleton, we have selected the most representative and fluorescently brilliant indicators.

4. Conclusion

This study offers a thorough evaluation of AuNS as both photothermal agents and nanothermometric probes using XAS. The linear relationship observed between the Debye-Waller factor and temperature demonstrated the sensitivity of AuNS in detecting photoinduced heating, with temperature measurement uncertainties ≈ 3–5°C, and revealed significant photothermal gradients within the cellular environment. Indeed, the local temperatures measured at the nanoscale around AuNS were higher than global temperature measurements, highlighting substantial thermal gradients. Besides, compared to hybrid nanomaterials, AuNS exhibit a relatively lower thermal gradient, suggesting more controlled and localized heating effects. Importantly, the study confirms that AuNS remain intact within cells, with no apparent thermal degradation, making them reliable for prolonged use in therapeutic applications. The research highlights their dual role as effective photothermal agents and precise temperature sensors in controlled cancer treatment applications.

This work also establishes a clear connection between nanothermally induced effects and cellular damage. It demonstrates

© 2024 The Author(s). Advanced Healthcare Materials published by Wiley-VCH GmbH

21922659, 2025, 11, Downloaded from https://advanced.onlinelibrary.wiley.com/doi/10.1002/adhm.202403799 by ESPCI ParisTech, Wiley Online Library on [30/09/2025]. See the Terms and Conditions (https://onlinelibrary.wiley.com/terms-and-conditions) on Wiley Online Library for rules of use; OA articles are governed by the applicable Creative Commons License

how varying irradiation doses influence overall cell-cell interactions, cellular structure, and integrity at the cellular scale. Higher laser powers were found to increase cell death and spheroid breakdown, reflecting the thermal effects around the nanoparticles, while lower hyperthermia conditions enhanced cellular response.

Overall, this study represents the pioneering detailed investigation into the multiscale thermal effects of AuNS, examining their nanospatial extent around activated heating sources in tumor tissues and their impact on cellular structure and viability. By elucidating the interplay between nanoscale heating and cellular responses, this study contributes to the broader field of nanomedicine and holds promise for developing innovative strategies in targeted cancer therapies.

5. Experimental Section

Gold Nanostar Synthesis: Gold nanostars were synthesized by a seed-mediated-growth method. Initial gold seeds of ≈14 nm were synthesized by a modified Turkevith method: 95 mL of 0.5 mM $HAuCl_4$ in ultrapure water was heated and brought to boil. Then, 5 mL of 1 wt. % of sodium citrate tribasic dihydrate was quickly added under strong stirring and left to react for 15 min. After that, the sample was cooled down and stored in the fridge until further use.

The seed solution was taken from the fridge and left stirring until it reached room temperature. The Au concentration of the seeds solution was measured in a UV–vis spectrometer using an extinction coefficient of 2.4 mM^{-1} cm^{-1} at a wavelength of 400 nm. A solution of PVP (MW 10 Kg mol^{-1}) was prepared at 1 mg mL^{-1} in ultrapure water. The amount of PVP added to the solution was calculated to be 60 molecules per nm^2 of nanoparticle surface. The PVP solution was added dropwise to the nanoparticle solution under mild stirring. The solution was left stirring for 1 h, and then centrifuged and redispersed in water two times. The final concentration was measured by UV–V is spectrophotometry.

For the synthesis of nanostars, 75 g of PVP (MW 10 Kg mol^{-1}) was dissolved in 1.5 L of DMF in an Erlenmeyer flask. Once dissolved, 8.19 mL of $HAuCl_4$ 50 mM in water was added and left to pre-reduce until all gold passed to Au^+, in this case during 5 min.[28] The seed solution (11.3 10^{-3} mmols of Au) was then quickly added and left for reaction for 2 h. The solution was centrifuged and the supernatant was discarded. The solution was further purified by centrifugation 3 times in ethanol and finally resuspended in ultrapure water.

Cell Culture, Nanoparticle Incubation, and Spheroid Formation: U87 human glioblastoma cells were cultivated in Dulbecco's Modified Eagle Medium (DMEM) supplemented with 10% fetal bovine serum and 1% penicillin-streptomycin at 37 °C in an incubator with 5% CO_2. When they reached high confluence, the cells were cultured in a supplemented DMEM medium for 24 h with varying concentrations of nanoparticle suspensions in T75 flasks. The concentrations of Au in the extracellular medium was [Au] = 200 × 10^{-6} M. Following nanoparticle incubation, the cells were washed and detached to form the spheroids. The cells were then counted and divided into suspensions of 200 000 to 300 000 cells in 1.5 mL-Eppendorf tubes. The suspensions were subjected to centrifugation at 1,000 rpm for 5 min, resulting in the formation of cell pellets. These pellets were incubated at 37 °C with 5% CO_2 for a period of 2 days, allowing spherical aggregates to develop. Following this incubation, the aggregates were immobilized by treatment with a 4% paraformaldehyde (PFA) solution for 30 min, followed by three subsequent washes using phosphate-buffered saline (PBS). Finally, the aggregates were stored in PBS for further analysis.

Transmission Electron Microscopy (TEM): TEM micrographs of samples in aqueous dispersions and inside cells were captured using a JEM1400 Flash (Jeol) transmission electron microscope, operated at 120 kV, at the transmission electron microscopy service of CBM-CSIC, Spain. Sections of tumor cells labeled with nanoparticles were also prepared in the same service. Both control and labeled cells underwent washing and fixation with a suspension of 4% paraformaldehyde (PFA) and 2% glutaraldehyde in 0.1 mol L^{-1} sodium cacodylate buffer (pH 7.4) for 2 h. Subsequently, they were gradually dehydrated in ethanol (30% to 100%) and stained with 1% osmium tetroxide containing 1.5% potassium cyanoferrate. The samples were then embedded in epoxy resin, cut with a microtome into sections, and mounted on grids for analysis.

X-Ray Diffraction (XRD): X-ray diffraction data were obtained at the Diffraction Facility of ICMM-CSIC, Madrid, Spain. Samples were placed on a glass slide and submerged in mineral oil. Suitable samples (Au nanoparticles-labeled cells) were selected with a kapton loop from MiTeGen, using a polarized optical microscope. Diffraction data was collected using Cu radiation with a Bruker D8 Venture diffractometer, equipped with three microsources (Cu, Mo, Ag) and a PHOTON III area detector. Data collection was performed with APEX5 software. DIFFRAC EVA software was used to obtain 1D XRD patterns.

Quantitative Elemental Analysis and Intracellular Uptake (ICP-OES): The concentration of Au in both solution and cells was determined using inductively coupled plasma optical emission spectrometry (ICP-OES) at the chemical analysis service of ICMM-CSIC, Spain, with an Optima 2100 DV PerkinElmer instrument. Nanoparticle solutions were prepared by adding 1 mL of aqua regia (a mixture of HNO_3:HCl in a 1:3 ratio) and heating them to 80 °C for 2 h. The sample was diluted in MilliQ water to achieve a final volume of 10 mL. Quantitative analysis of the elements was conducted using standard references for Au.

Optical Absorption Spectroscopy: The absorption spectra were recorded for aqueous suspensions and cells using a Cary 60 UV–Vis-NIR spectrometer (Varian) in the 300–1100 nm spectral range. Preparation of a cell lysate was performed to isolate endosomes from cell nuclei. The cells were suspended in a lysis buffer containing 250 mM sucrose and 3 mM imidazole. To enhance the release of labeled endosomes, mechanical disruption was induced using a needle syringe.

Photothermal Excitation Measurements: To assess temperature profiles, the labeled aggregates (3-4) were subjected to an 808 nm laser with a maximum power output of 1 W (Roithner Lasertechnik GmbH, Austria). The laser intensity was adjusted to 0.05, 0.15, 0.3, and 0.6 W. Measurements were taken after 10–15 min of irradiation, once the temperature stabilized, using an infrared thermal camera (FLIR, USA) to monitor the thermal increase.

Synchrotron hard X-Ray Absorption Spectroscopy (XAS): XAS spectra were recorded in fluorescence mode at the SAMBA beamline (SOLEIL synchrotron, France) using a multi-element high purity Germanium detector (HPGe, Mirion). Samples with AuNS were measured in multicellular aggregates (3-4) and deposited on Kapton films mounted on standard supports in a motorized stage. Spectra were acquired at the Au L_3-edge (11919 eV) across XANES and EXAFS regions. A liquid helium-nitrogen cryostat with vacuum/He-gas insulation enabled measurements from 100 to 350 K for calibration. An Au metallic foil was measured at every condition for energy calibration. Data were processed with Athena software, included in the Demeter system, for polynomial pre- and post-edge background subtraction. EXAFS fits were performed on the k^2-weighted signal Fourier-transformed in the 2.5–11.5 $Å^{-1}$ range, obtaining the radial distribution ≈ 1.0–5.0 Å from absorbing atoms (Au). Analysis calculations were conducted using Artemis software.[62]

Viability Assays of Cells and of Photoirradiated Spheroids: U87 cells were cultured in 24-well plates for 24 h with increasing concentrations of gold nanostars (ranging from 12.5 to 100 μg mL^{-1}) in a complete DMEM culture medium. Cell viability was assessed by a colorimetric method based on a resazurin solution assay. A 10% resazurin solution was added to the DMEM medium without red phenol and incubated for 2–3 h, then transferred to a 96-well plate. Fluorescence was analyzed by a microplate reader (excitation 570 nm, emission 585 nm, Bio-Tek instruments, Inc). Viability was normalized with unlabeled control cells.

The thermal damage effect after applying the photothermal treatments was evaluated in labeled spheroids subjected to different 808 nm power densities of laser. The spheroids were then immersed in a 10% Alamar Blue solution in DMEM without red phenol, incubated for 2 h. Metabolic activity was obtained by fluorescence analysis of the transferred solution

© 2024 The Author(s). Advanced Healthcare Materials published by Wiley-VCH GmbH

21922659, 2025, 11, Downloaded from https://advanced.onlinelibrary.wiley.com/doi/10.1002/adhm.202403799 by ESPCI ParisTech, Wiley Online Library on [30/09/2025]. See the Terms and Conditions (https://onlinelibrary.wiley.com/terms-and-conditions) on Wiley Online Library for rules of use; OA articles are governed by the applicable Creative Commons License

in a microplate reader. All reported experimental results were performed in triplicate. A thermostated device was used to ensure physiological temperature conditions (37 °C).

Alternatively, the cell survival was assessed with live/dead assay (LIVE/DEAD^{TM} Cell Imaging Kit Invitrogen R37601). The solution was prepared according to manufacturer's guidelines and the spheroids were incubated with it for 25 min at 37 °C, 5% CO_2. Confocal microscopy (Leica DMi8) was performed with × 25 magnification lens in water-immersion mode. The resulting images were obtained as 3D images (z-stacks, step size 2.0 µm, image size 1024 × 1024, resolution 2.2 pixels per micron) with two channels: Calcein Green & Texas Red, identifying live and dead signal respectively.

Immunofluorescence Staining of Photothermal Irradiated Spheroids: Following the laser exposure, spheroids were fixed with 4% paraformaldehyde for 1 h at room temperature, followed by three washes with PBS. They were then permeabilized with 0.1% Triton X-100 in PBS for 15 min at room temperature followed by blocking in a 2% bovine serum albumin (BSA), 0/1% Triton X-100 solution in PBS for 3 h at ambient temperature. Spheroids were then incubated with anti-E-cadherin primary antibody solution (Invitrogen SHE78-7) at 1:400 dilution in blocking solution overnight at room temperature. The next day, the samples were thoroughly rinsed 3x times with PBS and incubated with Alexa Fluor 488-conjugated goat anti-mouse IgG (H+L) highly cross-adsorbed secondary antibody, (ThermoFisher A11029) at 1:400 in blocking solution overnight at room temperature. Finally, following 3x washings with PBS, spheroids were incubated in a 300 nM DAPI solution (D3571, Invitrogen) at a 1:500 dilution with Alexa Fluor 555 Phalloidin (Thermofisher A34055) at 1:1000 in blocking solution at room temperature overnight. Lastly, spheroids were rinsed with PBS 3x times before acquiring images. Imaging was performed in z-stack sections with Leica DMi8 inverted confocal microscope (Leica Microsystems) using a 40x water immersion objective with voxel size of $0.2841 \times 0.2841 \times 0.7\ \mu m^3$.

Supporting Information

Supporting Information is available from the Wiley Online Library or from the author.

Acknowledgements

This work was funded by MCIN/AEI/10.13039/501100011033 (PID2021-127033OB-C21 (A. E.), PID2021-126323OA-I00 (A. M-N), PID2022-139467OB-I00 (J. R.), PID2020-114192RB-C41 (M. A. G.)), MCIU/AEI/10.13039/501100011033 and the European Union NextGenerationEU/PRTR (CNS2023-144689 (A. E.), CNS2023-144128 (A.M-N.), CNS2023-144447 (J. R.)), the European Union (ERC-2019-CoG project NanoBioMade 865629 (C. W.)), CSIC (PIE-20226AT024 (A. E.)) and Programa de Ayudas I+ D en Biomedicina de la Comunidad de Madrid (ASAP-CM S2022/BMD-7434). IMDEA Nanociencia acknowledges support from the Severo Ochoa program for Centers of Excellence in R&D (CEX2020-001039-S) and FPI grant PRE2020-96246 (R. L-M.). The authors thank Milagros Guerra for TEM sample preparation at the Electron Microscopy Service of the Centro de Biología Molecular Severo Ochoa (CBM, CSIC-UAM, Spain), the technical staff at ICMM-CSIC for ICP-OES measurements, and the Histology Facility at CNB-CSIC (Spain) for histological preparation of biological samples. The authors also thank the SAMBA beamline staff at SOLEIL Synchrotron (France) for their support during experiments. Finally, the authors acknowledge the Conexión Nanomedicina network from CSIC, Spain.

Conflict of Interest

The authors declare no conflict of interest.

Data Availability Statement

The data that support the findings of this study are available from the corresponding author upon reasonable request.

Keywords

Nanomedicine, Nanothermal therapy, Nanothermometry, Photothermia, Plasmonic nanoparticles, X-ray absorption spectroscopy

Received: October 3, 2024
Revised: November 8, 2024
Published online: December 11, 2024

[1] X. Huang, P. K. Jain, I. H. El-Sayed, M. A. El-Sayed, *Las. Med. Sci.* **2008**, *23*, 217.
[2] D. Jaque, L. M. Maestro, B. Del Rosal, P. Haro-Gonzalez, A. Benayas, J. Plaza, E. M. Rodriguez, J. G. Sole, *Nanoscale* **2014**, *6*, 9494.
[3] P. K. Jain, X. Huang, I. H. El-Sayed, M. A. El-Sayed, *Acc. Chem. Res.* **2008**, *41*, 1578.
[4] M. Rai, A. P. Ingle, S. Birla, A. Yadav, C. A. D. Santos, *Crit. Rev. Microbiol.* **2016**, *42*, 696.
[5] A. Espinosa, A. Curcio, S. Cabana, G. Radtke, M. Bugnet, J. Kolosnjaj-Tabi, C. Péchoux, C. Alvarez-Lorenzo, G. A. Botton, A. Silva, *ACS Nano* **2018**, *12*, 6523.
[6] B. Han, Y. L. Zhang, Q. D. Chen, H. B. Sun, *Adv. Funct. Mater.* **2018**, *28*, 1802235.
[7] L. Đorđević, F. Arcudi, M. Cacioppo, M. Prato, *Nat. Nanotechnol.* **2022**, *17*, 112.
[8] I. Marangon, C. Ménard-Moyon, A. K. Silva, A. Bianco, N. Luciani, F. Gazeau, *Carbon* **2016**, *97*, 110.
[9] M. P. Romero, H. H. Buzza, M. D. Stringasci, B. M. Estevão, C. C. Silva, M. A. Pereira-da-Silva, N. M. Inada, V. S. Bagnato, *Int. J. Nanomed.* **2021**, 1601.
[10] Y. Shen, H. D. Santos, E. C. Ximendes, J. Lifante, A. Sanz-Portilla, L. Monge, N. Fernandez, I. Chaves-Coira, C. Jacinto, C. D. Brites, L. D. Carlos, A. Benayas, M. Carmen Iglesias-de la Cruz, D. Jaque, *Adv. Funct. Mater.* **2020**, *30*, 2002730.
[11] R. Marin, A. Skripka, L. V. Besteiro, A. Benayas, Z. Wang, A. O. Govorov, P. Canton, F. Vetrone, *Small* **2018**, *14*, 1803282.
[12] A. Curcio, A. K. Silva, S. Cabana, A. Espinosa, B. Baptiste, N. Menguy, C. Wilhelm, A. Abou-Hassan, *Theranostics* **2019**, *9*, 1288.
[13] A. Espinosa, R. Di Corato, J. Kolosnjaj-Tabi, P. Flaud, T. Pellegrino, C. Wilhelm, *ACS Nano* **2016**, *10*, 2436.
[14] A. Espinosa, J. Kolosnjaj-Tabi, A. Abou-Hassan, A. Plan Sangnier, A. Curcio, A. K. Silva, R. Di Corato, S. Neveu, T. Pellegrino, L. M. Liz-Marzán, *Adv. Funct. Mater.* **2018**, *28*, 1803660.
[15] D. Xu, Z. Li, L. Li, J. Wang, *Adv. Funct. Mater.* **2020**, *30*, 2000712.
[16] R. Bardhan, S. Lal, A. Joshi, N. J. Halas, *Acc. Chem. Res.* **2011**, *44*, 936.
[17] J. Hu, F. Sanz-Rodríguez, F. Rivero, E. M. Rodríguez, R. A. Torres, D. H. Ortgies, J. G. Solé, F. Alfonso, D. Jaque, *Nano Res.* **2017**, *11*, 676.
[18] X. Huang, I. H. El-Sayed, W. Qian, M. A. El-Sayed, *J. Am. Chem. Soc.* **2006**, *128*, 2115.
[19] R. n. Ahijado-Guzmán, G. González-Rubio, J. s. G. Izquierdo, L. Bañares, I. n. López-Montero, A. Calzado-Martín, M. Calleja, G. Tardajos, A. s. Guerrero-Martínez, *ACS Omega* **2016**, *1*, 388.
[20] J. Chen, C. Glaus, R. Laforest, Q. Zhang, M. Yang, M. Gidding, M. J. Welch, Y. Xia, *Small* **2010**, *6*, 811.
[21] W. Lu, C. Xiong, G. Zhang, Q. Huang, R. Zhang, J. Z. Zhang, C. Li, *Clin. Cancer Res.* **2009**, *15*, 876.

© 2024 The Author(s). Advanced Healthcare Materials published by Wiley-VCH GmbH

21922659, 2025, 11, Downloaded from https://advanced.onlinelibrary.wiley.com/doi/10.1002/adhm.202403799 by ESPCI ParisTech, Wiley Online Library on [30/09/2025]. See the Terms and Conditions (https://onlinelibrary.wiley.com/terms-and-conditions) on Wiley Online Library for rules of use; OA articles are governed by the applicable Creative Commons License

[22] A. M. Goodman, Y. Cao, C. Urban, O. Neumann, C. Ayala-Orozco, M. W. Knight, A. Joshi, P. Nordlander, N. J. Halas, *ACS Nano* **2014**, *8*, 3222.
[23] S. K. Dondapati, T. K. Sau, C. Hrelescu, T. A. Klar, F. D. Stefani, J. Feldmann, *ACS Nano* **2010**, *4*, 6318.
[24] H. Yuan, C. G. Khoury, C. M. Wilson, G. A. Grant, A. J. Bennett, T. Vo-Dinh, *Nanomed.: Nanotechnol., Biol. Med.* **2012**, *8*, 1355.
[25] F. Tian, J. Conde, C. Bao, Y. Chen, J. Curtin, D. Cui, *Biomaterials* **2016**, *106*, 87.
[26] L. Rodríguez-Lorenzo, R. de La Rica, R. A. Álvarez-Puebla, L. M. Liz-Marzán, M. M. Stevens, *Nat. Mater.* **2012**, *11*, 604.
[27] A. Espinosa, A. K. Silva, A. Sánchez-Iglesias, M. Grzelczak, C. Péchoux, K. Desboeufs, L. M. Liz-Marzán, C. Wilhelm, *Adv. Healthcare Mater.* **2016**, *5*, 1040.
[28] S. Barbosa, A. Agrawal, L. Rodríguez-Lorenzo, I. Pastoriza-Santos, R. A. Alvarez-Puebla, A. Kornowski, H. Weller, L. M. Liz-Marzán, *Langmuir* **2010**, *26*, 14943.
[29] H. Chatterjee, D. S. Rahman, M. Sengupta, S. K. Ghosh, *J. Phys. Chem. C* **2018**, *122*, 13082.
[30] H. Wang, X. Liu, X. Li, W. Lu, L. Jiang, *ChemistrySelect* **2016**, *1*, 659.
[31] K. Chandra, K. S. Culver, S. E. Werner, R. C. Lee, T. W. Odom, *Chem. Mater.* **2016**, *28*, 6763.
[32] H. Tan, N. Hou, Y. Liu, B. Liu, W. Cao, D. Zheng, W. Li, Y. Liu, B. Xu, Z. Wang, *Nanomed.: Nanotechnol., Biol. Med.* **2020**, *27*, 102192.
[33] D. Wu, P. Zhao, L. Wu, L. Lin, G. Yu, L. Xu, J. Yue, *ACS Appl. Bio Mater.* **2020**, *3*, 4590.
[34] D. Miao, Y. Yu, Y. Chen, Y. Liu, G. Su, *Mol. Pharmaceutics* **2020**, *17*, 1127.
[35] S. Wang, P. Huang, L. Nie, R. Xing, D. Liu, Z. Wang, J. Lin, S. Chen, G. Niu, G. Lu, *Adv. Mater.* **2013**, *25*, 3055.
[36] L. Zhang, X.-Q. Yang, J.-S. Wei, X. Li, H. Wang, Y.-D. Zhao, *Theranostics* **2019**, *9*, 5424.
[37] Z. Li, F. Yang, D. Wu, Y. Liu, Y. Gao, H. Lian, H. Zhang, Z. Yin, A. Wu, L. Zeng, *Nanoscale* **2020**, *12*, 22173.
[38] M. P. Ogáyar, R. López-Méndez, I. Figueruelo-Campanero, T. Muñoz-Ortiz, C. Wilhelm, D. Jaque, A. Espinosa, A. Serrano, *Nanoscale Adv.* **2024**, *6*, 4635.
[39] D. Jaque, F. Vetrone, L. nanothermometry, *Nanoscale* **2012**, *4*, 4301.
[40] J. G. Ovejero, I. Armenia, D. Serantes, S. Veintemillas-Verdaguer, N. Zeballos, F. López-Gallego, C. Grüttner, J. M. de la Fuente, M. a. d. Puerto Morales, V. Grazu, *Nano Lett.* **2021**, *21*, 7213.
[41] D. Ruiz, B. del Rosal, M. Acebrón, C. Palencia, C. Sun, J. Cabanillas-González, M. López-Haro, A. B. Hungría, D. Jaque, B. H. Juarez, *Adv. Funct. Mater.* **2017**, *27*, 1604629.
[42] P. Haro-González, L. Martínez-Maestro, I. Martín, J. García-Solé, D. Jaque, *Small* **2012**, *8*, 2652.
[43] P. Neumann, I. Jakobi, F. Dolde, C. Burk, R. Reuter, G. Waldherr, J. Honert, T. Wolf, A. Brunner, J. H. Shim, *Nano Lett.* **2013**, *13*, 2738.
[44] A. Riedinger, P. Guardia, A. Curcio, M. A. Garcia, R. Cingolani, L. Manna, T. Pellegrino, *Nano Lett.* **2013**, *13*, 2399.
[45] J. T. Dias, M. Moros, P. del Pino, S. Rivera, V. Grazú, J. M. de la Fuente, *Angew. Chem., Int. Ed.* **2013**, *52*, 11526.
[46] Y. Zhang, J. Yu, D. J. Birch, Y. Chen, *J. Biomed. Opt.* **2010**, *15*, 020504.
[47] B. Van de Broek, D. Grandjean, J. Trekker, J. Ye, K. Verstreken, G. Maes, G. Borghs, S. Nikitenko, L. Lagae, C. Bartic, *Small* **2011**, *7*, 2498.
[48] A. Espinosa, G. R. Castro, J. Reguera, C. Castellano, J. Castillo, J. Camarero, C. Wilhelm, M. A. García, A. l. Muñoz-Noval, *Nano Lett.* **2021**, *21*, 769.
[49] R. López-Méndez, J. Reguera, A. Fromain, E. S. Abu Serea, E. Céspedes, F. Terán, F. Zheng, A. Parente, M. Á. García, E. Fonda, C. Wilhelm, J. Camarero, A. l. Muñoz-Noval, A. Espinosa, *Adv. Health. Mater.* **2023**, *12*, 2301863.
[50] R. Gupta, D. Sharma, *Nanoscale Adv.* **2021**, *3*, 3663.
[51] K. M. Yamada, E. Cukierman, *Cell* **2007**, *130*, 601.
[52] S. C. Brüningk, I. Rivens, C. Box, U. Oelfke, G. Ter Haar, *Sci. Rep.* **2020**, *10*, 1653.
[53] L. Beola, L. Asín, R. M. Fratila, V. Herrero, J. M. De La Fuente, V. Grazú, L. Gutiérrez, *ACS Appl. Mater. Inter.* **2018**, *10*, 44301.
[54] M. Quintanilla, I. García, I. de Lázaro, R. García-Alvarez, M. Henriksen-Lacey, S. Vranic, K. Kostarelos, L. M. Liz-Marzán, *Theranostics* **2019**, *9*, 7298.
[55] A. Fromain, J. E. Perez, A. Van de Walle, Y. Lalatonne, C. Wilhelm, *Nat. Commun.* **2023**, *14*, 4637.
[56] M. Nabil, P. Decuzzi, P. Zunino, *R. Soc. Open Sci.* **2015**, *2*, 150447.
[57] J. Liu, L. Kang, I. Ratnayake, P. Ahrenkiel, S. Smith, C. Wang, *J. Colloid Interface Sci.* **2021**, *601*, 556.
[58] A. C. Daulagala, M. C. Bridges, A. Kourtidis, *Int. J. Mol. Sci.* **2019**, *20*, 2756.
[59] J. E. Perez, I. Nagle, C. Wilhelm, *Biofabrication* **2020**, *13*, 015018.
[60] D. J. Rosen, S. Yang, E. Marino, Z. Jiang, C. B. Murray, *J. Phys. Chem. C* **2022**, *126*, 3623.
[61] J. J. Rehr, R. C. Albers, *Rev. Modern Phys.* **2000**, *72*, 621.
[62] B. Ravel, M. Newville, A. R. T. E. M. I. S. ATHENA, *J. Synchrotron Radiat.* **2005**, *12*, 537.
[63] E. M. Scutigliani, Y. Liang, H. Crezee, R. Kanaar, P. M. Krawczyk, *Cancers* **2021**, *13*, 1243.
[64] T. Zhou, M. Yu, B. Zhang, L. Wang, X. Wu, H. Zhou, Y. Du, J. Hao, Y. Tu, C. Chen, *Adv. Funct. Mater.* **2014**, *24*, 6922.
[65] J. Dong, J. I. Zink, *ACS Nano* **2014**, *8*, 5199.
[66] S. Rohani, M. Quintanilla, S. Tuccio, F. De Angelis, E. Cantelar, A. O. Govorov, L. Razzari, F. Vetrone, *Adv. Opt. Mater.* **2015**, *3*, 1606.
[67] K. Nigoghossian, S. Ouellet, J. Plain, Y. Messaddeq, D. Boudreau, S. J. Ribeiro, *J. Mater. Chem. B* **2017**, *5*, 7109.
[68] M. L. Debasu, D. Ananias, I. Pastoriza-Santos, L. M. Liz-Marzán, J. Rocha, L. D. Carlos, *Adv. Mater.* **2013**, *25*, 4868.
[69] L. M. Machesky, *FEBS Lett.* **2008**, *582*, 2102.
[70] X. Li, J. Wang, *Int. J. Biol. Sci.* **2020**, *16*, 2014.
[71] C. M. Fife, J. A. McCarroll, M. Kavallaris, *Br. J. Pharmacol.* **2014**, *171*, 5507.
[72] J. M. Peng, R. Bera, C. Y. Chiou, M. C. Yu, T. C. Chen, C. W. Chen, T. R. Wang, W. L. Chiang, S. P. Chai, Y. Wei, *Hepatology* **2018**, *67*, 2226.
[73] M. R. Ali, Y. Wu, Y. Tang, H. Xiao, K. Chen, T. Han, N. Fang, R. Wu, M. A. El-Sayed, *Proc. Natl. Acad. Sci. USA* **2017**, *114*, E5655.
[74] Y. Wu, M. R. Ali, B. Dong, T. Han, K. Chen, J. Chen, Y. Tang, N. Fang, F. Wang, M. A. El-Sayed, *ACS Nano* **2018**, *12*, 9279.
[75] X. Ma, R. Hartmann, D. Jimenez de Aberasturi, F. Yang, S. J. Soenen, B. B. Manshian, J. Franz, D. Valdeperez, B. Pelaz, N. Feliu, *ACS nano* **2017**, *11*, 7807.

© 2024 The Author(s). Advanced Healthcare Materials published by Wiley-VCH GmbH

21922659, 2025, 11, Downloaded from https://advanced.onlinelibrary.wiley.com/doi/10.1002/adhm.202403799 by ESPCI ParisTech, Wiley Online Library on [30/09/2025]. See the Terms and Conditions (https://onlinelibrary.wiley.com/terms-and-conditions) on Wiley Online Library for rules of use; OA articles are governed by the applicable Creative Commons License

Résumé

L'adénocarcinome canalaire pancréatique (PDAC) demeure l'une des pathologies cancéreuses les plus létales, avec un taux de survie a cinq ans inferieur a 12%. Cette extrême agressivité repose sur une combinaison unique de facteurs : une hétérogénéité tumorale marquée, une résistance intrinsèque aux thérapies conventionnelles et surtout un microenvironnement tumoral (TME) dense et réactif, dominé par une fibrose massive ou stromal desmoplastique. Ce stroma, riche en fibroblastes actives, en matrice extracellulaire (ECM) et en composes matriciels tels que le collagène et l'acide hyaluronique (HA), ne constitue pas un simple échafaudage structural mais un acteur biologique à part entière du développement tumoral. Il influence profondément la prolifération, la plasticité épithélio-mésenchymateuse (EMT), la migration et la résistance thérapeutique des cellules cancéreuses pancréatiques.

Les modelés précliniques classiques — lignes cellulaire 2D, sphéroïdes, organoïdes ou modèles animaux — peinent à reproduire cette complexité spatio-fonctionnelles. Les modèles organ-on-chip ont émergé comme une approche prometteuse pour combler cette lacune, en permettant la reconstruction contrôlée d'architectures tissulaires tridimensionnelles sous flux et la mesure dynamique de réponses biologiques er thérapeutiques. Toutefois, l'adaptation de ces technologies au PDAC reste un défi majeur, en raison de la rigidité et de l'hétérogénéité de sa matrice, de la coexistence d'états cellulaires multiples (épithéliaux, mésenchymateux, quasi-mésenchymateux) et de la difficulté à maintenir la viabilité et les interactions stroma-tumeur dans des environnements microfluidiques confines.

S'appuyant sur ces constats, cette thèse vise à exploiter le potentiel des plateformes PDAC-on-chip pour à la fois : (i) étudier les interactions complexes entre les cellules tumorales et leur microenvironnement, et (ii) évaluer l'efficacité et les mécanismes d'action de nouvelles stratégies thérapeutiques, en particulier la photothermie induite par des nanoparticules (NP-PTT). L'objectif global est de développer un cadre expérimental progressif — du modèle simplifie au modèle stromalement enrichi — permettant de comprendre les déterminants physico-biologiques de la progression et de la réponse

thérapeutiques du PDAC.

Chapitre 1 – Contexte et enjeux biologiques et technologiques

Le premier chapitre présente une synthèse approfondie de la littérature consacrée a la biologie du PDAC et a son microenvironnement tumoral. Il met en évidence le rôle central du stromal desmoplastique, caractérisé par l'accumulation de collagène, d'acide hyaluronique et de protéines matricielles qui créent une barrière mécanique et chimique a la diffusion des agents thérapeutiques. L'activation des fibroblastes pancréatiques en cellules stellaire activées ou fibroblastes associés au cancer (CAFs) est décrite comme un moteur clé de la fibrose et de l'immunosuppression. Ces cellules secrètent de multiples facteurs paracrines favorisant l'EMT et la résistance au traitement.

Le chapitre expose ensuite les avancées récentes des technologies organ-on-chip, en soulignant leurs avantages pour le PDAC : contrôle spatial précis des gradients, intégration de matrices complexes, compatibilité avec l'imagerie dynamiques et possibilité d'analyses multiparamétriques. Enfin, il introduit la NP-PTT comme stratégie innovante de traitement localisé, exploitant des nanoparticules capables de convertir la lumière en chaleur, induisant une cytotoxicité localisée et une reprogrammation du microenvironnement.

Chapitre 2 – Développement et validation d'un modèle simplifie de PDAC-on-chip pour la NP-PTT

Le deuxième chapitre explore l'intégration de la thérapie photothermique induite par les nanoparticules magnétiques (MagnNP-PTT) dans un modèle simplifie de PDAC-on-chip. Cette approche vise à pallier les limites actuelles des évaluations précliniques de NP-PTT, souvent réalisé dans des modèles 2D ou animaux peu représentatif du microenvironnement pancréatique humain. L'enjeu était double : établir un protocole robuste permettent l'application contrôlée d'un stimulus photothermique sur des sphéroïdes tumoraux humains et analyser, dans un environnement tridimensionnel, la double action de la NP-PTT sur les cellules tumorales et sur la matrice extracellulaire.

Pour cela, un système microfluidique tridimensionnel a été conçu afin de reproduire la croissance sphéroïdale de cellules cancéreuses pancréatiques humaines dans une matrice de collagène I mimant la composition du tissu tumoral. Les nanoparticules de

magnétite utilisées ont été incorporées dans le modèle pour assurer la diffusion autour et a l'intérieure des sphéroïdes. L'irradiation laser a ensuite permis d'induire une élévation thermiques localisée, modulée de manière précise par l'intensité lumineuse et la concentration de nanoparticules.

Les résultats ont démontré la faisabilité technique et la stabilité thermique du système, ainsi que la possibilité de corréler quantitativement la dose énergétique applique à la réponse biologique observée. L'analyse a relevé une cytotoxicité sélective au sein des sphéroïdes exposes a la NP-PTT, tandis que les structures non ciblées restaient intactes. Parallèlement, des modifications structurales de collagène ont été observée, suggérant un effet concomitant sur la matrice extracellulaire : relâchement et altération locale des fibres, contribuant potentiellement a la désorganisation du microenvironnement tumoral.

Ces observations soulignent le double impact de la NP-PTT, agissant a la fois sur les cellules cancéreuses et sur la matrice, et confirment l'intérêt de cette approche dans le contexte du PDAC, ou le stroma constitue une barrière majeure aux thérapies conventionnelles. La plateforme PDAC-on-chip s'est ainsi révélé être un outil puissant pour disséquer ces interactions complexes dans un environnement contrôle, impossible à reproduire dans des modèles 2D ou animaux.

Enfin, la discussion approfondie qui suit le corps de l'article publie dans *ACS Nano* (2025) met en lumière les principaux défis méthodologiques et translationnels rencontrés : la quantification précise de la dose thermique effectivement reçue par les cellules, la diffusion et l'agrégation des nanoparticules, la résolution spatiale des mesures de température, ainsi que la variabilité intrinsèque des structures matricielles. Ces limites ont conduit à identifier plusieurs pistes d'amélioration visant à accroitre la robustesse et la pertinence physiologique du modèle.

Sur le plan structurel, l'association du collagène a d'autres protéines matricielles, l'introduction de stratégies de réticulation contrôlées et l'optimisation de la géométrie de la puce permettraient de réduire la variabilité architecturale et d'améliorer la stabilité mécanique. Sur le plan cellulaire, l'intégration progressive de fibroblastes stromaux, de cellules endothéliales puis immunitaires offrirait une vision plus complète des effets de la NP-PTT sur les différentes populations cellulaires du microenvironnement tumoral. Enfin, le couplage de la plateforme a des outils de suivi avances — tel que la thermométrie locale,

le traçage quantitatif des nanoparticules ou l'imagerie biophysique en temps réel — renforcerait la précision des corrélations entre paramètres physiques et réponses biologiques.

Dans cette optique, le chapitre 2 établit les bases d'un cadre méthodologiques modulaire pour l'évaluation de la NP-PTT dans le PDAC, ouvrant la voie a des approches combinatoires et mécanistiques. Ces avancées ont directement inspiré le chapitre 3, qui poursuit la complexification du modèle PDAC-on-chip en introduisant les composantes stromal clés — notamment l'acide hyaluronique et les fibroblastes associe au cancer — afin d'évaluer leur rôle dans la régulation de la transition épithélio-mésenchymateuse (EMT) et d'accroitre encore la pertinence physiologique du modèle.

Chapitre 3 – Complexification du modèle : rôle de facteurs sécrétés par les fibroblastes associés au cancer et de l'acide hyaluronique dans la transition épithélio-mésenchymateuse du PDAC-on-chip

Le troisième chapitre prolonge les travaux précédents en développant une seconde génération de modèles PDAC-on-chip, plus représentatifs du microenvironnement tumoral humain. L'objectif principal est d'évaluer la transition épithélio-mésenchymateuse (EMT) dans un contexte ou différents signaux stromaux — notamment l'acide hyaluronique (HA) et les fibroblastes associe au cancer (CAFs) — sont intégrés et modulés de manière contrôlée. L'EMT, processus clé de plasticité cellulaire favorisant la migration et la résistance du PDAC, demeure difficile à reproduire *in vitro*, en raison de la dépendance forte aux signaux mécaniques et biochimiques émanant du stroma.

Dans un premier temps, l'étude a explore l'effet du HA selon son poids moléculaire (moyen ou bas) et son mode d'intégration (incorporation dans la matrice, milieu ou exposition cellulaire directe avant l'auto-organisation en sphéroïdes). Les résultats ont révélé que le HA de poids moléculaire intermédiaire pouvait induire une augmentation significative de l'expression du récepteur CD44 et une modulation transitoire des marqueurs d'EMT (augmentation de la vimentine et diminution de l'E-cadhérine), surtout lorsque l'exposition survenait avant la formation du sphéroïde. Ces observations suggèrent que la nature dynamique de l'interaction cellule-HA et la disponibilité de la molécule a la

surface cellulaire jouent un rôle déterminant dans la plasticité phénotypique.

La seconde partie du chapitre a consisté à intégrer des cellules stellaires pancréatiques primaire et des fibroblastes associes au cancer dans le système microfluidique, soit en co-culture directe, soit *via* leurs milieux conditionnes. Cette approche a permis de dissocier les effets paracrines (*via* secrétions de cytokines et facteurs de croissance) des effets de contact direct. Les expositions au milieu conditionné de CAFs ont provoqué une induction marquée et soutenue de l'EMT, soulignant le rôle prépondérant des signaux paracrines dans la modulation de la plasticité tumorale. À l'inverse, les cultures en contact direct avec les CAFs n'ont pas montré d'effet significatif sur les marqueurs d'EMT, suggérant que les interactions mécaniques ou de contact cellule-cellule ne suffisent pas, à elles seules, à déclencher ce processus dans les conditions expérimentales étudiées.

Enfin, l'étude a examiné la stabilité temporelle des états EMT sur plusieurs jours de culture, révélant que le soutien continu en HA est nécessaire pour maintenir un phénotype mésenchymateux, tandis que l'effet induit par le milieu conditionné de CAFs persiste même après le retrait du stimulus, jusqu'au jour 6. Ces résultats mettent en évidence la distinction entre des signaux matriciels dépendants d'une présence physique prolongée et des signaux paracrines plus durables, reflétant les conditions *in vivo* où la production et la dégradation du HA — régulées par les enzymes HAS et HYAL — participent à un équilibre dynamique souvent rompu dans les tumeurs.

La discussion élargie qui suit le corps du chapitre revient sur la controverse scientifique persistante concernant les effets pro- ou anti-tumoraux de HA selon sa taille moléculaire : certains travaux attribuent aux fragments de faible poids un rôle activateur de l'invasion, tandis que le HA de haut poids serait plutôt anti-tumoraux. Nos résultats apportent une contribution à ce débat en montrant que, dans un contexte PDAC-on-chip, le poids moléculaire intermédiaire exerce l'effet inducteur plus marque, révélant un comportement non linéaire et dépendant du contexte cellulaire.

Ce chapitre marque une étape clé dans la construction d'un modèle PDAC-on-chip multi-composant, capable de reproduire les interactions dynamiques entre cellules tumorales, matrice et cellules stromales. Il ouvre la voie à des études intégratives associant, à terme, des organoïdes dérivés de patients et des lectures multi-omiques spatialisées, afin

d’aboutir à des modèles véritablement prédictifs pour l’évaluation thérapeutique personnalisée.

Ce travail démontre la pertinence des modèles PDAC-on-chip comme plateformes intégrées pour étudier les interactions tumeur–microenvironnement et évaluer de nouvelles stratégies thérapeutiques dans des conditions physiologiques contrôlées. En combinant microfluidique de précision et complexification progressive, il établit un cadre expérimental apte à relier mécanismes biologiques et réponses thérapeutiques.

Les perspectives ouvertes portent sur l’intégration de composantes immunitaires, l’usage de lectures multi-omiques et d’imageries quantitatives avancées, ainsi que la connexion de puces modulaires pour modéliser la dissémination et la résistance tumorales.

Cette thèse pose ainsi les bases d’une nouvelle génération de modèles précliniques du PDAC, alliant innovation technologique et pertinence biologique pour accélérer les avancées translationnelles.